

High-fidelity aerodynamic shape optimization of wind turbine blades

by

Tristan Dhert

A dissertation submitted in partial fulfillment
of the requirements for the degree of
Master of Science
(Aerospace Engineering)
in Delft University of Technology
2015

Thesis adviser:

Professor Turaj Ashuri, The University of Texas at Dallas, USA
Professor Joaquim R. R. A. Martins, University of Michigan, Ann Arbor, USA
Doctor Alexander van Zuijlen, Delft University of Technology, The Netherlands

Scientists discover the world that exists; engineers create the world that never was.

— Theodore von Kármán

© Tristan Dhert 2016

All Rights Reserved

ACKNOWLEDGEMENTS

The work presented in this dissertation could not have reached its current state without the help of a number of people. First of all, I would like to express my gratitude towards my advisors: Professor Joaquim R.R.A. Martins and Professor Turaj Ashuri. Without their faith in me, I would not have gotten the opportunity to perform research at the University of Michigan. Apart from giving me constantly good advice, their help in solving numerous problems has been from a great importance to successfully finish my dissertation. Their constant push and listening ear were indispensable for achieving significant results of this ambitious project. I would like to thank Doctor Alexander van Zijl for proofreading and providing more research suggestions in this work.

I would like to thank my colleagues at the Multidisciplinary Design Optimization Laboratory (MDOlab) for their support and suggestions. It has been a great experience and absolute pleasure to work with a multicultural and bright group. Special thanks goes to Gaetan Kenway, without his expertise and guidance, this work would not have been possible. Also, special thanks goes to Song Chen, I appreciate his relentless motivation, expertise in mesh generation, and support. I am Nitin Garg thankful in our development for the low speed preconditioner. I would also like to thank John Hwang, David Burdette, Jason Kao, Zelu Xu, Peter Lyu, John Wurts, and Davide Ivaldi for organizing numerous events after working hours. I would like to thank my office mates, Kentaro Hara, Yuntao Chen, Wai-Lee Chan, Anand Singh, and Brad Maeng, for their support, expertise and interesting discussions during dinner. Furthermore, special thanks to Thomas Economon, who supported me in obtaining SU2 results for rotating flow problems. Also I am thankful to thank Edwin van der Weide for his impressive expertise in CFD. Without his work, no significant analysis results would be obtained.

Most importantly, I would like to express my sincerest gratitude to my parents who have encouraged me all these years. Without their support and love, I would not have successfully finished my degree in Aerospace Engineering.

TABLE OF CONTENTS

ACKNOWLEDGEMENTS	ii
LIST OF FIGURES	vi
LIST OF TABLES	ix
LIST OF APPENDICES	x
LIST OF ABBREVIATIONS	xi
LIST OF SYMBOLS	xiii
SUMMARY	xvi
CHAPTER	
I. Introduction	1
1.1 Motivation	1
1.2 Thesis objective	1
1.3 Main and key research questions	2
1.4 Thesis outline	3
II. Literature review	4
2.1 Aerodynamic models for wind turbines	5
2.1.1 Momentum theory	5
2.1.2 Blade element momentum theory	8
2.1.3 Vortex and panel models	10
2.1.3.1 Induced velocity	10
2.1.3.2 Prescribed and free wake methods	12
2.1.3.3 Vortex methods	13
2.1.3.4 Panel methods	14
2.1.4 Computational fluid dynamics	15
2.1.4.1 Governing equations of fluid dynamics	15
2.1.4.2 Turbulence modelling	16
2.1.4.3 Boundary conditions	20
2.1.4.4 Mesh generation	22
2.1.4.5 CFD applications on wind turbines	24
2.2 Aerodynamic shape optimization of wind turbine blades	29
2.2.1 Low-fidelity optimization	29
2.2.2 High-fidelity optimization	32
2.3 Discussion and conclusion	35

III. Aerodynamic shape optimization methodology	37
3.1 Experimental set-up of NREL VI blade	37
3.2 Mesh generation	39
3.2.1 CAD design of NREL VI blade	39
3.2.2 Surface and volume mesh	41
3.3 CFD model	44
3.3.1 Governing equations in Arbitrary Lagrangian-Eulerian (ALE) form	44
3.3.2 Spatial discretization	47
3.3.3 Pseudo-time stepping	48
3.3.4 Turkel’s low speed preconditioner	49
3.3.5 Boundary conditions	51
3.4 Shape parametrization	52
3.5 Mesh deformation	53
3.6 Discrete adjoint method	54
3.7 Optimization procedure of the NREL VI blade	56
3.7.1 Problem statement	57
3.7.2 Optimization algorithm	58
3.7.3 Optimization approach	59
3.8 Limitations and assumptions	60
IV. Verification and validation of optimization method	62
4.1 Verification of optimization procedures	62
4.1.1 Mesh generation and perturbation	63
4.1.2 Verification of SUMad simulations	64
4.1.3 Residual analysis	65
4.1.4 Grid convergence study	67
4.1.5 Sensitivity analysis	69
4.2 Validation of CFD simulation results	72
4.2.1 Pressure coefficient distributions	72
4.2.2 Flow separation analysis	79
4.2.3 Torque and thrust analysis	82
4.2.4 Wake analysis	84
4.2.5 Comparison of turbulence models	86
4.2.6 Turkel’s low speed preconditioner	88
4.2.7 Periodic boundary conditions	89
4.3 Discussion and conclusion	90
V. Aerodynamic shape optimization results	92
5.1 Optimization with level 2 mesh	92
5.1.1 Pitch angle	93
5.1.2 Twist variables	94
5.1.3 Shape variables	95
5.1.4 Shape and twist variables	98
5.2 Optimization with level 1 mesh	99
5.2.1 Shape and twist variables with 100% thickness constraints	99
5.2.2 Shape and twist variables with 75% thickness constraints	100
5.2.3 Comparison between 75% and 100% thickness constraints	100
5.2.4 Thrust consideration after optimization	101
5.3 Optimization with level 0 mesh	102
5.3.1 CFD results with optimized level 1 mesh perturbations	102

5.3.2	Comparison between modified and original NREL VI blade	103
5.4	Optimization convergence analysis of modified NREL VI blade	104
5.5	Multipoint optimization	106
5.6	Discussion and conclusion	107
VI.	Final remarks	110
6.1	Conclusion	110
6.2	Contributions	112
6.3	Recommendations	112
APPENDICES	115
A.1	Unstructured computational domain	116
A.2	Convergence analysis	117
A.3	SU2 analysis results	118
A.4	Computational cost	119
A.5	Discussion and conclusion	120
B.1	Thrust Comparison between RANS-based CFD solvers	121
B.2	Flow separation behavior of the modified NREL VI blade	122
BIBLIOGRAPHY	123

LIST OF FIGURES

Figure

2.1	Simple momentum theory	5
2.2	Velocity vectors at disc plane	8
2.3	Possible flow field representation methods	11
2.4	Vortex method representations	14
2.5	Idealized spectrum of turbulent kinetic energy of isotropic turbulence with respect to wave number k . The small scales with low energy from $k(c)$ are filtered out by LES.	19
2.6	Law-of-the-wall for smooth surfaces. The logarithmic layer is valid until $y^+ = 500 - 1000$	21
2.7	Combination of overset and multi-block configuration for structured mesh of a multi-megawatt wind turbine [134]	23
2.8	Hybrid mesh of NACA 0012 airfoil with high orthogonal cells at boundary layer and unstructured cells at outer region	23
2.9	Adaptive mesh refinement of transonic flow over NACA 0012 airfoil [142]	24
2.10	Adaptive mesh refinement of the wake of the NREL VI blade [153]	26
2.11	Vortical flow field at nacelle section; red dot is representing the nacelle anemometer [159]	27
2.12	Different vortical wake resolutions in a plane bisecting the turbine. The change in resolution is obtained by refining the mesh [168].	28
2.13	Bézier parametrization method for airfoils [176]	30
2.14	FFD volume (left) and B-spline surface representation (right) of DPW4 geometry [219]	33
2.15	Drag minimization of the BWB aircraft configuration while constraining lift coefficient. Note that the optimization removed the shock surface, which resulted in a considerable reduction of drag [235].	34
3.1	Blade surface pressure and five-hole probe locations [250]: More pressure tabs are located at the leading edge for achieving increased resolution of the pressure distribution.	38
3.2	CAD designs of the NREL VI blade	41
3.3	Spherical volume mesh created by in-house code ‘PyHyp’	42
3.4	Reference shapes of computational domains for various amounts of volume cells. Note that the inflow and outflow are considered to be far field boundary conditions in SUMad	43
3.5	Characteristic condition number versus Mach number [262]. 2D PC: characteristic condition number after optimal 2D preconditioning. 3D PC: characteristic condition number after optimal 3D preconditioning	49
3.6	FFD volume approach on the NREL VI rotor	52
3.7	Mesh perturbation of the NREL VI blade at $z = 3.3$ m	54
3.8	Flow chart of the aerodynamic shape optimization of the NREL VI rotor	60

4.1	Verification of surface mesh. Note that the cylinder has a band of very small surface cells due to blunt trailing edge. This can be alleviated when using unstructured meshing.	64
4.2	Verification of SUMad for rotational flow problems	65
4.3	RMS residual of density with corresponding force and moment coefficients	66
4.4	Stagnation of RMS residual of density due to flow separation at cylinder and transition part of the NREL VI blade	66
4.5	Residual behavior for different wind speeds	67
4.6	Residual and load coefficient behavior for modified NREL VI blade at 7 m/s	67
4.7	Grid convergence analysis of torque	68
4.8	Pressure distribution convergence at $z/R = 95\%$	69
4.9	Accuracy of complex step and finite difference [273]	70
4.10	Forward finite difference approximation for design variables with respect to torque	71
4.11	Sensitivity surfaces of upper and lower NREL VI blade: $\partial C_{Mx}/\partial x$	72
4.12	C_p distributions at $U_\infty = 5\text{m/s}$	73
4.13	C_p distributions at $U_\infty = 7\text{m/s}$	74
4.14	C_p distributions at $U_\infty = 10\text{m/s}$	75
4.15	C_p distributions at $U_\infty = 13\text{m/s}$	76
4.16	C_p distributions at $U_\infty = 15\text{m/s}$	77
4.17	C_p distributions at $U_\infty = 20\text{m/s}$	78
4.18	C_p distributions at $U_\infty = 25\text{m/s}$	79
4.19	Flow separation behavior for various wind speeds on the NREL VI blade: moderate flow separation starts at 10 m/s. The blade is in deep stall condition at 20 m/s.	80
4.20	Relative velocity fields at $z/R = 63\%$ with various flow separation conditions	81
4.21	Torque values for various wind speeds	82
4.22	Torque comparison between RANS-based CFD models	83
4.23	Thrust values for various wind speeds	84
4.24	Vorticity magnitude contour and iso-surface of the wake	85
4.25	A higher tip speed ratio results in higher vortex shedding frequency	86
4.26	Comparison of turbulence models with respect to surface streamlines at 15 m/s	87
4.27	Torque comparison between Menter's SST and SA turbulence model	87
4.28	Convergence history of Turkel's low speed preconditioner at 7 m/s	88
4.29	C_p distributions at $V_\infty = 7\text{m/s}$ using Turkel's low speed preconditioner	89
4.30	C_p distributions at $V_\infty = 7\text{m/s}$ using periodic boundary conditions	90
5.1	Optimization history with pitch angle as design variable	93
5.2	Pitch angle optimization of modified NREL VI blade	94
5.3	Twist distribution optimization of the modified NREL VI blade	95
5.4	Level 2 optimization with shape variables of modified NREL VI blade	96
5.5	Mesh failure during optimization with shape variables	96
5.6	Level 2 optimization with shape variables and 100% thickness constraints of modified NREL VI blade	97
5.7	Level 2 optimization with shape and twist variables and 100% thickness constraints of modified NREL VI blade	98
5.8	Level 1 optimization with shape and twist variables and 100% thickness constraints of modified NREL VI blade	99
5.9	Level 1 optimization with shape and twist variables and 75% thickness constraints of modified NREL VI blade	100
5.10	Pressure coefficient distribution comparison of 75% and 100% thickness constraint optimization	101
5.11	twist and torque distribution comparison of 75% and 100% thickness constraint optimization	101
5.12	Significant thrust increase with 100% thickness constraint optimization with shape and twist design variables	102
5.13	Level 0 mesh with design variables of level 1 of modified NREL VI blade	103

5.14	Pressure coefficient comparison of optimized NREL VI blade in modified and original configuration	103
5.15	Surface streamline comparison of optimized original and modified NREL VI blade	104
5.16	Optimization convergence analysis of modified NREL VI blade	105
5.17	Multipoint optimization of modified NREL VI blade at 7 m/s	106
5.18	Comparison of torque curve between baseline and optimized modified NREL VI blade	107
5.19	Comparison of multipoint and single-point optimization at 7 m/s	108
A.1	Unstructured surface mesh of NREL VI wind turbine blade	116
A.2	Unstructured volume mesh of NREL VI wind turbine blade	117
A.3	Convergence analysis of SU2 for NREL VI wind turbine blade	117
A.4	C_p distributions at $U_\infty = 7$ m/s	118
A.5	C_p distributions at $U_\infty = 13$ m/s	119
B.1	Thrust comparison of various RANS-based CFD solvers	121
B.2	Flow separation behavior of the modified NREL VI	122

LIST OF TABLES

Table

3.1	Averaged sequence S operation conditions	39
3.2	Dimensions of NREL VI wind turbine blade: The origin of the reference frame is given by $[x_0, y_0, z_0] = [0, 0, 0]$	40
3.3	Forward automatic differentiation of $f(x, y) = xy + \sin(x)$	56
4.1	Gradient approximations using solid mesh warping. Note that the adjoint method is as accurate as the finite difference, since the torque fluctuates at fourth decimal.	71
5.1	Increase in torque for different mesh resolutions after optimization	105
5.2	Increase in thrust of various optimization results	109
5.3	Performance of high fidelity aerodynamic shape optimization of the NREL VI blade	109
A.1	Computational time of SUMad and SU2 at attached flow conditions for NREL VI blade	120

LIST OF APPENDICES

Appendix

A.	NREL VI wind turbine blade computations with SU2	116
B.	Additional SUMad results and optimization	121

LIST OF ABBREVIATIONS

ABL	Atmospheric Boundary Layer
AEP	Annual Energy Production
ALE	Arbitrary Lagrangian-Eulerian
BB	Baldwin-Barth
BEM	Blade Element Momentum
BFGS	Broyden-Fletcher-Goldfarb-Shanno
BIEM	Boundary Integral Equation Method
BWB	Blended-Wing-Body
CAD	Computer-Aided Design
CFD	Computational Fluid Dynamics
CFL	Courant-Friedrichs-Lewy
COE	Cost Of Energy
CPU	Central Processing Unit
CRM	Common Research Model
DES	Detached-Eddy Simulation
DNS	Direct Numerical Simulation
FFD	Free Form Deformation
FEM	Finite Element Method
ICEM	Integrated Computer Engineering and Manufacturing
JST	Jameson-Schmidt-Turkel
LES	Large Eddy Simulation
LM	Lunderskov Møbelfabrik
MDO	Multidisciplinary Design Optimization
MPI	Message Passing Interface
MUSCL	Monotone Upstream-Centered Scheme for Conservation Laws
NACA	National Advisory Committee for Aeronautics

NASA	National Aeronautics and Space Administration
NREL	National Renewable Energy Laboratory
PDE	Partial Differential Equation
RANS	Reynolds-Averaged Navier-Stokes
RMS	Root Mean Square
RSTM	Reynolds Stress Transport Model
SA	Spalart Allmaras
SNOPT	Sparse Nonlinear OPTimizer
SU2	Stanford University 2
SUMad	Stanford University of Michigan adjoint
SUmb	Stanford University multi-block
SST	Shear Stress Transport
SGS	Sub-Grid Scale
UAE	Unsteady Aerodynamics Experiment
VISCEL	Viscous and Aeroelastic Effects on Wind Turbine Blades

LIST OF SYMBOLS

Latin Symbols

A	Jacobian matrix / Roe matrix
a	Axial flow induction factor / Speed of sound
a'	Tangential flow induction factor
B	Intercept of logarithmic law / Jacobian matrix
c	Chord
C_p	Power coefficient / Pressure coefficient
c_p	Specific heat capacity at constant pressure
C_t	Thrust coefficient
$C_{f,x}$	Local skin friction coefficient
E	Turbulent kinetic energy / Total absolute energy of a fluid
e	Unit vector
F	Body force / Inviscid flux
G	Convolution kernel / Viscid flux
g	Body force per unit mass
I	Objective function / Identity matrix
i	index / Imaginary number
j	index
k	index / Wave number
k_s^+	Roughness Reynolds number
m	index
P	Preconditioner matrix
p	pressure
Q	Body force representing combined effect of centrifugal and Coriolis force
R	Gas constant / Residual / Radius
r	Local radius
S	Face area of control volume

T	Temperature
t	Time / Thickness
U	Velocity
u'	Velocity fluctuation
u_*	Friction velocity
u_ω	Velocity of co-rotating reference frame
U_{disc}	Velocity at actuator disc
U_{ind}	Induced velocity
$U_{d,\infty}$	Far downstream velocity
$U_{u,\infty}$	Far upstream velocity
W	Conserved state variables of Navier-Stokes equations
x	Position / Local position in x -direction w.r.t. reference frame / Local reference length / Design variable
x'	Location at which the integral is evaluated
x_{rad}	Radial speed ratio
y	Local position in y -direction w.r.t. reference frame
y^+	Dimensionless wall distance
z	Local position in z -direction w.r.t. reference frame

Greek Symbols

α	Effective angle of attack / Right eigenvector of Roe Matrix
Δ	Filter width
δ	Dirac function
Γ	Vortex/Circulation strength
κ	von Kármán constant
λ	Tip speed ratio / Eigenvalues of Roe matrix
ν	Kinematic viscosity
ω	Angular or rotational velocity
ϕ	Angle between resulting velocity and rotor plane
Ψ	Solenoidal vector potential field
ρ	Fluid density
τ	Shear stress
Θ	Scalar potential field
θ	Angle between rotor plane and zero lift direction / Initial angle of rotation

Other Symbols

=	Equal to
Δs	Off-wall distance
\leq	Lower or equal to
Pr_{lam}	Laminar Prandtl number
Pr_{turb}	Turbulent Prandtl number
Re_x	Local Reynolds number

Subscripts

0	Initial conditions
∞	Free-stream conditions
c	Compressible conditions
rel	Relative conditions

Superscripts

\mathcal{T}	Numerical flux representation / Order of magnitude
\bar{x}	Averaged quantity / Filtered quantity
\tilde{x}	Approximation representation
\underline{x}	Matrix representation
\vec{x}, \boldsymbol{x}	Vector representation

SUMMARY

High-fidelity aerodynamic shape optimization of wind turbine blades

by

Tristan Dhert

Recent improvements in accuracy and efficiency of numerical simulation techniques in the field of engineering have led to an increasing interest in applying high-fidelity models for wind turbine design. Computational Fluid Dynamics (CFD) based on Reynolds-Averaged Navier-Stokes (RANS) equations in a co-rotating reference frame has shown promising results for performing design analysis. However, using high-fidelity techniques for wind turbine blade design optimization is not yet fully understood. Especially, high-fidelity aerodynamic shape optimization for wind turbine blades has not yet been employed in the industry due to its computational inefficiency when large number of design variables are used with traditional techniques such as finite difference derivatives and gradient-free optimization methods.

This dissertation presents an efficient and robust high-fidelity aerodynamic shape optimization methodology for rotating flow problems. The high-fidelity optimization method consists of a multi-block, structured RANS-based CFD simulation tool, a discrete adjoint method, a shape parametrization method, a mesh perturbation technique and a gradient-based optimizer. Steady-state solutions are obtained by the RANS-based CFD analysis method based on a co-rotating reference frame. The turbulence model is a segregated one-equation SA model. Total derivatives of the flow solution and constraint(s) are computed by a discrete adjoint method. For reducing the computational cost of computing partial derivatives that are required in the discrete adjoint method, forward automatic differentiation is used. Once the total derivatives and flow solution are computed, the gradient-based optimizer based on sequential quadratic programming computes a better design by using an augmented Lagrangian formulation with quasi-Newton approximations for the Hessian. The change in design variables obtained by the optimizer is parametrized with a Free Form Deformation (FFD) volume approach. After performing surface perturbations, the mesh is deformed using a hybrid mesh deformation scheme, that combines an algebraic and linear elasticity method. The linear elasticity method based on finite elements is used for large perturbations, while the algebraic method attenuates small perturbations. When the optimality condition is satisfied, the iterative procedure ends with the optimal design.

Verification and validation of the developed codes are performed using the NREL VI wind turbine. The RANS-based CFD solver is validated by comparing numerical results with NREL VI sequence S experimental data. The solver resolves attached flow conditions accurately, while sepa-

rated flow conditions lead to inaccurate flow solutions due to insufficient transition and turbulence modeling. DES can resolve the inaccuracy associated with separated flow conditions. Total derivatives of the adjoint method are verified by comparing derivatives of the complex and finite difference method. The quality of (perturbed) meshes are verified by using mesh quality metrics. Correct shape parametrization is assured after careful examining the direction and magnitude of the deformations.

Since the NREL VI wind turbine blade rotates at a constant angular velocity, the power generation is considered to be only dependent on torque. Therefore, the objective of the optimization is maximizing the torque coefficient with shape, twist, and pitch design variables. Thickness constraints between 15% and 50% are added for representing a wing box. The thickness constraints impose thicknesses of the blade to increase only up to 300% of the original thickness. No reduction in thickness with respect to the baseline design at that region of the blade is possible in order to fit the original wing box. For future research, the objective and constraint function(s) can be easily adapted to more realistic and modern rotating flow problems.

From the aerodynamic shape optimization of the NREL VI blade, an increase of at least 22.4% in torque is achieved. The airfoil shapes tends to become more cambered and less thick. The nose of the airfoil is more aligned to the inflow. At root section of the wind turbine blade, the trailing edge of the airfoil acts as a flap in order to obtain higher loads at low relative velocity. Three different mesh refinements are employed for optimization. The first mesh is a coarse mesh that is used for verification purposes of the optimization procedure. The second mesh is employed for obtaining accurate aerodynamic shape optimization results. The final design variable values of the medium refined mesh are projected on the most refined mesh, because computational costs would be too high for performing optimization. An increase of 29.1% in torque is achieved, indicating that the increase in optimized torque for more refined meshes will be higher when using coarser meshes. Since wind turbines are operating in a range of wind speeds, multipoint optimization from cut-in to rated wind speed is performed. Similar results as in single-point optimization are achieved. An increase of 22.2% in Annual Energy Production AEP is obtained.

The adjoint method and high-fidelity aerodynamic shape optimization methodology allow designers to examine accurately the trade-off between various design variables at the early stage of the design process. For future research purposes, aerostructural and aeroelasticity optimization can be employed with the same framework.

CHAPTER I

Introduction

1.1 Motivation

Recent improvements in high performance computing has increased the usage of high-fidelity numerical models and optimization techniques in academia and industry. Computational Fluid Dynamics ([CFD](#)) tools and optimization algorithms have been employed to shorten design cycle times and to analyze large design spaces efficiently. With these tools, designers can obtain more detailed designs earlier in the design process, allowing them to understand the trade-offs and making better decisions. High-fidelity aerodynamic shape optimization can result in high computational costs when applying traditional gradient approximation techniques, such as finite difference or complex step method. Recent developments in adjoint methods have dramatically improved the computational efficiency of aerodynamic shape optimization. However, due to the complexity of [CFD](#) solvers, it is still a challenging task to implement an adjoint method.

Performing accurate [RANS](#)-based [CFD](#) simulations on wind turbines requires expertise knowledge, since it involves multiple areas of science, such as computational modeling, aerodynamics, and programming. To date, high-fidelity models are only used for detailed design at the end of the design process and no considerable gradient-based high-fidelity aerodynamic shape optimization is employed. Given the global increase in wind energy and restricted area for wind energy development, improvements in wind turbine performance without major increase in capital cost are necessary. Therefore, a robust and efficient high-fidelity aerodynamic shape optimization methodology with an adjoint method for wind turbines will be developed. The methodology will be applied on the [NREL](#) VI wind turbine blade for examining the impact of aerodynamic shape optimization.

1.2 Thesis objective

The project goal of this research is to develop a high-fidelity aerodynamic shape optimization method for wind turbine blades by combining a [RANS](#)-based [CFD](#) model with a gradient-based optimization technique. The framework should be efficient and robust for solving large-scale aerodynamic design optimization problems. The main tasks of this research are listed below:

- Perform [RANS](#)-based [CFD](#) analyses.
- Implement efficient gradient computation to the [RANS](#) equation using discrete adjoint method.

- Verify total derivatives using finite difference and complex step method.
- Implement and verify mesh perturbation method.
- Validate RANS-based CFD analysis.
- Optimize the power generation of the NREL VI wind turbine blade using the aerodynamic shape optimization framework

1.3 Main and key research questions

Based on the motivation and the objective of this research, the main research question is what the impact is of performing a high-fidelity aerodynamic shape optimization methodology on a wind turbine blade design. In order to assess the main research question, four key research questions need to be answered:

- What is the problem statement of the aerodynamic shape optimization?

The problem statement will be focussed on optimizing aerodynamic variables that are relevant to wind turbine blades. It is known that COE is an important key factor for designing wind turbines, but given the focus on aerodynamics it is not relevant for this research. In the near future, COE will become an important factor when structures and costs are added. Geometrical and shape design variables will be employed for aerodynamic shape optimization

- How accurate is the RANS-based CFD solver?

In order to obtain a high-fidelity aerodynamic shape optimization, the analysis method must be validated for obtaining the accuracy level. The validation will be achieved by comparing experimental results with computational results. It will become clear that the choice of wind turbine blade will be mainly dependent on the availability of qualitative experimental data. For future research, other wind turbine blades can be used when the accuracy is known from this validation procedure.

- What are the changes and consequences of the optimized design?

When the aerodynamic shape optimization is performed, the optimal design can have different airfoil shapes along the span. This will have definitely a positive effect on the performance of the wind turbine blade. In order to assess these effects, comparison should be made between the baseline and optimized design.

- What are the requirements to perform high-fidelity aerodynamic shape optimization?

Besides acquiring the knowledge for performing aerodynamic shape optimization, the computational cost will be a key factor on the viability of aerodynamic shape optimization method. Computational cost will involve how many processors are required to solve an optimization at a reasonable computational time. Also the robustness of the optimization is essential for successfully achieving optimal solutions.

1.4 Thesis outline

The current state of aerodynamic models for wind turbines is presented in the literature review given in Chapter II. High-fidelity aerodynamic shape optimization has not been extensively used for wind turbines. Therefore, the literature review discusses high-fidelity aerodynamic shape optimization techniques related to aerospace applications in order to obtain proper knowledge for applying the same optimization method on wind turbine blades. The aerodynamic shape optimization methodology is discussed in Chapter III. This chapter gives an overview of the modules in this methodology. It also presents an application of the framework by applying aerodynamic shape optimization to the NREL VI blade. The first part of Chapter IV verifies the modules of the aerodynamic shape optimization framework. Subsequently, the RANS-based CFD solver is validated by comparing computational results with NREL VI sequence S experimental data. Once the framework is verified and validated, aerodynamic shape optimization of the NREL VI wind turbine blade is performed in Chapter V. The effect of mesh refinement and types of design variables is investigated. Also, single and multipoint optimized designs are compared. In Chapter VI, conclusions, contributions, and recommendations are summarized.

CHAPTER II

Literature review

While most of the other sources of renewable energies are at the proof of concept stage [1, 2], wind energy is becoming a mature and reliable source of energy. Therefore, the share of wind-generated electricity is continuously increasing, and it is expected to meet a target of 1000 GW of wind energy by 2030 [3]. Extracting wind energy efficiently is a complex task that requires special design methods and considerations [4]. This complexity increases as the size of wind turbines keeps growing, particularly for future offshore applications [5].

Given the continuous upscaling challenges [6, 7], and the multidisciplinary nature of wind turbines, a trade-off between aerodynamic performance, structural efficiency, operational and manufacturing costs has to be taken into account. Therefore, improvements in wind turbine performance applying Multidisciplinary Design Optimization (MDO) could become an important tool to evaluate the trade-off between wind turbine performance and economics of wind energy [8]. Numerous studies have shown different approaches ranging from optimizing the rotor design to plant layout [9]. All optimization procedures employ various fidelity models varying from analytical models to Computational Fluid Dynamics (CFD) simulations coupled with structural finite element analysis.

Most common objective functions for multidisciplinary design optimization for wind turbines are maximizing Annual Energy Production (AEP), minimizing Cost Of Energy (COE), or multi-objective functions such as maximizing power while minimizing thrust or bending moments [10]. Various optimization techniques include gradient-based methods (conjugate gradient method, method of feasible descent, and sequential quadratic programming) and gradient-free methods (genetic algorithms, Nelder–Mead simplex, and particle swarm optimization). Gradient-based optimizations are fast but sensitive to non-smooth design spaces, while gradient-free optimizations are robust but inefficient for large number of design variables [11].

Currently, most wind turbine blade designs are based on low-fidelity aerodynamic shape optimization, due to their easy implementation and its fast convergence to feasible solutions. However, these models do not represent compressibility and viscosity effects. This results in designs neglecting complex flow phenomena and consequently reducing the reliability and producing unpredictable power outputs. In order to alleviate this problem, high-fidelity models can be implemented in the optimization process. The disadvantage of using these high-fidelity models is its high computational cost and complexity in implementation.

The method described in this dissertation is suitable for capturing aerodynamics loading and performance only. However, for performing optimization of the blade, other design considerations

such as airfoil performance decline [12], inertial and hydrodynamic loads [13, 14], and environmental uncertainties [15] need to be also accounted for, which is not the interest of this work.

The remainder of this chapter is organized as follows. First, a brief overview of aerodynamic analyses and optimization applications on wind turbine blades will be presented. No significant high-fidelity aerodynamic shape optimization of wind turbines has been performed. Therefore, it was decided to review some high-fidelity optimization of aerospace applications to existing aerospace technologies on wind turbine blades. Then, conclusions will be drawn in which the goal and research question of the dissertation will be presented.

2.1 Aerodynamic models for wind turbines

Optimization problems require an analysis model to quantify the objective function and constraints. These analysis models are coupled to an optimization algorithm, which iterates the design variables. In most cases, the accuracy of the optimized solution is dependent on the analysis model. In this section, various aerodynamic models applied on wind turbine blades are explained and discussed, from low-fidelity models to high-fidelity models. The momentum theory will be explained first in which the rotor is represented as a disc. By applying the momentum theory and blade element theory, the performance of the actual geometry of the wind turbine rotor can be predicted with a reasonable accuracy. However, due to its two-dimensional behaviour, vortex and panel methods are developed that could simulate three-dimensional effects. Models based on vortex and panel methods do not have the proper capabilities of resolving complex flow behavior, viscosity, and compressibility effects. As a result of these limitations, CFD simulations are employed using moving meshes or rotating reference frames.

2.1.1 Momentum theory

Momentum theory models the mechanism of extracting kinetic energy by means of an actuator disc. The theory has been developed by Rankine [16] and has been elaborated further by Greenhill and Froude [17]. It is often used as a preliminary prediction tool before more advanced tools are applied on the design of the system.

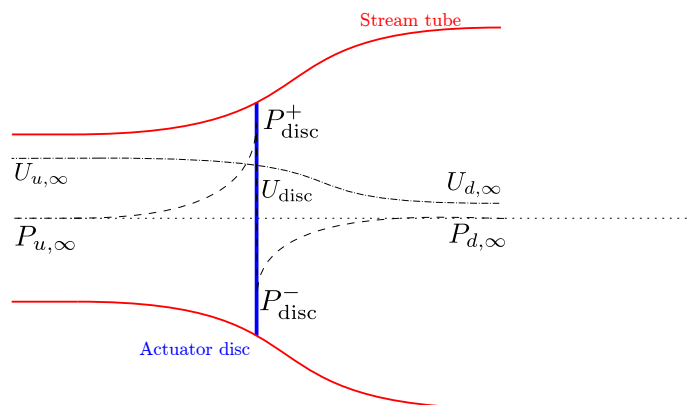


Figure 2.1: Simple momentum theory

The extraction of kinetic energy can be explained by referring to Fig. 2.1: Assuming that the

affected mass of air does not interact with the free-stream flow, a stream-tube can be drawn around the actuator disc that extends from upstream to downstream. The mass flow rate is constant, because no air crosses the boundary of the stream tube. Given that the air is incompressible and that the flow must slow down across the actuator disc, the cross-sectional area of the stream tube is forced to increase in order to keep a constant mass flow rate. Since kinetic energy is extracted, a sudden drop in the velocity at the actuator is expected. Due to the unrealistic associated forces, this can not happen and the velocity decreases gradually across the actuator disc until the flow reaches atmospheric pressure. The static pressure in front of the actuator disc increases as a result of reduction in velocity. When the flow reaches the actuator disc, the static pressure will drop suddenly. After the abrupt change in static pressure, the wake returns to atmospheric pressure reaching equilibrium condition. In order to obtain this condition, the cross-sectional area of the stream tube increases again. Since there is only a difference in velocities far upstream and far downstream, the actuator disc extracts kinetic energy. The assumptions of momentum theory are the following:

- No rotation is imposed on the flow by the actuator disc
- The stream tube boundary (slipstream) separates the affected flow by the actuator disc from flow outside the actuator disc
- Thrust loading is uniform over the actuator disc
- The static pressure in and out the stream tube far downstream and upstream of the actuator disc are equal to free-stream atmospheric conditions
- The design of the actuator disc is irrelevant (No frictional drag)

From the explanation above, the actuator disc theory can be derived from the continuity equation, the axial momentum equation, and applying the Bernoulli equation upstream and downstream of the actuator disc. Since the flow already slows down at the actuator disc, an induced velocity should be imposed on the free-stream velocity. This is usual done by use of an axial flow induction factor a . From this, the far downstream velocity $U_{d,\infty}$ can be related to the far upstream velocity $U_{u,\infty}$:

$$U_{d,\infty} = (1 - 2a) U_{u,\infty}. \quad (2.1)$$

Given the pressure difference at the actuator disc, the thrust and power coefficient are related to the axial flow induction factor:

$$C_t = 4a(1 - a), \quad (2.2)$$

$$C_p = 4a(1 - a)^2. \quad (2.3)$$

The power coefficient can be maximized by calculating the axial flow induction factor of which the derivative of the pressure coefficient is zero. Betz [18], Lanchester [19], and Joukowsky [20] showed that the maximum power coefficient is $16/27$. The Lanchester-Betz-Joukowsky limit [21] represents the maximum amount of kinetic energy that can be extracted from the wind independent of the design of the actuator disc.

For further information on various flow states related to the axial flow induction factor, the following is presented [22]: In order to apply the momentum theory, the flow should stay in the so-called windmill state, where the value of the axial flow induction factor is between $0 < a < 0.5$. Experiments have shown that the axial flow induction factor can only go up to 0.4 in order to have a valid actuator disc model [23]. When the axial flow induction factor is in the interval of $0.5 \leq a \leq 1$, the wake velocity becomes negative and a turbulent wake state appears in which recirculation is present downstream of the actuator disc. If the axial flow induction factor is higher than 1, the state of the flow can be considered as a flow in which a propeller is acting as a brake, i.e. energy is added to the flow so that a high thrust is acting downstream. A special case occurs when $a = 1$: The flow through the actuator disc is blocked and it is in a vortex ring state. Since the momentum theory is violated for $0.5 \leq a \leq +\infty$, empirical modifications are required [24] [25]. Negative values of the axial flow induction factor will set the flow in a propeller state. And when $a = 0$, the flow is in a zero slip case.

As an extent to the momentum theory, torque is considered to be acting on the actuator disc, which results in rotational energy. As a result, the total kinetic energy of the flow is decomposed in translational energy, rotational energy, and kinetic energy captured by the actuator disc. It is clear that when taking the rotational energy into account, the maximum extracted power is less than the Lanchester-Betz-Joukowsky limit. When applying a rotating annular stream-tube analysis, the tangential flow induction factor a' can be related to the axial flow induction factor a :

$$a' = \frac{1 - 3a}{4a - 1}. \quad (2.4)$$

When the induction flow factors are calculated, the radial speed ratio x_{rad} can be solved:

$$x_{\text{rad}} = \sqrt{\frac{a(1-a)}{a'(1+a')}}. \quad (2.5)$$

The radial speed ratio increases as the axial flow induction factor reaches 1/3. In order to compute the optimal power coefficient for a specific tip speed ratio, the following equation should be solved with the corresponding optimal flow induction factors:

$$C_p = \frac{8}{\lambda^2} \int_0^\lambda a' (1-a) x^3 dx_{\text{rad}}, \quad (2.6)$$

where λ is the tip speed ratio. Solving the above equation for multiple tip speed ratios, it can be shown that the energy loss due to rotation is small for tip speed ratios larger than 6. In other words, the amount of extracted power converges to the Lanchester-Betz-Joukowsky limit when the tip speed ratio increases [26].

Even though the rotation of the wake has been taken into account, the expansion of the wake is not implemented in this analysis: Due to the rotation of the wake, an additional fall of static pressure occurs in the wake. By this observation, it can be suggested that a significant error is introduced in this theory. However, this assumption does not greatly affect the correctness of the solution for wind turbines with a high tip speed ratio [27]. Wind turbines operating at low tip speed ratios, however, will be compromised in this theory.

In order to reproduce the momentum theory even more accurately, the Navier-Stokes equations

can be applied by use of semi-analytical/analytical methods or by use of finite difference methods [28]. Also, unsteady actuator disc models can be developed using computational modeling [29].

2.1.2 Blade element momentum theory

According to the momentum theory, the design of the actuator disc is irrelevant to the extraction of kinetic energy. The Blade Element Momentum (BEM) theory, however, incorporates the design of the actuator for power extraction. This results in calculating aerodynamic loads, moments, and the power of the turbine in different settings, such as wind speeds, pitch angles, and rotational speeds. This method can also be used for time-varying purposes and fluid-structure interaction [30]. BEM theory combines the momentum theory with the blade element theory developed by Froude, Taylor, and Drzewiecki [31]. The loads can be calculated by subdividing the blade in several elements, as such the flow problem becomes two-dimensional, where load coefficients are calculated by extrapolating given two-dimensional airfoil characteristics. Using this assumption, three-dimensional flow phenomena are not included. Another assumption is that the axial flow induction factor is radially constant (it is shown that the axial flow induction factor varies [32]). Shown in Fig. 2.2, the angle of attack is determined by the velocity components expressed in terms of wind speed, flow induction factors, and rotational speed of the rotor. Subsequently, the aerodynamic coefficients of the airfoil are extrapolated from the angle of attack.

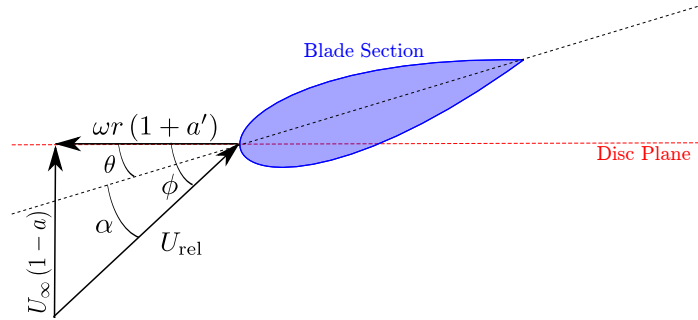


Figure 2.2: Velocity vectors at disc plane

From this observation, the resultant relative velocity can be calculated and used for calculating the loads of the segments. Using the aerodynamic coefficients and the momentum theory, two implicit equations are iteratively solved for the axial and rotational flow induction factor as follows:

1. Initialize axial and angular flow induction factor
2. Compute flow angle and local angle of attack
3. Find the lift -and drag coefficient of the airfoil with the corresponding angle of attack
4. Compute tangential and normal components with respect to the disc plane
5. Compute axial and rotational flow induction factor
6. Iterate until a certain tolerance has been reached for the flow induction factors

When the flow induction factors are converged to a certain tolerance, the loads on each element can be computed. From the loads, the elements can be integrated to obtain power, thrust, and bending moments. Given the above steps, two corrections can be added for higher accuracy of the algorithm:

1. Prandtl's tip loss factor [33]: Since the vorticity of the wake is different for an actuator that has an infinite amount of blades compared to a finite number of blades, it is necessary to correct this assumption. Other tip loss corrections exist as well and are described by [34].
2. Glauert correction on the axial flow induction factor: As stated in Section 2.1.1, the axial flow induction factor cannot exceed a value of 0.4 for representing an ideal wind turbine state. Therefore, correction methods are developed for preventing the axial flow induction factor to exceed 0.4. Empirical relationships are made in order to represent the thrust coefficient more accurately as a function of the axial flow induction factor [35].

The assumptions and methods of the classical BEM theory are presented above. It is clear that the steps of the iteration method can be modified in order to include phenomena specific to wind turbines. Some of these modified BEM models include yawed flow conditions in which the radial independence is violated [36, 37, 38, 39]. This phenomenon occurs frequently in reality, since the wind direction is not always perpendicular aligned with the rotor disc. As a result of flow misalignment, wind turbine blades can suffer fatigue. Also, BEM theory can be configured to simulate time-dependent flow phenomena. This means that the equilibrium wake assumption* of the momentum theory will be violated. This happens when the flow field over the wind turbine blade is changing over time due to unsteady wind conditions, blade control, and blade deformations. By rewriting the dynamic differential equations in the annular momentum equations, unsteady phenomena can be captured by BEM theory. Some of these unsteady phenomena are the following: Dynamic stall [40, 41, 42], dynamic wake/inflow [43], etc.

One of the main challenges in BEM theory is to find a proper estimation for high load cases in which static stall can occur. Also many wind turbine designs are dependent on stall regulations for limiting energy extraction and preventing structural damages during high wind speeds. Therefore, it is important to estimate this phenomenon accurately enough in order to have a proper approximation of the power output, especially the peak power. The BEM theory should not only be able to predict the power output correctly but stall effects since most wind turbines make use of stall control. Many methods are used for estimating static stall: Empirical relationships can be developed in order to correct for these errors. One of these empirical relations extrapolate lift and drag data up to an angle of attack of 90° [44]. Also wind tunnel data can be used for estimating post-stall properties. Besides static stall, stall delay, induced by rotation, can also be incorporated resulting in more accurate predictions [45].

Due to three-dimensional effects associated with wind turbine blades, it is necessary to have methods that can reliably extrapolate airfoil data. One of these methods is using wind tunnel measurements. However, these measurements are often limited to the maximum lift coefficient, because most of the data is based on attached flow conditions and lack in Coriolis and centrifugal effects. Therefore, when extracting airfoil measurements, it is recommended to incorporate stall and rotation effects for two-dimensional airfoil data [46, 47]. CFD is another option that computes three-dimensional blade data, that are used for aerodynamic coefficients in BEM theory for further

*there is an instantaneous equilibrium between momentum fluxes far upstream and downstream

analysis [48]. This approach also allows for design of specialized airfoils for wind turbine blades [49]. Other methods include correcting two-dimensional airfoil data for three-dimensional rotational effects and correcting pressure distributions [50, 51]. Other variants and extensions to BEM also exist such as double multiple stream tube theory [52] that have been applied to design analysis of wind and wave turbines [53, 54, 55, 56].

2.1.3 Vortex and panel models

Vortex and panel models are representing the potential flow field through a distribution of simple ideal flows, such as sources, doublets and vortices. Later on, in the 20th century, Prandtl developed a method that could find aerodynamic properties of lifting surfaces using vortex representations in flows. The so-called Prandtl lifting line theory [57, 58] provides an analytical method for estimating induced drag and lift for finite lifting surfaces. The hypothesis of Prandtl's theory states that each spanwise section of a finite wing can be represented by a bound vortex with strength $\Gamma(y)$ from which the sectional loads are calculated by applying the Kutta-Joukowski theorem [59, 60]. According to the Helmholtz theorem, a vortex filament cannot end in a fluid, and thus from the ends of the bound vortex filament two free vortices continue to trail downstream from the lifting surface to infinity. This vortex filament structure is called a horseshoe vortex. By applying the Biot-Savart law, the induced velocity of a vortex filament at a certain location can be calculated:

$$\mathbf{U}_{\text{ind}} = \int_{-\infty}^{\infty} \frac{\Gamma}{4\pi} \frac{d\mathbf{l} \times \mathbf{r}}{|\mathbf{r}|^3}. \quad (2.7)$$

When superimposing an infinite amount of horseshoe vortices on the finite wing, each with a small strength and all coincident along a single line (lifting line), the induced velocity field or downwash distribution can be calculated at the lifting line by applying the Biot-Savart law. Using parameters of the local airfoil section of a finite wing, the induced angle of attack can be related to downwash. Furthermore, by applying the Kutta-Joukowski theorem, the fundamental equation of Prandtl's lifting-line theory is obtained. From this integro-differential equation, the vortex strength is calculated. Applying Fourier transformations, a system of independent equations can be solved. Once the circulation distribution is known, the lift distribution and the induced drag can be deduced from the Kutta-Joukowski theorem. Prandtl's lifting line theory is still widely used today. However, the theory applies only for a single lifting surface with no sweep, no dihedral and medium to high aspect ratios. Therefore, multiple modifications and new developed theories based on the classical lifting line theory are developed.

From the same concept as the classical lifting line theory, multiple methods are developed for representing an incompressible and inviscid flow field around wind turbine blades. In this section, the cornerstone of vortex and panel methods will be introduced: induced velocity. Afterwards, models of wind turbine wakes by use of vortex/panel methods are discussed. Finally, a general explanation on the vortex and panel methods with its applications are presented.

2.1.3.1 Induced velocity

A flow field can be described through velocity vectors or distributions of sources (sinks) and vortices. As depicted in Fig. 2.3, these concepts are not separate entities but are alternative

descriptions of the flow field from which new aerodynamic concepts are developed. This categorizes two different methods in solving the flow field: The grid-based Computational Fluid Dynamics (CFD) solves \vec{u} and the boundary-integral method uses sources $\vec{\sigma}$ and vortices $\vec{\omega}$.

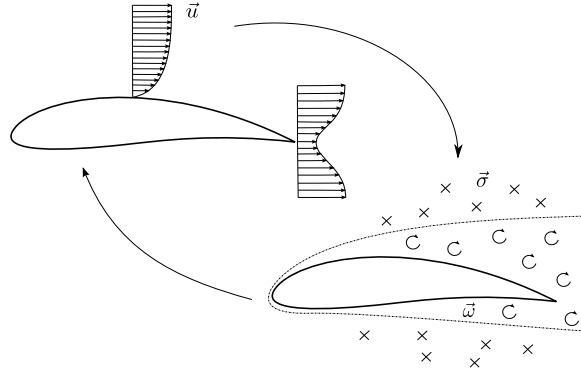


Figure 2.3: Possible flow field representation methods

From this observation, the term ‘induced velocity’ is somehow unfortunate, because it associates with the velocity field while it is actually associated with the field distribution of sources and vortices. The general form of the induced velocity field is shown by using an appropriate potential representation of the velocity field, namely the Helmholtz decomposition [61]:

$$\mathbf{U} = \nabla\Theta + \nabla \times \Psi, \quad (2.8)$$

where Θ is a scalar potential field satisfying the Laplace equation and Ψ is a solenoidal vector potential field that satisfies the Poisson equation. Given the definition of vorticity and assuming that the fluid is incompressible:

$$\nabla^2\Psi = \nabla(\nabla \cdot \Psi) - \nabla \times (\nabla \times \Psi) = -\nabla \times (\nabla \times \Psi) = -\nabla \times \mathbf{U} = -\boldsymbol{\Omega}. \quad (2.9)$$

Since the vorticity field is of interest, the Poisson equation without boundaries can be solved in convolution form:

$$\Psi(\mathbf{x}) = \frac{1}{4\pi} \int \frac{\boldsymbol{\Omega}(\mathbf{x}')}{|\mathbf{x} - \mathbf{x}'|} d\text{Vol}, \quad (2.10)$$

where \mathbf{x} and $d\text{Vol}$ are the locations where the potential and the vortex filament are computed, \mathbf{x}' is the location at which the integral is evaluated, which is taken over the region where the vorticity is non-zero. The general form of the induced velocity field can be obtained when taking the curl of the solenoid vector field:

$$\mathbf{U}_{\text{ind}}(\mathbf{x}) = -\frac{1}{4\pi} \int \frac{(\mathbf{x} - \mathbf{x}') \times \boldsymbol{\Omega}(\mathbf{x}')}{|\mathbf{x} - \mathbf{x}'|^3} d\text{Vol}. \quad (2.11)$$

From the general induced velocity field, different wake forms can be developed according to the vorticity field. In its simplest form, the wake can be described as a series of ring vortices. This would require to have a vorticity field that is represented by a number of line vortices:

$$\boldsymbol{\Omega}(\mathbf{x}) = \Gamma\delta(\mathbf{x} - \mathbf{x}'), \quad (2.12)$$

where Γ is the circulation strength, δ is the Dirac delta function, and \boldsymbol{x}' is the curve defining the location of the vortex lines. When combining Eq. 2.11 and 2.12, simple vortex models can be derived to compute flow fields of wind turbine blades. It can be noted that Eq. 2.11 is similar to the Biot-Savart law. However, the Biot-Savart law has two flaws when computing the induced velocity:

1. There exists a singularity point at the axis of rotation in the vortex filament
2. Evaluating the induced velocity very close to the vortex filament will result in non-physical large values.

In order to solve these two flaws, a cut-off radius can be used, in which the induced velocity smoothly goes to zero when approaching the core of the vortex filament. In most cases, the cut-off radius value varies between 0 and 0.1 [62]. Another possible solution for the problem is based on the viscous core correction model, that introduces a finite core size for a vortex filament [63]. In most cases, a desingularized algebraic profile is employed by use of a constant viscous core size or a diffusive core growth with time based on the Lamb-Oseen model. The algebraic models for vortex induced velocity profiles is a common method in engineering applications, because of its simplicity and computational efficiency. The most common model is the algebraic model of Scully & Sullivan [64]. Furthermore, Vatistas proposed a family of desingularized algebraic swirl-velocity profiles for stationary vortices [65]. Given the general form of the induced velocity, it is clear that it can be modified by changing the state of vortex filaments as such it can represent certain aerodynamic configurations, e.g., representing the flow field of a wing tip. As a consequence, most vortex or panel methods are modified for one certain engineering application.

2.1.3.2 Predescribed and free wake methods

Given the non-linearity of fluids, inflow distributions are highly dependent on wake structures of wind turbine blades. This requires proper modeling of the wake structure and wake strength for resolving inflow accurately. As a consequence, a better prediction in performance of wind turbine blades can be obtained. Using the vortex filament method, wind turbine wakes can be simulated by two modeling techniques: the prescribed wake model and the free wake model.

The prescribed wake is shed from the trailing edge downstream with a prescribed shape that consists of a sheet of vorticity approximated by a series of points connected with a straight vortex filament. Since the shape is prescribed and thus no extensive Biot-Savart calculations are required, the computational efficiency is high. However, only well-known wake structures or steady-state solutions can be modeled with this technique. Unsteady flow phenomena or complicated wake structures can only be represented by free wake models. An often used prescribed modeling technique is by representing the wake as a helix given by Eq. 2.13 where r is the radius of wake, ω is rotational velocity, θ_0 is initial angle of rotation, t is time, and U_∞ is the free-stream velocity:

$$\begin{bmatrix} x \\ y \\ z \end{bmatrix} = \begin{bmatrix} r \cos(\omega t + \theta_0) \\ r \sin(\omega t + \theta_0) \\ U_\infty t \end{bmatrix}. \quad (2.13)$$

Using the helix equation, the wake does not expand and moves downstream with a constant velocity, which implies that there is no interaction between vortex filaments in the wake. Other possible

techniques are based on measurements and semi-empirical relationships. Applications on prescribed wake modeling are referred to the following references [66, 67]. Unsteady prescribed wake models exist as well [68, 69].

Free wake methods represent a number of vortex wake elements that are able to move freely based on the local velocity field. The vortex filaments or panels are placed at the trailing edge of the blade and the induced velocities are calculated. In the next time step, with the information of the free-stream velocity and the induced velocity, the trailing vortex is shed downstream at the calculated location. This is the first segment of the wake. In the following time steps, besides calculating the induced velocity field of the blade, the induced velocity field of the segments of the wake are taken into account as well. Since the Biot-Savart law has to be evaluated for each time step, free wake models are computationally expensive. Another issue is that free wake methods have stability problems when vortex elements are approaching each other. This can be remedied by using a cut-off radius or a viscous core correction model (see Section 2.1.3.1). The advantage of this method is its ability to calculate unsteady flow phenomena and complicated wake structures, such as yawed wake structures and dynamic inflow. For further information on free wake models, see [70, 71].

Given that the flow is incompressible and inviscid, wakes can be extended to infinity. However, for both methods, the velocity field induced by the far wake on the blades is so small that it can be neglected. Therefore, the wake can be subdivided in regions in which different methods are applied as such that the computational efficiency increases. Another common practice is extending the wake three to four times the diameter of the rotor plane downstream and stop there with computing.

2.1.3.3 Vortex methods

In vortex methods, the wind turbine blade and wake are represented by lifting lines [72] or surfaces [71]. Wind turbines blades are represented by bound vortices at spanwise locations, which have each a circulation strength that is dependent on the amount of lift created locally. Given the variation of the circulation from the blade and the assumed irrotational free-stream flow, a trailing wake and a shed wake (temporal variation) is generated in order to ensure the total circulation over each section of the blade to remain constant in time. When the circulation strength is found, the induced velocity for every position is found by applying the Biot-Savart law. Afterwards, the induced angle of attack is computed as such that the effective angle of attack can be deduced. Subsequently, loads and moments of wind turbines can be estimated. Different types of vortex methods exist: the lifting line method and the lifting surface method [73, 74].

The lifting line method considers wind turbine blades as lifting lines, i.e. the Prandtl lifting theory can be applied. When the induced angle of attack, and consequently the effective angle of attack, is computed, two-dimensional aerodynamic properties of an airfoil can be extrapolated (see Sec. 2.1.2). Another method to find the aerodynamic coefficients resides in using the thin airfoil theory. Besides representing the blade by lifting lines, the wake needs to be modeled as well (see Sec. 2.1.3.2). Before assessing a performance analysis of the wind turbine, the tolerance value of the iteration method should converge to a certain value. This tolerance value is depending on the change of circulation strength between the previous and current iteration step.

The lifting surface theory represents the blade in more detail: a distribution of lifting lines over a surface or usually over the camber of the blade is employed, as such that the overall vortex strength

$\gamma(x, y)$ of the surface parallel to the span of the blade varies in spanwise y and chordwise x direction. Since each lifting line has a system of trailing vortices, the superposition of all trailing vortices will result in another vortex sheet parallel to the chord of the blade in which the strength $\delta(x, y)$ varies as well along the x and y direction. These two vortex sheets results in a lifting surface. Given the blade, multiple lifting surfaces are placed as such that at any given point on the surface the normal and induced velocity can be computed. At each point on the surface, a boundary condition should be satisfied in order to have flow alignment with the surface: There should be zero normal flow across the blade surface. From this, the sum of the wall normal velocity at each control point including the induced velocity of the bound and trailing wake vortices, the free stream and rotational velocity must be zero. Given this, the vortex strength $\gamma(x, y)$ and $\delta(x, y)$ for each section can be computed. Modelling the wake can be done as described in Section 2.1.3.2. Instead of using lifting surfaces, a superposition of horseshoe vortices can be applied on the surface of the blade. This approach is called the vortex lattice method [75].

Vortex methods are mostly utilized in the field of wind turbines for its ability in representing the wake. Despite of this feature, there are still improvements to be made, such as representing viscous effects and separation phenomena [76, 77]. Another application of these potential methods is combining CFD simulations for far field conditions while computing loads and moments with a vortex method [78].

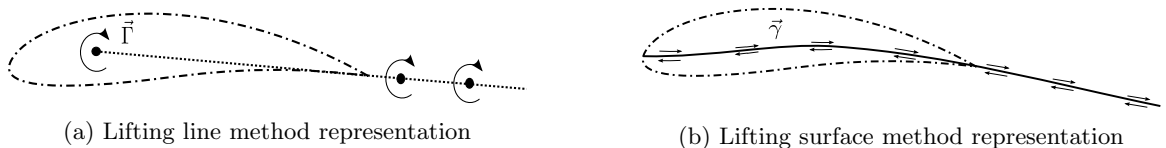


Figure 2.4: Vortex method representations

2.1.3.4 Panel methods

Assuming that flow is ideal, the solution of the flow field is considered to be a solution of the Laplace equation with a certain boundary condition. Given that simple singular flows are solutions of the Laplace equation, superposition of various simple ideal flows can be used for representing a complex flow problem. This provides the required complexity for solving complex geometry. The commonly used singular solutions for panel methods are source, vortex and doublet distributions. In order to attain flow alignment of the object, a tangent-flow boundary condition is subjected to a control point of a surface panel. The induced velocity field of the singular solutions is still computed by use of the Biot-Savart law.

The general procedure of panel methods is discretizing the wind turbine blade in surface panels in which each panel has a singular flow solution. In most cases, a combination of doublet and source distribution are used for three dimensional problems. The source distribution is needed for displacing the unperturbed flow as such it represents the boundaries of the blade. The doublet or dipole distribution is responsible for the lift and drag. Given the surface panels and the control points, the tangent-flow boundary condition is applied on these control points. From this, a system of linear algebraic equations can be solved for the unknown strength parameters. Note that the Kutta condition needs to be applied as well. For further information on panel methods, see [79].

An alternative to panel methods are the Boundary Integral Equation Method (**BIEM**) that are based on integral forms, which are more robust and more computationally efficient than the differential form. The **BIEMs** represent the object as a stagnant flow from which the unknowns are solved on the surface grid. Viscous effects can be taken into account by superimposing a boundary layer. The main advantage of **BIEM** is that it can represent the blade accurately without discretizing the entire flow field. However, flow separation is still an issue. For further information on this method for wind turbine blades, see [80].

2.1.4 Computational fluid dynamics

Computational Fluid Dynamics (**CFD**) is extensively used for analysis and design of engineering applications [81]. It applies numerical methods on partial differential equations in order to approximate flow physics. Some of these numerical methods are finite elements, finite differences, and finite volumes that are using spatial and time discretizations. In order to make these approximations more accurate, mesh refinement, smaller time domains and applying higher-order discretization schemes are considered. In wind turbine applications, **CFD** has led to accurate numerical solutions that can replace aerodynamic experimental data. However, there are still deficiencies making the performance analysis of a wind turbine difficult. One of these deficiencies is modelling an accurate representation of the wake due to strong flow length scale variations. Another difficulty is the correct prediction of the transition and separation of the boundary layer.

In this section, the governing equations of fluid dynamics are presented. Afterwards, turbulence modelling is discussed, where Large Eddy Simulation (**LES**) and Reynolds-Averaged Navier-Stokes (**RANS**) simulations are presented with respect to wind turbine applications. Next, boundary conditions and mesh generation are discussed and an overview of **CFD** on wind turbine applications will be presented.

2.1.4.1 Governing equations of fluid dynamics

The fundamental governing equations of fluid dynamics are the cornerstones of every **CFD** model. These governing equations are the continuity, momentum and energy equations, which are mathematical representations of the following three physical principles: conservation of mass, Newton's second law, and conservation of energy. The following governing equations are presented in the conservation form, i.e. the finite control volume is fixed in space with the fluid moving through it. The continuity equation, that represents the conservation of mass, can be given according to the Einstein notation:

$$\frac{\partial \rho}{\partial t} + \frac{\partial}{\partial x_j} (\rho u_j) = 0. \quad (2.14)$$

From the above equation, the time-rate-of-change of the mass of the fluid element is zero, i.e. the substantial derivative of mass ρ is zero. The momentum equations can be derived by applying Newton's second law $F_i = ma_i$ on a finite control volume:

$$\frac{\partial}{\partial t} (\rho u_i) + \frac{\partial}{\partial x_j} (\rho u_i u_j + p \delta_{ij} - \tau_{ji}) = \rho g_i, \quad (2.15)$$

where the divergence of τ_{ji} is the shear stress of the fluid (viscous stress), and ρg_i represents the body forces per unit volume acting on the fluid. When shear stress in a fluid is proportional to the velocity gradients, it is called a Newtonian fluid:

$$\tau_{ij} = \mu \left(\frac{\partial u_i}{\partial x_j} + \frac{\partial u_j}{\partial x_i} \right) - \frac{2}{3} \mu \frac{\partial u_k}{\partial x_k} \delta_{ij}. \quad (2.16)$$

Otherwise, it is called a non-Newtonian fluid. These three momentum equations are called the Navier-Stokes equations. Applying the conservation of energy on a finite control volume, the energy equation can be shown below:

$$\frac{\partial}{\partial t} (\rho E) + \frac{\partial}{\partial x_j} (\rho u_j E + u_j p + q_j - u_i \tau_{ij}) = \rho g_j u_j, \quad (2.17)$$

where q_j is the heat flux. The above mentioned equations represent a system of 5 equations with six variables. The equation of state is applied for solving the last unknown variable. In other words, applying the law of Navier-Stokes, the equation of state, and the law of Fourier, the fluid behaviour can be completely solved. When the inertia terms are much bigger than the viscous terms, the Navier-Stokes equations can be simplified to the Euler equations without body forces:

$$\frac{\partial}{\partial x_j} (\rho u_j) = 0 \quad (2.18)$$

$$\frac{\partial}{\partial t} (\rho u_i) + \frac{\partial}{\partial x_j} (\rho u_i u_j + p \delta_{ij}) = 0 \quad (2.19)$$

$$\frac{\partial}{\partial t} (\rho E) + \frac{\partial}{\partial x_j} (\rho u_j E + u_j p) = 0 \quad (2.20)$$

Note that the thermal conductivity is usually assumed to be zero, which results in no heat flux. When considering the Euler equations, the equation of state and an isentropic flow, it is clear that Eq. 2.20 is redundant to determine ρ and u_i . Due to the lack of viscosity, the Euler equations cannot resolve boundary layers, which results in poor predictions of aerodynamic performance. Not only the aerodynamic performance will be inaccurate, but the resolution of complex flow phenomena, such as flow separation, is very poor or just non-existent. Therefore, it is decided to omit the Euler equations for discussion. When considering a steady-state flow, the time derivatives in the above equations are zero or in other words the variables u_i, ρ, p and E are independent of time.

Since turbulent flows show a large fluctuations in vorticity, the Navier-Stokes equations can be rewritten by taking the curl of the Navier-Stokes equations. This will result in the non-conservation form of the vorticity equation:

$$\frac{D\omega_i}{Dt} = \omega_j \frac{\partial v_i}{\partial x_j} - \omega_i \frac{\partial v_j}{\partial x_j} + \epsilon_{ijk} \frac{1}{\rho^2} \frac{\partial \rho}{\partial x_j} \frac{\partial p}{\partial x_k} + \epsilon_{ijk} \frac{\partial}{\partial x_j} \left(\frac{1}{\rho} \frac{\partial \tau_{km}}{\partial x_m} \right) + \epsilon_{ijk} \frac{\partial F_k}{\partial x_j}, \quad (2.21)$$

where F_k represents the summation of the external body forces, τ is the viscous stress tensor, and ϵ_{ijk} is the permutation symbol.

2.1.4.2 Turbulence modelling

In order to include turbulence with a relatively low computational cost, Reynolds-Averaged Navier-Stokes (RANS) equations can be applied. These equations are based on the Reynolds de-

composition in which a quantity is decomposed in a time-averaged and fluctuating quantity [82]:

$$u(x, y, z, t) = \overline{u(x, y, z)} + u'(x, y, z, t), \quad (2.22)$$

where the overbar represents the time averaged quantity and the prime denotes the fluctuating quantity. When applying the decomposition on the Navier-Stokes equations, the **RANS** equations can be written in Einstein notation:

$$\rho \left(\frac{\partial \overline{u}_i}{\partial t} + \frac{\partial}{\partial x_j} (\overline{u}_j \overline{u}_i) \right) = -\frac{\partial p}{\partial x_i} + \frac{\partial \tau_{ij}}{\partial x_j} - \frac{\partial}{\partial x_j} (\rho \overline{u'_i u'_j}) \quad (2.23)$$

Given the above momentum equations, the last term expresses the influence of the turbulent fluctuations on the mean flow that significantly enhances the momentum transport. The extra term $-\rho \overline{u'_i u'_j}$ is called the Reynolds stress or turbulent shear stress, which represents a symmetric equation that incorporates six unknown values. This leads to a closure problem in which turbulence models, empirical correlation methods or data base methods are applied to solve this problem [83]. Most RANS models used in engineering applications employ turbulence models, in which the Boussinesq eddy viscosity hypothesis is satisfied [84]: The turbulent stresses in **RANS** momentum and energy equations are assumed to be equal to the product of the isotropic eddy viscosity coefficient and the mean velocity strain rate. In order to obtain the eddy viscosity, various methods are developed. Some of these methods employ direct dependence on the mean flow quantities (linear eddy viscosity models) and other methods use additional equations for turbulence velocity and time scales (non-linear eddy viscosity models).

In order to reduce the overview on turbulence models, only relevant models applied to wind turbine applications are briefly discussed. The linear eddy viscosity models include algebraic models (Cebeci-Smith, Johnson-King, and Baldwin-Lomax) [85], one-equation models (Spalart Allmaras **(SA)** and Baldwin-Barth **(BB)**) [86, 87], and two-equation models (k- ϵ , k- ω , and Menter's Shear Stress Transport **(SST)**) [88, 89, 90]. The most common models for wind turbine applications are the k- ω **SST**, **SA**, and **BB** models. Note that the above turbulence models have been extensively modified. Therefore, the following discussion will be based on the original models.

The k- ϵ and k- ω models are two common two-equation models in fluid mechanics that model eddy viscosity by use of the turbulence kinetic energy k and turbulent dissipation rate ϵ or specific dissipation rate ω . The two turbulence models employ two transport equations in which history effects like convection and diffusion of turbulent energy are taken into account. Both of these models use wall functions, which means it does not simulate the buffer region of the boundary layer. The k- ϵ model is popular for engineering applications due to its good convergence and low memory requirements. Moreover, it performs well for external flow problems with complex geometries. The drawback is that it exhibits inaccurate solutions for adverse pressure gradient separation and internal flow problems. The k- ω model is more sensitive to good convergence characteristics and has a strong free-stream sensitivity. Sometimes, it has problems solving the initial guess of the solution. However, the k- ω model proves to be superior at predicting stall behaviour, whereas k- ϵ models do not predict stall for wind turbine applications [91]. In order to alleviate the disadvantages of the k- ω model, the k- ω **SST** model was developed, in which the k- ω model is used for the inner part of the boundary layer while the k- ϵ model is used in free shear flow. This results in a more robust and accurate turbulence model. In most cases, the k- ω model is employed where the k- ϵ model is inaccurate.

Both models often underestimate the velocity defects in wake regions due to their high dissipation and vorticity dependence in the production term [92]. Since the $k-\omega$ models are superior to the $k-\epsilon$ models for rotating flow problems, researchers kept improving the $k-\omega$ model for wind turbine applications [93, 94]. Nowadays, discretization methods using **RANS** with $k-\omega$ can show remarkable agreements with **NREL VI** probe measurements [95].

The **BB** turbulence model is a modified $k-\epsilon$ model avoiding numerical difficulties associated with that model. The difference with the $k-\epsilon$ resides in the independence on the algebraic length scale. The model performs much better than the Baldwin-Lomax in not overestimating the eddy viscosity at separated regions away from the wall. Due to its sensitivity in the free stream region and its reduced accuracy, its usage in the aerospace community is less common and the **SA** model is preferred. Since the production term of the **BB** model is dependent on vorticity of the flow, it is shown that the eddy viscosity tends to be dramatically higher at strong vortex cores [92]. This results in poor representations in wake and stall regions of wind turbines. The main advantage of using the **BB** model resides in its simplicity.

The **SA** turbulence method models the eddy viscosity using Reynolds numbers, the transport equation, magnitude of vortices, algebraic constants, and a characteristic exponential equation that drives the eddy viscosity to zero upstream of the transition point [86]. Since the production term of the **SA** model is based on vorticity, it tends to produce too much eddy viscosity decreasing the model's accuracy at stall [92]. The main advantage of the **SA** model is that it differentiates the fluid behavior in the free stream and in the boundary layer resulting in a robust method that is compatible for any type of mesh. It also yields a fairly rapid convergence of the residuals reducing computational costs.

A different approach for solving the Reynolds stress tensor is called the Reynolds Stress Transport Model (**RSTM**), which is based on differential equations instead of the Boussinesq eddy viscosity hypothesis [96]. These **RSTMs** are superior to the above discussed turbulence models since it eliminates the assumption of turbulent stress related to mean strain stress. It models every component of the Reynolds stress tensor, which results in six additional partial differential equations containing terms that have to be modeled by use of second order closure relationships. Since every additional partial difference equation has to be solved, **RSTM** becomes much more complicated and results in too high computational costs for engineering applications. Also, **RSTM** appears to be very sensitive on the type of flow problem.

Several studies for stall-control wind turbines have shown that **RANS** models are insufficient for resolving separated flow regions [97]. In order to obviate this problem, Detached-Eddy Simulation (**DES**) has shown promising results [98]. **DES** is a hybrid approach of **RANS** and **LES**: The near-wall flow is modelled using a **RANS** model that is coupled to an **LES** model away from the surface [99, 100]. Since the eddy viscosity of both models are similar, the change between these two eddy viscosities can be easily set up based on wall distance functions. However, the lack of resolved length scales in the **RANS** region causes unresolved Reynolds stress and smaller length scales in that part of the **LES** region closest to the interface of the **RANS** region [101]. This results in larger velocity gradients between these regions. **DES** is considered to be more computational expensive than the **RANS** model due its higher grid refinement.

Another flow limitation of **RANS** modelling is the inaccurate prediction of laminar-turbulent transition [102]. The location of transition is a major challenge that affects the pressure profile of the

blade, which consequently results in inaccurate predictions of the performance of wind turbines [103]. A similar challenge is the prognosis of laminar separation bubbles that affects airfoil performance and power generation. In order to alleviate this problem, transition models can be combined with turbulence models. Some of these transition models are the Eppler, Chen Tyson and Michel's laminar-turbulence transition model [104].

Large Eddy Simulation (**LES**) is another turbulence modelling technique that uses low pass filtering on the Navier-Stokes equations for eliminating small (length and time) scales of flow solutions [105]. The size of the small length scales that are eliminated from the flow solutions depends on the turbulence theory, computational resources, and the particular investigated flow phenomenon. **LES** has the ability to resolve unsteady, anisotropic turbulent flows dominated by large scale structures and turbulent mixing. This is a great advantage over **RANS**, because it is able to resolve flow separation and large scale vorticity. However, the computational cost of **LES** is significantly higher than for **RANS**. Given that **LES** uses a filtering operation that splits the flow field in a resolved (large scales) and an unresolved (small scales) part of the flow, the sub-grid velocity can be defined as the difference between the flow velocity and the filtered velocity:

$$u'_i(x_i, t) = u_i(x_i, t) - \bar{u}_i(x_i, t), \quad (2.24)$$

where the filtered velocity is defined as a convolution integral:

$$\bar{u}_i(x_i, t) = \int u_i(\xi_i, t) G_i(x_i - \xi_i, \Delta) d\xi_i, \quad (2.25)$$

where $G_i(x_i - \xi_i, \Delta)$ is the convolution kernel and Δ is the filter width. The decomposition of the large and small scales of the flow field can be considered as a resemblance of the Reynolds decomposition of **RANS** models: When applying the filtering operation on the Navier-Stokes equations, an extra term, called the Sub-Grid Scale (**SGS**) stresses, appears that represents the effect of small scales on large scales. Several models can be applied for calculating **SGS** eddy viscosity, such as the Smagorinsky model [106], dynamic models, regularization models, and variational multi-scale models [107, 108, 109]. Depicted in Fig. 2.5, the influence of the filtering width with the length scales of flow is presented. Another difficulty of **LES** resides in its application to wall-bounded flows in which mesh refinements in all directions are required [110]. Consequently, this results in very high computational costs.

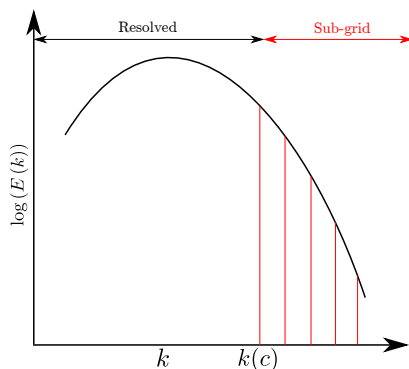


Figure 2.5: Idealized spectrum of turbulent kinetic energy of isotropic turbulence with respect to wave number k . The small scales with low energy from $k(c)$ are filtered out by **LES**.

2.1.4.3 Boundary conditions

The prescription of the inflow conditions for a wind turbine is still today an ongoing challenge in CFD simulations. The turbulence, sheared velocity profile, anisotropy, and the unsteady nature of the inflow are some of the parameters that have a large impact on the flow field behind the rotor and consequently the performance of wind turbines. Therefore, the inflow conditions should be represented as close as possible to real atmospheric conditions. In the case of RANS simulations, the Atmospheric Boundary Layer (ABL) can be represented by the Monin-Obukhov similarity theory [111], in which stability corrections to vertical profiles in the surface layer are made. This involves the variation of mean flow and turbulence characteristics of the surface layer that are independent of time. For LES, two different types of unsteady inflow models exist: synthesized inlet methods and precursor simulation methods. The synthesized inlet methods are producing synthesized turbulence based on simple statistical parameters (mean velocity, turbulent kinetic energy, Reynolds stresses, two-point and two-time correlations, etc.) or based on spectral methods in the Fourier space. The algebraic methods are trying to fit target statistics of turbulence to resemble the correct turbulent kinetic energy [112, 113]. For further information, see previous work on synthesized inlet methods [114, 115]. A mix of the above two mentioned methods is also possible [116]. Precursor simulation methods use a supplementary simulation that provides inflow conditions for the main simulation. The data is usually extracted and rescaled for the main simulation. This method is mostly applied when the upstream flow of the main simulation can be reasonably approximated by a simple generic flow. Since the method uses an additional simulation, ground boundary conditions can be added. Another advantage is that the turbulent inflow is a solution of the Navier-Stokes equations. However, the disadvantage is that it is computationally expensive and that it is difficult to resemble the correct turbulent characteristics. Some of the applications of these methods are shown in the following references: [117, 118].

Wall boundary conditions are required at solid surfaces: when a moving fluid comes in contact with a solid body, the fluid will not have any velocity relative to the body at the contact surface. This is also known as the no-slip condition for viscous flows. The no-slip condition, a Dirichlet boundary condition, results in various methods on resolving boundary layers. Direct Numerical Simulation (DNS) resolves all eddy scales in the near-wall region, which requires a vast number of cells. In fact, the number of cells in the near-wall region for DNS scales with Re^3 , while the outer layer only requires $\text{Re}^{0.6}$ [110]. This shows that the computational cost contribution of the inner layer with respect to the total computational cost of the simulation is much higher than the computational cost of the outer layer with respect to the Reynolds number. The reason for this discrepancy in the computational cost is that smaller cells are required at the near-wall region to resolve small eddy scales that occur at the vicinity of the wall, while at the outer layer larger cells can be used for resolving larger eddy scales. Due to this high computational cost, engineering applications with high Reynolds numbers cannot currently be solved with DNS. In order to reduce the computational cost related to near-wall regions, various wall models are developed that allow to shift the first grid node at the wall outwards. Most of these wall models are based on the fact that the velocity profile in a turbulent boundary layer is a self-similar behavior when performing the appropriate scaling with parameters, such as $U^+ = U/u_*$ and $y^+ = yu_*/\nu$. This observation, or the *law-of-the-wall*, proposed by von Kármán [119], is based on experimental results with the following assumptions: attached flow, small pressure gradients and time-averaging. As a consequence of these assumptions, various wall

models exhibit bad representations for flow separation and high pressure gradients (see Sec. 2.1.4.2). Recently, it has been shown that the law-of-the-wall is not universal, since the logarithmic fit based on the von Kármán constant κ varies with respect to the type of wall-bounded flows [120]. Given this variation in κ , accurate drag predictions of RANS and LES by use of wall models is difficult to achieve, especially for high Reynolds numbers [121]. Other models or laws, such as the power law and the Lie group, have been developed in order to circumvent the experimental dependence, but there are difficulties with implementation and validation. The difficulty in retrieving more accurate κ values is due to measurement equipment that cannot resolve small flow scales associated with high Reynolds numbers for engineering applications. Another issue with the law-of-the-wall is that it is based on smooth surfaces, which in reality is not usually the case: surfaces are polluted by insects, dirt and smog. Therefore, various modifications on the law-of-the-wall have been developed. Nikuradse [122] has experimentally shown that various roughness surfaces exhibit the same slope of the logarithmic layer $1/\kappa$, but has a different intercept B . Cebeci and Bradshaw [123] modified the logarithmic law by adding a roughness function ΔB dependent on roughness Reynolds number k_s^+ . Given the turbulent behaviour of all these wall models, no transition between laminar and turbulent flows can be simulated with the basic wall models. Therefore, multiple transition models have been developed (see Sec. 2.1.4.2 for more details). Even though wall models have some major issues in representing boundary layers, its reduction in computational cost makes RANS and LES still one of the most used high-fidelity models of today. Depicted in Fig. 2.6, an accurate representation of the boundary layer by use of RANS or LES requires at least one cell within the linear viscous sublayer $0 \leq y^+ \leq 5$. However, in most engineering applications, the first cell at $y^+ = 1$ with a growth rate of 1.15 in the normal direction of the wall is preferred in order to capture the boundary layer. When considering inviscid Euler equations, the non-slip condition does not hold, which is also known as the Euler slip condition. In most cases, the slip condition applies a laminar shear profile where the boundary layer is independent of the Reynolds number [124].

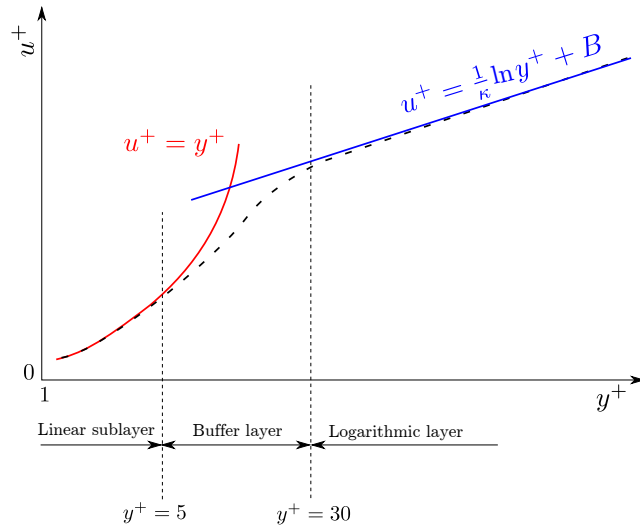


Figure 2.6: Law-of-the-wall for smooth surfaces. The logarithmic layer is valid until $y^+ = 500 - 1000$.

In order to reduce computational cost and increase spatial accuracy, spatial periodic boundary conditions can be employed when physical geometry and flow behaviour are repetitive. In case of

wind turbine rotors, this behaviour will only exist when the inflow is perpendicular to the disc plane of the wind turbine rotor, and when the solution is steady-state. If these requirements are fulfilled, the periodic boundary conditions can be applied at the boundary where the flow starts to repeat. This results in just simulating one part of the computational domain and thus computational cost is reduced significantly. Besides wind turbine rotor simulations, infinite wind farms or turbulent inflow fields by use of precursor method can also use periodic boundary conditions [125]. Notice that translational and rotational periodic boundary conditions exist.

Pressure boundary conditions are applied for unknown flow distributions where pressure distributions are known. This is often used as outflow and inflow conditions for wind turbines, especially the outflow conditions where the flow distribution of the wake is unknown. The pressure distribution for the inflow and outflow condition are mainly based on atmospheric pressure distributions.

2.1.4.4 Mesh generation

CFD simulations for wind turbine rotors require a suitable computational mesh. In order to achieve this computational domain, the blade geometry should be described by its airfoil sections, twists, thicknesses, and the location of the blade sections in span-wise direction. These blade sections are interpolated in a three-dimensional Computer-Aided Design (CAD) geometry that is used for meshing. Even though a variety of grid generation techniques are available, the generation of a high quality mesh is still a demanding and complex task. In most cases, the development of a high-quality mesh requires even more time than solving the actual flow problem. Three grid generation approaches exist [126]: structured body-fitted mesh method, unstructured body-fitted mesh method, and Cartesian cut cell method.

The Cartesian cut cell method is an alternative to body-fitted mesh methods: The approach basically cuts the background Cartesian mesh with the interested solid body. As a consequence, the quality of some cut cells is very poor, which may result in convergence issues. In order to overcome this problem, cell merging techniques have been developed [127]. The Cartesian cut cell approach has been successfully applied to potential flows, inviscid Euler equations, and incompressible viscous flows [128, 129, 130]. The main advantage of this technique is the automated meshing process, which consequently reduces the development time significantly. The computational cost for moving grids is low compared to other conventional mesh perturbation techniques used for body-fitted meshes, because only cells adjacent to the moving boundary need to be adapted [131]. Also, the related skewness for traditional mesh perturbation techniques is not present when employing the Cartesian cut cell method. However, the major drawback of employing this technique occurs when conventional finite volume methods are used: Accuracy reduces at the cut cells near the boundary layer, which is detrimental for predicting aerodynamic performance [132].

For most wind turbine applications, the mesh generation is based on body-fitted mesh methods. This means that the mesh is fitted around the solid body. The difficulty of using body-fitted meshes is that the fitting of straight cells near curved walls will result in gaps between the cell and the actual geometry. When using low-order schemes, this issue can be reduced by adding more nodes at the curved walls, which results in larger number of cells and higher computational costs. When using higher-order schemes [133], straight surfaces of cells can be changed to curved surfaces corresponding to the curve of the wall. The computational cost and the difficulty of generating body-fitted meshes are more of a concern, since most complex geometries are still manually meshed. In particular,

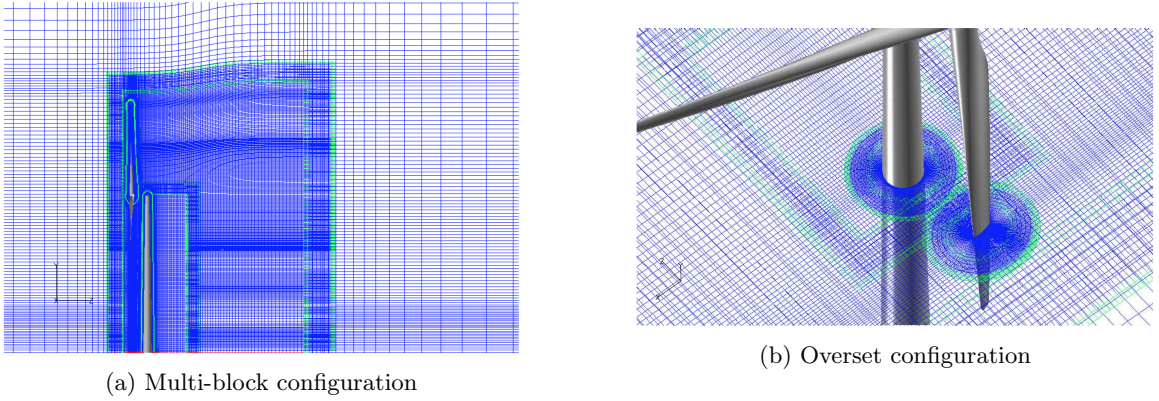


Figure 2.7: Combination of overset and multi-block configuration for structured mesh of a multi-megawatt wind turbine [134]

structured meshes are difficult to handle for complex geometries due to their single block domain configuration. Shown in Fig. 2.7, this difficulty can be alleviated by applying multi-block, overset, and zonally patch configurations.

The main advantage of structured meshes is its ability to accurately resolve boundary layers due to its orthogonality. Special attention is required for off-wall distance Δs calculated by using flat-plate boundary layer theory where $y^+ = 1$.

Unstructured grids simplify the mesh generation, because of using tetrahedral elements instead of using orthogonal hexahedral elements. This requires more memory since node numbers and connectivity tables need to be stored, while structured grids require only i, j, k coordinates. The major drawback of employing unstructured meshes is the numerical diffusion associated with tetrahedral elements. This result in inaccurate predictions of boundary layers due to misalignment of the predominant flow direction and a not well-defined direction normal to the wall. The development of hybrid mesh generators resolved the issue by placing high orthogonality cells near the wall while using unstructured cells at outer regions. A hybrid mesh around the [NACA 0012](#) airfoil is shown in Fig. 2.8.

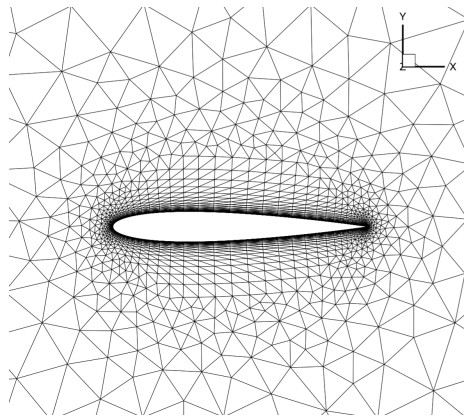


Figure 2.8: Hybrid mesh of [NACA 0012](#) airfoil with high orthogonal cells at boundary layer and unstructured cells at outer region

As the complexity of CFD simulations increases due to complex geometries and various flow

length scales, manual generation of an efficient and accurate mesh becomes extremely difficult. This is especially true when the user does not know where mesh (un)refinements are required to resolve particular flow regions. Uniform mesh refinement is not an option since it is computationally expensive. Therefore, various adaptive mesh refinement methods have been developed in order to minimize the discretization error while keeping the development and computational time of a computational grid at a reasonable level. This approach consists of the following components [135]: the formulation of cell-refinement parameters from localized error estimates, a meshing algorithm that applies the refinement parameters, and a mesh-adaptation strategy that minimizes the cost of the simulation. In order to localize the sensitivity of mesh refinements, adjoint techniques can be employed (note that other methods exist, such as finite difference) [136, 137]. These techniques have proven to be very accurate and fast for all flow regions. Adaptive mesh refinement is especially successful for transonic and supersonic flow, where mesh refinements are required for proper shock resolutions. Most of these techniques rely on Cartesian cut cell meshes for Euler equations. However, several developments have shown that adaptive mesh generation can be applied to body-fitted meshes for Navier-Stokes equations [138, 139]. Shown in Fig. 2.9, a mesh of [NACA 0012](#) airfoil in transonic flow is refined by use of adaptive mesh generation. For further information on mesh refinements, see the following references [140, 141].

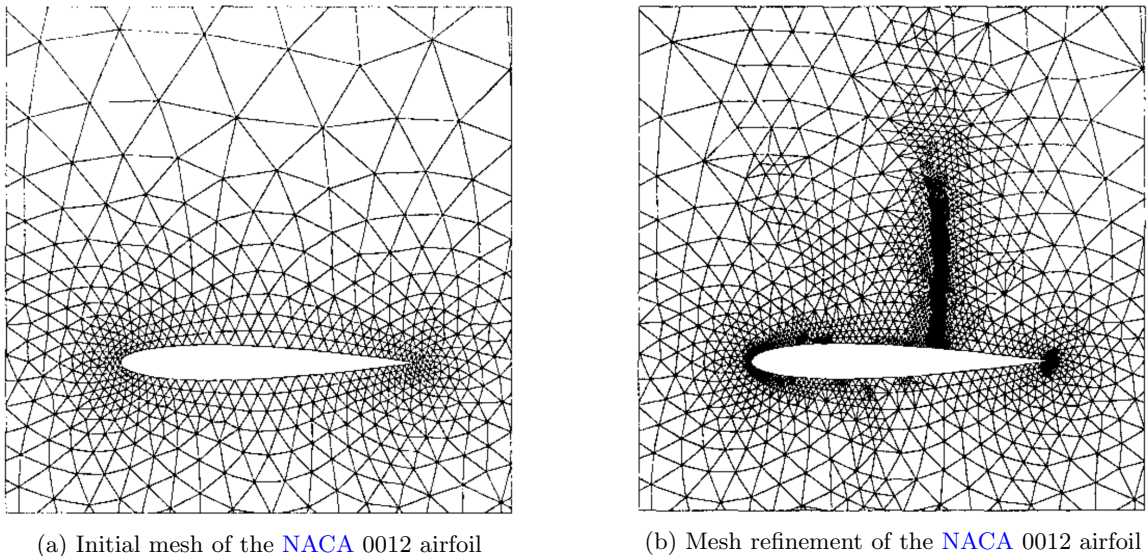


Figure 2.9: Adaptive mesh refinement of transonic flow over [NACA 0012](#) airfoil [142]

2.1.4.5 CFD applications on wind turbines

The first steady [CFD](#) simulation on rotating wind turbine rotors was performed by Sørensen and Hansen [143]. The incompressible [RANS](#) model with the turbulence model $k-\omega$ [SST](#) was employed for multiple wind turbine blades: one bladed wind turbine and a three bladed wind turbine. It was observed that the power curve of the simulated wind turbine was well predicted up to wind speeds of 10 m/s. Beyond that wind speed, the accuracy of the prediction deteriorated, because the model was not able to resolve separated flow due to insufficient mesh resolution and inaccuracies related to turbulence modelling. Another incompressible [RANS](#) simulation with $k-\omega$ [SST](#) of the

NREL VI wind turbine blade was performed for several load cases in order to show the capabilities of three-dimensional CFD simulations [144]. The computed results showed good agreement with the measurements performed at NASA Ames wind tunnel for fully attached flows. A large deviation was observed at 10 m/s, due to the incapability of resolving boundary layer transition. Due to flow separation, the torque values for higher wind speeds were underestimated. Currently, most RANS-based CFD simulations overpredict these torque values, which is an indication that these state-of-the-art solvers are still missing an essential part of the flow physics. Le Pape [95] used a compressible multi-block RANS-based solver that is able to simulate two-dimensional airfoil and three-dimensional blade performances using steady and unsteady formulations. A Choi and Merkel low speed preconditioner has been developed for circumventing numerical problems associated with low Mach numbers [145]. Two turbulence models, $k-\omega$ and $k-\omega$ SST, have been compared and it is shown that the $k-\omega$ SST correctly estimates the initial separation at 10 m/s, which consequently results in better predictions in aerodynamic performance. The density residuals appeared to be stagnating for all wind speeds, which indicates the quasi-steady nature of the flow problem. The force and moment coefficients, on the other hand, converged for attached flow conditions. While for separated flows, force and moment coefficients fluctuated within a small interval. Further analyses have shown good torque value agreements in attached flow regions between NREL VI wind turbine blades with and without root. The VISCEL Joule III project assessed and validated existing three-dimensional Navier-Stokes solvers for various NREL and LM wind power blades [78, 146]. The conclusion of this research was that most of the numerical codes had achieved consistent solutions for fully attached flows, while solutions for flow separation were varying. Simms et al. [147] have made a blind comparison of various CFD solvers that resulted in the same conclusion as the VISCEL Joule III project.

Duque [148] applied an overset steady-state RANS-based CFD model with a BB turbulence model on the NREL VI wind turbine blade. The resulting torque values were quite precise with respect to experimental results for attached and stall flow regions. At Risø, the multi-block, structured, incompressible solver ‘EllipSys3D’ is employed for DES and RANS simulations on the NREL VI wind turbine blade [149]. The study was focussed on static and dynamic stall regions. It was shown that DES simulations resulted in more three-dimensional flow structures compared to two-equation RANS turbulence simulations, e.g., higher resolution of vortices. However, no particular improvements were seen on global blade characteristics. Possible reasons for this poor performance are the following: high twist of the blade can cause possible errors from either root or tip to be transported to the rest of the blade, lack of transition modelling, and improper grid resolution and time step. Li et al. [150] obtained the same conclusion, but significant improvements in transient responses are seen. Another study has shown that DES can improve the ability of capturing separated flows [151]. Based on the above research and given the higher computational cost of DES simulations, it is recommended to apply RANS simulations on wind turbine rotors. Zahle et al. [134, 152] used an overset, structured, incompressible RANS-based method in which rotor and tower interaction are investigated (tower dam effect and tower shadow effect) using the $k-\omega$ SST model. It is shown that the interaction induces transient loads on the blade by unloading and reloading the blade when entering or leaving the tower. A reduction in torque of 1 to 2% is observed due to tower shadow effect as well as dynamic stall behaviour, triggered when exiting the shadow. Furthermore, it is observed that tower shedding frequency is strongly affected by the rotor. Potsdam and Mavriplis [153] used an unstructured

(un)steady **RANS**-based solver for analysing the effect of unstructured computational meshes on the prediction of the performance of the **NREL VI** wind turbine blade. Various load comparisons between structured and unstructured meshes are performed. The **SA** turbulence model has shown that it overpredicts and delays the torque at the beginning of flow separation at 10 m/s. Thrust was reasonably well predicted. The Roe scheme showed better convergence, robustness, smoothness, and low Mach properties than the central scheme with artificial dissipation. This might be caused by the higher level of dissipation rather than a more accurate discretization. Furthermore, adaptive mesh refinement was performed on mixed-element unstructured meshes. Depicted in Fig. 2.10, the wake of the **NREL VI** rotor is better resolved when adaptive mesh refinement is applied. Wissink et al. [154] applied a Cartesian adaptive mesh refinement for wakes of helicopters.

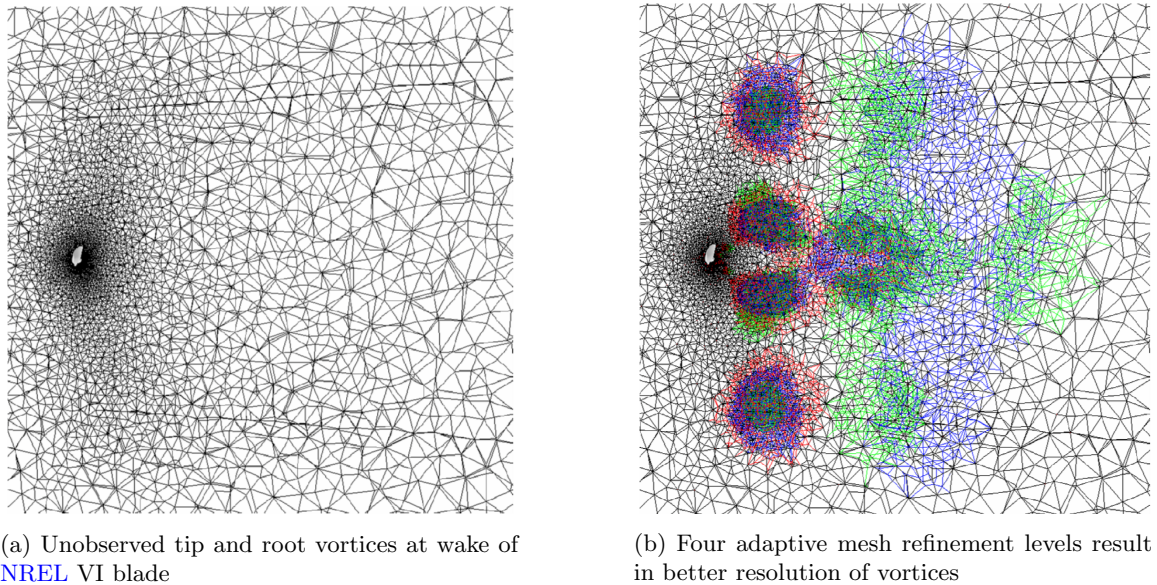


Figure 2.10: Adaptive mesh refinement of the wake of the **NREL VI** blade [153]

Various investigations have shown that transition modelling is necessary to predict correct power generation over the whole range of wind velocities. Yelmule and Anjuri [155] used a structured steady two-equation **RANS**-based solver with periodic boundary conditions in combination with Langtry and Menter correlation based Gamma-Theta transition model. The obtained torque graph fitted better with respect to experimental results. In particular, the torque values for separated flow regions were correctly simulated. However, there was still an overprediction in torque for 10 m/s due to highly transient effects at the onset of stall. Sørensen et al. [156] applied **DES** simulations with a Menter transition model on wind turbine airfoil DU-96-W351. The **DES** with transition model has shown to be numerically robust and similar to transition modelling for **RANS** computations. Deep stall regions of the airfoil are well resolved, but overpredictions arose when simulating at low angles of attack.

Tip geometry designs on wind turbine blades by use of **CFD** simulations have shown promising results. Hansen and Johansen [157] compared tip loss models of **BEM** by applying **RANS**-based **CFD** simulations on standard and swept tips of wind turbine blades. It was proven that the tip loss models are consistent with **CFD** simulation results. The only difference was the radial distribution of the axial induction factor at the tip. Johansen and Sørensen [158] made a comparison between various

winglets on wind turbine blades by use of **RANS**-based simulations. The main purpose of adding winglets at wind turbine blades is to reduce the induced drag by changing the downwash distribution. Due to tower clearance issues, it is recommended to point the winglet upstream. In this investigation, it was shown that all winglets contributed a small increase in power production. Pointing the winglet downstream increased the power production even more. However, thrust increased as well. Therefore, a trade-off between thrust and power is recommended. Besides tip geometries, research on nacelles/hubs have been performed. Zahle and Sørensen [159] investigated the influence of hub on nacelle anemometers by employing **RANS**-based **CFD** simulations. Depicted in Fig. 2.11, the vortical wake patterns make it difficult to apply simple corrections to measured quantities of nacelle anemometers, especially for off-design conditions. Johansen et al. [160] made a comparison study of different hub designs by use of **RANS**-based **CFD** simulations. It is shown that hub design has an influence on the inboard region of the blade: when choosing the proper nacelle design no flow separation is observed and higher power production is obtained. Employing flatback airfoils (thick trailing edge airfoils) for wind turbine applications have become a hot research topic, due to its alleviation of structural constraints, reducing blade weight, and maintaining power performance of the wind turbine rotor. Chao and van Dam [161] have confirmed, through **RANS**-based **CFD** simulations, that power performance is kept the same when comparing the baseline rotor with the flatback rotor. Kim et al. [162] have made a comparison study between **RANS**, **LES**, and **DES** for aeroacoustic analyses on flatback airfoils. **DES** is found to be adequate for predicting aerodynamic noise generation. The general aerodynamic noise of blunt trailing edge airfoils seems to be generated by vortical flow in the vicinity of the trailing edge. Ranft et al. [163] predicted the overall aeroacoustic of the **NREL VI** rotor, in which aerodynamic noise is computed by a $k-\omega$ **SST RANS**-based **CFD** simulation and the radiation noise is calculated by the Ffowcs Williams and Hawkings equation [164]. It is found that the leading edge and blade tip are primarily responsible for broadband noise generation.

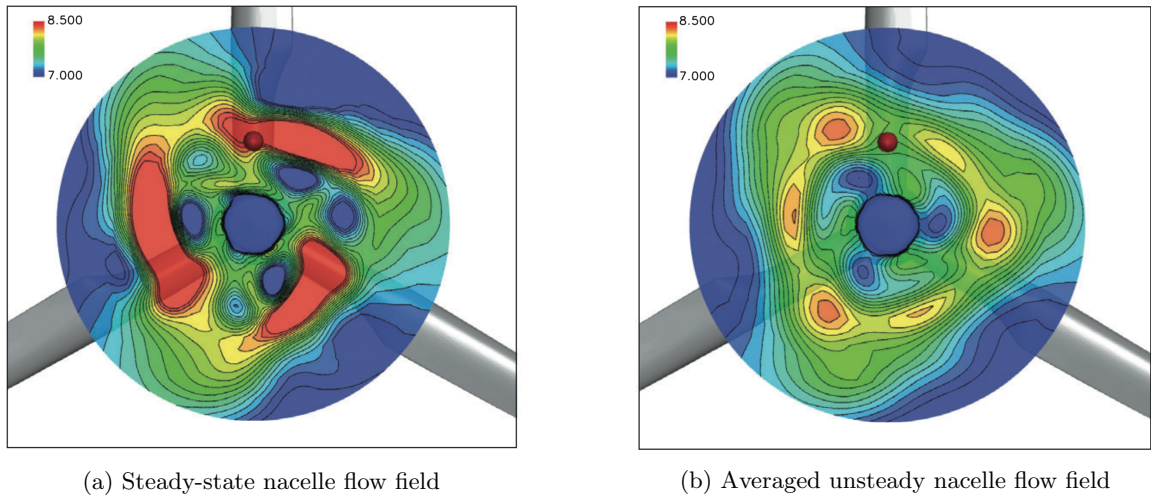


Figure 2.11: Vortical flow field at nacelle section; red dot is representing the nacelle anemometer [159]

Three-dimensional **CFD** simulations are employed for extracting airfoil characteristics that consequently exhibit viscous and three-dimensional aerodynamic effects. These airfoil data can then be

applied in **BEM** models without using current correction models. Johansen and Sørensen [49] have developed such a method. For fully attached flows, **RANS**-based **CFD** with transition prediction models are employed, while for separated flows, **DES** simulations are applied in order to assure correct prediction of performance of wind turbine rotors. Another extraction method is developed by Hansen et al. [165].

In reality, most wind turbine rotors are misaligned with the incoming wind, which results in complex flow behaviours that cannot be solved by low-fidelity models. In contrast with most axial flow cases, periodic boundary conditions cannot be used for yaw effects, which results in larger computational meshes and higher computational costs. Due to its azimuthal variation, yaw computations require time accurate simulations (no steady-state solutions exist), which severely increases the computational time. Sezer-Uzol et al. [166] did not only investigate **LES** on the **NREL VI** rotor, they also did some research on yaw misalignment, where an asymmetric wake structure has been resolved. Madsen et al. [39] obtained good agreement between **RANS**-based results and experimental results on a range of $\pm 60^\circ$ yaw angle. However, the **RANS**-based solver seemed to overestimate the local flow angle at 45° yaw angle. Tongchitpakdee et al. [167] studied yaw effect for the whole velocity region of the **NREL VI** rotor with **RANS**-based **CFD** simulations. It was shown that using the **SA** turbulence model with Eppler's transition model results in overall agreements with experiments for all wind speed regions, except for speed regions between 7 and 15 m/s.

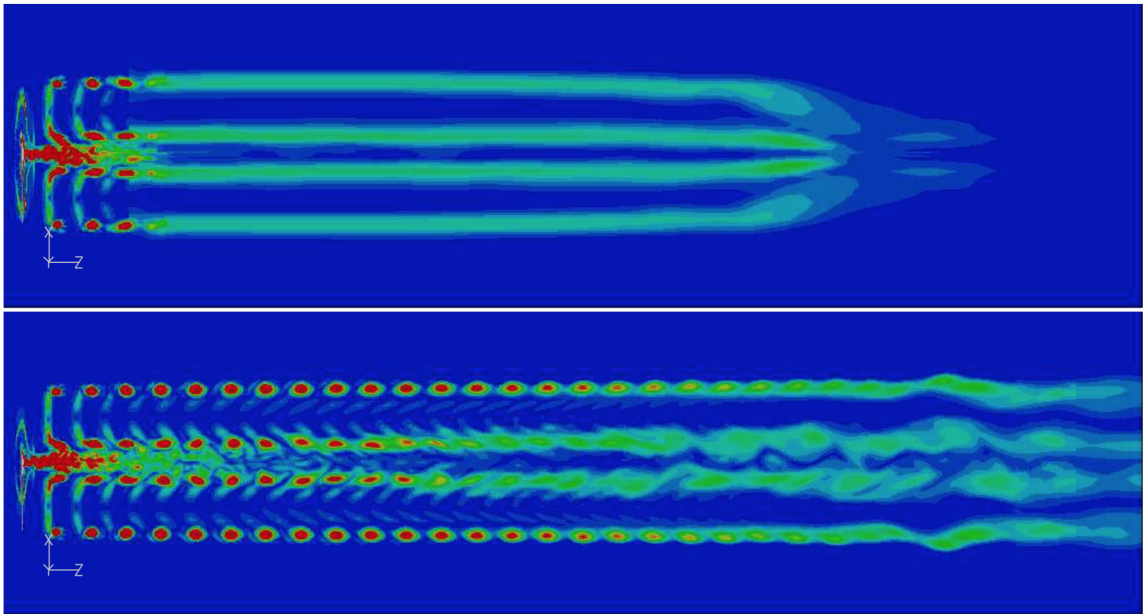


Figure 2.12: Different vortical wake resolutions in a plane bisecting the turbine. The change in resolution is obtained by refining the mesh [168].

Tip and root vortices are typically not preserved for more than half or one rotor diameter downstream due to numerical diffusion resulting from discretization schemes and inadequate refinement of the mesh. Further up downstream, the characteristic helical vortex structures diffuse into a continuous sheet of vorticity and eventually diffuse entirely. In Section 2.1.3, the influence of the wake with respect to the induced velocities at the rotor has shown to be important for correct load and power predictions. As a result, Schmitz and Chattot [169] have made a coupling between a Navier-Stokes

solver (near-field) and a panel solver (wake) in order to reduce numerical diffusion and computational cost. It was shown that the coupling resulted in very good agreements with experimental results for fully attached flows. For mild or fully separated flows, the coupling overpredicted shaft power. Zahle and Sørensen [168] investigated the importance of the wake with CFD predictions on rotor performance. It is shown that it is only necessary to resolve the near wake (less than $0.5D$) to obtain correct induction on the rotor. In fact, the influence of the vortical wake on power performance is very limited: 1.2% torque difference was shown between a coarse and refined mesh. Two vortical wake resolutions, in which numerical diffusion slowly reduces the resolution, are shown in Fig. 2.12. Other investigations on wake analysis and performance predictions of wind farms have been executed. In most cases, LES with actuator disc, actuator line, or actuator surface are employed for wind farm analysis. For further information, see the following references: [170, 171].

2.2 Aerodynamic shape optimization of wind turbine blades

Depending on the need of stakeholders, low-fidelity or high-fidelity analysis models are chosen for the optimization procedure. If the optimization design process of wind turbines has to be finished within days, low-fidelity models are the best choice. When stakeholders want to have a highly optimized and accurate design, resulting in high computational costs, high-fidelity analysis models are recommended. In other words, computational time and accuracy are two main decision factors for choosing the type of analysis model. Low-fidelity aerodynamic shape optimization includes aerodynamic models that are not able to capture accurate complex flow phenomena, such as compressibility and viscosity effects. Some of these low-fidelity models are actuator disc models, BEM models, and vortex and panel methods. High-fidelity optimization models include CFD methods, such as Euler equations, RANS equations, and LES. Besides the performance of the analysis model, the performance of optimization procedures is also dependent on the type of optimization: gradient-based optimization and gradient-free optimization. Various studies have shown that gradient-based optimization is the fastest for smooth design spaces [11]. It is only advisable to use gradient-free optimization when the design space is non-differentiable, disconnected, non-convex, mixed (discrete, continuous, permutation).

In this section, current applications on aerodynamic shape optimization of wind turbine blade will be presented. Note that high-fidelity aerodynamic shape optimization models are not used for wind turbine blades. Therefore, further literature study on aerospace applications are required before they can be applied on wind turbine blades.

2.2.1 Low-fidelity optimization

Recent developments in the wind energy sector are based on systems engineering, in which various models of engineering disciplines are combined. These disciplines include aerodynamics, structures, electricity, and finance. Given this complexity, all related models in this systems engineering approach are low-fidelity in order to reduce the computational time as such that a complete wind turbine or wind plant can be designed and optimized in a couple of days. In most cases, the optimization method is gradient-free, since the design space is unfavourable for gradient-based optimization (e.g., design spaces that are discontinuous, multi-modal, etc.). These studies can be classified into two main categories, i.e. support structure design studies and rotor design studies.

Since this research is focussed on rotor design, only optimization studies that involve rotor are presented. For support structure design studies the interested reader can refer to [172, 173, 174].

During the last decade, various wind turbine airfoil families have been optimized. Most of the optimizations were considering desirable airfoil characteristics for wind turbine blades. Li et al. [175] combined response surface methods and uniform experimental designs for optimizing lift to drag ratio of wind turbine airfoil designs. It was shown that the method was a time-saving and effective method for preliminary optimal designs of wind turbine blades. Bizzarrini and al. [176] optimized tip wind turbine airfoils using the RFOIL solver with genetic and gradient-based optimizers. As for other airfoil optimizers, the Bézier geometry parametrization method is used, seen in Fig. 2.13. Another work [177] focused on the design of tip wind turbine airfoils has used the same method. Grasso [178] extended the work by developing a hybrid optimization platform where gradient-based and gradient-free optimization techniques are used for new designs of airfoil families at root regions of wind turbine blades. Structural considerations are taken into account during the optimization. Flatback airfoils at inboard regions of wind turbine blades have been optimized as well with as multi-objective to increase lift to drag ratio and maximum lift [179]. Ju et al. [180] optimized airfoils by including a multi-objective optimization procedure in which the maximum lift, lift to drag ratio, and minimizing the sensitivity of roughness at the leading edge are taken into account.

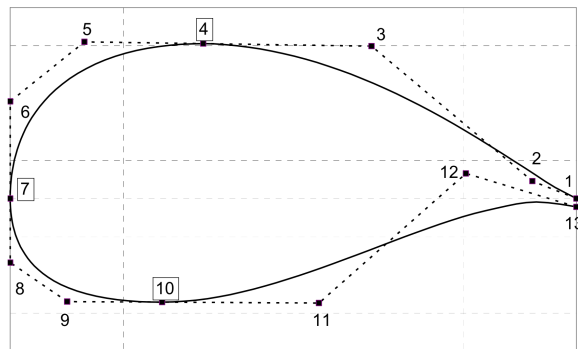


Figure 2.13: Bézier parametrization method for airfoils [176]

Most rotor aerodynamic analyses in wind turbine design are based on **BEM** theory, in which the equations are iteratively solved for axial and tangential induction factors. In most optimizations based on **BEM** theory, the airfoil shape is not perturbed and only geometrical and physical parameters of the wind turbine blade are considered as design variables. It is shown that this aerodynamic technique suffers from instabilities and convergence issues for some regions in the design space [181]. This results in difficulties for solving gradient-based optimization. In order to alleviate this problem, gradient-free optimization methods can be applied [182, 183, 184]. Or the design space of **BEM** theory can be smoothed. Ning [185] recently developed a gradient-based optimization with **BEM** theory in which it transforms the two-variable, fixed-point problem into an equivalent one-dimensional root-finding problem. Also, a smooth description of the airfoil force coefficients is developed for guaranteed convergence.

Mendez and Greiner [186] developed a method based on **BEM** to obtain optimal chord and twist distributions in wind turbine blades in order to maximize the mean power depending on the Weibull wind distribution. Liu et al. [187] developed a similar method by maximizing the annual energy

production. Xuan et al. [188] maximized the annual energy production while minimizing noise level by varying airfoil shapes and geometrical variables of the blade. Clifton-Smith [189] extended **BEM**-based optimizations by using different tip loss factors. Ashuri et al. [8] employed an integrated aeroservoelastic approach to do the rotor optimization for minimizing the levelized cost of energy. The optimization includes the tower and controller design, as well as the cost and mass models of all the other components.

In order to quantify uncertainties, Lee et al. [190] developed a blade aerodynamic shape optimization with a probabilistic approach. Kenway and Martins [191] coupled **BEM** theory with Finite Element Method (**FEM**) in a gradient-based optimization in which the energy output is maximized while considering site-specific wind conditions. This research optimized the aerodynamic shape and structural sizing simultaneously to obtain the right trade-offs between these two disciplines. Several researchers have also applied aero-elasticity codes (based on **BEM**) on optimization methods. Ashuri et al. [192] developed an optimization framework that uses an aeroelastic code to do time domain unsteady aerodynamics and structural design optimization of wind turbines to minimize the cost of energy. Jeong et al [193] employed FAST in order to minimize the unsteady aerodynamic loads. Fuglsang and Thomsen [194] extended the low-fidelity aero-elasticity optimization procedure to a wind plant of 1.5 to 2.0 MW wind turbines by minimizing the cost of energy. Xudong et al. [195] presented an aeroelasticity optimization tool for wind turbine blades that optimizes twist, chord, and relative thickness. Three eigenmodes (first and second flap-wise modes and the first edgewise mode), the axial displacement of the whole rotor, and the azimuth displacement of the blades were taken into account during optimization. Wang et al. [196] approached a multi-objective optimization that maximized the power coefficient at 9 m/s and minimized the blade mass. The blade mass and mass distribution was estimated by using the normal stress equations in the condition of free bending of thin-walled beams.

Besides only employing **BEM** methods on optimization procedures, **CFD** simulations have been combined with **BEM** for validation purposes or for obtaining two-dimensional data of airfoils with three-dimensional flow characteristics [197]. This resulted in more accurate optimization results compared to **BEM** models based on analytical interpolation tools for retrieving airfoil force coefficients. However, the section representation of the wind turbine blade in **BEM** models causes still inaccuracies, e.g., the flow behaviour between two sections cannot be represented. In order to alleviate this problem, other aerodynamic models are employed in which the flow behaviour of the whole blade is simulated. Vortex and panel methods are some of these low-fidelity models. It is shown that even though the models do not take compressibility and viscosity effects into account, aerodynamic shape optimization with panel codes can result in satisfying results [198].

In addition to these optimization studies, there are also some research works in this area that facilitate the optimization process. Ashuri et al. developed an analytical technique to parametrize the properties of the blade as a function of external geometry and structural design variables of the blade [199]. This is a useful method since it provides the updated input data for aeroelastic solvers during an iterative optimization process. Also a method to incorporate the controller design during the optimization study is presented by [200]. This method allows optimizing the aerodynamics and structural design variables of the rotor at the same time with designing a controller, and offers better optimization results compared to the cases where the controller is not involved. Capponi et al. [201] presented a nonlinear upscaling method for providing an initial set of design variables for any wind

turbine size of interest. As a demonstration, an initial rotor design for a 20 MW wind turbine blade is provided using this method that can be used to start the optimization with.

2.2.2 High-fidelity optimization

Since high-fidelity aerodynamic shape optimization models are governed by a system of non-linear Partial Differential Equations (PDEs), it is relatively hard to perform an accurate differentiation of the system of PDEs (sensitivity analysis). This is one of the reasons of limited availability of results from high-fidelity aerodynamic shape optimization results based on gradients. Mesh perturbation techniques and geometry parametrization methods are other reasons for this limited availability, but are left out from this discussion. Two main approaches in acquiring derivatives for optimization exist:

1. **Continuous:** The continuous/variational approach differentiates the system of PDEs before discretization by direct differentiation or by introducing Lagrange multipliers that are defined by a set of continuous linear equations adjoint to the system of PDEs [202, 203].
2. **Discrete:** The governing system of PDEs is first discretized. Afterwards, perturbations on design variables are induced in order to compute the derivative by use of finite difference or complex step. Another approach is using an adjoint method that can be either discrete or continuous [204]. This technique requires only one function evaluation irrespective with the number of design variables. Consequently, this technique is favourable for gradient-based optimizations with large number of design variables.

Note that these methods are extremely tedious and are often circumvented by employing gradient-free optimization techniques which are considered to be computationally inefficient. For further information on adjoint methods, see [205].

Currently, no considerable research on high-fidelity aerodynamic shape optimization on wind turbine blades is available. However, one attempt has been made in which a RANS solver and a continuous adjoint approach have been employed for the NREL VI wind turbine blade [206]. The optimization result was a 4% increase in torque, but only three optimization iterations were computed. This might indicate that some numerical/computational difficulties occurred during the optimization process or no sufficient time in the development was available. Another approach is employing two-dimensional RANS solvers for optimizing wind turbine airfoils [207, 208]. In the aerospace community, however, extensive knowledge on this topic is available. Therefore, it is decided to focus on these specific aerospace applications in order to have an indication on how to apply these computational methods on wind turbine blades.

In the 1970's, full-potential small perturbation inviscid flow simulations were the first analysis models used in gradient-based optimization in which the sensitivity analysis was performed by finite-difference. During this period, Hicks et al. [209] applied these techniques on airfoil optimization and extended it towards a three-dimensional solver to optimize a wing with 11 design variables such as shape and twist [210]. During the 1980's, computer speed and memory were improving dramatically, which consequently resulted in numerous aerodynamic shape optimization procedures that included CFD models, numerical optimization techniques, and sensitivity analyses. However, there were still difficulties associated with storing data of sensitivity derivatives and with performing numerical

optimization procedures. Also, the Central Processing Unit (CPU) time for solving the Euler or Navier-Stokes equations was still considered to be a difficulty in combination with optimization. This resulted in various numerical/computational methods on reducing memory and CPU time, such as pseudo-time methods [211], Jacobian matrix-vector products [212], and parallel computing architectures [213]. Currently, research efforts are more focussed on the development of three-dimensional meshes on complex geometry. It is shown that the application of CFD models is restricted by the availability and capabilities of mesh generation models. For structured-grid solvers, the main difficulty is its handling of complex geometry, in which structured grids are bounded by a single domain. This resulted in various domain-decomposition methods, such as multiblock [214], zonally patch [215], and overlap grid algorithms [216]. Unstructured meshes were developed in order to circumvent this problem. However, unstructured meshes exhibit bad numerical characteristics in boundary layers, which result in inaccurate aerodynamic performance predictions. Therefore, hybrid mesh models were developed in which orthogonal cells were placed at the boundary layer, while the rest of the domain is covered with unstructured cells. Mesh perturbation methods and geometry parametrization techniques for optimization have been developed as well. Most mesh deformation models are related to algebraic and linear elasticity models [217, 218, 219, 220]. While geometry parametrization can have various forms [221], such as Free Form Deformation (FFD), polynomials, splines, CAD based, etc. The most common geometry parametrization method is shown in Fig. 2.14: FFD volume with its control points.

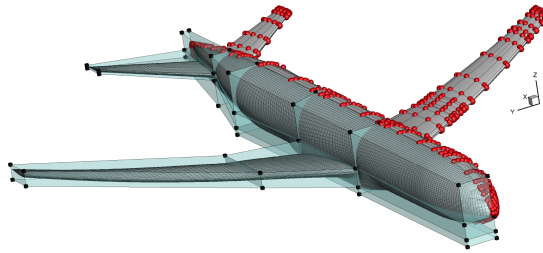


Figure 2.14: FFD volume (left) and B-spline surface representation (right) of DPW4 geometry [219]

As the aerodynamic shape optimization matured, more design variables were required to achieve more realistic designs. Since the computational time of optimizations using finite difference dramatically increases with the number of design variables, new sensitivity analyses with an efficient computational cost were developed. Pironneau applied as first the adjoint method on the Stokes equations and incompressible Euler equations [222, 223]. Afterwards, Jameson [224] performed an aerodynamic shape optimization with the inviscid compressible Euler equations with an adjoint method. This technique was applied on a transonic wing with objective to reduce the inviscid drag. It was shown that the cost of solving the adjoint equations is comparable to solving the flow equations. The used numerical optimization technique was the quasi-Newton method and was proven to be robust for aerodynamic shape optimizations. Since then, numerous applications on adjoint implementations of Euler equations have been performed by various researchers. Reuther et al. [225, 226] applied an inviscid structured Euler model with a continuous adjoint on a transonic business jet wing and on a supersonic transport aircraft configuration. This was executed on a parallel computing architecture and both optimizations were finished within a day of computer time, which demonstrated that high-fidelity aerodynamic shape optimization is feasible for industrial purposes.

The adjoint method was also compared to finite differences. It was shown that the adjoint method is faster and more accurate than finite difference. The mesh perturbations were executed by use of the WARP-MB mesh perturbation algorithm. As a further investigation, a high fidelity aero-structural optimization on a supersonic transport aircraft configuration was performed, in which a coupling between structures (FEM) and aerodynamics (CFD) were executed [227].

Over the past years, CFD models for performing aerodynamic shape optimization have been extended to RANS models with various turbulence models. This resulted in more realistic optimized designs due to its representation capabilities of viscous effects. Anderson and Bonhaus [228] optimized airfoil shapes with a discrete adjoint and SA turbulence model. Drela [229] had performed aerodynamic shape optimization on airfoils for various wind regions in which boundary layer transition has shown difficulties during optimization. Two-dimensional research has been extended to a three-dimensional RANS model, in which the ONERA M6 wing was minimized for drag with thickness and camber design variables at two chordwise locations[230]. Other similar optimization problems have been executed, such as minimizing drag of the DLR-F6 wing-body configuration by varying 96 design variables [231, 232]. Lyu et al. [233] minimized the drag of the ONERA M6 wing with 192 design variables and have made a comparison between compressible Euler and RANS equations. A significant difference in both optimizations were observed, which demonstrated the importance of viscous effects. The aerodynamic shape optimization has been extended to realistic aircraft configurations [234, 235]. In Fig. 2.15, the FFD box and the optimized result of the Boeing Blended-Wing-Body (BWB) aircraft are presented.

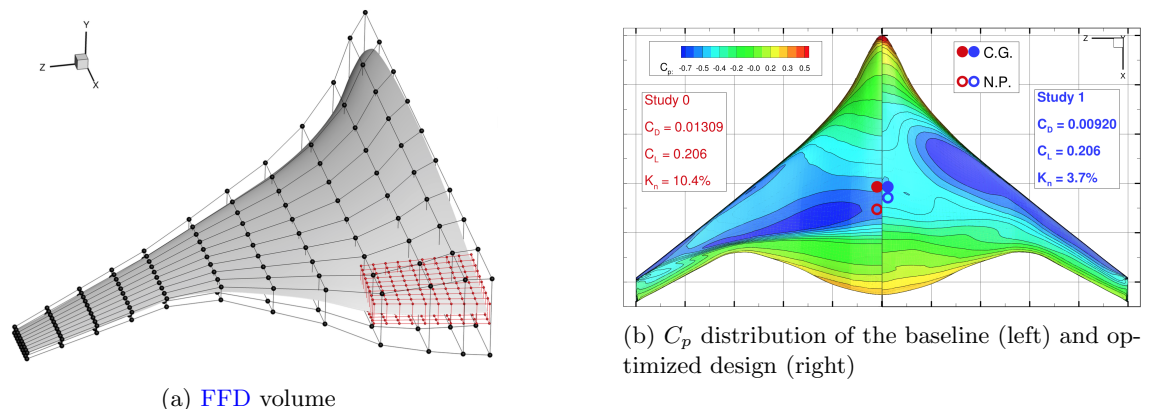


Figure 2.15: Drag minimization of the BWB aircraft configuration while constraining lift coefficient. Note that the optimization removed the shock surface, which resulted in a considerable reduction of drag [235].

Nowadays, various CFD models, adjoint implementations, numerical optimization techniques, and geometry parametrizations are available. This resulted in benchmark propositions in which numerous researchers are challenged to execute the same optimization problem and compare their results against the benchmark solution. One of these benchmark solutions is the transonic Common Research Model (CRM) wing with as objective to reduce the drag while maintaining lift and constraining geometric variables and pitching moment. Lyu et al. [236] have shown that multiple local minima exist for the RANS equations, but the objective values were within 0.1 drag counts of each other and the geometries differ by only 0.4% of the mean aerodynamic chord. It is shown

that optimized solutions are very sensitive for sudden changes during operations, e.g., gust loads on aircraft. This requires a method in which the optimized solution would be more robust for these uncertainties: multipoint optimization. This technique takes various conditions into account solving for one certain optimized solution, e.g., one optimized solution for various wind speeds.

Given the increase of interest in high-fidelity aerodynamic shape optimization techniques, helicopter blades have been optimized as well. Since the flow behaviour between helicopter blades and wind turbine blades are similar, high-fidelity optimization for helicopter blades can be applied for wind turbine blades. Le Pape and Beaumier [237] presented a gradient-based optimization framework with **RANS** equations of the ONERA 7A and 7D rotors in hover condition. The sensitivity analysis was executed by finite difference. Later on, several researcher have extended the aerodynamic shape optimization by use of adjoint approaches: Nielsen et al. [238] used a discrete adjoint in which 44 sections with camber and thickness variable were optimized. Dumont et al. [239] also applied a discrete adjoint approach. Choi et al. [240] optimized the UH-60 helicopter blade by minimizing torque while keeping the same thrust. This optimization method used time-spectral -and discrete adjoint methods in order to incorporate unsteady or periodic flows, such as helicopter rotors in forward mode. Allen et al. [241] developed a more flexible rotor optimization procedure, in which an efficient domain element shape parametrization method is used and is linked to global radial basis functions in order to perturb the surface and volume mesh without losing significant mesh quality. For further information on aerodynamic optimization of helicopter rotors, see [242].

Besides aerodynamic shape optimization, aero-structural and aero-elasticity optimization capabilities have been evolved over the years, in which adjoint coupling methods are employed [243]. These optimizations do not only rely on high-fidelity aerodynamic models, but also on high-fidelity structural models, such as **FEM**. Since this research is solely focussed on aerodynamic shape optimization, it is decided to present a short reference list of state-of-the-art aero-structural optimizations [244, 245, 246].

2.3 Discussion and conclusion

In this literature review, it is shown that **BEM** theory is the most used model for wind turbine design, because of its simplicity, low computational cost, and relatively good accuracy. However, its incapacibilities of representing viscous flows, rotating effects, three-dimensional flow phenomena, and compressibility effects are major drawbacks for performing aerodynamic shape optimization. Even though literature review has shown that **BEM** models can incorporate aerodynamic coefficients computed by **CFD** models, its discrete representation of the blade results in interpolation errors between blade sections. **CFD** simulations alleviate these issues and would be, consequently, a perfect successor of **BEM** models. Although, its high computational cost and poor representation of flow separation are still major concerns that can be resolved in the future by higher computational power and by better turbulence and transition models.

It is clear that high-fidelity aerodynamic shape optimization for wind turbine blades is still immature with respect to aerospace engineering applications. In fact, no serious results have been published yet. Even though low-fidelity aerodynamic shape optimization for wind turbine blades exist, the associated accuracy is not satisfactory with respect to current optimization results in the aerospace engineering sector. Some might say that the computational cost for high-fidelity

models is disadvantageous with respect to low-fidelity models. However, looking at the evolution of computing power, it is expected that the computational cost will be reduced significantly in the future [247]. With respect to industry, various aerospace companies have already employed high-fidelity aerodynamic shape optimization methods [248, 249]. This implies that there is a possibility that the wind turbine industry will eventually use high-fidelity models for their system engineering design optimizations as well. If that is not the case, the developed optimization technique can still contribute in other similar rotor applications, such as helicopters. In other words, high-fidelity aerodynamic shape optimization for wind turbine blades has the potential to become the new design tool for wind turbine rotors.

The next paragraph in this dissertation goal will handle the [NREL VI](#) wind turbine blade as a baseline design for high-fidelity aerodynamic shape optimization. The reason for choosing this type of blade is the significant availability of [CFD](#) simulation results and experimental results. The analysis model will be a [RANS](#)-based [CFD](#) model with a one-equation turbulence model. The first step of the optimization is computing the flow state variables and the residuals of the baseline/initial design. Afterwards, the gradients of the objective function with respect to the design variables will be found by either an adjoint method, finite difference or complex step. In case of finite difference or complex step, geometry parametrizations and mesh perturbations are required for each design variable beforehand in order to compute the gradients. This will result in a lot of analysis simulations and, consequently, high computational costs, i.e. the adjoint method is preferred. When gradients and objective are computed, the gradient-based optimization algorithm will compute the direction and step towards the optimal point. Once it finds a better point, the optimizer will pass over the new shape variables to the geometry parametrization method and the mesh perturbation model as such that a new mesh of the new rotor design can be created. After that, the [CFD](#) model will be simulated again. This whole process is iterative and can only be finished when a certain threshold is met. In most cases, when the step towards a better solution is smaller than the threshold value, the optimization is considered to be converged.

CHAPTER III

Aerodynamic shape optimization methodology

High-fidelity aerodynamic shape optimization with large numbers of design variables results in prohibitively high computational cost when improper techniques are employed. For this work, an efficient gradient-based optimization methodology is presented for solving aerodynamic shape optimization problems related to rotating flow problems. As a benchmark case, the power output of the [NREL VI](#) wind turbine blade is maximized by varying shape, pitch, and twist variables. Since the rotor rotates at a constant angular velocity for all wind speeds, power generation is only dependent on torque. Therefore, it is decided to maximize torque for obtaining an optimal power output. Various components of the optimization framework are explained for identifying possible bottlenecks and for obtaining considerable knowledge of each method. It should be noted that numerical optimization is still not a plug-and-play tool. When the components of the framework are discussed, the problem statement and approach of the optimization are presented.

Since the [NREL VI](#) wind turbine blade has an extensive amount of qualitative experimental results, the wind turbine blade will be used for verification and validation purposes of the high-fidelity aerodynamic shape optimization method. In [Section 3.1](#), the experiment of the [NREL VI](#) blade is discussed. The [CAD](#) and mesh generation of the [NREL VI](#) blade are presented in [Section 3.2](#). The analysis method is presented in [Section 3.3](#), where the structure of the [RANS](#)-based [CFD](#) solver ‘[SUMad](#)’ is explained. The mesh deformation method and the discrete adjoint method are discussed in [Section 3.5](#) and [3.6](#), respectively. When all components of the optimization are discussed, the problem statement and approach of the optimization are explained in [Section 3.7](#). A brief list of limitations and assumptions of the optimization method are presented in [Section 3.8](#).

3.1 Experimental set-up of [NREL VI](#) blade

In May 2000, the National Renewable Energy Laboratory ([NREL](#)) completed the Unsteady Aerodynamics Experiment ([UAE](#)), which tested an extensively instrumented wind turbine, called the [NREL VI](#) wind turbine blade, in the [NASA-Ames](#) 24.4 m by 36.6 m wind tunnel [250, 147]. The [NREL VI](#) wind turbine blade is a modified Grumman Wind Stream-33 blade [251]. The 10.058 m diameter, two-bladed, stall-regulated wind turbine rotor with full span pitch control has a power rating of 20 kW. The blades are twisted and mildly tapered. The [NREL VI](#) blade is discretized over the whole span with S809 airfoils. In order to advance wind turbine technology, the loads and moments acting on the wind turbine structure are measured for validation purposes of modeling tools. For maximizing the benefits from testing, [NREL](#) decided to form a science panel of advisers

consisting of wind turbine aerodynamics and modeling experts throughout the world. The science panel specified the conditions and configurations under which the wind turbine blade should be operated in the wind tunnel. The panel also defined the test objectives for effective wind turbine modeling tool development and validation.

Various measurement were obtained over a wide range of operating conditions, such as downwind and upwind configurations. Yawed and unsteady pitch configurations were also executed. The experimental measurements included blade pressures, integrated air loads, section inflow conditions, shaft torque, bending moments, tip acceleration, and wake visualization. The [NREL](#) data system acquired time series measurements, while the [NASA](#) data system acquired statistical, corroborating measurements. The atmospheric conditions and pressure measurements in the wind tunnel (and outdoor) were managed by the [NASA](#) data system. As a verification tool, two sonic anemometers were installed upwind of the turbine for monitoring the wind tunnel wind velocity. The surface pressure of the blade was measured by taps that were carefully installed during manufacturing the [NREL](#) VI blade. The 22 pressure taps were aligned along the chord and were installed at five primary spanwise locations: 30%, 46.6%, 63.3%, 80%, and 95% span. The unit of the pressure taps is pressure coefficient. In Fig. 3.1, the exact locations of the pressure tabs are shown. Note that five-hole probes are as well attached to the blade for providing dynamic pressure, local flow angle, and spanwise flow angle measurements. The bending moments were measured at the root of each blade and on the low-speed shaft with strain gauges.

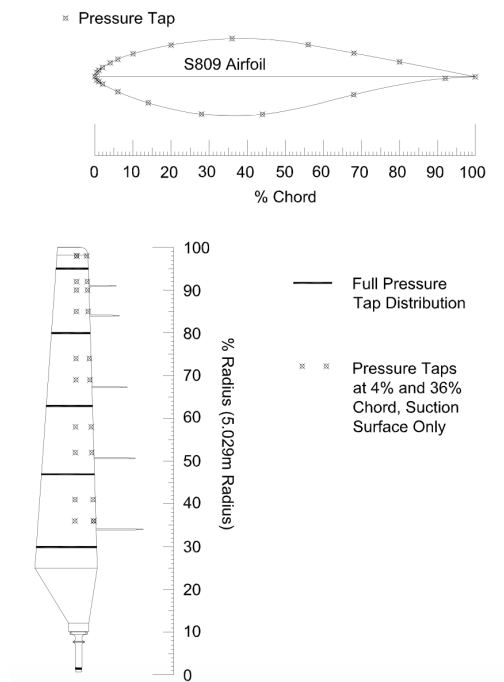


Figure 3.1: Blade surface pressure and five-hole probe locations [250]: More pressure tabs are located at the leading edge for achieving increased resolution of the pressure distribution.

The [UAE](#) achieved exceptional data accuracy and reliability. This means that the data can be used for developing and validating wind turbine aerodynamic codes. In this research, [SUMad](#) will

be used for analyzing and optimizing wind turbine blades. In order to benchmark the accuracy of this in-house RANS-based CFD simulation tool, the experimental data will be used for validation. Since SUMad will only obtain steady-state results, the sequence S experimental data will be used, which represents an upwind, rigid turbine with a zero-yaw and zero-cone angle. The wind speed ranges from 5 m/s to 25 m/s. The blade tip pitch is 3 degrees and the two-bladed rotor rotates at approximately 72 rotations per minute for all wind speeds.

Given that most measurements of the NREL VI are time dependent, an averaged value should be obtained for each variable in order to represent steady-state conditions. Therefore, a MATLAB script is written that processes 15625 measurements per channel representing a variable. In Table 3.1, the sequence S operating conditions for each wind speed are shown.

Table 3.1: Averaged sequence S operation conditions

U [m/s]	Rotational speed [RPM]	ρ [kg/m ³]	$\mu \times 10^{-5}$ [kg/(ms)]	T [C°]	$P_{\text{tot}} \times 10^5$ [Pa]
5.0385	71.6851	1.2435	1.7948	11.5606	1.0195
7.0163	71.8667	1.2458	1.7927	11.1318	1.0199
10.0471	72.0962	1.2459	1.7919	10.9714	1.0196
13.0695	72.0940	1.2266	1.8057	13.7263	1.0152
15.0982	72.0619	1.2240	1.8082	14.2351	1.0151
20.1309	72.0088	1.2214	1.8094	14.4767	1.0145
25.1088	72.1622	1.2197	1.8092	14.4369	1.0141

3.2 Mesh generation

Mesh generation is one of the most important aspects in the accuracy of CFD simulation results. The discretization errors are mainly dependent on the resolution of the mesh: a finer mesh resolution will result in lower discretization errors and consequently a more accurate flow solution. However, the associated computational cost increases with higher mesh resolutions. Therefore, a trade-off between accuracy and computational cost should be performed before extensive analyses and optimizations are made.

In this section, the development of the computational domain of the NREL VI wind turbine blade is presented. First, a CAD of the NREL VI blade is developed by extrapolating S809 airfoil sections along the span. Afterwards, various structured computational domains are automatically or manually developed. The various mesh refinements are made for various types of applications, such as verification and convergence analysis.

3.2.1 CAD design of NREL VI blade

The dimensions of the NREL VI blade are described in reference [250], where the blade is discretized in various S809 airfoil sections. These sections are positioned at certain x, y, z coordinates fixed on the leading edge and are connected with each other by interpolation. The dimensions of the transition between the cylinder and the actual blade are not specified. Therefore, it is decided to interpolate between the last cylinder section with the first airfoil section. The transition part is designed as such that it is slender. The coordinates, chord, and rotation along the reference

axis for the 24 sections can be found in Table 3.2. Given that there is interpolation between discretized sections, it must be noted that the CAD presentation of the NREL VI blade can have small discrepancies compared to the real design.

Table 3.2: Dimensions of NREL VI wind turbine blade: The origin of the reference frame is given by $[x_0, y_0, z_0] = [0, 0, 0]$.

Type of section	x [m]	y [m]	z [m]	chord [m]	rotation along z -axis [degrees]
Cylinder	-0.109	0	0.508	0.218	0
Cylinder	-0.109	0	0.660	0.218	0
Cylinder	-0.0915	0	0.883	0.183	0
S809	-0.2211	0	1.257	0.737	20.040
S809	-0.2184	0	1.343	0.728	18.074
S809	-0.2133	0	1.510	0.711	14.292
S809	-0.2091	0	1.648	0.697	11.909
S809	-0.1998	0	1.952	0.666	7.979
S809	-0.1908	0	2.257	0.636	5.308
S809	-0.1881	0	2.343	0.627	4.715
S809	-0.1815	0	2.562	0.605	3.425
S809	-0.1722	0	2.867	0.574	2.083
S809	-0.1629	0	3.172	0.543	1.150
S809	-0.1626	0	3.185	0.542	1.115
S809	-0.1536	0	3.476	0.512	0.494
S809	-0.1446	0	3.781	0.482	-0.015
S809	-0.1371	0	4.023	0.457	-0.381
S809	-0.1353	0	4.086	0.451	-0.475
S809	-0.126	0	4.391	0.420	-0.920
S809	-0.1167	0	4.696	0.389	-1.352
S809	-0.1143	0	4.780	0.381	-1.469
S809	-0.1074	0	5.029	0.358	-1.775

The trailing edge of the blade is blunt for making the meshing procedure easier. Another reason for choosing blunt trailing edges is that it is practically impossible for manufacturers to develop blades with perfect sharp trailing edges. Therefore, it is chosen to have a trailing edge height of approximately 1% of the chord. A smooth tip is added for making the meshing procedure easier. Furthermore, the blade is rotated with 4.775 degrees around the z -axis for obtaining a tip pitch angle of 3 degrees. Once the two NREL VI blades are constructed, a cylindrical part with diameter of 0.218 m and height of 1.016 m is constructed for connecting the two blades. Later on, it will be clear that the cylindrical and transition part is not needed for optimization purposes and thus the root part of the two blades at 0.508 m and -0.508 m is smoothed like the tip region. In Fig. 3.2, both rotor configurations are shown.

The two-bladed rotor will be positioned perpendicularly with respect to the free-stream flow for obtaining a symmetric and steady wake structure. According to the blade element theory (Section 2.1.2), the lower part of the blade should be faced towards the free-stream flow and the leading edge is pointed towards the angular velocity vector.

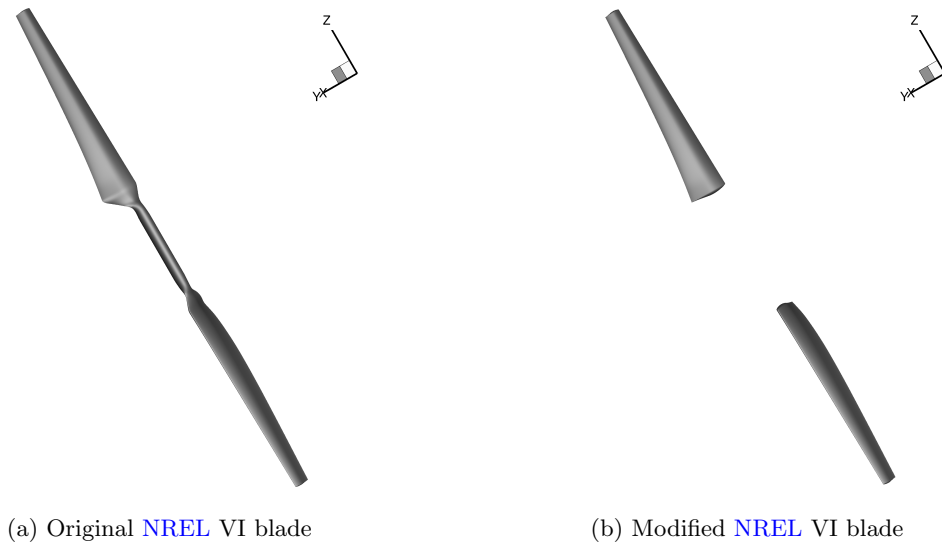


Figure 3.2: CAD designs of the NREL VI blade

3.2.2 Surface and volume mesh

Due to different computational domains*, CFD simulation results of one particular flow problem between different CFD solvers can differ significantly. The unstructured mesh format makes it relatively easy to develop a computational domain resulting in the most preferable meshing tool in the industry. Its computational format, on the other hand, is difficult for developing new CFD models. Also, its tendency to resolve inaccurate boundary layers makes it less attractive for research purposes (see Section 2.1.4.4). The structured mesh, at the other hand, has opposite properties compared to unstructured meshes. Given that SUMad will be used for aerodynamic shape optimization, the development of the structured mesh will be discussed below. The procedure of obtaining the unstructured mesh in SU2 can be found in Appendix A.

The surface mesh is essential when using automatic volume mesh generators that are marching volume cells out of the surface. The surface mesh of the NREL VI blade is constructed by conforming a box with a structured mesh over the CAD design of the wind turbine blade. Since the design of the blade is complex, the box is divided in smaller pieces, such that the local mesh of a specific part can be modified in order to obtain a higher mesh quality. These modifications can be executed by changing the amount and distribution of points on edges of the local box. The construction of the surface mesh is performed by the software Integrated Computer Engineering and Manufacturing (ICEM) CFD. When obtaining a sufficient surface mesh quality, the in-house code ‘PyHyp’ hyperbolically marches the surface mesh out until it has reached a spherical far field. In Fig. 3.3, a section of the volume mesh created by ‘PyHyp’ is shown. This volume mesh can be modified according to the inputs of the in-house code, such as radius of the spherical far field, off-wall spacing, radial distribution of the amount of volume cells, etc. Once the volume cells are created, the boundary conditions can be applied on the computational domain. The NREL VI blade has wall boundary conditions and the spherical far field is subjected to a far field boundary condition. The diameter of the spherical far field is twenty times larger than the diameter of the NREL VI blade in order to

*Note that other causes, such as different computational methods, are excluded from this explanation

assure there will be no considerable interaction effect between far field boundary and wall boundary conditions. A constant growth rate of 1.2 on volume cells are applied.

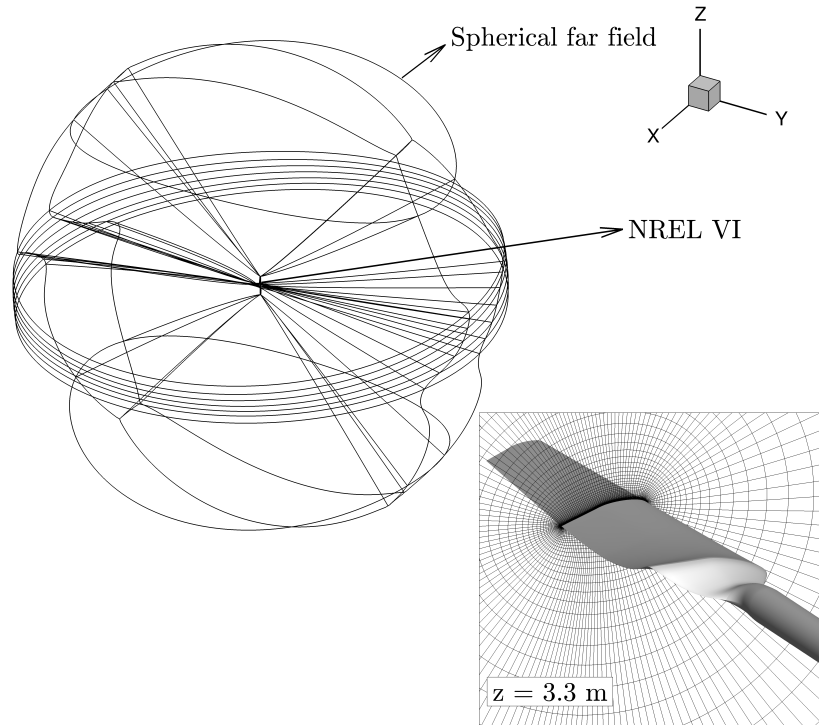
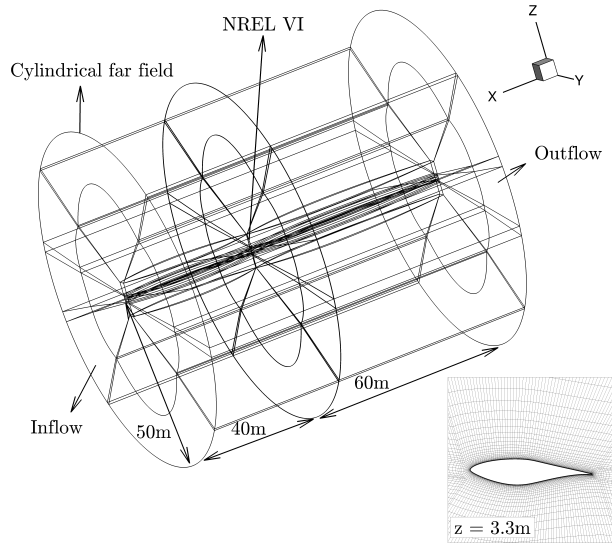
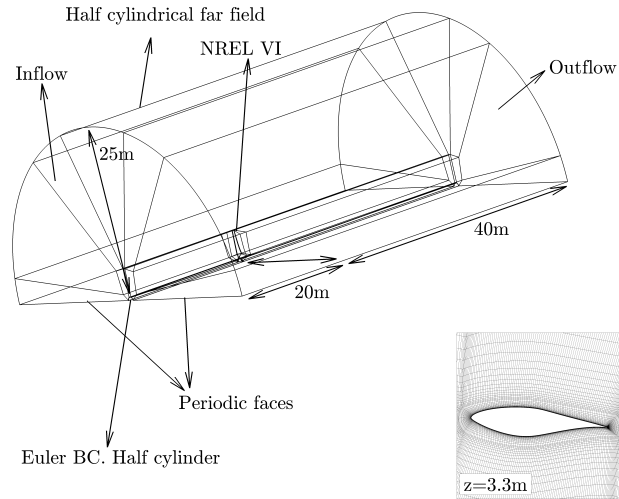


Figure 3.3: Spherical volume mesh created by in-house code ‘PyHyp’

When a spherical far field is not desired, the construction of a surface mesh is not required. Instead, the volume mesh is directly designed by [ICEM CFD](#) where each edge of the far field, [CAD](#) design, and connections between the two entities is modified for obtaining a good mesh quality. The distribution of the points on the edges are changed for obtaining a smooth transition between edge connections and for reducing mesh size by making cell sizes larger towards the far field. Two different far field shapes are used for this manual procedure: cylinder and half cylinder shape. The half cylinder shape is employed for periodic boundary condition purposes where cells at the straight faces of the half cylinder are considered to be mirrored. Note that a small half cylinder is made around the rotation axis to facilitate the mesh generation. The boundary condition for this half cylinder is an Euler wall condition, such that no boundary layer is created. In [Fig. 3.4](#), the boundary conditions and dimensions of both computational domains are shown. Notice that the distribution of volume cells is less smooth compared to the volume cells generated by ‘PyHyp’. This is expected since the cylindrical meshes are generated manually. During this research, various numbers of volume cells are used on the prescribed computational domains presented in [Fig. 3.4](#) for optimization and verification purposes. When using the modified [NREL VI](#) design, the same computational domain shapes are employed as in [Fig. 3.4](#).



(a) Computational domain of approximately 10.6 million cells with cylindrical far field shape



(b) Computational domain of approximately 5.6 million cells with periodic boundary conditions

Figure 3.4: Reference shapes of computational domains for various amounts of volume cells. Note that the inflow and outflow are considered to be far field boundary conditions in [SUMad](#)

A sufficient number of cells near the wall is required to capture the boundary layer accurately. Therefore, the off-wall spacing is calculated by applying the turbulent flat-plate boundary theory, where the local skin friction coefficient is obtained from the one-seventh-power law:

$$C_{f,x} = \frac{0.027}{(\text{Re}_x)^{\frac{1}{7}}}, \quad (3.1)$$

where the local Reynolds number can be determined by the following:

$$\text{Re}_x = \frac{\rho U x}{\mu}, \quad (3.2)$$

where ρ is the density, U the free-stream velocity, x the local reference length, and μ the dynamic viscosity. When considering compressible flows, the density and dynamic viscosity vary according to the position of the wind turbine blade as well. Once the skin friction coefficient is found, the friction velocity is calculated by the following equation:

$$u_* = \sqrt{\frac{C_{f,x} U^2}{2}}. \quad (3.3)$$

Eventually, the off-wall spacing Δs is determined by:

$$\Delta s = \frac{y^+ \mu}{u_* \rho}. \quad (3.4)$$

As previously described in Section 2.1.4.3, the boundary layer can be sufficiently captured when $y^+ = 1$. The Reynolds number is calculated in function of the given dynamic viscosity, free-stream velocity, and free-stream density of the experiment (Section 3.1). The length scale of the given Reynolds number is set to be one. The reason for this approach is that SUMad requires the Reynolds number for calculating the experimental dynamic viscosity. Once the Reynolds number is calculated, the off-wall spacing is obtained. Note that the off-wall spacing is in the order of 10^{-5} to 10^{-6} m which means that large numbers of volume cells are required to fill the computational domain (approximately 10^6 to 10^7 volume cells).

3.3 CFD model

The accuracy of optimization results is mainly dependent on the analysis model. In this research, a RANS-based CFD simulation tool, called Stanford University of Michigan adjoint (SUMad) which is based on the Stanford University multi-block (SUMb) solver, will be employed for analysis. SUMad solves the Euler, laminar Navier-Stokes, and RANS equations in either steady, unsteady, or time-spectral modes [252]. The CFD solver was originally developed for analyzing large-scale turbo-machinery flow, but has also successfully been employed for external flow applications [253]. SUMad is a finite-volume, cell-centered multi-block solver that provides options for a variety of turbulence models with one, two, and four equations and a variety of adaptive wall functions. Since SUMad has extensively been modified for external flow applications and optimization procedures, the option for solving rotational flow problems can have some solving issues. Therefore, it is decided to give a brief overview of the methodology in solving rotational flow problems for obtaining a better insight of the analysis model. Besides obtaining better insight, further developments on solving rotating flow problems, such as periodic boundary conditions and Turkel's low speed preconditioner, are made.

3.3.1 Governing equations in ALE form

When considering an isolated rotor rotating at a constant angular velocity $\boldsymbol{\omega} = [\omega_x, \omega_y, \omega_z]^T$ with the rotor plane perpendicular to a uniform steady wind in a fixed reference frame, the flow

field is intrinsically unsteady. Since the optimization procedure assumes steady-state solutions, this configuration will not work. However, when applying the same configuration in a co-rotating reference frame with the rotor, a steady-state solution can be obtained. For clarity, this does not mean that the computational domain is rotating, but the flow field incorporates a rotational term. Note that unsteady flow fields can still exist when there are unsteady effects such as flow separation. Assuming that both reference frames have the same origin, the velocity of the co-rotating reference frame \mathbf{u}_ω can be related with the velocity in a fixed reference frame \mathbf{u} :

$$\mathbf{u} = \mathbf{u}_\omega + \boldsymbol{\omega} \times \mathbf{x}, \quad (3.5)$$

where $\mathbf{x} = [x - x_0, y - y_0, z - z_0]^T$ is the position vector pointing from the origin of the reference frame (x_0, y_0, z_0) to a point in the flow domain (x, y, z) . The time derivative of a time dependent vector function $\mathbf{f}(t)$ in a co-rotating reference frame is given by:

$$\frac{d\mathbf{f}(t)}{dt} = \left(\frac{d\mathbf{f}(t)}{dt} \right)_\omega + \boldsymbol{\omega} \times \mathbf{f}(t) \quad (3.6)$$

As described in Section 2.1.4.1, the conservation of momentum of an arbitrary time-independent control volume Ω with permeable boundary $\partial\Omega$ is governed by the Navier-Stokes equations. When implementing the above two relationships in the momentum equations in a fixed reference frame, the conservation of momentum can be expressed in the integral conservation form with co-rotating motion (assuming that there are no external forces):

$$\frac{\partial}{\partial t} \int_{\Omega} \rho \mathbf{u} \, d\Omega + \int_{\partial\Omega} \rho \mathbf{u} \left([\mathbf{u} - (\boldsymbol{\omega} \times \mathbf{x})]^T \cdot \mathbf{n} \right) \, dS = - \int_{\partial\Omega} (p\mathbf{n} - \boldsymbol{\tau} \cdot \mathbf{n}) \, dS - \int_{\Omega} \rho (\boldsymbol{\omega} \times \mathbf{u}) \, d\Omega, \quad (3.7)$$

where ρ is the local density, p the static pressure, $\boldsymbol{\tau}$ the viscous stress tensor from which the fluid behavior is assumed to be Newtonian, $\mathbf{u} = [u, v, w]^T$ the local velocity of the fluid, and $\mathbf{n} = [n_x, n_y, n_z]^T$ the outward pointing unit normal vector. When scaling parameters are applied, more insight in the Navier-Stokes equations can be obtained. For instance, the dimensionless Reynolds number $Re = \frac{\rho_0 U L}{\mu_0}$ appears at the viscous flux term. Since wind turbines for large parts are performing at relatively high Reynolds numbers ($10^5 - 10^7$), the inertial forces are predominant meaning that the viscous term can be neglected resulting the Euler equations. However, at the root region of the blade or for low relative wind speeds, the viscous forces cannot be neglected. Therefore, it is decided to continue with the Navier-Stokes equations. When combining the momentum equations with the equations of conservation of mass and energy, the motion of a fluid is described by the following integral conservation vector form:

$$\frac{\partial}{\partial t} \int_{\Omega} \mathbf{W} \, d\Omega + \int_{\partial\Omega} [\underline{\mathbf{F}}(\mathbf{W}) - \underline{\mathbf{G}}(\mathbf{W})] \cdot \mathbf{n} \, dS - \int_{\Omega} \mathbf{Q}(\mathbf{W}) \, d\Omega = \mathbf{0}. \quad (3.8)$$

The state variables of vector \mathbf{W} are expressed by the following:

$$\mathbf{W} = [\rho, \rho \mathbf{u}, \rho E]^T. \quad (3.9)$$

Note that E is the total absolute energy. Assuming that the flow is a calorically perfect gas with γ

being the ratio of specific heats and R being the gas constant, the pressure p and density ρ can be related with the perfect gas law:

$$p = (\gamma - 1) \rho \left(E - \frac{\mathbf{u} \cdot \mathbf{u}}{2} \right). \quad (3.10)$$

Subsequently, the temperature T is achieved by the following:

$$T = \frac{p}{\rho R} \quad (3.11)$$

The inviscid flux tensor $\underline{F}(\mathbf{W})$ with co-rotating motion is defined as:

$$\underline{F}(\mathbf{W}) = \left[\rho [\mathbf{u} - \boldsymbol{\omega} \times \mathbf{x}]^T, \rho \mathbf{u} [\mathbf{u} - \boldsymbol{\omega} \times \mathbf{x}]^T + p \mathbf{I}, p \mathbf{u}^T + \rho E [\mathbf{u} - \boldsymbol{\omega} \times \mathbf{x}]^T \right]^T. \quad (3.12)$$

When applying the Reynolds decomposition on the Navier-Stokes equations, an additional term appears that is called the turbulence Reynolds stress. This results in a closure problem of the **RANS** equations that can be solved by the Boussinesq hypothesis: turbulence Reynolds stresses can be related to the mean velocity gradients and turbulent viscosity in a manner analogous to the relationship between the stress and strain tensors in laminar Newtonian flow. When substituting the Boussinesq relationship in **RANS** equations, the viscous flux term $\underline{G}(\mathbf{W})$ can be decomposed in the following expression:

$$\underline{G}(\mathbf{W}) = \mu_1 \underline{F}_{\text{visc1}}(\mathbf{W}) + \mu_2 \underline{F}_{\text{visc2}}(\mathbf{W}), \quad (3.13)$$

where the viscous terms are $\underline{F}_{\text{visc1}}(\mathbf{W}) = [0, \tau, \tau \cdot \mathbf{u}]^T$ and $\underline{F}_{\text{visc2}}(\mathbf{W}) = [0, 0, c_p \nabla T]^T$. It can be noted that there are two different viscosities, which are both in function of the laminar and turbulent viscosity, respectively μ_{lam} and μ_{turb} . The laminar viscosity, or dynamic viscosity, is considered to be only dependent on the temperature. In most cases, the Sutherland's law can be applied for ideal flows:

$$\mu_{\text{lam}} = \mu_0 \frac{T_0 + C}{T + C} \left(\frac{T}{T_0} \right)^{3/2}, \quad (3.14)$$

where μ_0 is the dynamic viscosity at reference temperature T_0 and C the Sutherland's constant of the fluid. The turbulent viscosity, at the other hand, is obtained from an eddy viscosity turbulence model. In this research, the one-equation Spalart-Allmaras turbulence model [86] is employed, in which a transport equation is solved for $\tilde{\nu}$. Once the transport equation is computed, the turbulent viscosity can be related with $\tilde{\nu}$ and local state variables. Once both viscosities are solved, μ_1 and μ_2 are found:

$$\mu_1 = \mu_{\text{lam}} + \mu_{\text{turb}}, \quad \mu_2 = \frac{\mu_{\text{lam}}}{\text{Pr}_{\text{lam}}} + \frac{\mu_{\text{turb}}}{\text{Pr}_{\text{turb}}} \quad (3.15)$$

where Pr_{lam} and Pr_{turb} are the laminar/dynamic and turbulent Prandtl numbers, respectively. Notice that solving the turbulent viscosity is performed separately from the actual computation of the Navier-Stokes equations (segregated turbulence modeling).

As a last remark, when incorporating the co-rotating reference frame, the momentum equations gain an extra body force that represents the combined effect of the centrifugal and Coriolis force. This extra term $\underline{Q}(\mathbf{W}) = [0, -\rho(\boldsymbol{\omega} \times \mathbf{u}), 0]^T$ does not appear in the energy equation, since the forces are perpendicular to the direction of the motion and thus no work is produced.

3.3.2 Spatial discretization

In **SUMad**, the system of integral conservation equations is solved numerically by discretizing the flow field in control volumes. The finite volume method is based on structured meshes, which makes the spatial discretization easier compared to unstructured meshes (see Section 2.1.4.4). When considering a hexahedral control volume cell Ω_j , the integral of the flux over the boundary of the control volume can be approximated as a summation of the flux over each one of the six faces of the control volume:

$$\int_{\partial\Omega_j} [\underline{F}(\mathbf{W}) - \underline{G}(\mathbf{W})] \cdot \mathbf{n} \, dS = \int_{\partial\Omega_j} \underline{T}(\mathbf{W}) \cdot \mathbf{n} \, dS = \sum_{i=1}^{i=6} \mathcal{T}(\mathbf{W}_{\text{left}}, \mathbf{W}_{\text{right}}, \mathbf{n}_i) S_i, \quad (3.16)$$

where $\mathcal{T}(\mathbf{W})$ is the numerical flux approximation of the actual flux $\mathbf{T}(\mathbf{W})$, \mathbf{W}_{left} and $\mathbf{W}_{\text{right}}$ are the state variables on the left and the right of interface i respectively, S_i is the area of interface i . The numerical flux is assumed to be constant across the interface. The semi-discrete form of the integral conservation equations is given by:

$$\frac{d\overline{\mathbf{W}}_j}{dt} = -\frac{1}{\Omega_j} \sum_{i=1}^{i=6} \mathcal{T}(\mathbf{W}_{\text{left}}, \mathbf{W}_{\text{right}}, \mathbf{n}_i) S_i + \overline{\mathbf{Q}}_j, \quad (3.17)$$

where the overline represents a control-volume averaged value defined by

$$\overline{\mathbf{W}}_j = \frac{1}{\Omega_j} \int_{\Omega_j} \mathbf{W} \, d\Omega \quad \text{with} \quad \Omega_j = \int_{\Omega_j} d\Omega,$$

The spatial discretization in **SUMad** has various methods. For brevity, only the relevant spatial discretization methods are briefly explained. Given the numerical flux, a first-order accurate spatial discretization can be achieved by employing an upwind scheme with control-volume-averaged state variable vectors along the interface. Since the convective flux exhibits a hyperbolic behavior, an accurate flux at the interface between two control volumes can be achieved by finding an approximate solution of the Riemann problem. Roe's approximate Riemann solver [254] linearizes the Riemann problem as such that a Jacobian matrix $\underline{A}(\mathbf{U}) = \partial\mathbf{T}/\partial\mathbf{U}$ appears that can solve the linearized system:

$$\frac{\partial\mathbf{U}}{\partial t} + \frac{\partial\mathbf{T}(\mathbf{U})}{\partial x} = \frac{\partial\mathbf{U}}{\partial t} + \underline{A}(\mathbf{U}) \frac{\partial\mathbf{U}}{\partial x} = \mathbf{0}. \quad (3.18)$$

The Jacobian matrix is approximated by the Roe matrix $\tilde{\underline{A}}$ that retains the properties of the original problem: consistency with the exact Jacobian matrix, the system is hyperbolic, and conservation is assured. Once every entry of the Roe matrix is obtained, the numerical flux of an interface between two control volumes is computed by solving the local linear system $\mathbf{T} = \tilde{\underline{A}}\mathbf{U}$:

$$\mathcal{T}(\mathbf{W}_{\text{left}}, \mathbf{W}_{\text{right}}, \mathbf{n}_{j+\frac{1}{2}}) = \frac{1}{2} [\mathcal{T}(\mathbf{W}_{\text{left}}) + \mathcal{T}(\mathbf{W}_{\text{right}})] - \frac{1}{2} \sum_{k=1}^{k=5} \tilde{\alpha}_k \|\tilde{\lambda}_k\| \tilde{\mathbf{K}}^{(k)}, \quad (3.19)$$

where $\tilde{\alpha}_k$ are representing the wave strengths associated with the direction of the right eigenvector of Roe matrix $\tilde{\mathbf{K}}(:, k)$ and $\tilde{\lambda}_k$ the eigenvalues of the Roe matrix. The state variables at the left and right side of the interface are volume-averaged quantities. This spatial discretization method

is first-order accurate, but can achieve second-order accuracy when using linear reconstruction of the quantities of state variables at the interface. Instead of using volume-averaged state variables in Eq. 3.19, a weighted average of gradients at the interface is employed. However, in some cases, large gradients due to discontinuities can result in oscillatory behavior of the solution. Therefore, it is necessary to limit these gradients. As a result, various flux limiters are developed, such as Monotone Upstream-Centered Scheme for Conservation Laws (**MUSCL**) [255], Van Albada [256], and Van Leer [257]. Since wind turbines are not performing in transonic/supersonic conditions, it is expected that no flux limiter is required for avoiding oscillatory solutions. For further information on linear reconstruction, see [258]. Note that all computations with Roe scheme are performed with linear reconstruction for this research subject, i.e. second-order accuracy for spatial discretization.

Another discretization method for the numerical flux is the Jameson-Schmidt-Turkel (**JST**) scheme that employs a central discretization method. The **JST** scheme is known to be unstable. Therefore, artificial dissipation is added to remove energy of modes with wavelengths that are too small to resolve in the mesh. These wavelengths occur when discontinuities (shocks in transonic/supersonic flows) appear in the flow field. With the addition of artificial dissipation, the numerical flux can be approximated between two control volumes by the following:

$$\mathcal{T}(\mathbf{W}_{\text{left}}, \mathbf{W}_{\text{right}}, \mathbf{n}_{\frac{1}{2}}) = \frac{1}{2} [\mathbf{T}(\overline{\mathbf{W}}_j) + \mathbf{T}(\overline{\mathbf{W}}_{j+1})] - \mathbf{D}_{j+\frac{1}{2}}, \quad (3.20)$$

where $\mathbf{D}_{j+\frac{1}{2}}$ is the artificial dissipation term and the state variables are volume-averaged. The dissipation term can be divided in a second-order shock capturing term $\mathbf{D}_{j+\frac{1}{2}}^{(2)}$ and a fourth-order background dissipation term $\mathbf{D}_{j+\frac{1}{2}}^{(4)}$:

$$\mathbf{D}_{j+\frac{1}{2}} = \mathbf{D}_{j+\frac{1}{2}}^{(2)} - \mathbf{D}_{j+\frac{1}{2}}^{(4)}. \quad (3.21)$$

Subsequently, these dissipation terms consist of artificial dissipation coefficients that have as purpose to change the order of accuracy depending on the flow behavior. When there are strong variations in pressure the fourth-order coefficient will vanish and the second-order term becomes approximately first-order, which results in a local first-order accurate **JST** scheme. For smooth behavior in pressure, the fourth-order artificial dissipation coefficient is non-zero and the second-order dissipation coefficient is small resulting in a local second-order accurate **JST** scheme. For further information on defining the second and fourth-order artificial dissipation term of the **JST** scheme [259].

3.3.3 Pseudo-time stepping

For steady-state problems, the time derivative term in Eq. (3.8) should disappear. Although, the time derivative is used to iterate from an initial solution to the steady-state numerical solution. The flow simulation starts with uniform free-stream conditions in every control volume cell of the computational flow domain and by use of a pseudo-time integration method the flow solution converges to a steady-state solution. In this **CFD** simulation, an explicit multi-stage Runge-Kutta method is employed for obtaining a steady-state solution. A Newton's method, that uses the steady-state solution of the Runge-Kutta method for obtaining an even more tight convergence, is also available in **SUMad**. However, due to the quasi-steady characteristics of the **NREL VI** blade shown in Section 4.1.3, the Newton's method diverges and thus it is concluded not to use this method.

When considering the time derivative of Eq. (3.17) as the residual of the pseudo-time integration

for a control volume j , the semi-discrete governing equations can be rewritten:

$$\mathbf{R}_j(\overline{\mathbf{W}}^{(m)}) = -\frac{1}{\Omega_j} \sum_{i=1}^{i=6} \mathcal{T}(\mathbf{W}_{\text{left}}(\overline{\mathbf{W}}^{(m)}), \mathbf{W}_{\text{right}}(\overline{\mathbf{W}}^{(m)}), \mathbf{n}_i) S_i + \mathbf{Q}_j(\overline{\mathbf{W}}^{(m)}), \quad (3.22)$$

where $\overline{\mathbf{W}}^{(m)}$ are the volume-averaged state variables at pseudo-time level m . The Runge-Kutta pseudo-time stepping method integrates the flow solution at pseudo-time level m with multiple stages to the subsequent level $m + 1$:

$$\begin{aligned} \tilde{\mathbf{W}}^{(0)} &= \overline{\mathbf{W}}^{(m)}, \\ \tilde{\mathbf{W}}^{(k)} &= \tilde{\mathbf{W}}^{(0)} + \alpha_k \Delta t_j \mathbf{R}_j(\tilde{\mathbf{W}}^{(k-1)}), \quad k = 1, \dots, 4 \\ \overline{\mathbf{W}}^{(m+1)} &= \tilde{\mathbf{W}}^{(k)}, \end{aligned} \quad (3.23)$$

where the local time step t_j can be determined from the Courant-Friedrichs-Lewy (CFL) condition. The local time step can vary for each volume cell, since time accuracy of the solution is not relevant. The coefficients α_k are responsible for the stability of the scheme. The Runge-Kutta scheme is considered to be second-order accurate in time. For further information on finding the local time stepping or coefficients α_k , see [260].

3.3.4 Turkel's low speed preconditioner

For low-speed flows, the system of compressible governing equations are stiff because the ratio of the acoustic wave speed $u + a$ to the convective speed u is large [261]. This ratio, also known as the characteristic condition number K , should be close to one so that the acoustic wave speed is equal to the convective speed resulting in capturing all information of the flow field in a control volume for a specific local time step. Shown in Fig. 3.5, not all information can be captured in low-speed and transonic flow conditions, while preconditioning does result in getting all the information.

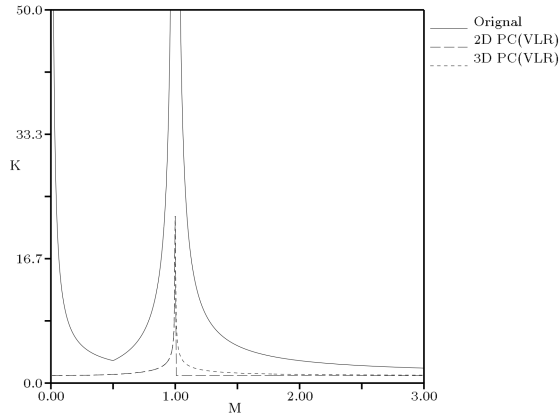


Figure 3.5: Characteristic condition number versus Mach number [262]. 2D PC: characteristic condition number after optimal 2D preconditioning. 3D PC: characteristic condition number after optimal 3D preconditioning

As a result, the convergence to a steady-state solution for low-speed flows with a density-based solver is low. In order to alleviate this problem, low speed preconditioning of the time evolution of the governing equations can be employed. Preconditioning methods basically change the eigenvalues of the system of compressible flow equations in order to minimize the large disparity between the acoustic wave speed $u + a$ and waves convected at fluid speed u . This is executed by performing a wave propagation analysis on the simplified quasi-linearized **RANS** equation with the yet unknown inverse preconditioner matrix \underline{P}^{-1} :

$$\underline{P}^{-1} \frac{\partial \mathbf{W}}{\partial t} + \underline{A} \frac{\partial \mathbf{W}}{\partial \mathbf{x}} + \underline{B} \frac{\partial \mathbf{W}}{\partial \mathbf{y}} + \underline{C} \frac{\partial \mathbf{W}}{\partial \mathbf{z}} = \mathbf{0}, \quad (3.24)$$

where $\mathbf{W} = [\rho, \rho \mathbf{u}, \rho E]^T$ is the state variable vector, $\underline{A}, \underline{B}, \underline{C}$ flux Jacobian matrices of the system. Once the analysis is performed, the preconditioner matrix is obtained. Notice that preconditioning the system results in very bad time accuracy. However, since steady-solutions are only of interest, this drawback is not relevant for this problem.

In **SUMad**, a general form of the preconditioner matrix is employed where two types of preconditioning methods can be obtained depending on two parameters. When considering $\alpha = 0$ and $\delta = 1$, the generalized form of the preconditioned matrix changes to the Choi-Merkel preconditioning method [145]. When changing δ to zero, the generalized preconditioner matrix becomes Turkel's preconditioner matrix [263]. The generalized preconditioner matrix is described by the following [264]:

$$\underline{P}_0 = \begin{bmatrix} \frac{\beta M_T^2}{a^2} & 0 & 0 & 0 & 0 & -\frac{\beta M_T^2 \delta}{c^2} \\ -\frac{\alpha u}{\rho a^2} & 1 & 0 & 0 & 0 & \frac{\alpha u \delta}{\rho c^2} \\ -\frac{\alpha v}{\rho a^2} & 0 & 1 & 0 & 0 & \frac{\alpha v \delta}{\rho c^2} \\ -\frac{\alpha w}{\rho a^2} & 0 & 0 & 1 & 0 & \frac{\alpha w \delta}{\rho c^2} \\ 0 & 0 & 0 & 0 & 1 & 0 \\ 0 & 0 & 0 & 0 & 0 & 1 \end{bmatrix}, \quad (3.25)$$

where a is the speed of sound, ρ the density of the fluid, $\{u, v, w\}$ the velocity vectors along the Eulerian reference frame, and βM_T^2 can be formulated as:

$$\beta M_T^2 = \min \{ \max \{ K_1 (u^2 + v^2 + w^2), K_2 (u_\infty^2 + v_\infty^2 + w_\infty^2) \}, a^2 \} \quad (3.26)$$

with

$$K_1 = K_3 \left(1 + \frac{1 - K_3 M_0^2}{K_3 M_0^4} M^2 \right),$$

where $\{u_\infty, v_\infty, w_\infty\}$ are free-stream velocity vectors along the Eulerian reference frame, M the free-stream Mach number, and M_0 the specific Mach number to activate the low-speed preconditioning method. The specific Mach number is set to 0.2, because it is expected that no convergence problems would occur for higher values than 0.2. In case that $M > M_0$, βM_T^2 becomes a^2 . As a consequence, the preconditioner matrix becomes an identity matrix resulting in no preconditioning of the system of equations. It is suggested by Turkel [264] that K_3 should range between 1 and 1.10. K_2 is set to be 0.6. When the Mach number turns to be zero for certain control volumes, the preconditioning becomes singular.

Given that the generalized preconditioner matrix is defined for pressure-based solvers, the pre-

conditioner matrix should be transformed as such it can be used for the state variables set by [SUMad](#). This is achieved by using transformation matrices:

$$\underline{P} = \frac{\partial \mathbf{W}_c}{\partial \mathbf{W}_0} P_0 \frac{\partial \mathbf{W}_0}{\partial \mathbf{W}_c}, \quad (3.27)$$

where $\mathbf{W}_c = [\rho, \rho \mathbf{u}, \rho E]^T$ and $\mathbf{W}_0 = [p, \mathbf{u}, S]^T$. In order to capture the acoustic and convective wave speed, the local time step in the Runge-Kutta method needs to be recomputed by employing the spectral radius method on the Jacobian matrices of the system for finding maximum absolute eigenvalues.

$$\Delta t_j = \frac{\text{CFL}}{r(\underline{A}) + r(\underline{B}) + r(\underline{C})} \Omega_j \quad (3.28)$$

where $r(\cdot)$ represents the maximum absolute eigenvalue of the Jacobian matrix obtained by the spectral radius method.

3.3.5 Boundary conditions

For solving partial differential equations, boundary conditions are required to bound the flow solution. Some of these boundary conditions have a physical nature (wall boundary conditions), but others (periodic and far field boundary conditions) are artificial. All boundary conditions are imposed by halo/ghost cells. The number of halo cells depends on the stencil used: For second-order spatial accurate discretization, two halo cells are required. The flow conditions of the halo cells are dependent on the type of boundary conditions.

The Euler wall boundary condition enforces a slip condition at a solid wall by imposing an opposite velocity component perpendicular at the wall of the first control volume in the halo cell. The density of the halo cell is considered to be the same as the density of the first control volume. The pressure of the halo cell is obtained by linear interpolation of the first two control volumes at the wall. When considering viscosity effects, the wall boundary condition imposes a no-slip condition that uses wall functions for high Reynolds numbers [265].

Far field boundary conditions are necessary for imposing external flow conditions on the computational domain. In reality, the flow domain is too large for incorporating the domain in a computational domain. Therefore, far field boundary conditions can be used for reducing mesh size while keeping the same flow conditions. Note that far field boundary conditions can induce artificial effects when the far field boundary is too close with the object. Some of these artificial effects are reflection of pressure waves at the far field boundary. In order to impose external flow conditions in the computational domain, the flow conditions of the halo cells are simply specified by the user.

Periodic boundary conditions can be used when the flow exhibits spatial periodicity. In case of steady-state flow solutions for wind turbines, periodic boundary conditions are certainly advantageous, because it reduces the computational domain considerably. Thanks to the reduction of mesh size, a higher mesh resolution on the remaining part of the computational domain can be obtained. In order to develop periodic boundary conditions, it is necessary to have two identical mirrored flat faces for assuring correct transformation of state variables of two control volumes on top of each other the donor face to two halo cells at the recipient face. The transformation of the conserved variables to the halo cells is performed by a transformation matrix that is dependent on the rotation

at which the periodicity starts again. In case of the NREL VI blade, the rotation angle would be 180 degrees. In most cases, a gap between the two periodic faces are made for making mesh generation easier.

3.4 Shape parametrization

The FFD volume approach parametrizes the blade geometry by embedding the design inside a parallelepiped. This approach is known for having an efficient and compact set of geometry design variables, which makes it easier to manipulate complex geometries. Once the local coordinates of the vertices of the geometry are expressed on the FFD volume by performing a Newton search, the FFD control points can be deformed as such it transmits the deformation to the initial design. Basically, if the lattice structure deforms, the embedded object will deform as well. This FFD volume is a composite of B-spline tensor patches in three dimensions called a trivariate B-spline volume. In the B-spline volume, various control points are specified that will serve for the deformation of the embedded design. The reason for choosing B-spline volumes is that derivatives of any point inside the volume can be easily computed.

Two FFD volumes are designed for the two-bladed rotor, where each FFD box incorporates one NREL VI blade. Given the symmetry of the two-bladed rotor, it is decided to link the control points of one FFD volume to the other control points of the other FFD volume. This will assure that the perturbations of one blade will be symmetric with the other blade, i.e. for every perturbation two identical blades will be produced. Another advantage is that the amount of design variables for optimization are reduced by half which improves the computational efficiency considerably. In Fig. 3.6, the FFD volumes are shown with the original NREL VI rotor. Note that the cylindrical part has fixed control points, since the part does not contribute to the aerodynamic performance of the rotor. The two FFD volumes can also be used for the modified NREL VI rotor.

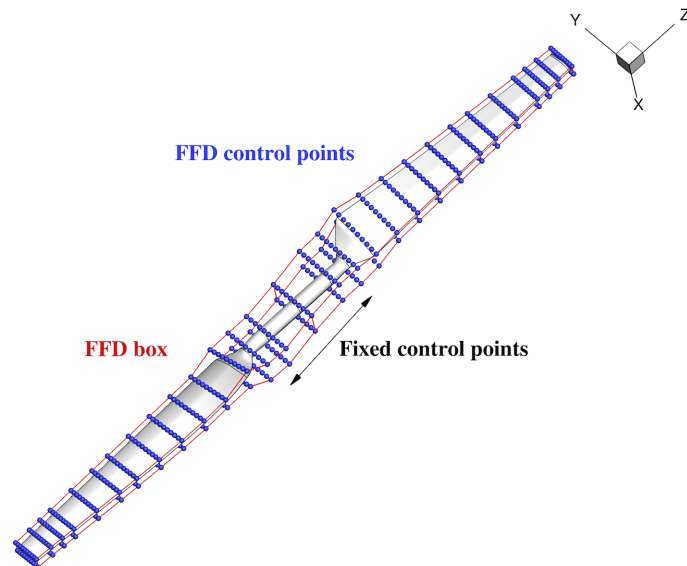


Figure 3.6: FFD volume approach on the NREL VI rotor

Different types of perturbations on the **FFD** volume can be employed. Shape deformations are actual changes in the x -direction on the surface of the blade and are frequently used for subtle improvements in the performance. Geometrical perturbations, on the other hand, can lead to severe improvements in aerodynamic performance. Some of these geometrical perturbations used in this research are pitch and twist. Both of these perturbations are rotating the blade or sections of the blade around an axis located at 25% of the chord of the blade. Other geometrical perturbations, such as chord and span deformations, are not used in this research, since it is expected that it would require a very robust mesh.

3.5 Mesh deformation

Once the **FFD** volumes can properly perturb the geometry of the **NREL VI** blade, the surface deformations need to be projected on the mesh for the **CFD** simulation tool to solve the modified computational domain. Unless the surface perturbation is smaller than the off-wall spacing, the mesh is perturbed by use of a hybridization form of algebraic and linear elasticity methods, developed by Kenway et al. [219]. Linear elasticity methods are known for producing high-quality perturbed (un)structured meshes. The linear spring analogy method represents mesh edges with fictitious springs with a spring constant inversely proportional to its length. This analogy method is computational expensive, because it needs to solve a system of equations as large as the number of internal grid points. Also, this technique can still produce tangled meshes. The torsional spring analogy method expands the linear spring analogy method with torsional springs at mesh vertices to prevent interpenetration of volume cells. This technique improves the robustness of the mesh deformation significantly, but it is very computational expensive. More recent three-dimensional applications have shown good performance [217].

The linear elasticity method, used in the hybrid scheme, considers the mesh as an elastic solid using the equations of linear elasticity. These equations are discretized using a finite-element method with linear shape functions on each finite element with its Young's modulus inversely proportional to its volume. For solving the equations of linear elasticity, Dirichlet boundary conditions are considered. This approach is convenient, since certain specifications on perturbing boundaries of the mesh can be set, e.g., no boundary perturbations can be applied for satisfying symmetric boundary conditions. This linear elasticity method has proven to be robust and it can obtain high quality meshes with large deformations [266]. As a drawback, the method is computational expensive.

The algebraic technique is developed by Reuther et al. [267], which resembles the transfinite interpolation method [268]. The main difference between these techniques is that the algebraic technique developed by Reuther et al. makes use of the relative interior point distribution in the initial mesh. The advantage of using this algebraic method is its efficiency. However, problems arise when the grid receives rotating perturbations resulting in low grid orthogonality. Also, when using a small block near the surface can result in tangled volume cells. The problem can be alleviated when allowing the blocks to the far field boundary. Since the mesh deformation method needs to be used for optimization purposes, the algebraic technique has been extensively modified for obtaining a better robustness. One of the modifications is the possibility of using multiple blocks near the surface without detrimental effects on the mesh quality.

The main idea of the hybrid method is to apply a linear elasticity method on a coarser approx-

imation of the mesh for large, low-frequency perturbations, while using an algebraic approach to attenuate small, high frequency perturbations. A brief overview on how the hybrid method works is given by the following:

1. Select a certain number of nodes per edge of the mesh. These number of nodes will form a coarser approximation of the initial mesh.
2. The coarser approximation of the initial mesh will be perturbed using the linear elasticity method.
3. Regenerating each block with linear or cubic-Hermite spine interpolation for obtaining a full mesh approximation
4. The algebraic technique resolves the remainder of the surface perturbations on the full mesh approximation

This hybrid scheme is written in Python, called ‘pyWarp’, and it has various types of options. One of these options is the possibility of choosing only the linear elasticity method or the algebraic technique. In Fig. 3.7, a comparison between the original and perturbed mesh of the NREL VI blade is shown.

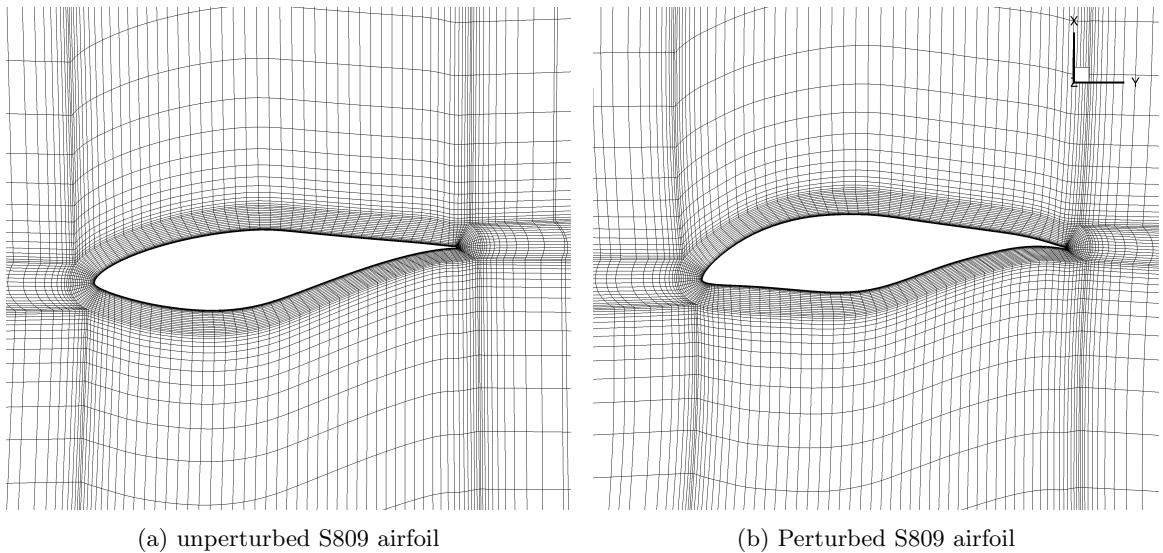


Figure 3.7: Mesh perturbation of the NREL VI blade at $z = 3.3$ m

3.6 Discrete adjoint method

High-fidelity aerodynamic shape optimization with large number of design variables requires an efficient gradient method for keeping the computational time down. Despite its easy implementation, the finite difference method is inefficient for a large set of design variables and has subtractive cancellation errors. The complex step method, on the other hand, alleviates the subtractive cancellation error and can result in machine accuracy. However, similar to finite difference, the complex step method is inefficient for large number of design variables. Since a single or multiple function

evaluation(s) are required for obtaining a gradient of one design variable when using finite difference or complex step, performing high-fidelity optimization with large number of design variables would not be possible. Therefore, the adjoint method is employed, which only needs one function evaluation disregarding the amount of design variables. Note that the computational cost does increase when the number of functions of interest increases.

The objective function I for an aerodynamic shape optimization is dependent on a variety of parameters. These parameters include the design of the wind turbine blade x , the flow solution represented by the state variables \mathbf{W} computed by SUMad, and the computational grid $\boldsymbol{\eta}$. The latter will be neglected in this discussion. In order to account all the indirect dependencies of the objective function with respect to a design variable, the total derivative of the objective function can be written as:

$$\frac{dI}{dx} = \frac{\partial I}{\partial x} + \frac{\partial I}{\partial \mathbf{W}} \frac{d\mathbf{W}}{dx} + \underbrace{\frac{\partial I}{\partial \boldsymbol{\eta}} \frac{d\boldsymbol{\eta}}{dx}}_{=0}. \quad (3.29)$$

The total derivative of the flow solution with respect to the design variable can be expressed differently by stating that the change in residual \mathbf{R} of the CFD solver is independent of the change in magnitude of the design variable x :

$$\frac{d\mathbf{R}}{dx} = \frac{\partial \mathbf{R}}{\partial x} + \frac{\partial \mathbf{R}}{\partial \mathbf{W}} \frac{d\mathbf{W}}{dx} = \mathbf{0}. \quad (3.30)$$

The above equation can be rewritten in function of $\frac{d\mathbf{W}}{dx}$:

$$\frac{d\mathbf{W}}{dx} = - \left[\frac{\partial \mathbf{R}}{\partial \mathbf{W}} \right]^{-1} \frac{\partial \mathbf{R}}{\partial x}. \quad (3.31)$$

When substituting the above equation with Eq. (3.29), the following equation is given as:

$$\frac{dI}{dx} = \frac{\partial I}{\partial x} - \frac{\partial I}{\partial \mathbf{W}} \left[\frac{\partial \mathbf{R}}{\partial \mathbf{W}} \right]^{-1} \frac{\partial \mathbf{R}}{\partial x}. \quad (3.32)$$

The adjoint vector $\boldsymbol{\psi}$ is defined as:

$$\boldsymbol{\psi} = - \left[\frac{\partial I}{\partial \mathbf{W}} \left[\frac{\partial \mathbf{R}}{\partial \mathbf{W}} \right]^{-1} \right]^T. \quad (3.33)$$

When employing the adjoint vector to Eq. (3.32), the following expression of the total derivative of the objective function can be used for computations:

$$\frac{dI}{dx} = \frac{\partial I}{\partial x} + \boldsymbol{\psi}^T \frac{\partial \mathbf{R}}{\partial x}. \quad (3.34)$$

The adjoint vector can be computed by solving the system of linear equations:

$$\left[\frac{\partial \mathbf{R}}{\partial \mathbf{W}} \right]^T \boldsymbol{\psi} = - \left[\frac{\partial I}{\partial \mathbf{W}} \right]^T. \quad (3.35)$$

From the adjoint formulation, there are still partial differential expressions that are required to be solved. When simply using finite difference or complex step, the purpose of using the adjoint method

is defeated. Obtaining an analytical solution for the adjoint method is possible for specific cases. However, given the general purpose of performing high-fidelity aerodynamic shape optimization, this is not an option and thus the adjoint method is required to be discretized. One method to discretize the adjoint equations is by linearizing the Navier-Stokes equations and subsequently derive an adjoint formulation based on the linearized equations. The adjoint formulation can then be discretized and solved. This continuous adjoint method is non-trivial for implementation in complex CFD solvers and it requires a lengthy development time. Another drawback is that the computed sensitivity is sometimes inconsistent with discretized governing equations.

In order to circumvent the disadvantages of the continuous adjoint method, the discrete adjoint method employs automatic differentiation on the discretized flow equations provided by SUMad. The automatic differentiation relies on a programming tool that transforms the source code for computing derivatives. These tools are relying on a systematic application of the chain rule to each line of the source code. Automatic differentiation or algorithmic differentiation provides two modes: forward and reverse mode. The forward mode uses the inputs and applies the chain rule along the source code execution path for obtaining derivatives, while reverse mode traverses the chain rule from outside to inside. As an example for forward automatic differentiation, consider the function $f(x, y) = xy + \sin(x)$, that can be systematically decomposed in a sequence of code statements x_1, \dots, x_n . When solving the partial differential equation $\partial f(x, y)/\partial x$, the seeding values of the variables are considered to be: $x'_1 = 1$ and $x'_2 = 0$. Shown in Table 3.3, the previous mentioned partial derivative is obtained by applying the chain rule. Note that the variables are considered to

Table 3.3: Forward automatic differentiation of $f(x, y) = xy + \sin(x)$

Sequential code statements	Chain rule
$x_1 = x$	$x'_1 = 1$
$x_2 = y$	$x'_2 = 0$
$x_3 = x_1 x_2$	$x'_3 = x'_1 x_2 + x_1 x'_2 = x_2$
$x_4 = \sin(x_1)$	$x'_4 = x'_1 \cos(x_1) = \cos(x_1)$
$x_5 = x_3 + x_4$	$x'_5 = x'_3 + x'_4 = x_2 + \cos(x_1)$

be independent. When the partial derivative with respect to y is from interest, the seeding value will change to $x'_1 = 0$ and $x'_2 = 1$.

The disadvantage of using reverse mode is its difficult implementation, but it requires less memory storage than the forward mode that stores every intermediate variable. In order to reduce the high computational cost of the forward mode, Lyu et al. [233] implemented a coloring method. For this research, the partial derivatives $\partial \mathbf{R}/\partial \mathbf{W}$, $\partial I/\partial x$, $\partial I/\partial \mathbf{W}$, and $\partial \mathbf{R}/\partial x$ are computed using the forward mode. In this work, the automatic differentiation tool ‘TAPENADE’ is employed [269]. For further information on adjoint methods for aerodynamic shape optimization, see the following references [233, 270].

3.7 Optimization procedure of the NREL VI blade

Defining the optimization problem is one of the most important aspects for performing optimization. The objective and constraint function(s) define the design space in which the optimum

should be found. In fact, the objective function will mainly dictate the final design of the wind turbine. Optimizing a wind turbine is a multidisciplinary process that can involve multiple objective functions, such as maximizing power extraction and minimizing blade mass. Currently, most wind turbine optimization procedures have a system engineering approach in which cost of energy is a key factor for optimization. However, given the large number of disciplines[†] involved in determining the cost of energy, it is not easy to formulate an objective that is suited for gradient-based optimization. Therefore, it is decided to mainly focus on the power extraction of wind turbines with simultaneously taking some aspects from other disciplines into account.

3.7.1 Problem statement

Since the NREL VI wind turbine blade rotates at a constant angular velocity for every free-stream velocity, power generation is considered to be only dependent on torque. From this observation, maximizing torque will directly maximize power generation of the wind turbine blade. From this point of view, the objective function of the optimization will be maximizing torque coefficient C_q , which is provided by SUMad. Most modern wind turbines are changing its angular velocity as well. However, given the complexity of performing optimizations with multiple Pareto fronts, it is decided to concentrate on one objective function.

A variety of design variables can be imposed on the rotor design. Given the time constraint of this research, it is decided to use only three types of design variables: shape variables, pitch variables, and twist variables. Shape variables \mathbf{s} impose perturbations on the surface of the blade in the x -direction (see Section 3.4), which consequently results in indirect influence of the pitch and twist angle of the blade. Twist variables $\boldsymbol{\xi}$ are perturbations around the axis located at 25% of the chord of the NREL VI blade. These perturbations will rotate a particular section of the blade. The pitch variable θ , at the other hand, rotates the full blade at the same axis of the twist variables. It is noted that a combination of these design variables can be redundant, because some of the design variables can take over the purpose of the other design variable, e.g., twist variables will take the pitch angle into account. On the other hand, it is possible that the combination of design variables can lead to a smoother and better result, e.g., shape variables can smooth the new twist distribution.

Given that aerodynamic shape optimization does not take the internal structure of the NREL VI into account, it is expected that the optimization will obtain designs that are not ideal from the structural point of view. Therefore, thickness constraints on the blade are imposed for incorporating an imaginary wing/torque box. The location of the wing box is between 15% and 50% of the chord of the blade x/c . In this region, the thickness of the blade t/c can only increase up to 300% of the original thickness $(t/c)_0$. The reason for not reducing the thickness at the location of the wing box is that the original wing box would still be able to fit in the optimized blade. These thickness constraints are called 100% thickness constraints. For research purposes, the thickness constraint of the blade will also be reduced to 75%. This is merely for comparison with respect to the 100% thickness constraint in order to gain some insight of the behavior of the optimization. Another reason for using thickness constraints is to prevent mesh failure when too large deformations are acting on the computational domain. If there is research time left, equality constraints on bending moments $C_{my,mz}$ and thrust C_t are added. These equality constraints are set to be equal to the

[†]Not only technical disciplines are from importance. Finance and politics are as important for developing a wind turbine.

values of the original [NREL VI](#) blade in order to obtain the same load conditions as the baseline design (except for torque). Another reason for constraining rotor thrust is that it has a significant financial cost on the total cost of the wind turbine due to its effect on the tower design.

As a verification method, the first optimization will only consist of one pitch angle with low mesh resolution for reducing computational cost. When the optimization procedure runs smoothly and correctly, twelve twist variables for each blade are tested. Once the optimization with twist variables is successful, 296 shape variables are tested with the coarse mesh. As last, the combination of twist and shape variables are employed for optimization. Notice that no other geometrical variables, such as span or chord, are used since it is expected that the mesh will fail quickly.

The single point optimization will involve maximizing torque coefficient C_q at one free-stream velocity: 7 m/s. The optimization problem is stated as follows:

$$\begin{aligned} \max_{\mathbf{s}, \phi, \theta} \quad & C_q(\mathbf{s}, \boldsymbol{\xi}, \theta) \\ \text{subject to} \quad & 1 \leq \frac{t/c}{(t/c)_0} \leq 3 \quad \text{at} \quad 0.15 \leq x/c \leq 0.5 \\ & C_{my,mz} = (C_{my,mz})_0 \\ & C_t = (C_t)_0 \end{aligned}$$

Since wind turbines must perform well for a range of wind speeds, a multipoint optimization would fit the purpose to maximize the power generation for a range of wind speeds. The multipoint optimization considers an objective function with an equal weighted average of torque coefficients from cut-in to rated wind speed. In this case, the cut-in wind speed is 5 m/s and the rated wind speed is 9 m/s. The weights of the average w_i can be changed according to the frequency distribution of wind speeds at a certain location. The multipoint optimization for various wind speeds $U_i = [5, 6, 7, 8, 9]$ is given by:

$$\begin{aligned} \max_{\mathbf{s}, \phi, \theta} \quad & \sum_{i=1}^5 w_i C_q(\mathbf{s}, \boldsymbol{\xi}, \theta, U_i) \\ \text{subject to} \quad & 1 \leq \frac{t/c}{(t/c)_0} \leq 3 \quad \text{at} \quad 0.15 \leq x/c \leq 0.5 \\ & C_{my,mz} = (C_{my,mz})_0 \\ & C_t = (C_t)_0 \end{aligned}$$

The multipoint optimization will result in one final design for the cut-in to rated wind speed. Note that both optimization problems are generalized for every design variable. For this work, only one or two types of design variables will be used for optimization. Also the thrust and bending moment constraints are optional.

3.7.2 Optimization algorithm

Due to the high computational cost of [RANS](#)-based [CFD](#) simulations, choosing an efficient optimization algorithm with reasonably low number of function evaluations is vital to keep the total computational cost relatively low. Gradient-free optimization methods might handle multimodal functions in a more robust way, but they require a large number of functions evaluations. These methods make high-fidelity aerodynamic shape optimization infeasible with the current computa-

tional resources for hundreds of design variables. Using adjoint gradient evaluations with gradient-based optimization alleviates these issues.

For this research, Sparse Nonlinear OPTimizer (**SNOPT**) will be employed for all the results [271]. **SNOPT** is a sequential quadratic programming method that is capable of solving large-scale non-linear optimization problems with thousands of constraints and design variables. It uses a smooth augmented Lagrangian merit function and the Hessian of the Lagrangian is approximated using a limited-memory quasi-Newton method (Broyden-Fletcher-Goldfarb-Shanno (**BFGS**) algorithm)[272]. The convergence criterion of **SNOPT** is the ratio between the largest component of the gradient of the Lagrangian merit function and the L2-norm of the vector of the Lagrange multipliers. This convergence criterion is called the optimality condition. The feasibility condition of **SNOPT** is the ratio of the largest violation of a constraint function with respect to the L2-norm of the vector of design variables.

3.7.3 Optimization approach

In order to interact with all the modules for performing optimization, a common programming language for all components of the optimization framework is required. Therefore, the Python language is employed for wrapping every component, e.g. the Fortran written **SUMad** is wrapped with Python. Once all components are correctly wrapped with Python, the modules can communicate by sending inputs and outputs to each other through one python script. Note that all modules are parallelized using the software library Message Passing Interface (**MPI**). Depending on the size of the computational domain, a cluster of 16 to 256 processors are used for optimization. In Fig. 3.8, the optimization procedure is shown.

The optimization procedure starts with defining a proper optimization problem, in which the objective and constraints function(s) are properly specified according to the needs of the stakeholder(s). The baseline design should be defined closely to the expected optimum of the objective function for reducing the number of function evaluations. For this case, it is expected that the **NREL VI** is far of the optimal condition since the thrust value is rather small for the given flow conditions, implying that a significant amount of torque can be added. Once the **CAD** and the computational domain of the **NREL VI** blade are developed, **SUMad** computes a steady-state flow solution. This solution includes the relevant variables for the objective and constraint function(s) and the residuals of the state variables. In order to obtain the total derivative of the objective function with respect to the design variables (Eq. (3.34)), the partial derivatives $\partial I/\partial x$, $\partial I/\partial \mathbf{W}$, and $\partial \mathbf{R}/\partial x$ are computed by using the forward automatic differentiation tool ‘TAPENADE’. The adjoint vector is obtained by solving the linear system of equations described in Eq. (3.35). This procedure also holds for additional total derivatives of constraint functions. When providing the total derivatives of the objective and constraint function(s) with the objective and constraint function values, **SNOPT** computes a better design. If the optimality condition is not satisfied, the new design variables are parametrized on the **FFD** volume and the corresponding perturbations are made on the blade. Subsequently, the computational domain is deformed according to the hybrid scheme discussed in Section 3.5. After the mesh deformation, **SUMad** recomputes the flow solution and the whole procedure starts over again until the optimization condition is satisfied. If the feasibility condition is not satisfied, the optimization procedure will automatically stop with mentioning the violated constraint function(s).

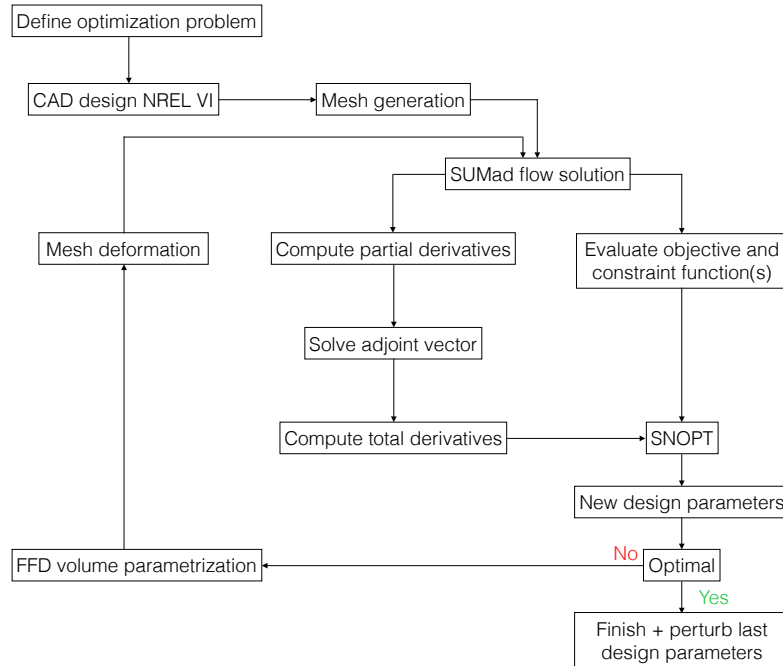


Figure 3.8: Flow chart of the aerodynamic shape optimization of the [NREL VI](#) rotor

3.8 Limitations and assumptions

As for every method, there are some limitations and assumptions. Given the complexity of the optimization procedure, it is decided to list the limitations and assumption per associated module:

1. [CAD](#) and computational domain of [NREL VI](#) blade:

- When control volumes have straight faces, the mesh will have conformity issues with respect to the [CAD](#) of the [NREL VI](#) blade. This will cause flow misalignment near the surface of the blade.
- The geometry of the transition and tip region are approximated, because correct measurements are unknown.
- In order to make meshing easier, two [NREL VI](#) blades are connected with a cylinder instead of using the complex hub design.

2. [SUMad](#):

- The inflow conditions are uniform, while in reality the [ABL](#) causes different inflow conditions at the rotor. Turbulence inflow should be taken into account as well.
- Given the averaged character in time and space of the [RANS](#) equations, the resolution of detailed turbulent fluctuations is low. As a consequence, flow separation and small scale interactions are difficult to predict accurately.

- Given the scalar dissipation of the [RANS](#) equations, wake resolutions are poor. In order to circumvent this problem, [DES](#) or [LES](#) should be used for wake analysis. This is one of the reasons why [RANS](#)-based [CFD](#) will not be used for wake analysis of wind turbine farms.

3. Shape parametrization and mesh deformation

- Even though the mesh deformation scheme is robust, very large deformations still lead to mesh failures. These very large deformations can happen when geometric design variables, such as span and chord, are employed for optimization.
- When periodic boundary conditions are used, optimization cannot be performed since the hybrid mesh deformation scheme will deform non-identically the periodic faces resulting in major numerical errors.

4. Discrete adjoint method

- Currently, only steady-state solutions can be used for adjoint computations. It would be more advantageous to extend the adjoint method in the time-domain. This could for instance resolve the problem with stagnating residuals, but also time-dependent optimizations can be performed.
- Even though the computational domain has an effect on the aerodynamic objective function, no partial derivative is included in the discrete adjoint method. This will certainly have a small effect on the accuracy of total derivatives obtained by the adjoint method.
- At the moment, the discrete adjoint method can only be used with the one-equation [SA](#) turbulence model, which is known for its bad performance in predicting flow separation.

CHAPTER IV

Verification and validation of optimization method

Optimization is not a plug and play tool: it requires a thorough knowledge of each optimization component to achieve sensible results. Verification will identify the capabilities and bottlenecks of the analysis method, while validation will quantify the accuracy of the method. Once verification and validation are performed, conclusions can be drawn on how optimization should be performed.

In this chapter, verification is performed on the compressible solver **SUMad** and the associated adjoint solver. Since **CFD** simulations are mainly dependent on the quality of the computational domain, mesh generation and mesh perturbation are thoroughly inspected for any elements that can deteriorate the quality. Once the mesh is approved, the numerical procedures of **SUMad** are tested for obtaining correct rotating flow fields. Subsequently, residual and grid convergence analysis show the capabilities and accuracy of **SUMad**. Since the ultimate goal of the dissertation is performing gradient-based optimization, the gradients computed by the adjoint method need to be verified. After verification, validation of **SUMad** on the **NREL** VI blade is executed. All forces and moments acting on the blade are related to pressure distributions along the blade. Therefore, it is decided to validate the pressure distributions with respect to measurements provided by the **NREL**. Once pressure distributions are validated, torque and thrust are validated. Since the **NREL** VI blade is stall-regulated, flow separation will be analyzed by visual inspection and by comparison between **SA** and Menter's **SST** turbulence model. Wake analysis will show that compressible solvers dissipate wake structures very quickly. Turkel's low speed preconditioner and periodic boundary conditions are validated as well.

4.1 Verification of optimization procedures

Before simulations can be validated, difficulties and errors in simulations should be identified and possibly solved. Due to the magnitude of the optimization problem, the verification is segmented in different components. First, the quality of meshes and perturbation of meshes are judged based on different metrics. Subsequently, **SUMad** is checked whether it is capable of correctly representing rotating flow problems. Once the mesh and the **CFD** solver are verified, residual and grid convergence analysis are executed for obtaining accurate results. Concerning optimization, the adjoint method is verified by comparing the gradients with other approximation methods, such as finite difference and complex step.

4.1.1 Mesh generation and perturbation

Without the capability of producing high quality meshes, CFD simulation results flow solutions with with poor accuracy. Therefore, it is essential to verify mesh quality before performing CFD simulations. Besides generating high-quality meshes, perturbed meshes during optimization should retain their quality for obtaining sensible optimization results. As a first verification, the CAD geometry of the NREL VI blade should be identical to the geometry prescribed by the following reference [147]. Since the surface of the geometry is extrapolated from two-dimensional sections, it is very likely that there will be small discrepancies between surfaces of the exact and approximate geometry. Also, the transition part and tip geometry will be estimated, because no thorough description of these regions are provided. Besides CAD geometry approximation errors, voids between off-wall cells and the geometry surface are inevitable resulting in flow misalignment near the exact boundary of the surface. In order to alleviate this problem, more nodes should be placed at curved surfaces, such as leading edge and tip regions. Also, corners and edges have to be taken into account. The amount of nodes is decided upon a grid convergence analysis described in Section 4.1.4.

Once the CAD geometry of the NREL VI blade is verified, the quality of the surface mesh is inspected by checking the smooth transition of surface cells. Shown in Fig. 4.1, the smoothness is mostly affected at corners and edges. Therefore, it is decided that a maximum growth rate of 1.2 between cell edges should apply. If this requirement is not met, more surface cells are added. Due to conforming issues, a large number of surface cells are required at curved surfaces, edges and corners. Furthermore, verification is performed on the final surface mesh to verify if it conforms the CAD geometry appropriately.

If the surface mesh is approved according to the above procedure, the structured volume mesh is generated. Three possible far field domains are created: cylinder, half cylinder, and sphere. The spherical far field domain is created by an in-house code PyHyp from which the volume mesh is hyperbolically marched out from the surface mesh using an O-grid topology to a spherical far field with a radius of 10 times the rotor diameter. The quality of the mesh is computed, using determinants of Jacobian matrices of cells, resulting in a minimum quality value of approximately 0.5. The cylinder and half cylinder are both made in ICEM CFD using an O-grid topology. The major difference between these two meshes for verification purposes is that periodic boundary conditions are applied on the straight surfaces of the half cylinder. These faces are required to be mirrored with respect to the x -axis and thus verification is needed to verify whether the surface cells of these faces are accurately mirrored. ICEM CFD has various verification tools for checking mesh quality. The first verification tool, that has been extensively used, is checking the variation in volume sizes of cells. When negative volumes appear, some of the cells cross the solid boundary or some settings of edges are incorrect. Also smooth transition, as in surface meshes, can be verified using verification tools of ICEM CFD. Another quality metric uses the determinant and metric tensors of the Jacobian matrix of cells, where size and skewness of cells are measured. After extensively modifying the volume and surface mesh, a minimum value of the quality metric of approximately 0.4 is obtained. Furthermore, a y^+ value of 1 is obtained and verified for all computational domains. The verification of the hybrid mesh generated by Pointwise for SU2 is discussed in Section A.

Besides verification of mesh generation, correct mesh perturbations are necessary for obtaining accurate optimization results. The direction in which the perturbation is moving is verified by visual inspection, e.g., a shift in twist angle should change the blade in the correct direction. Once all types

of perturbation are tested, the quality of the perturbed meshes for each optimization iteration are automatically verified according to the above explanation.

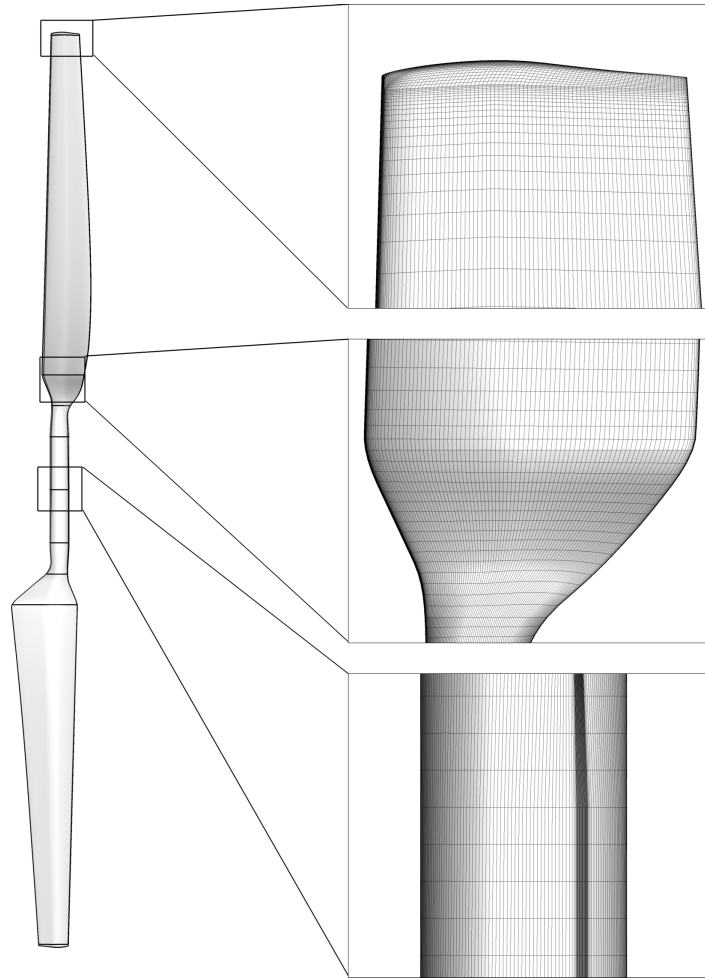


Figure 4.1: Verification of surface mesh. Note that the cylinder has a band of very small surface cells due to blunt trailing edge. This can be alleviated when using unstructured meshing.

4.1.2 Verification of **SUMad** simulations

SUMad has not been applied for a long time on rotating flow problems and various modifications have been added to the source code. Therefore, it is important to verify the rotating flow capabilities of **SUMad** again. Since the computational domains are verified in the above section, no problems should arise related to volume meshes. When applying the angular speed on the computational domain, **SUMad** did not pass on the value in the correct `.f90` pointer. After debugging, the first iterations were representing the rotational flow. However, after a few hundred iterations, the **CFD** simulation result showed accelerated flow downstream the blade, implying that there was still a programming error. Using different spatial schemes, such as **JST** or Roe, did not change this behavior.

As can be seen in Fig. 4.2, the **CFD** simulation result is correct when using the cylindrical mesh, while accelerated flow and even reversed flow is shown in the spherical mesh. From this figure, it can

be concluded that **SUMad** has a bug in which the rotational flux at the far field is not decomposed in proper directions with respect to the face of the cell. As a result, perturbations at the far field during optimization will induce numerical errors. Therefore, it is decided to use a mesh perturbation method that does not perturb the far field. The Roe scheme has shown better results than the **JST** scheme. In fact, the **JST** scheme diverges when the residual of density has reduced approximately four orders of magnitude. This unstable behavior is unfavorable for solving the adjoint method and thus it is decided to use the Roe scheme. A bug was found in **SUMad** in the periodic boundary conditions, in which it could not recognize the format of the file.

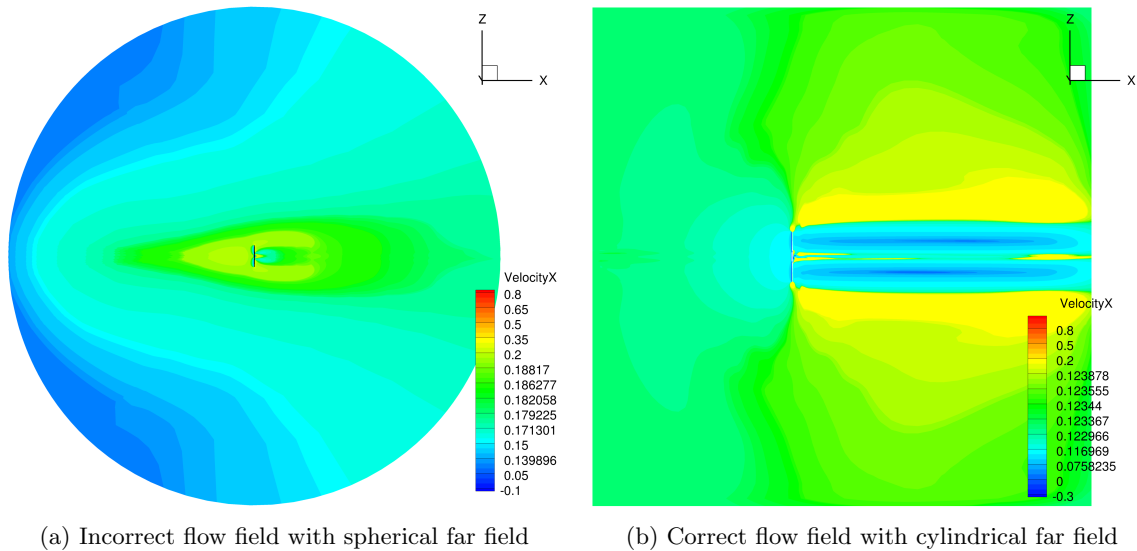


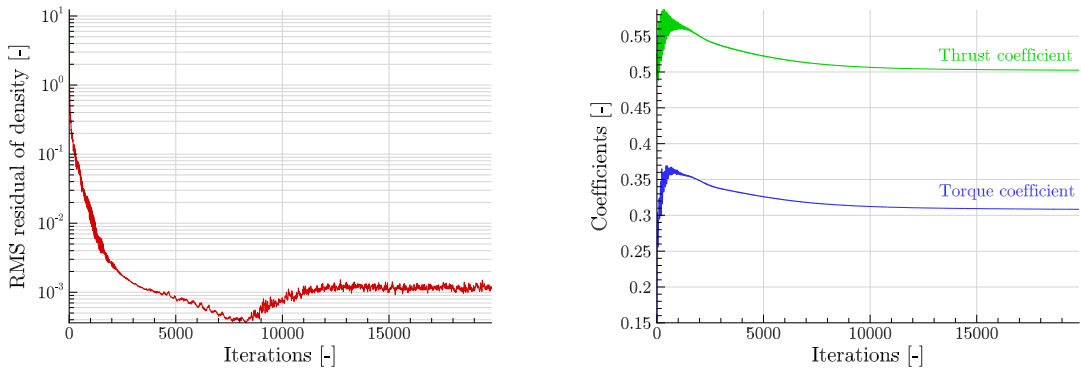
Figure 4.2: Verification of **SUMad** for rotational flow problems

Since optimization is executed in Python, the Fortran language of **SUMad** is required to be wrapped in Python. As a verification, the solution of **SUMad** directly ran by Fortran should be the same as the solution ran by Python. Some bugs were found in passing on parameters from Fortran to Python. The same verification procedure also holds for mesh perturbation methods.

4.1.3 Residual analysis

For steady-state compressible **CFD** solvers, the residual of density is a monitor variable that is required to meet a certain threshold in order to consider a flow solution to be converged. When applying **SUMad** on a high-quality structured mesh of the **NREL VI** sequence S blade, the Root Mean Square (**RMS**) residual of density does not converge towards a certain threshold. This could have issues with obtaining correct aerodynamic coefficients. However, it is shown in Fig. 4.3 that this is not the case. Therefore, instead of using **RMS** residual of density, a Cauchy convergence criteria can be used on force and moment coefficients, which set an amplitude value on a sequence of coefficients during the iteration procedure, i.e. when the sequence reaches the threshold amplitude, the simulation is considered to be converged.

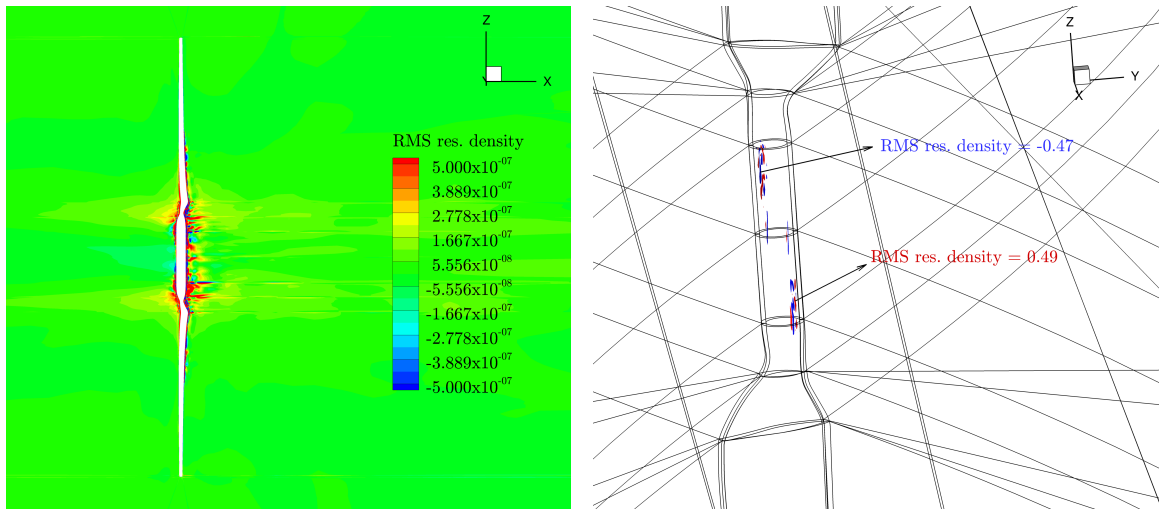
The reason for stagnating **RMS** residuals of density is that the flow is intrinsically unsteady at the cylinder of the **NREL VI** blade. Depicted in Fig. 4.4, the largest and smallest **RMS** residual of density are shown. Not surprisingly, the residuals are located at the cylinder. Also, the transition



(a) RMS residuals of density at 7 m/s behaving partially random due to unsteadiness in the flow (b) Thrust and torque coefficient at 7 m/s reaching an amplitude value of 10^{-6}

Figure 4.3: RMS residual of density with corresponding force and moment coefficients

part of the NREL VI blade has intrinsic unsteadiness that influences the nearby solution of the actual blade where the S809 airfoil is installed. In section 4.2.2, it will become clear that flow separation is causing these numerical difficulties. It can be concluded that modeling wind turbine blades with a steady-state solver will actually never converge to a steady-state solution due to intrinsic flow behaviors at cylinder and transition part. Therefore, CFD results in the coming sections are rather quasi-steady.



(a) RMS residual of density contours at 7 m/s (b) Maximum and minimum RMS residual of density

Figure 4.4: Stagnation of RMS residual of density due to flow separation at cylinder and transition part of the NREL VI blade

In Fig. 4.5, it is shown that the stagnation level of the RMS residual of density is increasing when free stream velocity increases. This is not a surprise, since more flow separation occurs at the blade as wind speed increases (see Section 4.2.2). Also, force and moment coefficients can not converge to a steady value due to flow separation resulting in unsteady loads. In order to damp out the oscillations in the force and moment coefficients, Roe scheme in combination with a limiter can

be used to smooth out large differences between gradients (see Section 4.2.3).

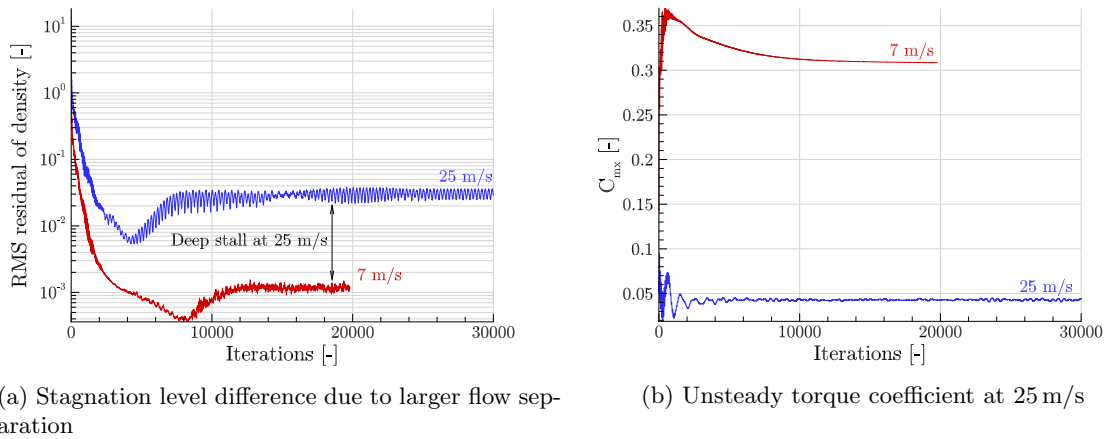


Figure 4.5: Residual behavior for different wind speeds

Concerning the feasibility of gradient-based optimization, stagnating **RMS** residuals of density will result in stagnation of the adjoint method. Consequently, no total derivatives can be computed for optimization. The first possible method of tackling this problem is deleting the cylinder and transition part of the **NREL VI** blade to avoid intrinsic unsteadiness. This will require additional validation in order to assure the same flow problem is solved as for the **NREL VI** blade flow problem, i.e. both rotors should have approximately the same force and moment coefficients. In Fig. 4.6, it is shown how the **RMS** residual of density of the modified **NREL VI** blade converges. As an addition to the low rate of convergence, Turkel’s low speed preconditioner method, described in Section 3.3.4 and validated in Section 4.2.6, can be used.

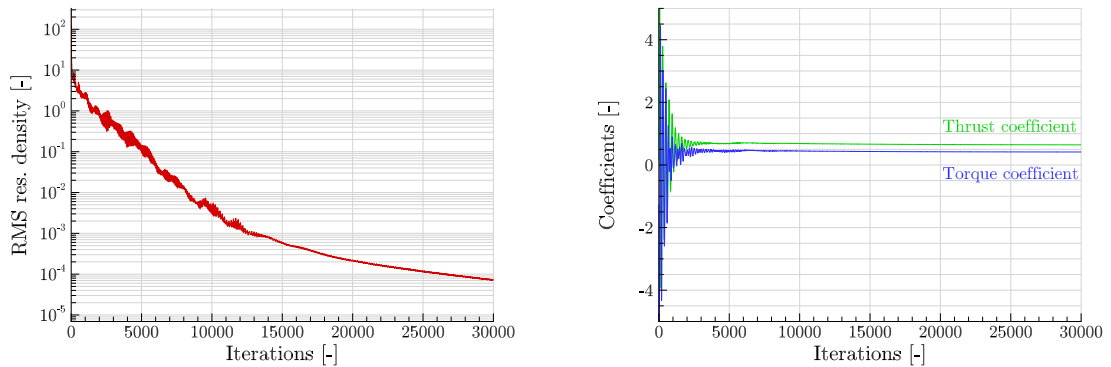


Figure 4.6: Residual and load coefficient behavior for modified **NREL VI** blade at 7 m/s

4.1.4 Grid convergence study

Grid convergence analysis is essential in every **CFD** simulation. It investigates the influence of mesh size on the accuracy of **CFD** simulation results. In this case, simulated torque values at 7 m/s with difference mesh sizes are compared with the experimental torque value. The particular wind

speed of 7 m/s will assure fully attached flow over the blade from which it is expected that CFD simulations would not have difficulties to accurately predict the performance of the NREL VI blade. In Fig. 4.7, grid convergence with respect to torque is shown.

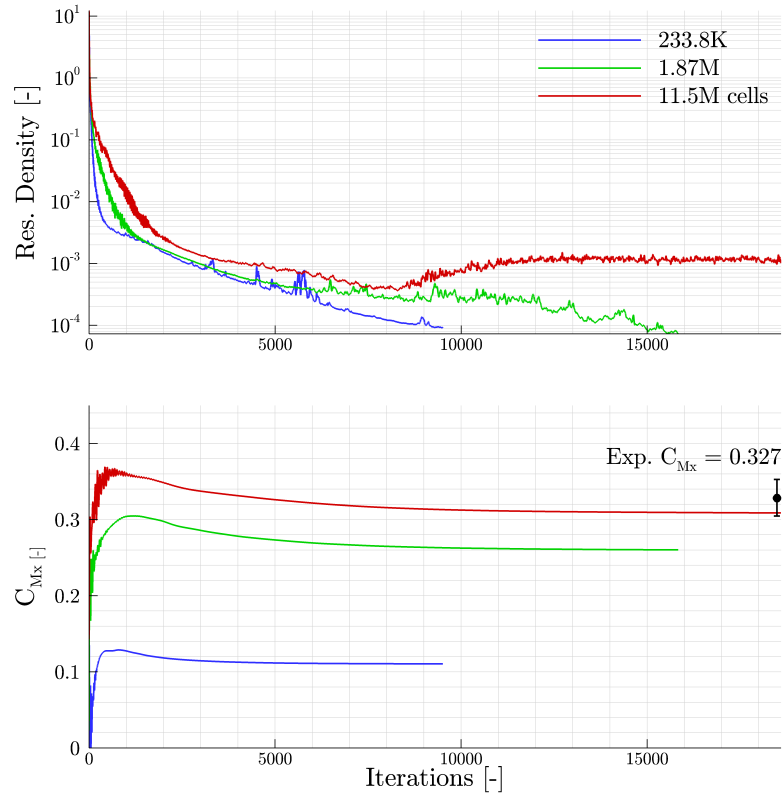


Figure 4.7: Grid convergence analysis of torque

It is clear that when increasing the number of cells, the accuracy of the model improves. Fig. 4.8 shows that the main reason for the increase in accuracy is due to better prediction in pressure coefficient distributions. Pressures at leading and trailing edge are difficult to predict when too few cells are included in the chord wise direction. Therefore, it is recommended to concentrate more cells towards the leading and trailing edge, while fewer cells are required in the middle part of airfoil sections. From the RMS residuals of density, it is shown that for a reduced number of cells no stagnation happens before the threshold value is obtained. This indicates that unsteady flow behavior is not well presented in coarser meshes. The largest mesh represents unsteadiness at cylinder and transition part, which results eventually in stagnation of residuals. Further analysis is performed on the influence of number of cells in the wake region with respect to torque values. No considerable effect is found, which confirms the research of Zahle et al. [168] in which it is shown that wake resolutions do not considerably affect predictions of power performance. However, it must be noted that SUMad has difficulties in resolving large circulations in the wake, so caution should be taken with this observation (see Section 4.2.4).

As conclusion, it can be stated that accuracy of torque is mainly dependent on the number of chord wise cells at the blade. No investigation has been performed on the influence of the

number of off-wall cells at the blade. However, it is expected that the boundary layer will be better resolved when increasing the number of cells at that direction. The number of cells in spanwise direction has also not been investigated. The reason for this is that it is expected that no large flow solution differences will occur due to the relative flat surface in the spanwise direction. However, approximately 150 surface cells in the spanwise direction are placed for taking possible cross-flow into account due to rotational effects. Influence on the amount of cells at the wake while maintaining 260 chord wise cells did not result in significant differences in torque values.

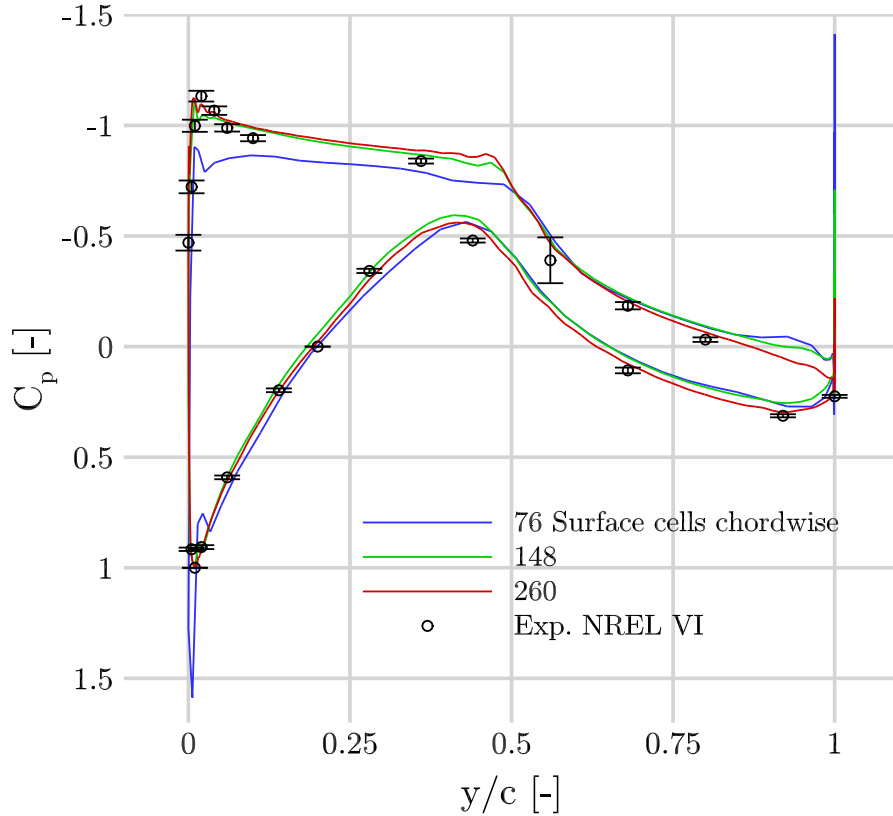


Figure 4.8: Pressure distribution convergence at $z/R = 95\%$

4.1.5 Sensitivity analysis

Assuring correct search directions in gradient-based optimization, the gradients computed by the adjoint method are required to be correct. Various procedures can be employed for verifying adjoint methods. Some of these procedures require finite difference and complex step. Both methods rely on the Taylor expansion, which approximate derivatives by perturbing the function \mathbf{F} with a small step size h . The difference in complex step and finite difference is that finite difference results in subtractive cancellation due to too small step sizes. Considering the forward finite difference scheme with its first order truncation error $\mathcal{O}(h)$,

$$\frac{\partial \mathbf{F}}{\partial x_i} = \frac{\mathbf{F}(\mathbf{x} + \mathbf{e}_i h) - \mathbf{F}(\mathbf{x})}{h} + \mathcal{O}(h), \quad (4.1)$$

the truncation error can dominate the solution, which is caused by subtractive cancellation. In order to prevent this phenomenon, an additional analysis on choosing a proper step size should be performed. Consequently, this results in higher computational costs due to many function evaluations. In most cases, finite difference schemes also require more than one function evaluation for approximating derivatives, which again result to higher computational cost.

The complex step derivative approximation, at the other hand, does not have the above mentioned subtractive cancellation restriction. When using complex step size ih in the Taylor series expansion, the first order approximation becomes the following [273]:

$$\frac{\partial \mathbf{F}}{\partial x_i} = \frac{\mathbf{F}(\mathbf{x} + ih\mathbf{e}_i)}{h} + \mathcal{O}(h^2). \quad (4.2)$$

Clearly, no subtractive cancellation appears and only one function evaluation is required to find derivatives. Consequently, this results in lower computational cost compared to finite difference. Also the truncation error is second order resulting in more accurate gradient approximations. Fig. 4.9 shows the subtractive cancellation phenomenon for finite difference. Complex step remains at machine accuracy for very small step sizes.

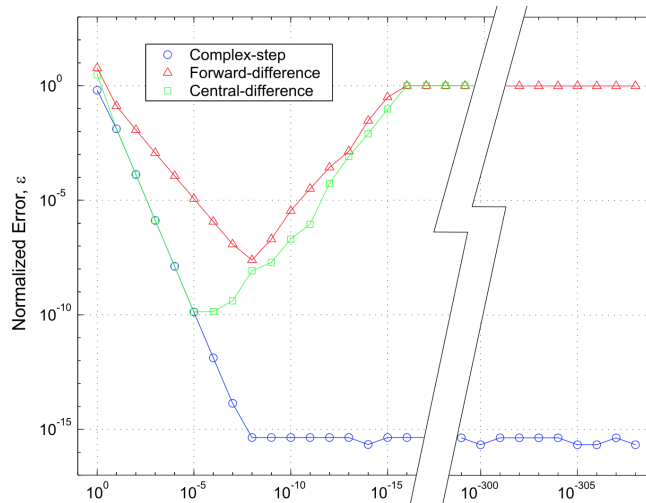


Figure 4.9: Accuracy of complex step and finite difference [273]

In this section, both gradient approximation methods will be used for verifying adjoint derivatives of the objective function with respect to design variables. In this case, the design variables are twist and shape of airfoil sections. For the sake of brevity, only one verification of one derivative of each design variable is presented. The complex step derivative approximation of shape design variables could not be used because some implementation difficulties were encountered in terms of perturbing shape variables in the complex domain.

The forward finite difference method requires an additional analysis on what step size should be taken for accurate gradient approximations. In Fig. 4.10, it is shown that step sizes of approximately 10^{-4} for both types of design variables result in accurate gradient approximations. Given the

minimum complex step value of $i \cdot 10^{-8}$ in Fig. 4.9, employing a step size of $i \cdot 10^{-20}$ for complex step would be sufficient for obtaining machine accurate derivatives.

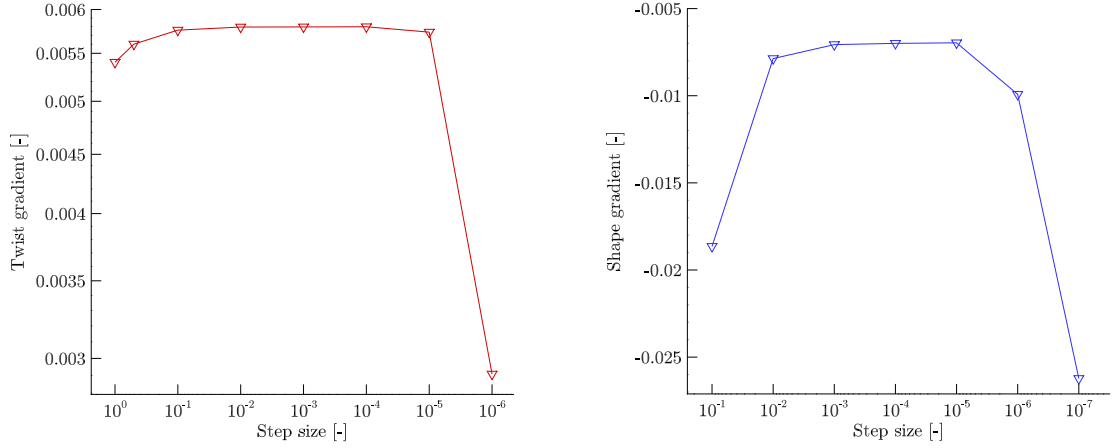


Figure 4.10: Forward finite difference approximation for design variables with respect to torque

In Table 4.1, a comparison is made between gradients of the above mentioned derivative approximation methods. It is found that algebraic mesh warping results in inaccurate derivatives compared to derivatives of solid mesh warping, due to perturbation at far field (see Section 4.1.1). The derivatives of the approximation methods using solid mesh warping agree within three orders of magnitude. It is noted that derivatives of shape variables appear to be more difficult to approximate than derivatives of twist variables. This can be explained by the fact that CFD simulation results, such as torque, are less sensitive to perturbing shape variables than twist variables.

Table 4.1: Gradient approximations using solid mesh warping. Note that the adjoint method is as accurate as the finite difference, since the torque fluctuates at fourth decimal.

	Twist	Shape
Forward	0.00579778	-0.00656330
Complex step	0.00579816	-
Adjoint	0.00579599	-0.00657001

The gradients approximated by the adjoint method for the first optimization iteration can be found in Fig. 4.11. It is clear that torque is most sensitive towards the tip, which is expected because most power is extracted at tip regions. Another observation is that the leading and trailing edge at lower surface will change opposite from each other. This can lead to more camber. However, note that this is for one optimization iteration, which implies that it is too early to conclude on how the optimal design would look like. Especially, when constraints are added to the optimization method. As conclusion, the adjoint method is verified and mesh perturbations can only be executed by solid mesh warping. Further developments in implementing the complex step for shape design variables are necessary for further verification.

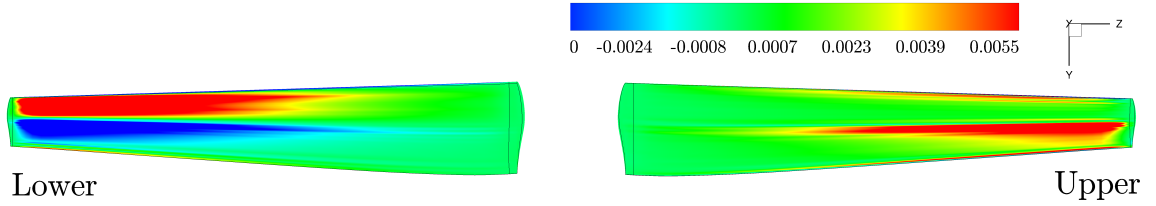


Figure 4.11: Sensitivity surfaces of upper and lower NREL VI blade: $\partial C_{M_x}/\partial x$

4.2 Validation of CFD simulation results

Estimating the accuracy of optimization results is only possible when the analysis method is validated. Therefore, experimental data provided by NREL are compared with CFD simulation results. No experimental data is available on wake structures. The pre-processed data for each wind speed is ordered in a list that consists of 876 channels in which different time dependent variables are measured. Since not all channels will be applied for validation, it is decided to use only relevant channels. The amount of data for each channel is 15625 measurements. Afterwards, these measurements are averaged in order to compare it with steady state CFD simulation results. For every experiment, there are uncertainties in measurements due to systematic and random errors. Therefore, it is decided to compute unbiased standard deviations of the samples. Note that it is assumed that the samples are independent from each other. Once the measurements are post processed by MATLAB, the experimental data can be used for comparison with computational results of SUMad. Further information on the experiment can be obtained in the following reference [147].

In this section, not only pressure and loads are compared with experimental and numerical data. The computational techniques such as Turkel's low speed preconditioner, periodic boundary conditions, Roe scheme with/without Van Albeda limiter are validated as well. Flow separation and wake structures are analyzed for obtaining a better insight in wind turbine aerodynamics and computational shortcomings. Since optimization is only possible when the residual of density converges, validation is necessary for the modified NREL VI blade without cylinder and transition part.

4.2.1 Pressure coefficient distributions

Following the grid convergence analysis described in Section 4.1.4, it is decided to use a mesh of approximately 11.5 million cells with 260 chord wise surface cells for validation. Three span wise sections are taken: The first section is taken at the root ($z/R = 0.3\%$), where it is expected that rotational effects will have a predominant influence on pressure distributions. The mid ($z/R = 0.63\%$) and tip ($z/R = 0.95\%$) section are expected to have no difficulties in predicting correct pressure distributions for fully attached flow regions. If the span of the blade would have been larger, compressibility effects will occur at tip regions. Since SUMad is a compressible CFD solver, compressibility effects should not be an issue. Incompressible solvers, at the other hand, could induce a small error in the flow solution.

In the following figures, experimental results are shown by upper and lower pointing triangles representing the upper and lower part of the airfoil section, respectively. Standard deviations of the

experimental pressure coefficients are plotted. It is shown that for higher wind speeds, standard deviations are becoming larger at the upper part of the blade, which represents greater unsteadiness caused by flow separation. The RANS-based CFD simulation results of the NREL VI sequence S blade are compared with experimental results, in which the pressure is non-dimensionalized by the following relationship:

$$C_p = \frac{p - p_\infty}{\frac{1}{2}\rho c (V_\infty^2 + (r\omega)^2)} \quad (4.3)$$

Also, comparison between measured pressure coefficients and pressure coefficients of the NREL VI blade without cylinder and transition part will be shown.

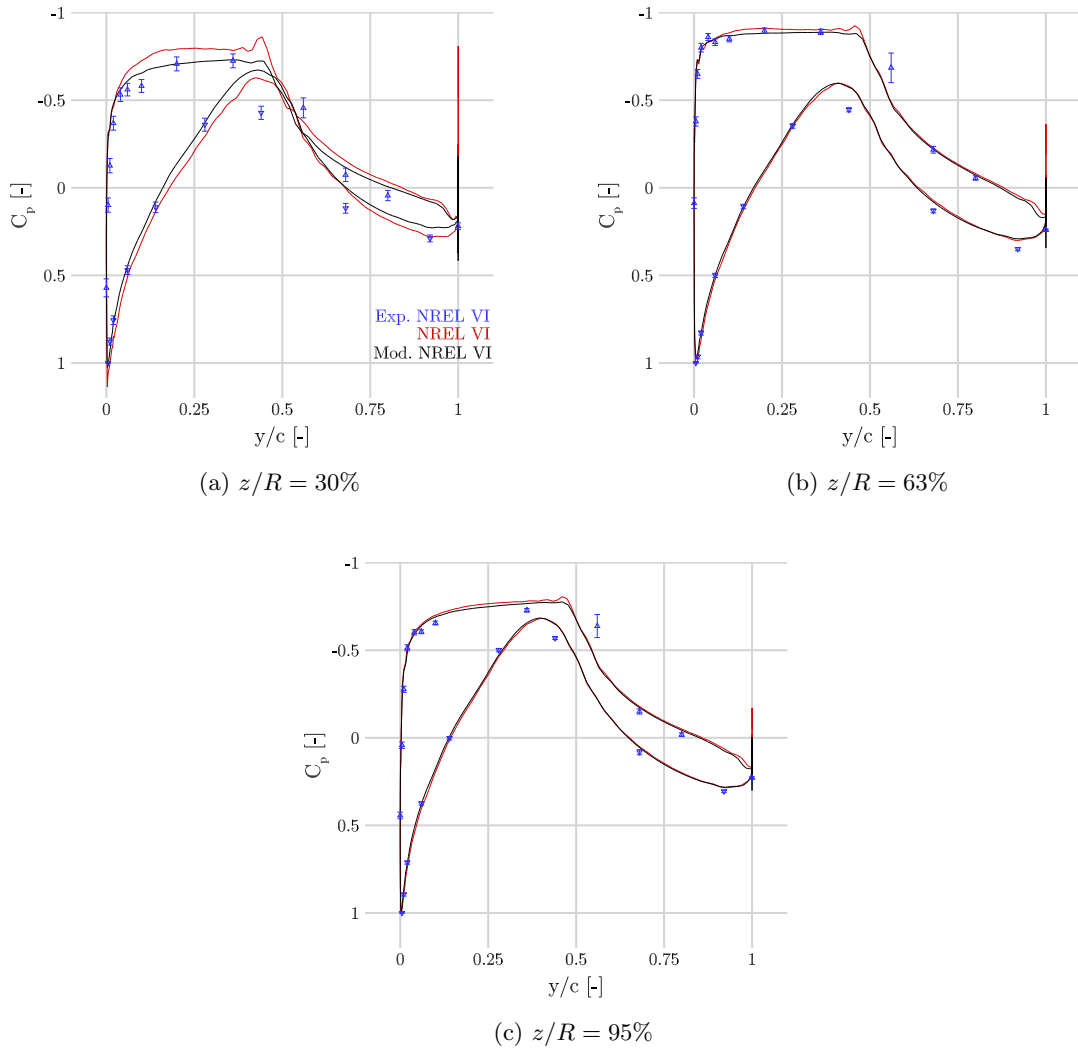


Figure 4.12: C_p distributions at $U_\infty = 5\text{m/s}$

Depicted in Fig. 4.12, the root section is not well predicted due to influence of stalled flow conditions at the cylinder and transition part of the original NREL VI blade (see Section 4.2.2). When looking at root region of the modified design, the lack of cylinder and transition part affect

the pressure distribution due to an additional vortex at the root. The other two sections are in good agreement with experimental results. Given the incompressible flow behavior, pressure coefficients at stagnation points should be equal to one. This is not the case for the stagnation point at root section for the original design, which is caused by numerical difficulties. Since RANS-based CFD simulations are relying on fully turbulent flows, no predictions of laminar boundary layers can be made. This can result in more negative values of suction pressure coefficient distributions due to thickening of the boundary layer. In all figures with fully attached flows, more negative prediction in pressure at suction side of the airfoil can be observed, especially along the trailing edge.

In Fig. 4.13, similar behavior for mid and tip section is observed. The root section is better predicted than the 5 m/s case. A high suction peak is observed at the leading edge, which is a result of a larger influence of flow separation at cylinder and transition part. Again difference in pressure distribution at root between the two designs is observed. Overall, there is a relatively good agreement with respect to the measured pressure distributions at 5 and 7 m/s.

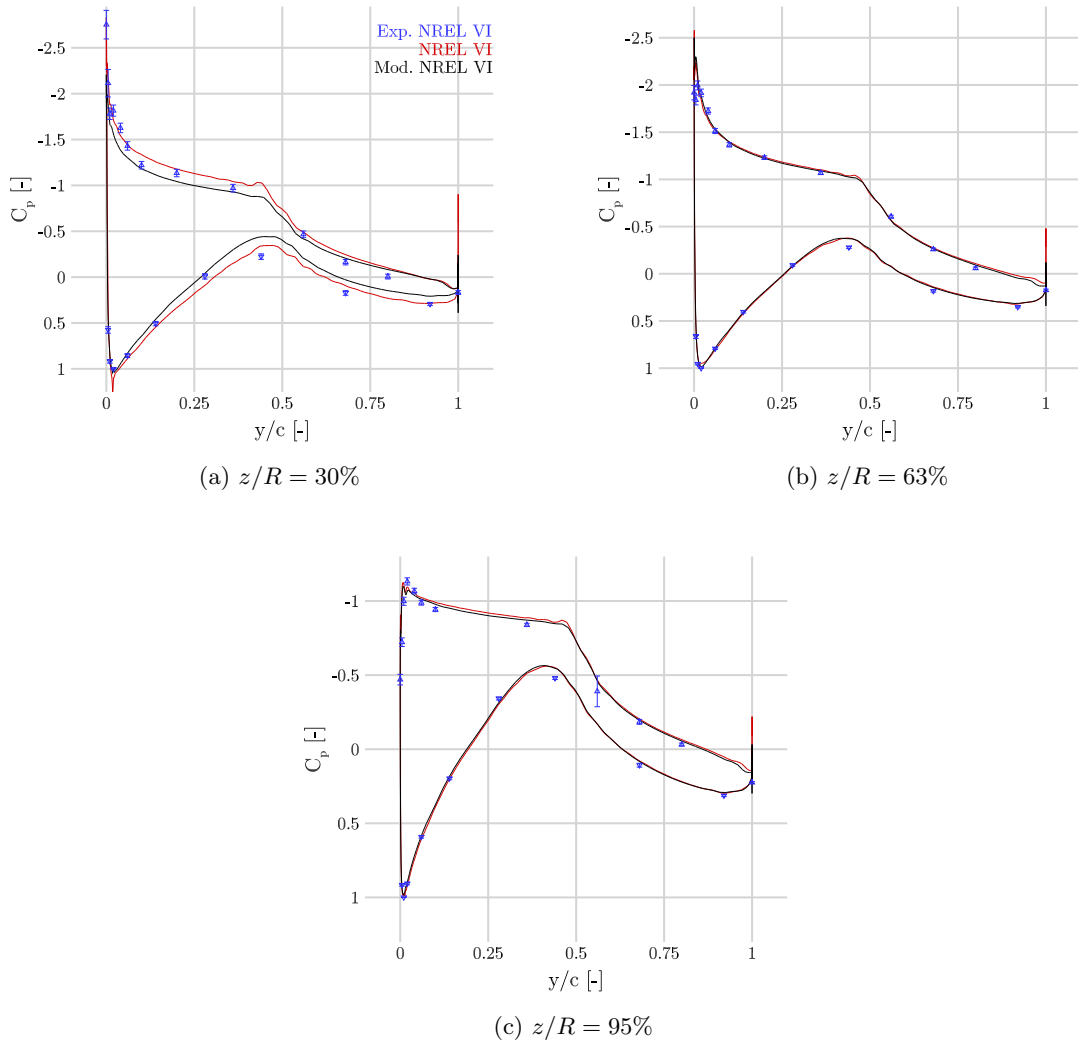


Figure 4.13: C_p distributions at $U_\infty = 7\text{m/s}$

In Fig. 4.14, suction pressure on trailing edge at root and mid regions are flattening out, which indicates flow separation. Looking close at the suction peak at root region, a discrepancy between experimental and CFD obtained pressures is observed. This indicates the presence of leading edge separation at the root region. In some cases, leading edge separation can be an indication of transient effects, such as dynamic stall. Since these CFD simulations are steady-state, no transient effects can be observed. However, it should not be a surprise that some of these effects occur in reality. Therefore, caution should be taken during fatigue analyses. Again the pressure distribution at root of the modified NREL VI blade is different than the original NREL VI blade.

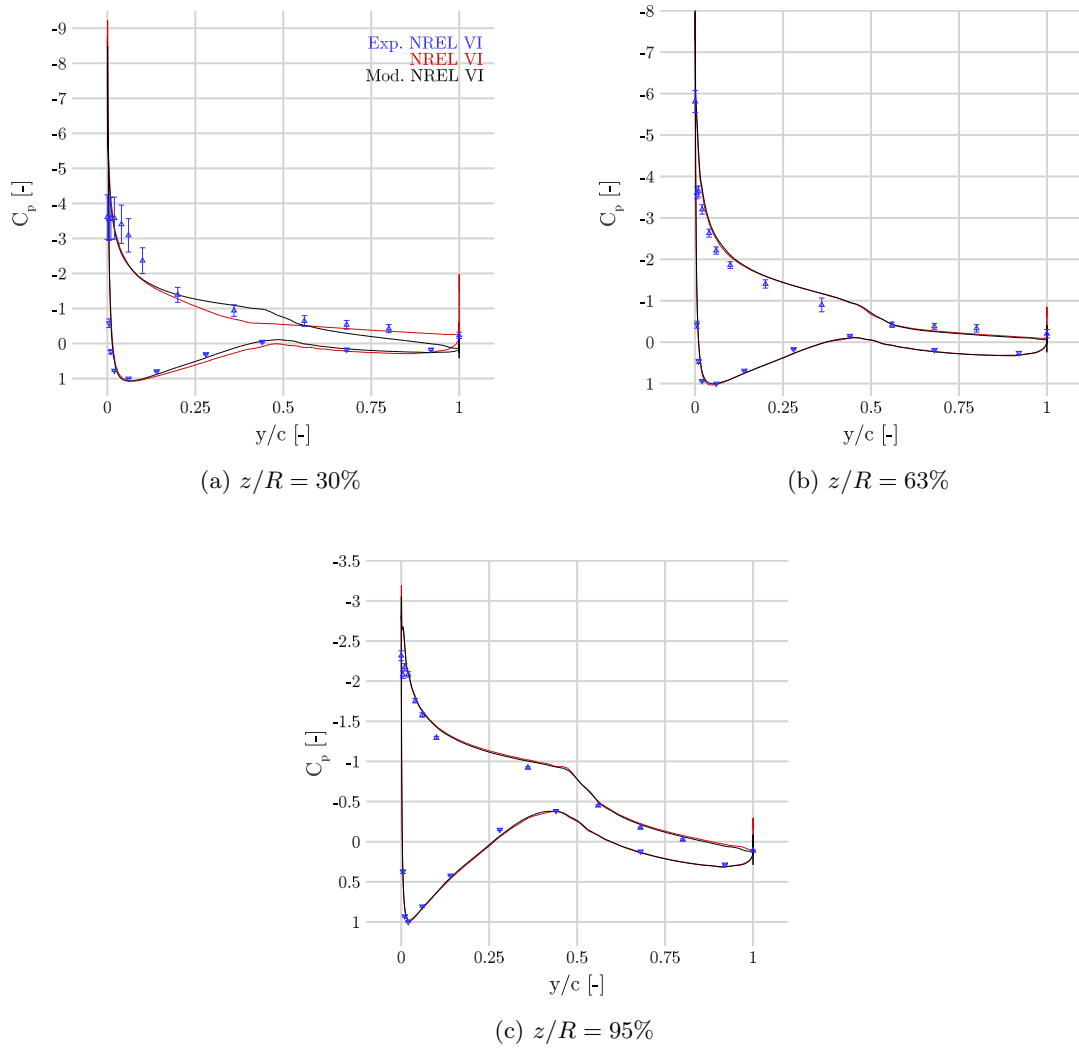


Figure 4.14: C_p distributions at $U_\infty = 10\text{m/s}$

In Fig. 4.15, the suction sides of pressure distributions at root and mid section are more or less flattened out, which means that flow is fully separated at the upper surface of the blade. The magnitude of standard deviations for these sections has increased, which is an indication of having fully separated flow. Both RANS-based CFD simulation results are not able to predict separation accurately: When comparing the lower part and upper part of the blade, it is clear that fully attached

flows at the lower part are well simulated while large discrepancies occur at the upper part. At tip region, the suction side of the pressure coefficient distribution seems to flat out, which means that flow is mildly separated or flow separation at mid section is influencing the pressure distribution at tip region.

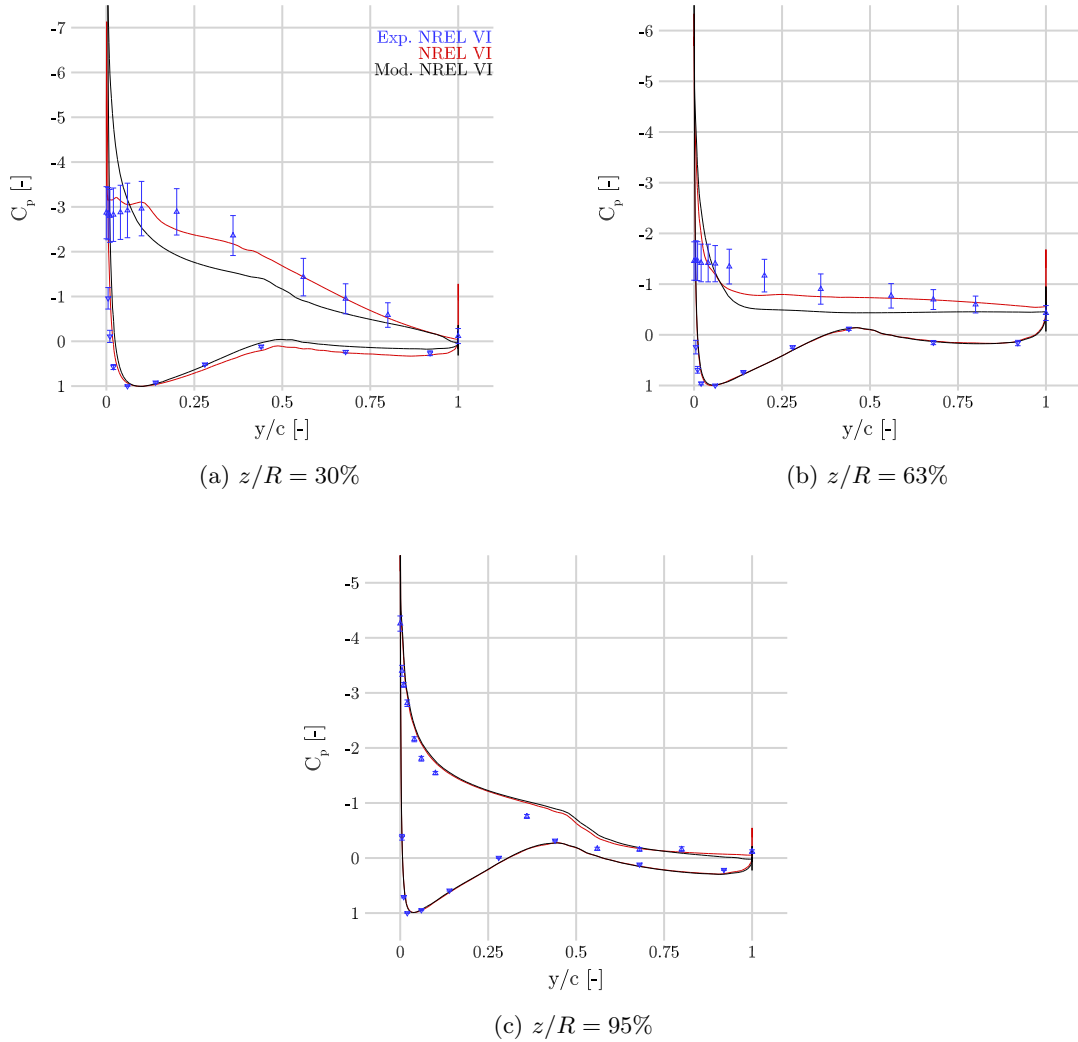


Figure 4.15: C_p distributions at $U_\infty = 13\text{m/s}$

In Fig. 4.16, similar behavior is observed. However, the overall magnitude of pressure coefficient distributions seems to reduce, which indicates that the blade gets into a deeper stall. Also, the standard deviations on the leading edge at tip region are increasing which implies that it receives more influence of separated flow. The suction pressure at the tip is flattened out which suggests that there might be flow separation. As expected, pressure distribution at root of the modified design is different than the pressure distribution of the original blade.

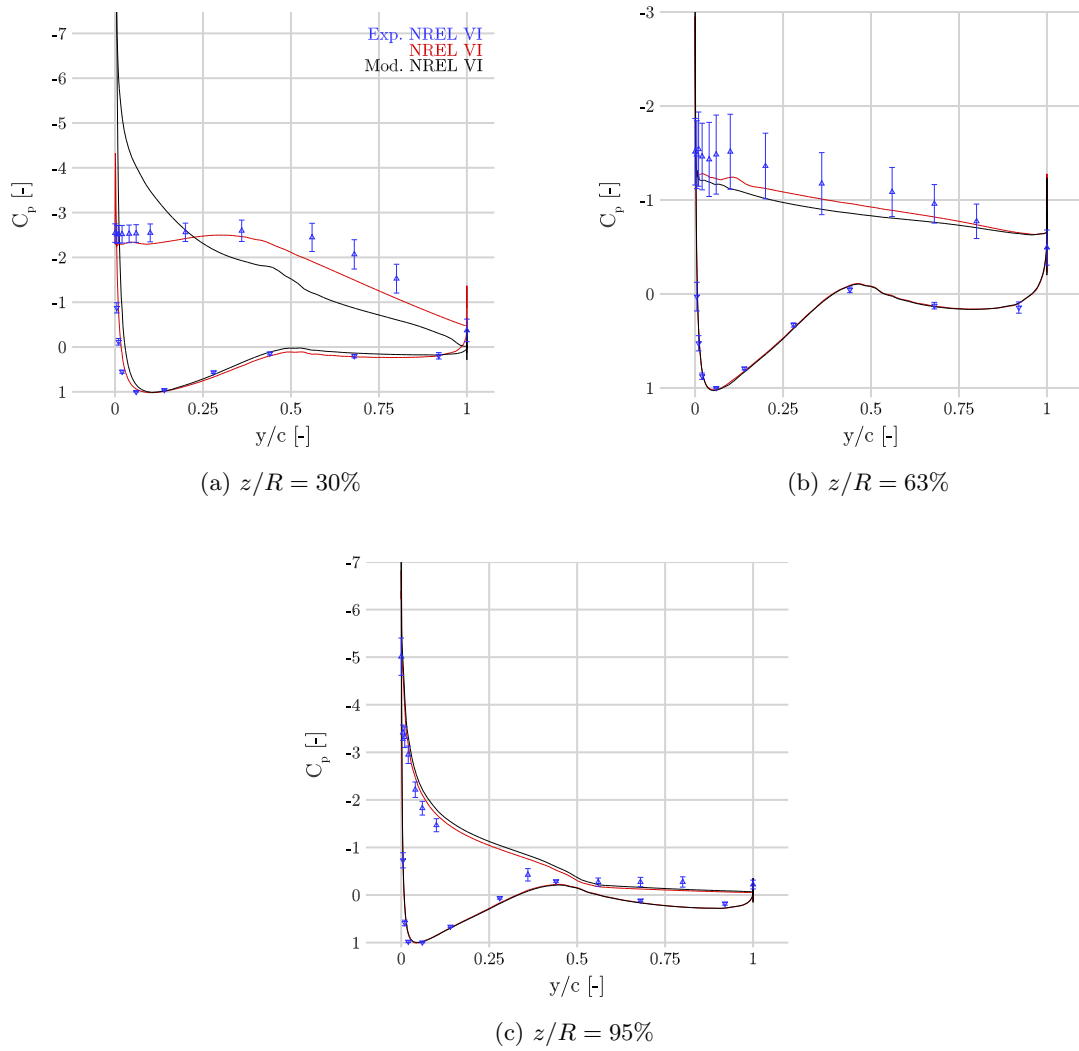


Figure 4.16: C_p distributions at $U_\infty = 15 \text{ m/s}$

In Fig. 4.17 and 4.18, the flow is separated over the entire span, which means that the NREL VI blade is under deep stall condition. Pressure coefficient deviations are observed at the suction side of the blade due to difficulty of RANS-based CFD models in solving complicated separated flows. Overall, a relatively good agreement between experimental and simulated results is achieved. This can be explained by the stall behavior of the S809 airfoil. In recent investigations, it is shown that the S809 airfoil belongs to a group of airfoils in which experimental and computational data have acceptable agreement at high angles of attack [274]. Also, DES simulations have proven that vortical interaction in the wake at high angles of attack for the S809 airfoil has limited effects on computational loads [275]. This means that even though the wake is not well resolved, good agreement between experimental and simulated results of the S809 airfoil can be obtained.

To conclude, validation on the NREL VI sequence S blade is performed. RANS-based CFD simulations can obtain highly accurate results for fully attached flows. When there is separation or there are regions influenced by separation nearby, RANS-based CFD models have difficulties

with accurately estimating aerodynamic loads. This problem can be alleviated by employing other turbulence models (see Section 4.2.5) or other simulation models, such as DES. Transition models could be another option in which loads can be better predicted during separation, especially for mildly separated flow regions.

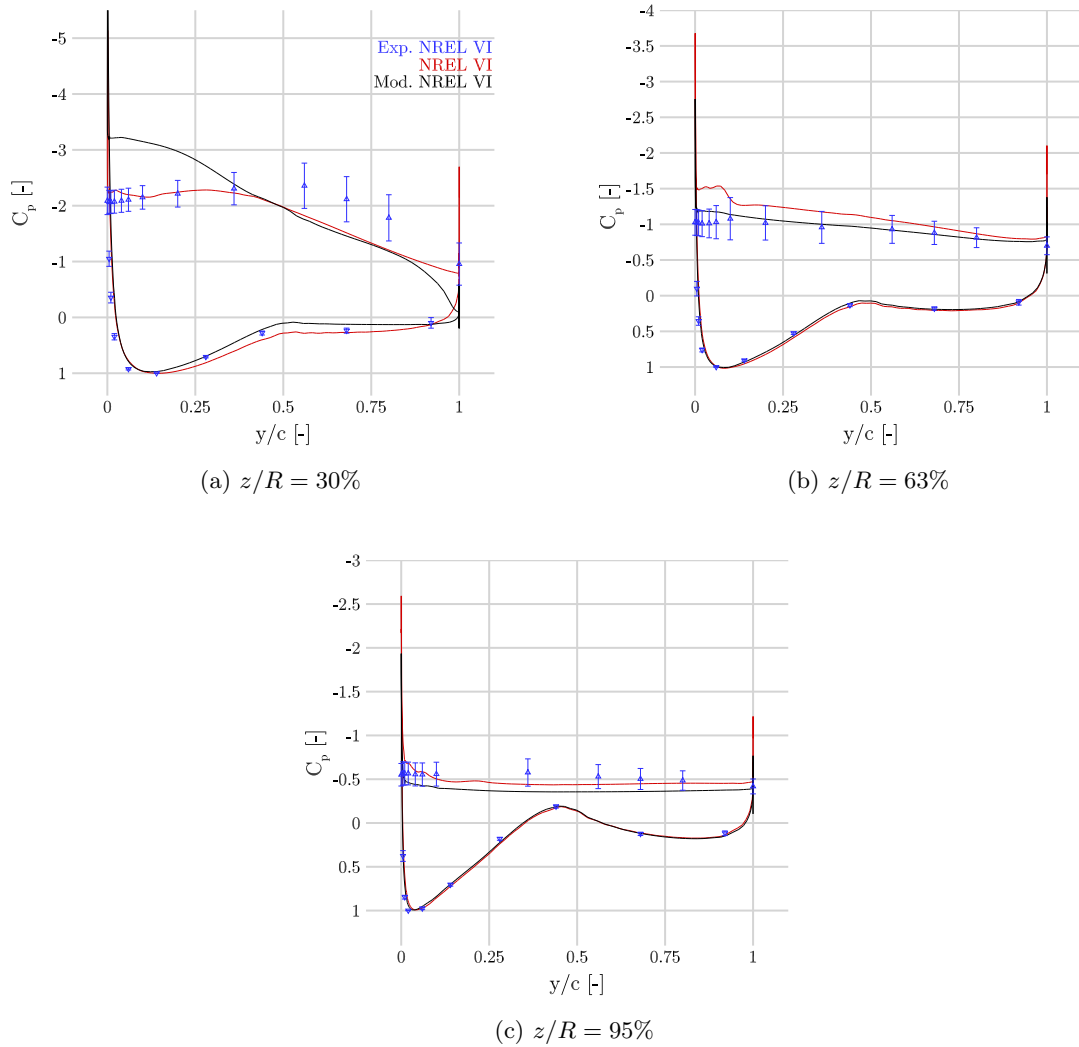


Figure 4.17: C_p distributions at $U_\infty = 20\text{m/s}$

At 10 m/s, there are indications of transient effects near the root region. Unfortunately, these cannot be simulated since RANS-based CFD simulations are steady-state. It is shown that flow separation propagates from root to tip region, which is expected since the angle of attack is higher at root regions. Another observation is that even though the flow is fully attached over the whole span, regions close to the cylinder and transition part, where separation takes place, are affected. Due to this complex nonlinear phenomenon, special care should be taken at these regions when optimizing the NREL VI sequence S blade. However, it is expected that the influence on power extraction will be small, because it is at the root region. Given that these RANS-based CFD simulations are not capable of accurately representing loads for separated flow, it is suggested that no optimization is

performed on separated regions for assuring correct simulation results. This would not restrict the optimization capabilities for wind turbines, since most modern wind turbines are performing in fully attached flow conditions.

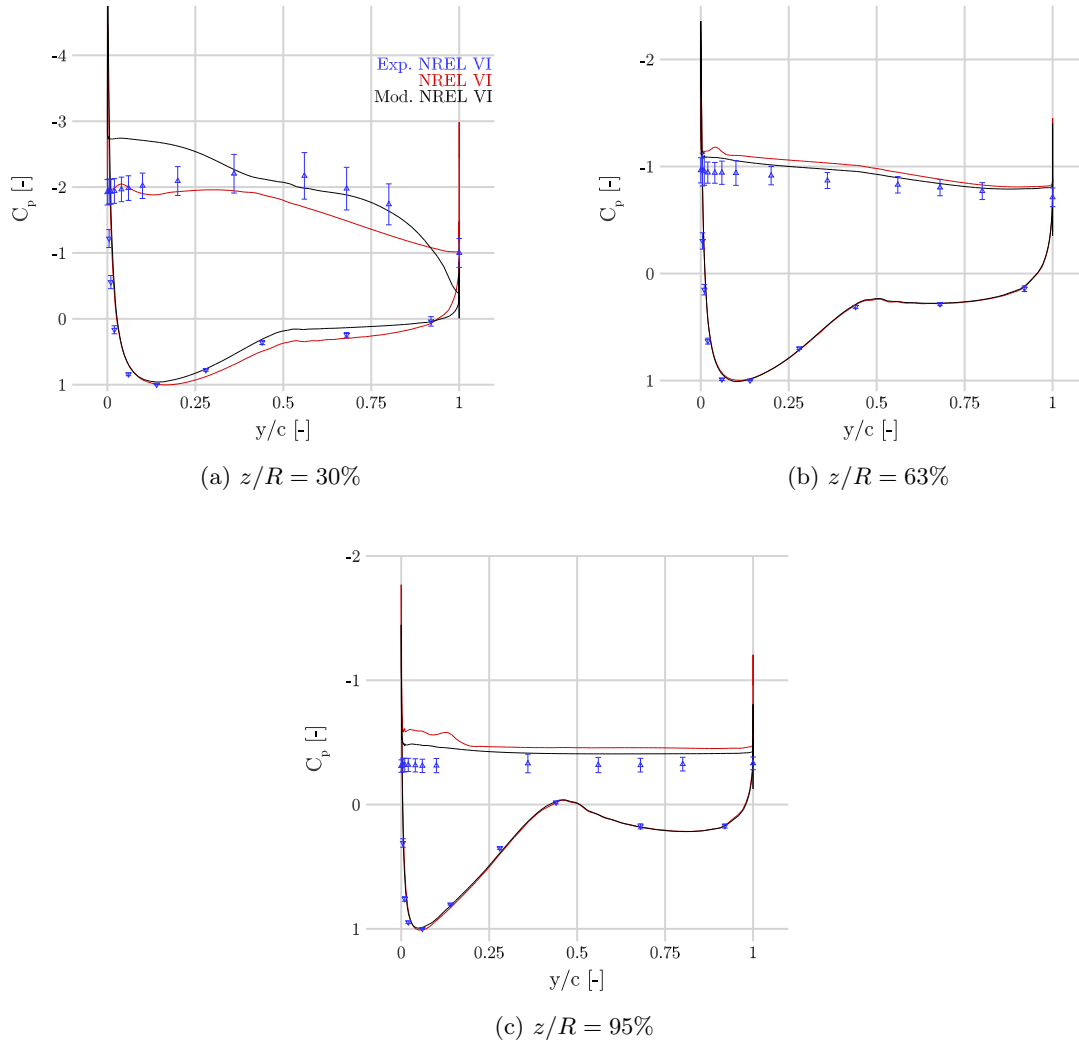


Figure 4.18: C_p distributions at $U_\infty = 25\text{m/s}$

Pressure distributions of the original NREL VI blade and modified NREL VI blade are compared. It is shown that pressure distributions at root region are not the same due to different flow phenomena, such as flow separation and circulation. However, pressure distributions at mid and tip region are approximately identical, which implies that accurate optimization can be performed on the modified NREL blade as substitution of the original design.

4.2.2 Flow separation analysis

Flow separation will be visualized by applying streamlines on the first cell of the boundary layer. With this visualization technique, some of the explanations given in Section 4.2.1 can be confirmed or can be rejected. Also streamlines in the outer layer of the flow field will be presented to give more

insight in the behavior of the SA turbulence model. Depicted in Fig. 4.19, various flow separation behaviors are shown. At 5 m/s, only separation occurs at the cylinder and transition part. When increasing the free stream velocity, flow separation at the cylinder and transition part will propagate towards the tip of the blade until flow is fully separated over the whole blade. Pressure coefficient distributions (suction side) are flattening out while the blade is getting into a deeper stall. This can be confirmed when looking at a free stream velocity of 10 m/s, where the suction side at the root is flattened out and where the pressure distribution is still intact at the tip. At 20 or 25 m/s, the blade is in deep stall condition where all suction sides are flattened out. Sometimes it is hard to find flow separation when only looking at pressure distributions, e.g., at 15 m/s, moderate flow separation at the tip is hard to predict by just looking at pressure distributions. Therefore, it is recommended to combine surface streamlines with pressure distributions for observing flow separation.

Due to rotation, boundary layer material is transported to a larger radial position resulting in cross flow. Therefore, the direction of the streamlines in separated flow regions are pointing towards the tip instead of the opposite direction of the relative velocity vector. This rotating effect results in stall delay at the inboard section of the blade and creates higher loads compared to non-rotating blades.

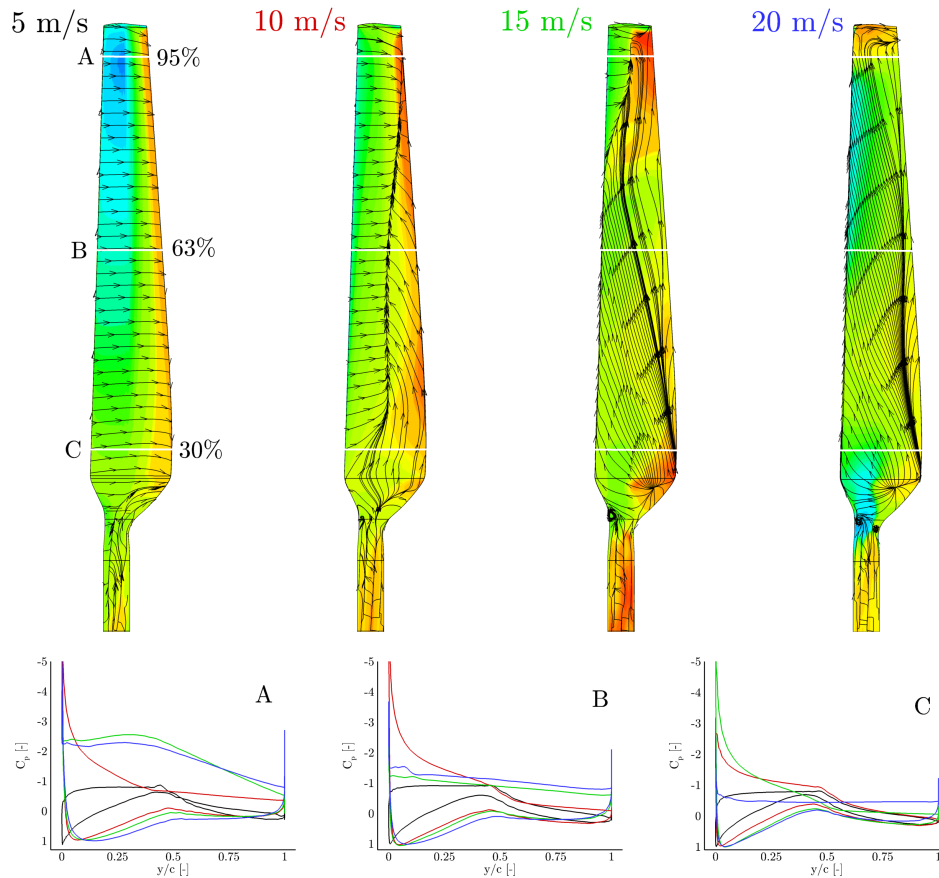
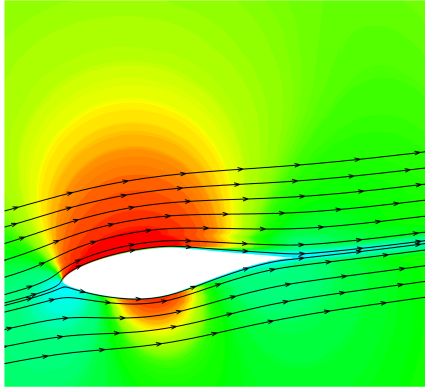


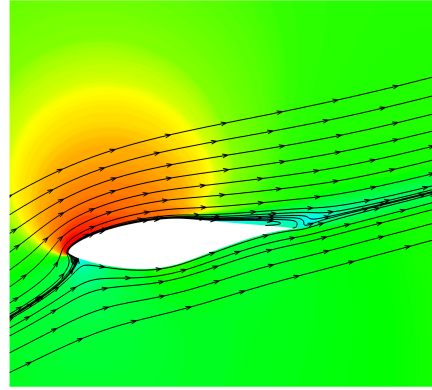
Figure 4.19: Flow separation behavior for various wind speeds on the NREL VI blade: moderate flow separation starts at 10 m/s. The blade is in deep stall condition at 20 m/s.

In Fig. 4.20, flow fields for various wind speeds are shown at $z/R = 63\%$. As expected, the angle

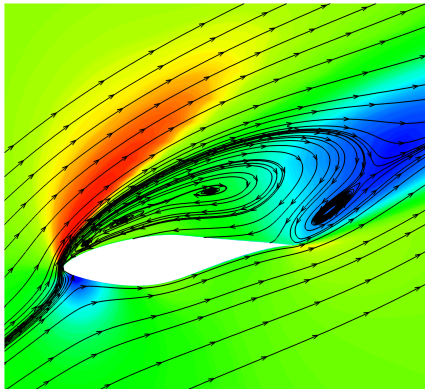
of attack increases as the free stream velocity gets higher. This eventually results in flow separation that starts at the trailing edge (see Fig. 4.20b) and propagates towards the leading edge (see Fig. 4.20c). For stall and deep stall conditions, circulation appears and is transported towards the tip due to centrifugal forces. Also, the magnitude of circulation is increasing with higher wind speeds resulting in deeper stall.



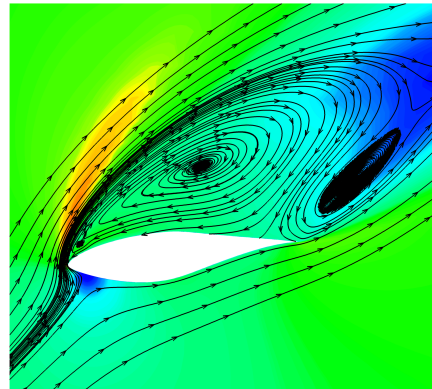
(a) Fully attached flow at $U_\infty = 5 \text{ m/s}$



(b) Trailing edge separation at $U_\infty = 10 \text{ m/s}$



(c) Stall condition at $U_\infty = 15 \text{ m/s}$



(d) Deep stall condition at $U_\infty = 20 \text{ m/s}$

Figure 4.20: Relative velocity fields at $z/R = 63\%$ with various flow separation conditions

Various flow conditions are observed that can be categorized as follows:

- Fully attached flow at $U_\infty = 5$ to 9 m/s : All regions can be modeled with a high accuracy. Special care should be taken at root region, since separated flow at cylinder and transition part influences the loads at root.
- Mildly to fully separated flow at $U_\infty = 10$ to 19 m/s : Flow separation propagates in two directions (from root to tip and from trailing to leading edge) until the flow is fully separated.

- Deep stall conditions at $U_\infty = 20$ to 25 m/s: The flow is fully separated from the [NREL VI](#) blade.

In case of interest, the behavior of flow separation of the modified [NREL VI](#) blade can be found in [Appendix B](#). The behavior is similar except for the root region.

4.2.3 Torque and thrust analysis

Since the [NREL VI](#) sequence S blade performs under constant angular velocity, the trend of power extraction is the same as torque. Therefore, various simulated torque values with different computational techniques are compared with experimental shaft torque. In [Fig. 4.21](#), all [CFD](#) simulated torque values have the same trend. Torque increases until the free-stream velocity is equal to 10 m/s. From there onwards flow starts to separate which consequently results in lower lift and higher drag coefficients. Since the free stream velocity is increasing, the reduction in lift coefficient is compensated which results in stagnating torque values. It is noted that all [CFD](#) simulations obtain accurate torque values for fully attached flows, while inaccurate values are achieved in separated flow regions.

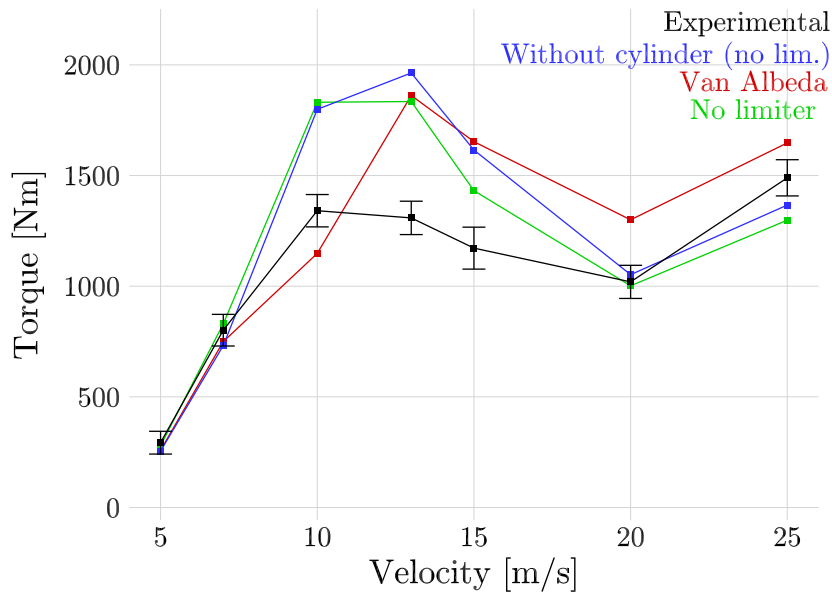


Figure 4.21: Torque values for various wind speeds

As mentioned in [Section 4.2.1](#), it is recommended to just optimize the wind turbine blade in fully attached flow regions, i.e. optimization is only accurate from cut-in wind speed of 5 m/s to rated wind speed of 9 m/s. It can be noted that Roe scheme with no limiter and the modified [NREL](#) blade without cylinder and transition part have an accurate torque value at 20 m/s. This is rather coincidental, because the flow behavior is the same as for 25 m/s. The largest discrepancy can be found at 10 m/s, which is caused by the lack of transition modeling and inadequate turbulence modeling. Also, in [Section 4.2.1](#) it is suggested that there are transients effects at the root which

makes it even more difficult for steady-state RANS-based CFD simulations. Roe scheme with Van Albada limiter seems to underpredict the torque value at 10 m/s, but afterwards it overpredicts the torque more than the other simulation results due to less separation. The NREL VI blade without cylinder and transition part shows the same torque behavior as the original NREL VI blade with Roe scheme without limiter. A negligible reduction at fully attached flow regions is observed due to lack of cylinder and transition part. As a result, the modified design can be used for gradient-based optimization without having problems with the adjoint technique. Concerning the SA model, flow separation is delayed and overestimated resulting in too high torque values.

Depicted in Fig. 4.22, various RANS-based CFD results of different researchers are compared with the obtained torque values of SUMad. No transition modeling is applied in any of these computations. It is clear that all models have difficulties with accurately modeling flow separation. Especially, the compressible solver elsA [95] appears to have major difficulties in resolving these complex flow phenomena. At 10 m/s, however, elsA predicts mildly separated flow accurately, which is in contrast with the other solvers. EllipSys3D [144] predicts stall regions from 13 to 15 m/s accurately, but does not seem to follow the increasing trend at 25 m/s. The structured overset solver OVERFLOW-D and unstructured solver NSU3D follow the same trend as SUMad [153], where flow separation at 20 m/s is fairly well predicted.

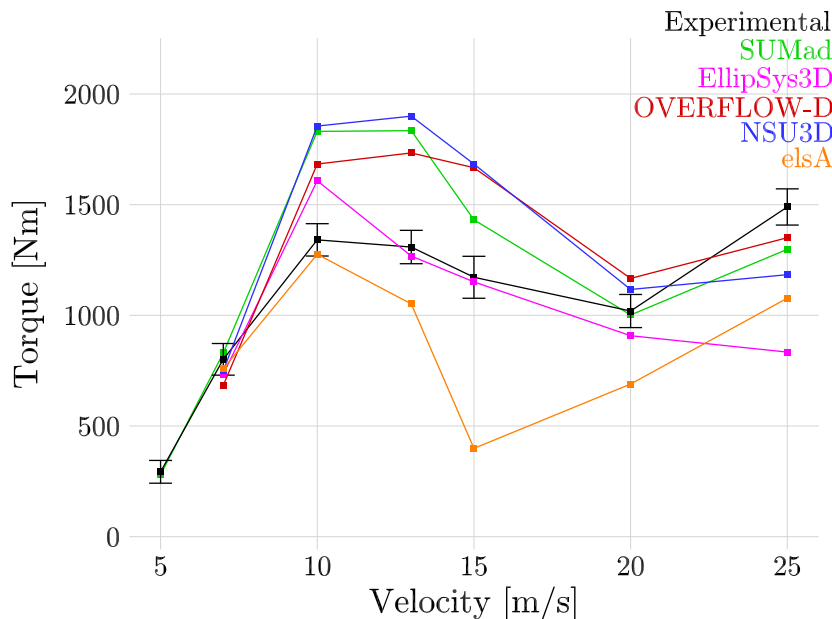


Figure 4.22: Torque comparison between RANS-based CFD models

Even though torque is crucial in computing the correct power output, other force and moment computations are important for validation as well. Especially, when it is intended to perform aerostructural or aeroelasticity analysis. Since thrust is a good indicator on how various forces are acting on the blade, it is decided to validate this particular force. Shown in Fig. 4.23, most simulation techniques, except for Van Albada limiter, are overpredicting thrust at 7 m/s. This behavior is also found in other RANS-based CFD simulation results. A possible explanation is that

while torque measurements are made from strain gauges, thrust measurements are estimated from integrated airloads at five instrumented pressure stations, which results in inconsistencies between torque and thrust comparisons. At higher wind speeds from 10 to 25 m/s, thrust is overestimated due to flow separation. Note that NREL VI blade without cylinder and transition part has a lower drag than the original design.

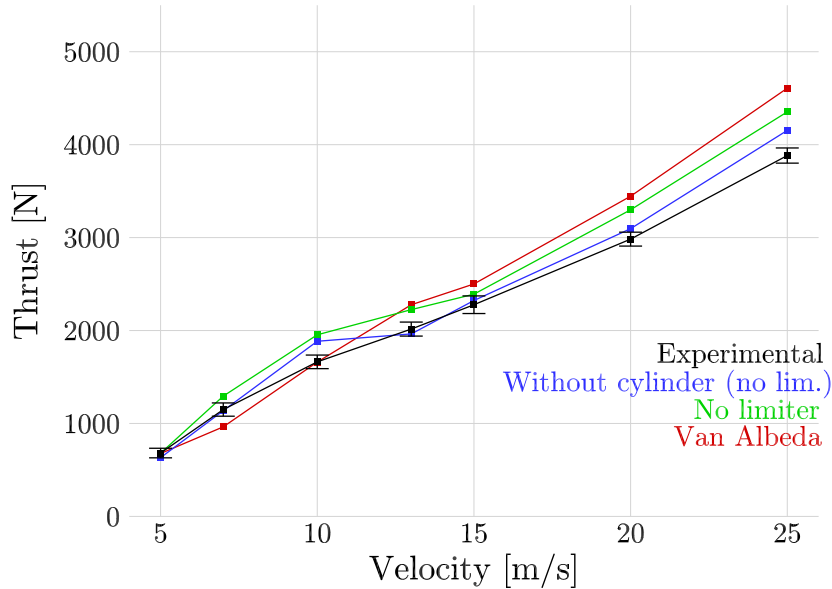


Figure 4.23: Thrust values for various wind speeds

As conclusion, it can be stated that accurate predictions in torque are possible with RANS-based CFD models as long as the flow is fully attached on the NREL VI blade. Once flow separation occurs, torque estimations become inaccurate. Comparison between the original NREL VI blade and the NREL VI blade without cylinder and transition part has shown that there is a negligible difference between torque and thrust. As a result, aerodynamic shape optimization can be performed with the modified design in fully attached flow regions.

4.2.4 Wake analysis

In low-fidelity models, wake parameters are often used for estimating power extraction: BEM theory uses axial and tangential flow induction factors based on the continuity, momentum, and Bernoulli equation. Vortex and panel methods are using free-wake or prescribed wake models that are based on the Biot-Savart law. Both of these models do not intrinsically resolve the wake. CFD models, at the other hand, have the capability of simultaneously estimating power extraction and resolving wake structures. In this section, the capabilities of the compressible solver SUMad concerning wake modeling will be shown.

Wake structures are usually turbulent flows that are characterized by low momentum diffusion, high momentum convection, and rapid variation of pressure and flow velocity in space and time. In order to visualize these complex flow phenomena, the Navier-Stokes equations can be rewritten by

applying a curl operator as such that vorticity dynamics of wakes can be simulated. Depicted in Fig. 4.24, the vorticity field of the wake in xz -plane is shown. Flow is shed away from the trailing edge. At tip and root region, flow rolls up resulting in helical vortices. Tip vortices are diffused very quickly due to the high dissipation characteristics of the Roe scheme and/or insufficient mesh resolutions at the wake [153]. A row of two tip vortices is observed, in which the vorticity magnitude of the second tip vortex has been significantly reduced due to dissipation and/or insufficient mesh resolution. The wake is rotating in the opposite direction of the rotor rotation for counteracting the torque produced by the blade. At approximately 60 m downstream from the blade, the wake is totally dissipated.

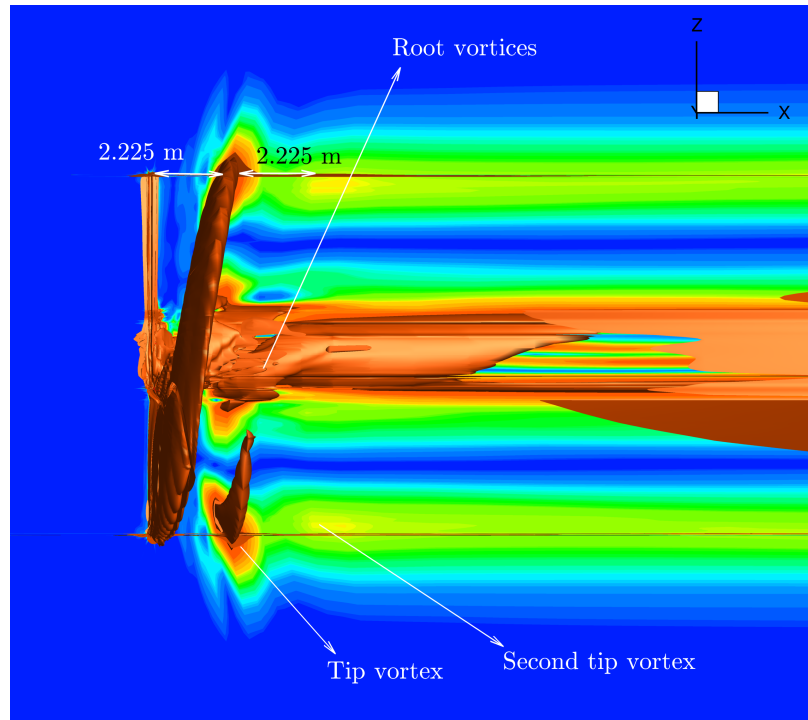


Figure 4.24: Vorticity magnitude contour and iso-surface of the wake

In various studies [276], it is shown that tip vortex shedding frequency is increasing when the tip speed ratio is increasing. Given that these RANS-based CFD simulations are steady-state, no frequency analysis on vortex shedding can be executed. However, when measuring the distance between two tip vortices Π , an indication can be given on how shedding frequency behaves, i.e. an increase in distance results in a reduction of shedding frequency and vice versa. Since the rotor rotation is constant for the NREL blade, the tip speed ratio is only dependent on the free stream velocity. Therefore, it is decided to plot the distance between two tip vortices versus wind speed. In Fig. 4.25, it is shown that the tip vortex shedding frequency clearly increases when the tip speed ratio increases (or when free stream velocity reduces in this case).

In addition to visualizing wake structures by use of vorticity, axial and tangential flow induction factors can be extracted from the wake. This is executed by taking slices in the near wake and extracting velocity vectors at these slices. From there on the axial and tangential induction factors can be calculated by normalizing them with the free stream velocity. As a result, it is observed

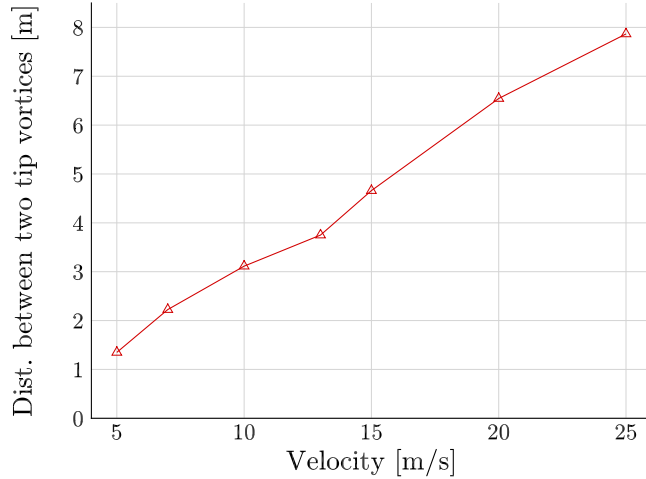


Figure 4.25: A higher tip speed ratio results in higher vortex shedding frequency

that both flow induction factors are radial dependent and varies along the wake. This magnitude of complexity cannot be obtained by any low-fidelity model. As a consequence, most low-fidelity models will induce an error in the predictions of power extraction due to inadequate assumptions.

As conclusion, **SUMad** is able to model the near wake regions of the **NREL VI** blade. However, due to numerical dissipation and/or mesh resolution, tip and root vortices quickly disappear further downstream. In order to alleviate this problem, a less dissipative turbulence model and more accurate dissipation matrix flux should be chosen. Also, the mesh at vortex regions should be refined. However, due to the Reynolds decomposition effect of **RANS** models, resolving large eddies will always be a problem. As a result, **DES** should be applied, where **LES** can resolve large eddies in the wake while **RANS** models can approximate flows close to the blade.

4.2.5 Comparison of turbulence models

Literature study has suggested that Menter's **SST** turbulence models are best for predicting power performance of wind turbines. Especially, flow separation is better predicted than one-equation turbulence models, such as **SA** turbulence models. In this section, a comparison between Menter's **SST** and **SA** turbulence model is performed by looking at torque values and behavior of flow separation. Depicted in Fig. 4.27, torque computed by Menter's **SST** seems to be more accurate at flow separation regions between 15 and 20 m/s. However, there is still a delay and overprediction of torque value when flow starts to separate, which is due to lack of transition modeling and transition effects. Note that Menter's **SST** is not differentiated for the adjoint method. This means that no optimization can be performed with this turbulence model. However, looking at torque values at fully attached flow regions, **SA** and Menter's **SST** turbulence are equally accurate, which implies that no sacrifice in accuracy is necessary for performing optimization. Fig. 4.26 shows that the **SA** model overestimates the attached flow at tip region when looking at surface streamlines. This results in a large torque value that is shown in Fig. 4.27. Since it is shown that flow separation propagates from root to tip and that the attached flow region of the **SA** turbulence model is larger, it can be stated that the

SA turbulence model delays flow separation more than Menter's SST turbulence model. Behavior of flow separation at cylinder, transition part, and root region between the two turbulence models is also different.

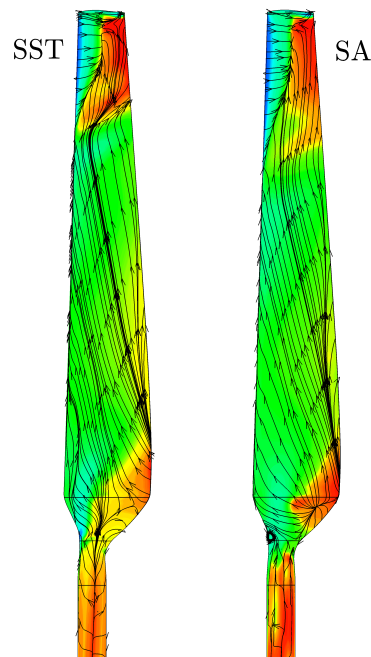


Figure 4.26: Comparison of turbulence models with respect to surface streamlines at 15 m/s

As conclusion, turbulence models have a large impact on predicting power performance of wind turbines. It is shown that the two-equation Menter's SST turbulence model predicts flow separation better than SA turbulence model. For fully attached flow conditions, both turbulence models would suffice to obtain accurate torque results.

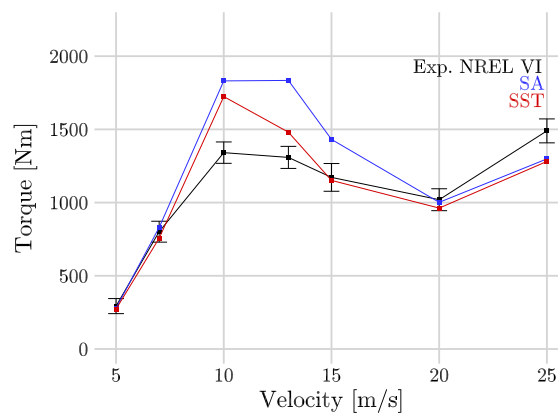


Figure 4.27: Torque comparison between Menter's SST and SA turbulence model

4.2.6 Turkel's low speed preconditioner

Compressible solvers have problems with converging low speed aerodynamic problems. As shown in Section 4.1.3, the RMS residual of density seems to stagnate due to flow separation at the cylinder and transition part of the NREL VI blade. In order to accelerate the behavior of the residuals as a mean to get convergence, Turkel's low speed preconditioner can be employed. Shown in Fig. 4.28, the convergence history of coefficients and RMS residual of density is shown. It is clear that the residuals are converging very slowly due to flow separation. Given the high computational cost of solving the preconditioner matrix of every cell and the required amount of iterations for adequate convergence, it is disadvantageous to use the preconditioner for optimization purposes. The required computational time of using Turkel's low speed preconditioner is 1268.3 proc hours while normal simulations last for 273.3 proc hours. Therefore, it is recommended to develop faster methods in the near future. Also, torque and thrust coefficients are fluctuating much more with respect to simulations without preconditioner (see Fig. 4.3). As a result, more iterations and computational time are required to obtain quasi-steady loads.

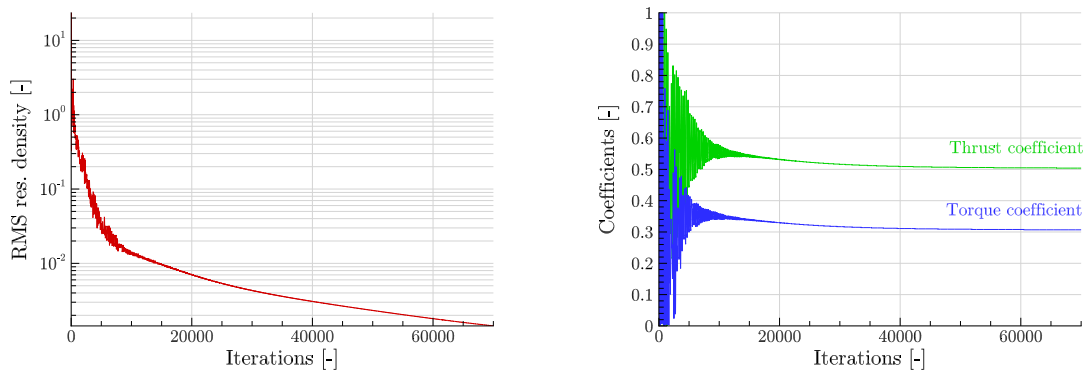


Figure 4.28: Convergence history of Turkel's low speed preconditioner at 7 m/s

Concerning validation, it is decided to model the NREL VI blade at 7 m/s. Fig. 4.29 shows that the pressure distributions are in good agreement with the measurements. Pressure distribution at the root is slightly off-set compared to original simulations due to different prediction in flow separation at cylinder and transition part.

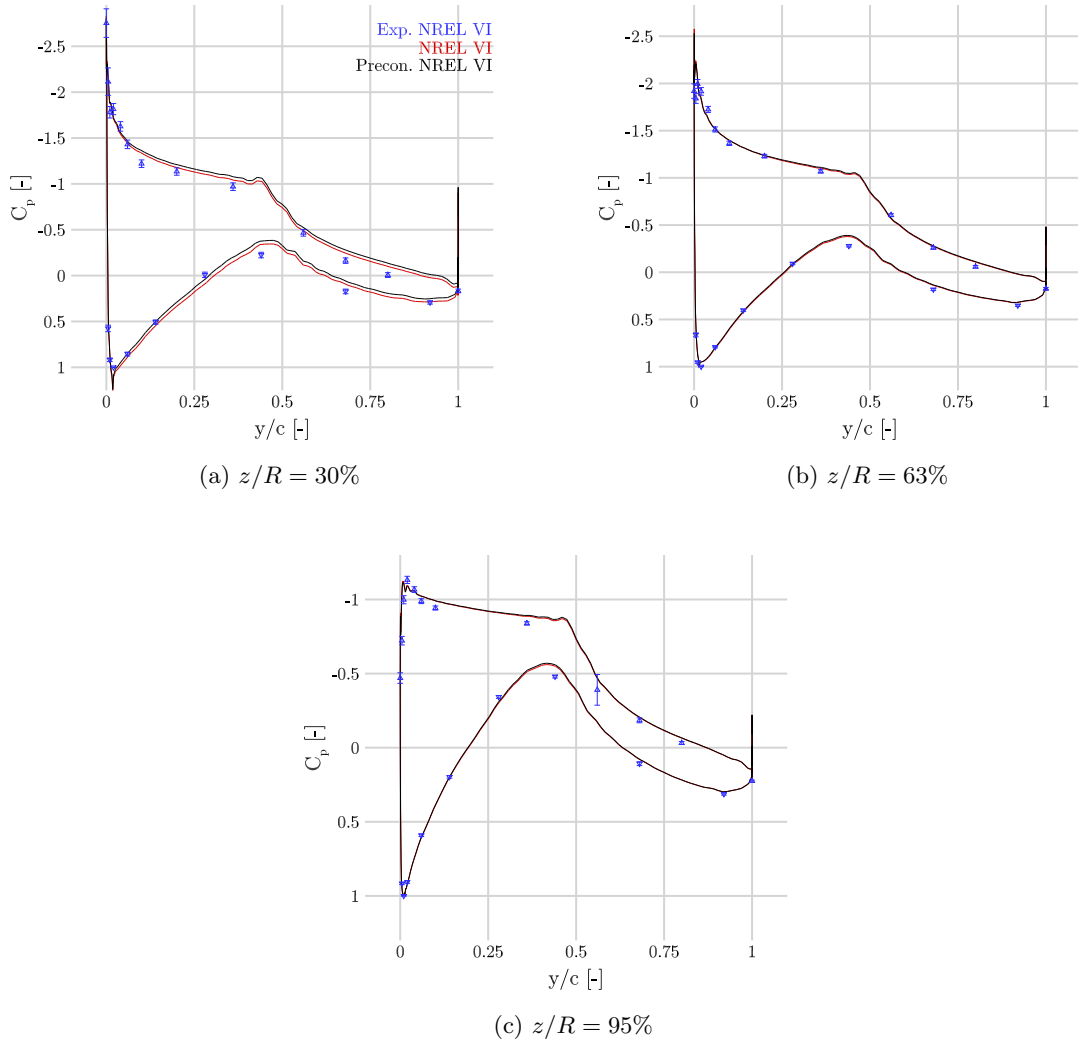


Figure 4.29: C_p distributions at $V_\infty = 7\text{m/s}$ using Turkel's low speed preconditioner

4.2.7 Periodic boundary conditions

The purpose of employing periodic boundary conditions is to reduce computational costs by simulating one rotating periodic part of the computational domain. Given that SUMad has been extensively modified, it is necessary to validate the periodic boundary conditions again. Depicted in Fig. 4.30, pressure distributions at mid and tip section are almost identical. At root section, however, discrepancies exist due to slip boundary condition imposed on the transition part of the two periodic boundary conditions.

As conclusion, periodic boundary conditions can be applied for obtaining accurate CFD results. However, the mesh perturbation method changes the periodic boundary conditions during optimization, which leads to non-identical periodic surfaces. As a result, errors are induced near the far field and consequently they can not be used as a method for accurately solving optimization problems.

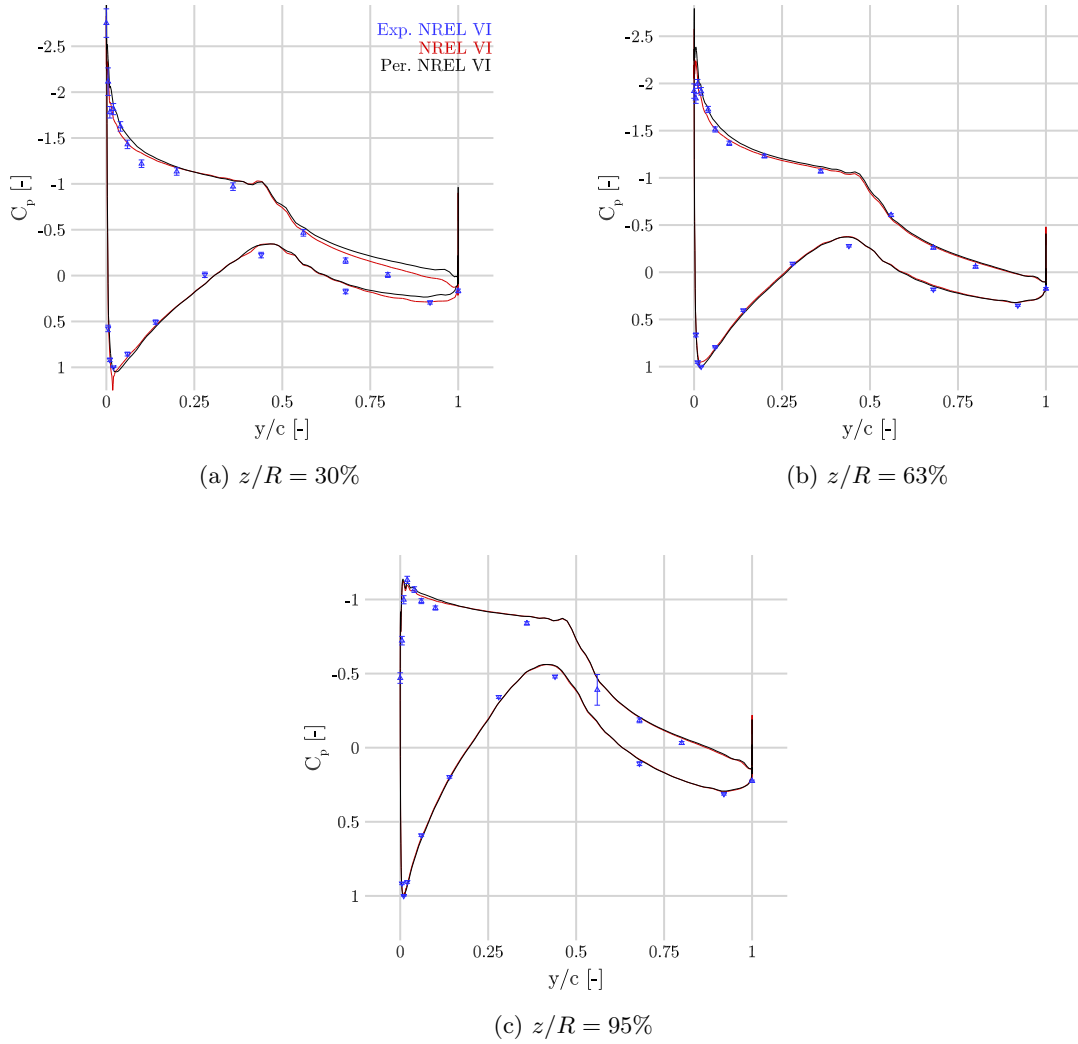


Figure 4.30: C_p distributions at $V_\infty = 7\text{m/s}$ using periodic boundary conditions

4.3 Discussion and conclusion

Verification and validation is performed on the [NREL VI](#) blade using the structured, compressible solver [SUMad](#). It is shown that the original design of the [NREL VI](#) blade cannot be used for gradient-based optimization, since the [RMS](#) residuals of density are stagnating due to intrinsic flow separation at cylinder and transition part. Turkel's low speed preconditioner would have been a first resort, but it is shown that its rate of convergence is too low resulting in too high computational costs. Instead, the cylinder and transition part of the [NREL VI](#) blade are deleted resulting in converging [RMS](#) residuals of density and adjoint method. Verification on the adjoint method has shown that gradients with respect to shape variables are less accurate than gradients with respect to twist variables due to smaller impact on the torque coefficient.

Validation is performed on the original and modified [NREL VI](#) blade. Both results were approximately the same and highly accurate for fully attached flows at 5 to 7 m/s. Once flow is separated,

no accurate results for both blades can be obtained. As a consequence, gradient-based optimization can only be performed at fully attached flow conditions with the modified [NREL VI](#) blade. Further analysis is performed on flow separation and wake structures. It is shown that Menter's [SST](#) turbulence model predicts loads better at flow separation than [SA](#) turbulence model. The Roe scheme is less dissipative than [JST](#) scheme resulting in better wake resolution. Periodic boundary conditions achieved accurate results for fully attached flows. However, it cannot be used since all mesh perturbation methods are influencing the periodic faces of the domain resulting in numerical errors.

CHAPTER V

Aerodynamic shape optimization results

RANS-based CFD simulations have shown highly accurate results for the NREL VI blade. However, no considerable optimization using CFD simulations has been achieved for wind turbine blades. In this chapter, various high-fidelity optimization results will be shown. The modified NREL VI blade is discretized by three computational domains that have different resolutions:

- Level 2: \pm 325 thousand volume cells
- Level 1: \pm 2.6 million volume cells
- Level 0: \pm 22 million volume cells

It is shown in Section 4.1.4 that the level 2 mesh will result in inaccurate results. However, its low computational cost makes it ideal to quickly obtain optimization results, i.e. it is a good verification tool for optimization purposes. For the level 2 mesh, various design variables are tested in order to find the proper optimization setup. Afterwards, the optimization setup is applied on the level 1 mesh from which a more accurate and consistent optimization result will be achieved. Since the level 0 mesh is too large for optimization purposes (too high computational cost), it is decided to project the optimized twist and shape variables on the level 0 mesh. Given the high accuracy provided by level 1 mesh, the same torque performance is expected for level 0 mesh. Furthermore, comparison will be made between the optimized modified NREL VI blade with the original NREL VI blade that has the same shape and twist perturbations of the optimization. Multipoint optimization will be performed over a range of wind speeds resulting in one optimized design.

5.1 Optimization with level 2 mesh

As a verification purpose, optimization with different design variables is performed on the level 2 mesh. Since the level 2 mesh is relatively small, it is expected that the computational cost of the optimization is low. Given the coarseness of the mesh, the CFD results of the optimization will not be accurate and consequently it will be difficult to draw a conclusion. However, some behaviors of the optimization can be extended to more accurate optimizations. In the following sections, the number of design variables will be steadily increased up to 496 design variables. It will be shown that constraints are necessary to obtain feasible solutions.

5.1.1 Pitch angle

As a first optimization, it is decided to start with the pitch angle as the only design variable. It is expected that the pitch angle will increase, resulting in a higher angle of attack, until maximum torque is achieved. Since torque is composed of drag and lift, the optimization will try to maximize the lift-to-drag ratio. Given that there is only one design variable, the optimality condition should be quickly satisfied. As shown in Fig. 5.1, only five optimization iterations were required to satisfy the optimality condition. This shows that gradient-based optimization is very quick in finding a maximum. The feasibility condition was not violated, indicating that the optimized design is realistic. An increase of 5.1% in torque is obtained by increasing the pitch angle by 5.14 degrees.

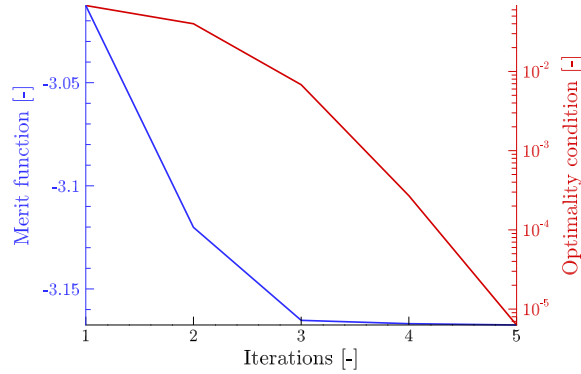


Figure 5.1: Optimization history with pitch angle as design variable

From Fig. 5.2, the magnitude of pressure distributions has increased after optimization resulting in higher loads and consequently torque. The largest increment of torque is located near the tip, which is expected since the largest power extraction of most modern wind turbine blades happens near the tip region. The largest difference of pressure can be found at upper part of the leading edge of the blade, while the pressure coefficient at trailing edge does not significantly change with respect to the baseline design. Also a larger region of negative pressure can be found at the upper surface of the blade at tip region, which shows that the optimizer is more sensitive towards the tip than the root for obtaining higher torque values. In Section 4.1.5, this behavior can be confirmed since the largest gradient values are located at tip region. A negative torque at the tip caused by tip loss effects compensate the optimized torque for a small part. Since the twist distribution has a solid rotation, it is proven that the optimization does only pitch the wind turbine blade. It is observed that when the pitch angle increases a little bit, flow separation occurs resulting in lower torque. This indicates that the optimization solution is high likely at a global maximum. Note that the optimized twist distribution is relative to the baseline distribution in which a decrease of twist angle results in a higher angle of attack (pitching up) and vice versa.

Optimizing the pitch angle results in a fairly good improvement of the performance of the NREL VI blade. The flow is fully attached at the blade and negative torque is observed due to tip loss effect or due to insufficient accuracy of the CFD simulation.

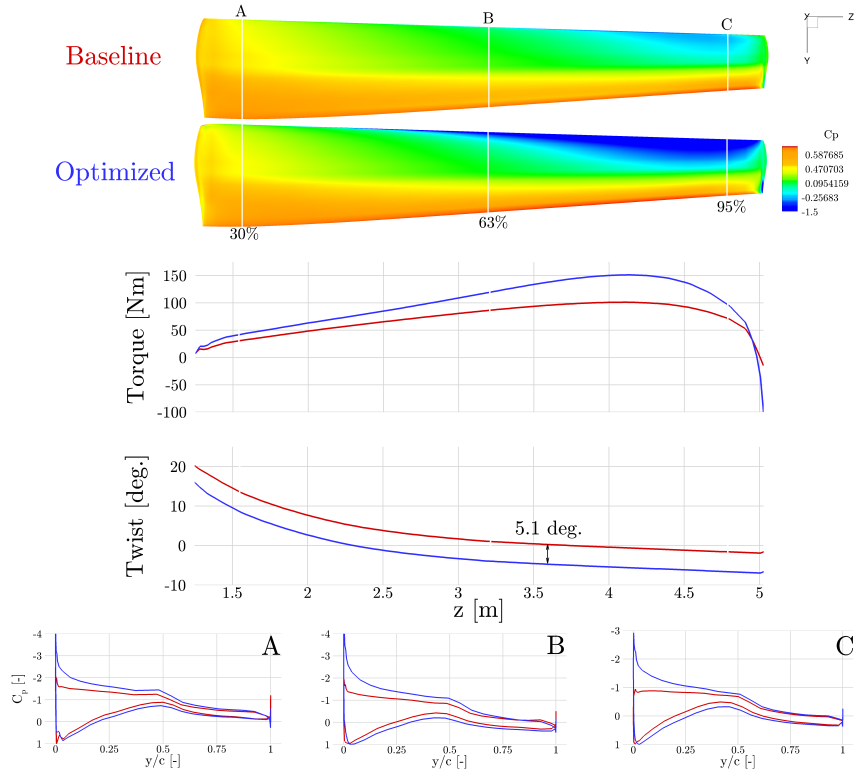


Figure 5.2: Pitch angle optimization of modified NREL VI blade

5.1.2 Twist variables

Instead of rotating the whole blade, segments of the blade are rotated by using eleven sections for each blade that are parametrized by FFD control points. In Fig. 5.3, the optimized twist distribution is shown to be non-smooth due to coarse distribution of twist variables or due to coarse surface mesh. This can be resolved by adding more FFD control points or by using a more refined computational domain. At tip region, the twist angle has a sudden reduction, which results in pitching down the tip of the blade even more than the baseline design. This can be explained by the fact that the optimizer tries to reduce the tip loss effect. However, it must be noted that the mesh is too coarse to resolve complex flow behavior at tip region implying that the twist distribution at the tip could be an incorrect behavior. When the optimizer tries to alleviate the negative torque at the tip, it has to sacrifice on the twist angle at other regions resulting in an increase of only 5.9% of the initial torque coefficient.

It is shown that optimizing the twist distribution of the NREL VI blade has a considerable effect on the performance of the NREL VI. However, caution should be taken on the accuracy of the optimization result, because the computational domain is very coarse resulting in incorrect flow phenomena. Some of these incorrect flow phenomena can be flow separation and three-dimensional effects such as tip loss effect.

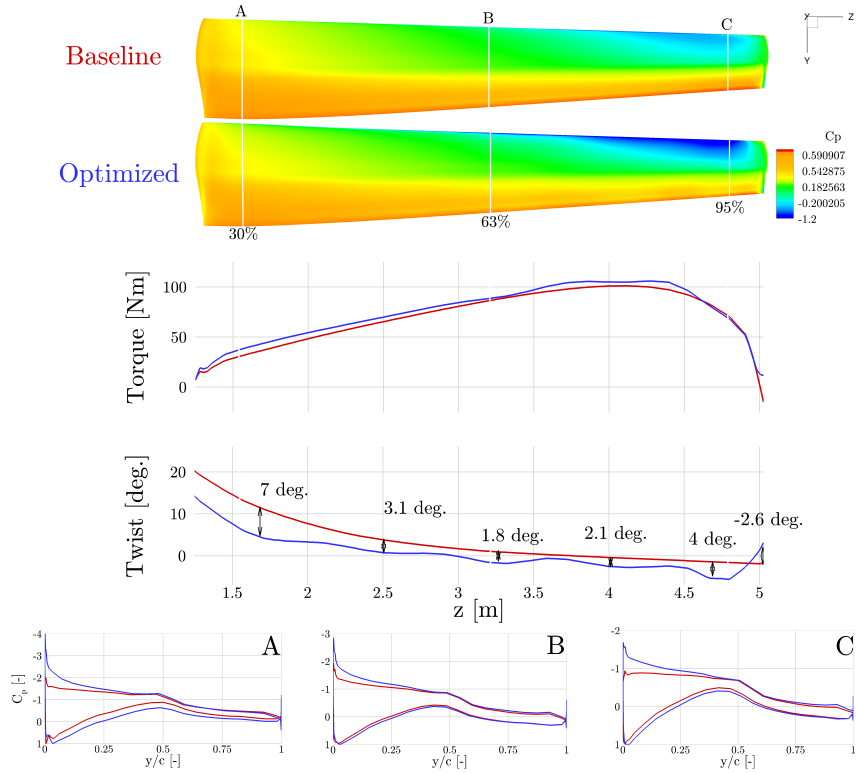


Figure 5.3: Twist distribution optimization of the modified NREL VI blade

5.1.3 Shape variables

Instead of using twist variables as design variables for optimization, 296 shape variables are employed. This increases the number of design variables considerably with respect to previous optimization problems resulting in large computational costs when using conventional gradient approximation techniques, such as finite difference or complex step. The shape variables are parametrized by the FFD box, discussed in Section 3.4. In the first optimization problem, only two constraints will be added. The thickness of leading and trailing edge cannot be reduced with respect to the initial thickness, since it is found that it reduces the mesh quality very quickly during the first optimization iterations. However, the thickness can increase by 300% with respect to the initial thickness. In Fig. 5.4, it is shown that the optimization reduces the thickness of the airfoil considerably, while more camber is obtained. This indicates that the optimizer is trying to maximize lift without taking a possible internal structure, such as a torque box, into account. As a result, very poor volume cells appear due to severe perturbations at the blade, which consequently results in an infeasible optimization result. Even though there is mesh failure, the optimization seems to result in a plausible correct design when only looking at the torque and twist distribution.

From Fig. 5.5, it is shown that some regions of the blade are inverted as such that some lower parts of the blade are considered to be upper parts and vice versa. Even though this is detrimental for the accuracy of the flow solution, SUMad and the optimization are able to continue with computing, which shows the robustness of the computational techniques.

Since the optimization result is considered to be infeasible, no thorough discussion on the result

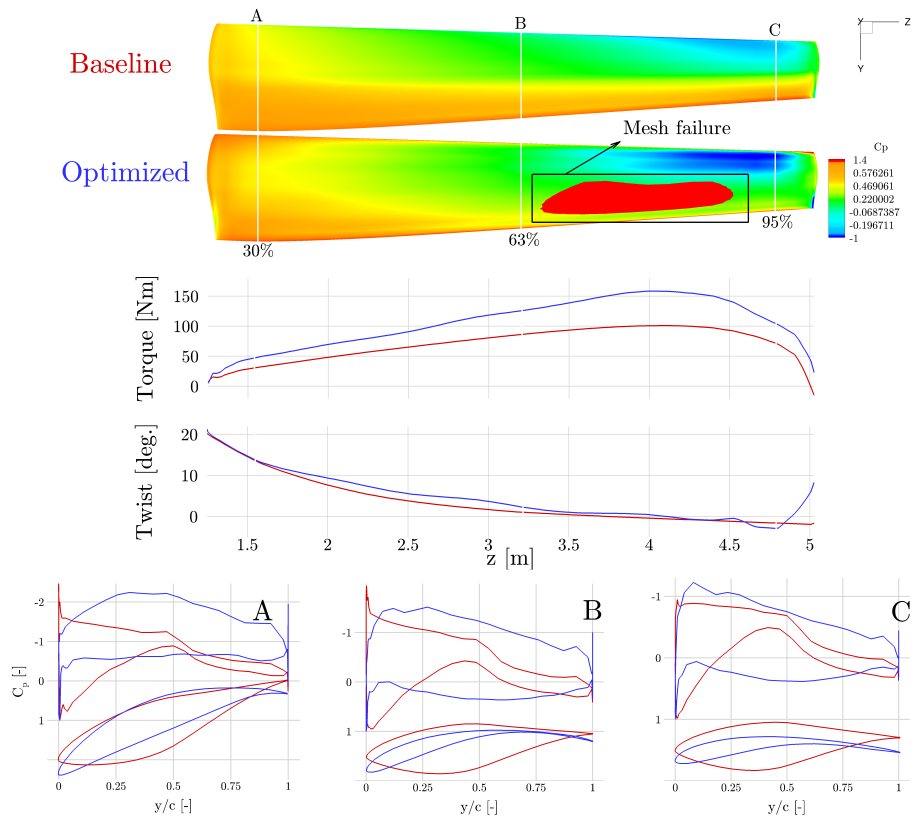


Figure 5.4: Level 2 optimization with shape variables of modified NREL VI blade

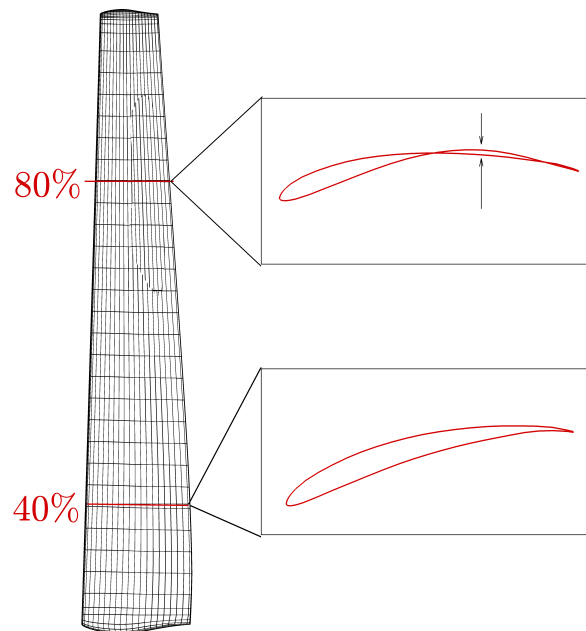


Figure 5.5: Mesh failure during optimization with shape variables

is presented. However, it is clear that the optimization is working as it should be, since it seems to camber the airfoil considerably for obtaining a higher lift. Another conclusion is that the optimization requires more constraints as such it can take a torque box into account and that it does not reduce the mesh quality. Therefore, it is decided to apply thickness constraints between 15% and 50% of the chord along the span of the NREL VI blade. The thickness constraints assure that the airfoil thicknesses cannot be reduced by its initial thickness and it can only increase 300% with respect to the initial thickness.

In Fig. 5.6, it is shown that additional thickness constraints result in a feasible optimization solution. The initial torque value is increased by 30.4%, where the largest increase can be found at tip region. The twist and torque distribution have still fluctuations due to severe coarsening of the mesh or FFD control points. The twist distribution at the tip region pitches up in order to reduce the plausible tip loss effect. However, as discussed before, this strange behavior in twist distribution can also be a result of a too coarse computational domain. The minimum pressure coefficient region of the blade has been shifted towards the tip at approximately 25% of the chord. Also the pressure difference between upper and lower part of the blade has been considerably increased. Furthermore, more cambering of the optimized airfoils is observed, especially at root region where higher cambering is necessary to obtain high loads at low relative velocity. The thickness of the upper part at leading edge of airfoils at mid and tip region have increased, while a reduction in thickness of the lower part at leading edge is observed.

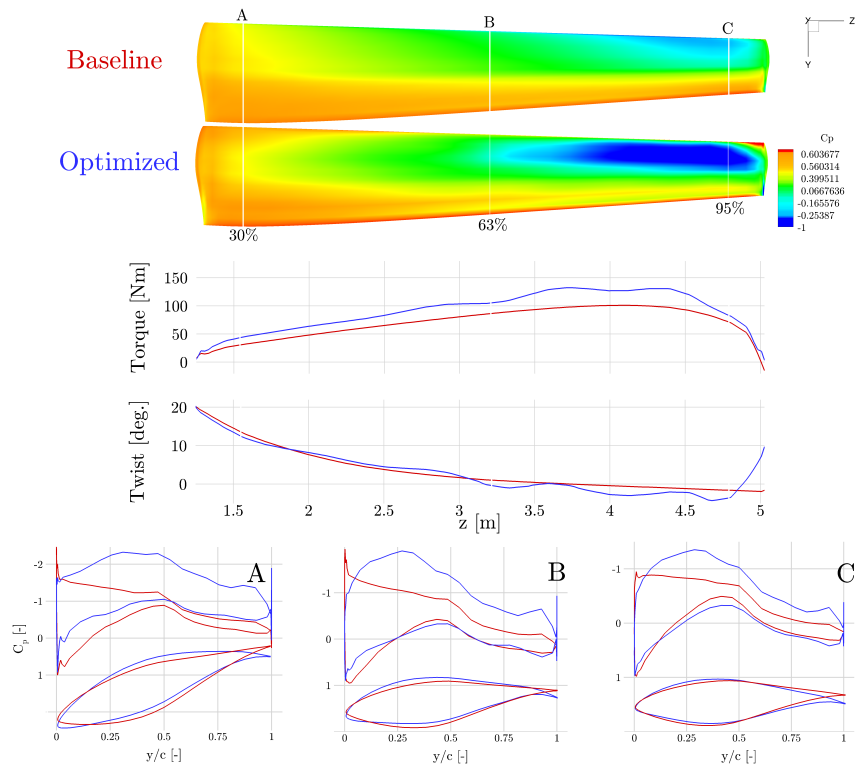


Figure 5.6: Level 2 optimization with shape variables and 100% thickness constraints of modified NREL VI blade

5.1.4 Shape and twist variables

It is shown in previous sections that shape or twist variables do not result in a smooth twist distribution. As a possible resort, both types of design variables can be combined. Since the thickness variables are required to have thickness constraints for assuring good mesh quality, it is decided to apply the same constraints as in the previous section. In Fig. 5.7, it is shown that the twist distribution is smoother than the previous ones. However, the strange twist distribution at tip region has not disappeared due to insufficient mesh resolution or due to tip loss effect. An increase of 31% in torque is achieved. Notice that there is only 0.8% difference compared to using only shape variables. This indicates that when only employing shape variables, the optimized twist distribution is already partially taken into account by these design variables.

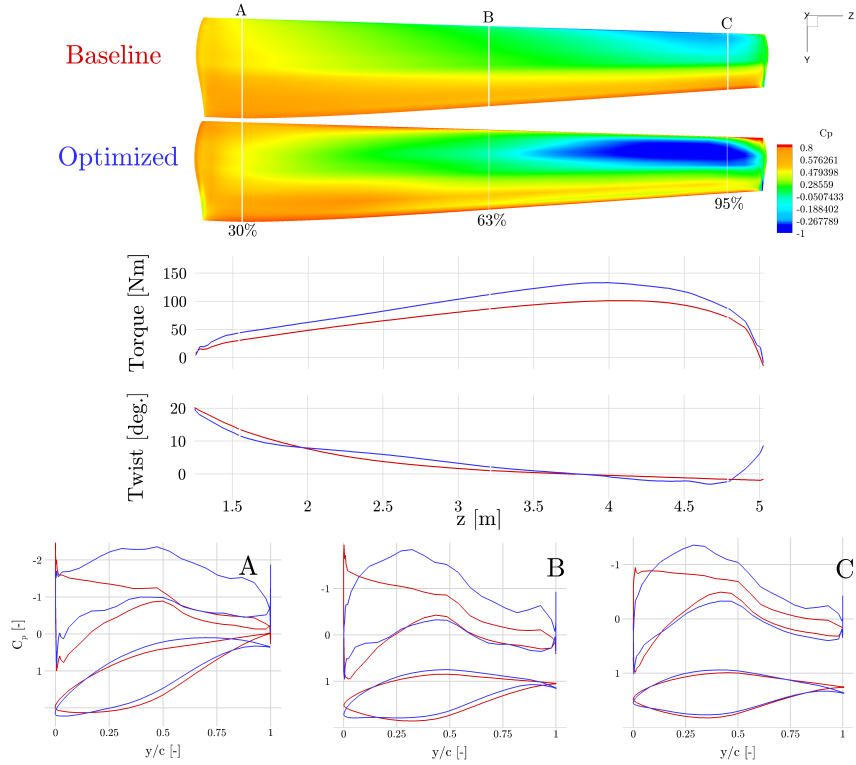


Figure 5.7: Level 2 optimization with shape and twist variables and 100% thickness constraints of modified NREL VI blade

Even though there are some fluctuations or mesh failures in the previous optimization results, all results tend to have the same behavior in optimizing torque: the highest increase in torque is found at tip region. In order to get smooth optimization results, the mesh resolution, number of FFD control points and/or a combination of design variables should be high enough. In the following sections, it will be shown that increasing the mesh resolution will alleviate the non-smooth representation of the twist distribution. This means that the number of FFD control points and the combination of design variables were adequate enough for the level 2 mesh.

5.2 Optimization with level 1 mesh

The following optimization results will be based on the level 1 mesh. In Section 5.1.4, the highest increase in torque was obtained. Therefore, it is decided to continue with the same optimization problem. It will be shown that the level 1 mesh achieves smooth optimization results indicating that the accuracy of the CFD simulation is essential for performing aerodynamic shape optimization.

5.2.1 Shape and twist variables with 100% thickness constraints

The same optimization procedure as in Section 5.1.4 is employed. In Fig. 5.8, it is shown that the fluctuations of the torque and twist distribution have disappeared. More importantly, the twist at the tip does not show a strange behavior compared to the previous sections. This means that the level 2 mesh is too coarse to represent complex flow phenomena at tip region resulting in inaccurate optimization results. Note that the optimization prefers to have more tip loss in order to achieve a larger torque value of the blade. The pressure coefficient distribution is smoother compared to the level 2 mesh. Also the area of the minimum pressure coefficient region at the tip has increased. An increase of 22.4% in torque with respect to the baseline level 1 mesh is achieved. This increase of torque is smaller compared to the level 2 mesh, which means that the level 2 optimization is unreliable due to the inaccuracy of the CFD simulation. As for the level 2 mesh, the optimized airfoils tend to be more cambered. And the thickness of the lower part of the leading edge of optimized airfoils at mid and tip region are reduced while the upper part at leading edge is increased. The trailing edge region of optimized airfoils at root region appears to become flaps in order to increase loads at low relative wind speeds.

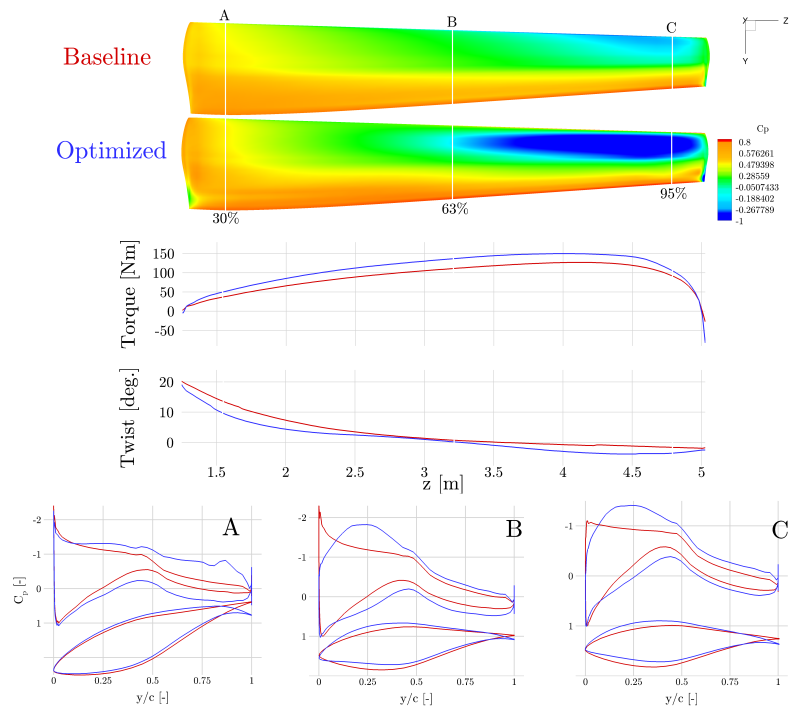


Figure 5.8: Level 1 optimization with shape and twist variables and 100% thickness constraints of modified NREL VI blade

5.2.2 Shape and twist variables with 75% thickness constraints

Instead of using 100% thickness constraint, 75% thickness constraints are applied on the blade in order to reduce 25% of the initial thickness between 15% and 50% of chord of the blade. Fig. 5.9 shows that the overall thickness of the optimized airfoils are reduced in order to achieve a higher lift. Notice that the pressure coefficient distribution between 15% and 50% of the chord at the lower part has increased considerably resulting in larger load and torque values. Therefore, a trade-off between aerodynamics and structures is necessary for obtaining a feasible and optimal design. Furthermore, the root and tip region of the blade are pitched even more down compared to the baseline design. An increase of 24.1% in torque is obtained.

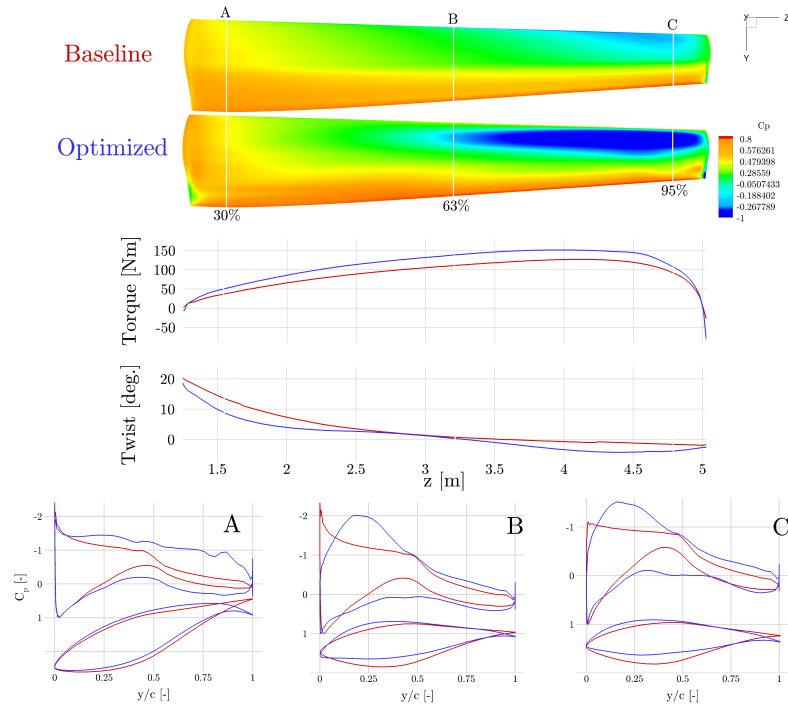


Figure 5.9: Level 1 optimization with shape and twist variables and 75% thickness constraints of modified NREL VI blade

5.2.3 Comparison between 75% and 100% thickness constraints

For obtaining a better understanding on how the optimization works, optimization results of the 75% and 100% thickness constraints were compared. It is shown that the 75% thickness constraint optimization results in a higher torque value than the 100% thickness constraint optimization: a difference of 1.7% is achieved. This is not a surprise, since it is shown in Section 5.1.3 that a higher torque can be obtained by reducing the thickness and increasing the camber of the original airfoil. In Fig. 5.10, both optimized airfoils are compared. It is clear that the sensitivity in increasing torque is higher at the lower part of the blade resulting in a flattening behavior at that region. As a consequence, the integrated area of the pressure distribution increases resulting in larger loads and moments. At root region, no significant difference is observed.

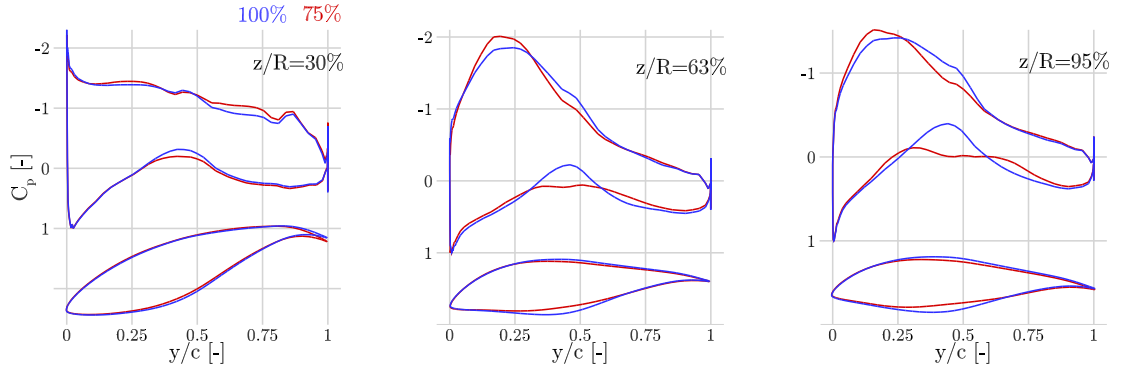


Figure 5.10: Pressure coefficient distribution comparison of 75% and 100% thickness constraint optimization

Given the optimized airfoil sections, the torque and twist distribution is compared in Fig. 5.11. The difference in torque can be mainly observed at tip region. The optimization design of the 75% thickness constraints is pitching up more than the optimal design of the 100% thickness constraints. Although at mid region, the optimal design of 100% thickness constraints is pitching more up than the 75% thickness constraint.

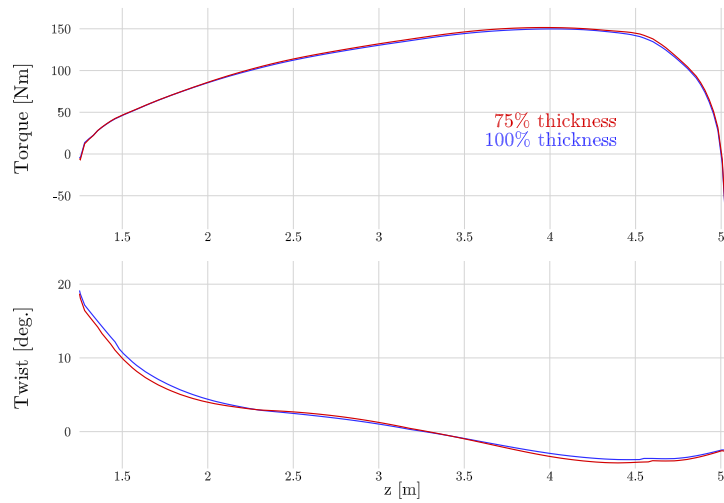


Figure 5.11: twist and torque distribution comparison of 75% and 100% thickness constraint optimization

5.2.4 Thrust consideration after optimization

As a side-effect of the above optimizations, the thrust of the optimized NREL VI blade increases significantly. It is shown in Fig. 5.12 that the largest increase is located at the tip region of the blade resulting in large bending moments. When considering aerostructural optimization, constraints on bending moments are necessary for preventing heavy and costly structures. In this research, no

bending moment constraints are used due to insufficient computational time. However, this requires further research, because it is expected that bending moment constraints will reduce the optimized torque considerably.

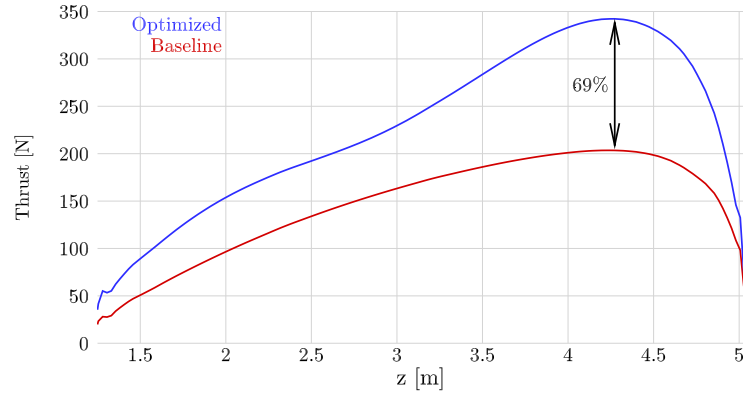


Figure 5.12: Significant thrust increase with 100% thickness constraint optimization with shape and twist design variables

5.3 Optimization with level 0 mesh

The level 0 mesh has approximately 22 million volume cells resulting in highly accurate CFD simulation results that are within the standard deviation of the experimental results (96% accurate with respect to averaged torque value). However, its computational cost is too high to perform optimization. Therefore, it is decided to project the level 1 mesh perturbations of the optimized airfoils and twist with 100% thickness constraints on the level 0 mesh. Since the level 1 mesh has already a high accuracy (86% accuracy with respect to averaged torque value), it is expected that no large differences would occur concerning the aerodynamic behavior of the blade when using the level 0 mesh. Although, given the increase in predicted torque for larger mesh resolutions and having smoother perturbations than the level 1 mesh, the increase in optimized torque should be higher when using the level 0 mesh.

5.3.1 CFD results with optimized level 1 mesh perturbations

Given that the twist and airfoil shapes are the same, it is decided to show only the pressure distribution of some sections of the blade. In Fig. 5.13, the pressure coefficient distributions are shown. It is clear that the pressure coefficient distributions are more smooth than the level 1 mesh. Also the pressure distribution at root region is better resolved in which the influence of the strong root vortex can be observed. An increase of 29.1% in torque is achieved, which is considerably higher than the optimized result of level 1 mesh. This can be explained by the fact that the tip and root vortices are better resolved and that components of torque, such as drag and lift, are predicted more accurately (see Section 4.1.4).

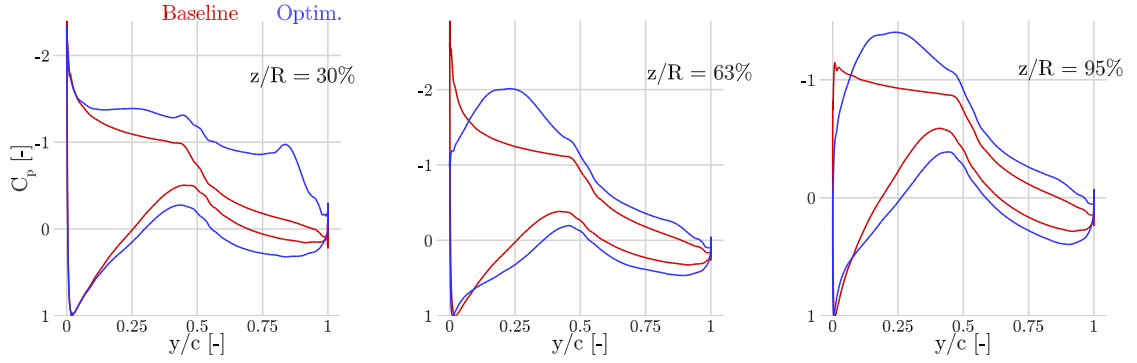


Figure 5.13: Level 0 mesh with design variables of level 1 of modified **NREL VI** blade

5.3.2 Comparison between modified and original **NREL VI** blade

In Section 4.2.3, it is shown that omitting the cylinder and transition part of the original **NREL VI** blade has a relatively small effect on the torque (2% to 5% difference at fully attached flow conditions) while maintaining steady residual convergence. Therefore, it is decided to use the modified blade for optimization purposes. As a second verification method, a comparison between the modified and original **NREL VI** blade with the optimized shape perturbations is performed. Previously mentioned, the increase in torque for the modified **NREL VI** blade is 29.1%. The original **NREL VI** blade, at the other hand, has an increase of 31.8% in torque. This small difference in optimized torque between the two blade designs can be explained by the slight differences in computational domains and different flow behavior at root region. Given the complexity in developing a similar mesh for the modified and original blade, it is not a surprise that there will be different discretization errors resulting in small differences in flow solutions. Shown in Fig. 5.14, small differences in pressure coefficients at mid and tip region can be assigned to these discretization errors.

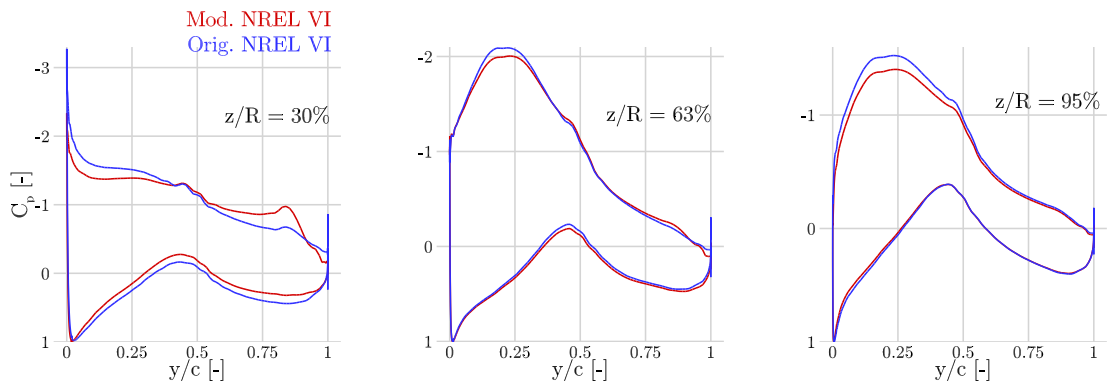


Figure 5.14: Pressure coefficient comparison of optimized **NREL VI** blade in modified and original configuration

Concerning different flow behavior at root region, comparisons between pressure coefficient distributions of the original and modified **NREL VI** blade are shown in Fig. 5.14. With the original **NREL VI** blade, the pressure coefficient distribution at root region are smoothen out due to influence

of the cylinder and transition part. Shown in Fig. 5.15, boundary layer material from the cylinder and transition part are radially transported towards the tip due to centrifugal forces (rotational effect). The flow separation at root region on the trailing edge is more pronounced for the original design than the modified blade, which can be a result of the previously mentioned rotational effect. Also it is noted that separated flow at tip region is flowing towards the root due to strong circulation at tip. Besides the rotational effect, the absence of the cylinder and transition part will result as well in a small reduction in torque.

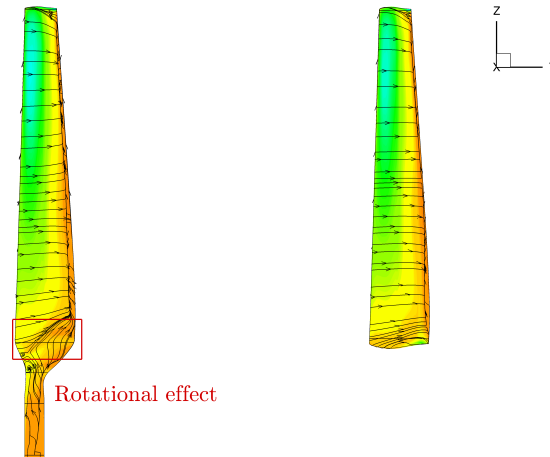


Figure 5.15: Surface streamline comparison of optimized original and modified [NREL VI](#) blade

It is concluded that the combination of using different computational domains and different designs results in a small discrepancy in torque. This small difference can be neglected, because the overall flow solution, except at root region, is approximately identical for the two blade designs. Therefore, it can be stated that optimization can be performed on wind turbine blades without using a transition part and cylinder.

5.4 Optimization convergence analysis of modified [NREL VI](#) blade

In previous optimization problems, various resolutions of computational domains are employed for reducing computational cost or increasing accuracy. However, no particular study has shown which proper amount of cells are required to obtain a relatively good trade-off between accuracy and computational cost. Therefore, It is decided to compare the optimization results of different mesh resolutions. The design variables are twist and shape variables with 100% thickness constraints. It is expected that the increment in torque due to optimization would increase with larger mesh resolutions, because from grid convergence study it is shown that the predicted torque increases with larger number of cells. Also larger mesh resolutions will result in smoother mesh perturbations resulting in higher torque values. However, it is shown in Table 5.1 that the largest increase in torque happens at the smallest mesh resolution. Afterwards it plunges to a 22.4% increase in torque and starts to build up again when a larger mesh resolution is used.

This strange behavior can be explained by the fact that [CFD](#) simulations are inaccurate for small mesh resolutions. Consequently, this translates to inaccurate optimization results. For the level 1

Table 5.1: Increase in torque for different mesh resolutions after optimization

	level 2	level 1	level 0
Increase in torque	31%	22.4%	29.1%

mesh size, at the other hand, the CFD simulation is accurate resulting in accurate optimization solutions which will have a consistent flow behavior when increasing the mesh resolution. This behavior is shown in Fig. 5.16. The level 2 mesh has a small number of surface cells leading to non-smooth optimized pressure coefficient distributions resulting in inaccurate torque values. Especially the leading edge at root region of the level 2 mesh has significant problems. Due to its small mesh size, the optimizer cannot take small flow effects into account, such as flow separation at trailing edge. The level 1 mesh leads to smooth and accurate pressure coefficient distributions resulting in accurate optimization. Notice that the level 0 mesh is not really optimized, but it does have consistent flow behavior with the level 1 mesh indicating that when optimization is performed on the level 0 mesh, the optimization solution would be consistent with the optimization solution of the level 1 mesh. In other words, it is expected that optimization with level 0 mesh will result in a slightly better optimized torque value than projecting the mesh perturbation on the level 0 mesh.

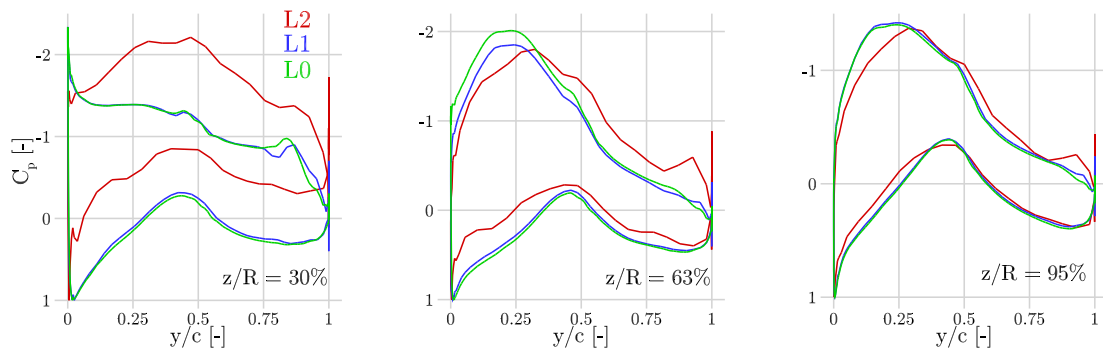


Figure 5.16: Optimization convergence analysis of modified NREL VI blade

It is concluded that the level 1 mesh is accurate for optimization purposes. It is shown that using coarse meshes are useful for preliminary optimization with as purpose to reduce computational time. Even though that the level 2 mesh exhibits inaccurate CFD results a similar optimization behavior associated with refined meshes can be obtained. Given the high accuracy of the optimization result of the level 1 mesh, it is suggested that optimization results of the level 0 mesh will not differ considerably with respect to results of the level 1 perturbations on the level 0 mesh. Note that this can only hold when the level 1 mesh has already a relatively good accuracy that can represent flow phenomena fairly well.

5.5 Multipoint optimization

In previous sections, the [NREL VI](#) blade is optimized for one free stream velocity. However, for most modern wind turbines, the power production happens between cut-in and rated wind speed. This means that a general optimization solution should be found for that region of wind speeds. In this case, the cut-in and rated wind speed for the [NREL VI](#) are considered to be 5 and 9 m/s respectively. It is shown in Section 4.2.2 that no or little flow separation happens at the [NREL VI](#) blade implying that accurate and consistent optimization can be performed in this wind speed region. The objective function is assumed to be an equal weighted average of the torque values at wind speeds from 5 up to 9 m/s with an increment of 1 m/s. The optimization problem will be performed with the level 1 mesh. And it will have shape and twist variables as design variables with 100% thickness constraints. As a reminder, the optimized design will be only one design for the whole velocity region.

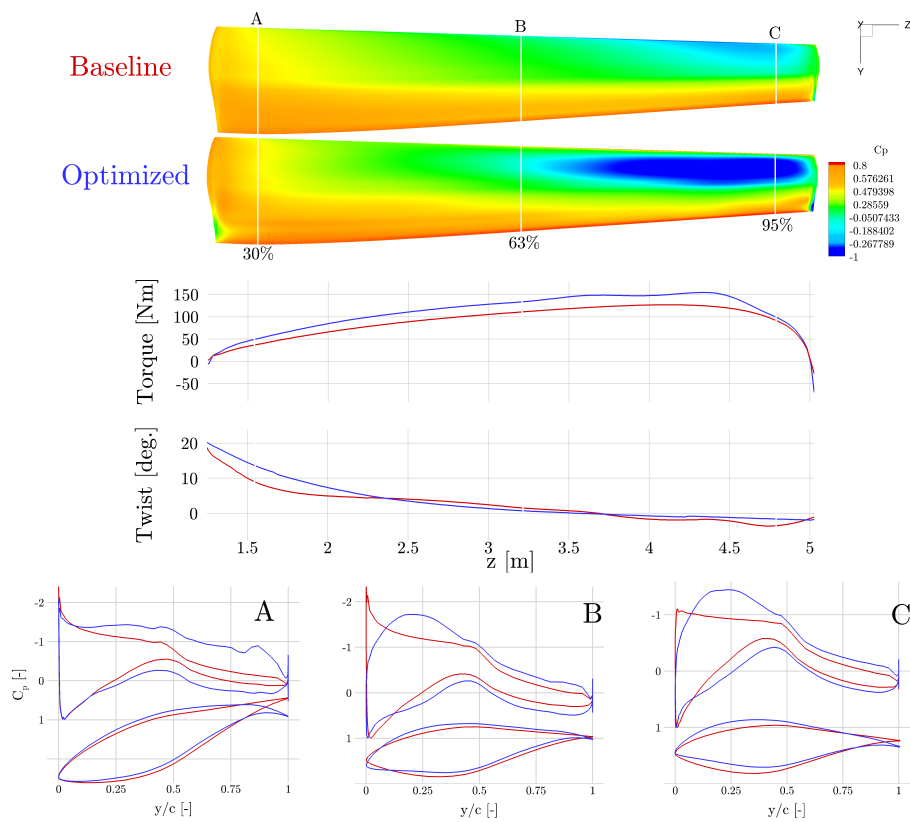


Figure 5.17: Multipoint optimization of modified [NREL VI](#) blade at 7 m/s

In Fig. 5.17, the multipoint optimization of the [NREL VI](#) blade is shown. It exhibits approximately the same behavior as for the single-point optimization at 7 m/s: the blade pitches up a little bit and the thickness at the lower part of airfoils reduces while it increases at the upper part of airfoils. More cambering of the blade is observed as well. The increase of torque values of each wind speed is shown in Fig. 5.18. No significant difference in the improvement of torque in the single-point and multipoint optimization at 7 m/s is observed. However, the other torques at different wind speeds have been improved considerably. It is noted that the improvements are approximately the

same.

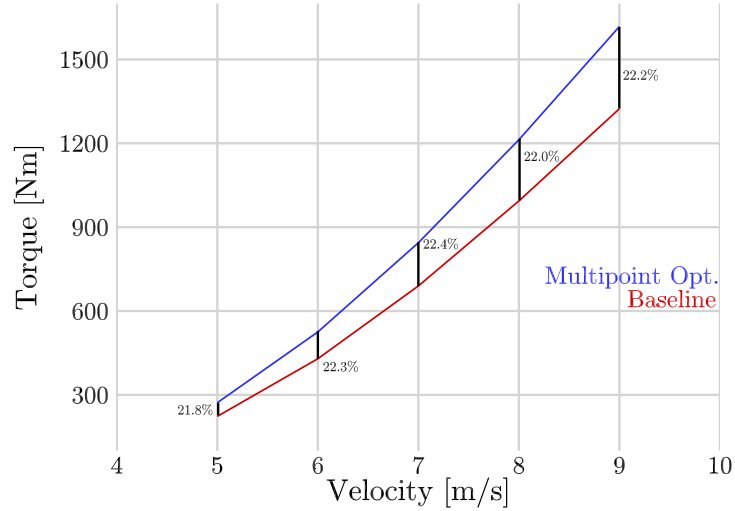


Figure 5.18: Comparison of torque curve between baseline and optimized modified NREL VI blade

Since the power curve from cut-in to rated wind speeds can be constructed, the AEP can be calculated. As an example, the AEP is calculated at the Dutch part of the North-Sea by using the Rayleigh probability density function with shape factor $k = 2$ and scale factor $c = 9.47$ [277]. The angular velocity is considered to be constant and equal to 7.5259 rad/s. The improvement of the AEP of the optimized NREL VI is 22.2%. Note that the AEP is only calculated from cut-in to rated wind speed.

As a comparison between the single-point and multipoint optimization, Fig. 5.19 shows the subtle differences between the two optimization methods at 7 m/s. It is clear that the multipoint optimization is pitching down the blade more compared to the single-point optimization. Along the blade, the multipoint optimized torque is slightly lower than the single-point optimized torque. In order to compensate this loss in torque, the multipoint optimization tries to change the twist distribution at tip region resulting in a small increase of torque. In general, the pressure coefficient distributions and airfoil shapes are approximately the same. A small increase in camber of the multipoint optimized airfoils is observed.

5.6 Discussion and conclusion

Various optimization results are presented with different design variables, constraints, and mesh resolutions. For all mesh resolutions, the optimization with twist and shape as design variables has shown the largest increase in torque. The level 2 mesh produces inaccurate optimization results, while the level 1 mesh yields accurate and consistent optimization designs that can be used for further analysis on more refined meshes. The level 1 optimization with shape and twist variables achieved an improvement of 22.4% in torque. When projecting the level 1 mesh perturbations on the level 0 mesh, a difference between the optimized torque of level 1 and level 0 mesh was 6.7%.

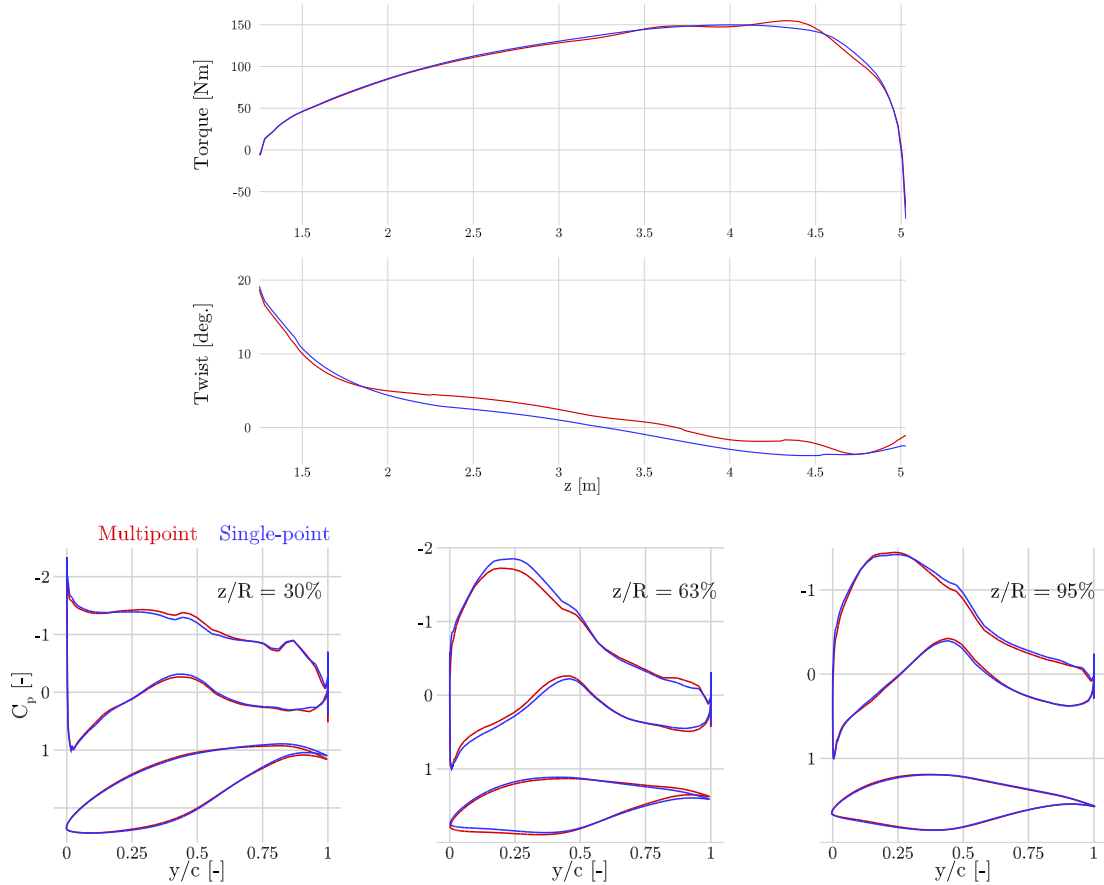


Figure 5.19: Comparison of multipoint and single-point optimization at 7 m/s

Even though this is a relatively high difference, the flow behavior was the same indicating that the possible optimization on the level 0 mesh would be close to the solution given by the perturbed level 0 mesh in Section 5.3.1. Flow separation at trailing edge appears on the optimized design, which can be explained by the fact that the optimal designs are close to maximum lift. As a second verification tool, the optimized design of the modified NREL VI blade is compared with the original NREL VI blade with the level 1 mesh perturbations. The difference in increase in torque of the two designs is 2.7% due to the presence of cylinder and transition part of the original NREL VI blade. Although, differences in the computational domain leading to different discretization errors can also contribute to this discrepancy.

Multipoint optimization has shown that a 22.2% of increase in AEP between 5 and 9 m/s can be obtained by using twist and shape variables. The multipoint optimized blade performs approximately the same for all wind speeds: an increase in torque of 22% is obtained. Comparing the multipoint optimization at 7 m/s with the single-point optimization has shown that there is not much difference in optimized airfoils (slightly cambering appears for the multipoint optimization). The twist distribution, on the other hand, is more pitched up for the single-point optimization than the multipoint optimization. The pitching down for the multipoint optimization is required to assure attached flow conditions for lower wind speeds. For all optimization results, the thrust

and, subsequently, bending moments are increased considerably. This is disadvantageous from the structural point of view, since it will increase the mass of the structure. Therefore, further research on constraining bending moments and thrust are recommended, and ultimately, aerostructural optimization will perform the adequate tradeoffs between aerodynamics and structures [246]. In Table 5.2, the increase in thrust of some relevant optimization results is presented.

Table 5.2: Increase in thrust of various optimization results

Optimization type	Max. thrust increase [-]
Level 2 mesh; Twist	16%
Level 2 mesh; Shape and twist	67%
Level 1 mesh; Shape and twist 100% thick. constr.	69%
Level 1 mesh; Shape and twist 75% thick. constr.	71%
Multipoint; Shape and twist at 7 m/s	59%

Furthermore, when combining twist and pitch for single-point optimization, the pitch variable seems to be redundant since the twist variable is taking the pitch into account. However, it is expected that when using multipoint optimization, the pitch variable will have different angles for each wind speed.

Every optimality condition using shape and twist design variables is not satisfied with a benchmark level of 10^{-6} due to the complexity of the design variables and the torque coefficient fluctuations at fourth decimal. When the optimizer increases the torque coefficient with small increments of approximately three orders of magnitude, the optimizer will terminate after numerical difficulties due to inconsistent optimal direction and step size. This problem can only be alleviated when the torque coefficient is converged more tightly. Note that all CFD simulations are converged with six orders of magnitude with respect to the residual of density. All optimizations are performed in parallel with 256 processors. In Table 5.3, the performance of several important optimizations is shown.

Table 5.3: Performance of high fidelity aerodynamic shape optimization of the NREL VI blade

Optimization type	Major iter. [-]	Optimality condition [-]	Computational time [s]
Level 2 mesh; Shape and twist	23	$10^{-1.89}$	5692
Level 1 mesh; Shape and twist	9	$10^{-1.94}$	29730
Multipoint; Shape and twist	15	$10^{-1.42}$	99905

CHAPTER VI

Final remarks

With the continuous upscaling of wind turbines, 10 to 20 MW machines are expected to appear in the market in the coming years [278, 279]. Therefore, it is important to adapt the existing tools and methods to enable the detailed design of such large machines. As a final remark of the dissertation, a conclusion is drawn on the aerodynamic shape optimization for rotating flow problems that is required for the design of future large wind turbines. The contributions of the author are listed and various recommendations are presented for future research purposes.

6.1 Conclusion

As a benchmark case, the high-fidelity aerodynamic shape optimization methodology is used to redesign the NREL VI wind turbine blade as presented in Chapter III. Prior to performing optimization, various modules of the optimization procedure are verified and the RANS-based CFD solver is validated using experimental results of the NREL VI sequence S blade. In Chapter IV, verification and validation are presented. All computational domains are verified for its mesh quality, its maximum y^+ value of 1, and conformity with respect to the correct CAD of the NREL VI wind turbine blade. After debugging the RANS-based CFD analysis, the computations are proven to be 96% accurate for attached flow conditions. The residual of the density stagnated for all cases, due to flow separation at the cylinder and transition part. As a consequence, the adjoint vector will not converge, which means that performing gradient-based optimization is not possible. In order to circumvent this problem, the cylinder and transition part of the NREL VI wind turbine is deleted. This design is also known as the modified NREL VI wind turbine blade. The flow solution at root section of the original wind turbine blade has discrepancies compared to computational results, since flow separation at cylinder and transition part of the wind turbine blade influences the accuracy of the numerical result. The largest discrepancy for both wind turbine blades for the velocity region between 5 m/s and 25 m/s is found at 10 m/s where the transition of attached and separated flow conditions occurs. This discrepancy is due to insufficient turbulence and transition modeling. For fully attached flows, the torque, thrust, and pressure distributions of both wind turbine designs are approximately identical and correct. This implies that using the modified NREL VI for optimization is a good representation of the original NREL VI wind turbine blade design. Further analysis is performed on the effect of the one-equation SA and two-equation Menter's SST turbulence model. It is shown that the SA turbulence model overestimates and delays flow separation. The Menter's SST turbulence model has the same behavior, although, in a lesser extent. Periodic boundary conditions

are employed for obtaining better mesh resolution with approximately the same computational cost of the full computational domain. Flow solutions using periodic boundary conditions show similar behavior as in the full mesh configuration.

The flow analysis of the [NREL VI](#) wind turbine has shown that the modified [NREL VI](#) blade results in approximately identical load conditions for attached flow conditions with respect to the original design. With converging residuals of density, the modified [NREL VI](#) wind turbine blade can be used in attached flow conditions for aerodynamic shape optimization purposes. In [Chapter V](#), single-point and multipoint optimization results are presented. The single-point optimization focusses on one wind speed (7 m/s), while the multipoint optimization takes a range of wind speeds into account. Three levels of mesh refinements are employed: coarse, medium refined, and fine mesh. The first level is a coarse mesh that is used for verifying the gradient-based optimization method. When using shape and twist design variables, the twist and torque distribution are smoothen out. When not using thickness constraints, the thickness of the blade is significantly reduced and cambered until mesh failure happens. The significant reduction of thickness makes the optimal design infeasible for practical applications. Given the mesh failure and the infeasibility, it is decided to use thickness constraints for all following optimization results. For the medium level of mesh resolution, an increase of 22.4% of torque for single-point optimization is obtained when using 100% thickness constraints. When 25% of reduction in thickness is allowed, an increase of 24.1% of torque is achieved. The shape of the optimized airfoils sections for both thickness constraints has showed more cambering and the nose is more pronounced towards the inflow. Instead of having high suction peaks at the leading edge, a smoother pressure distribution is obtained. At root region, the trailing edge of the airfoil behaves like a flap in order to gain more loads at low relative velocity. For the fine mesh, the shape and twist design variables of the medium refined mesh are projected on the fine mesh, because the computational cost would otherwise be too high. The same flow behavior as in the medium refined mesh is achieved with an increase of 29.1% in torque. The difference in increase of the medium refined and fine mesh is due to the asymptotic increase in torque when refining the mesh. The shape and twist design variables are as well projected on the original [NREL VI](#) wind turbine blade for quantifying the influence of the cylinder and transition part of the original [NREL VI](#) wind turbine blade. It is shown that there is no significant torque difference between the two designs. The flow behavior at root region is between the modified and original design, because flow separation at cylinder and transition part influences the root region due to rotational effect. For all optimization results, the rotor thrust increases significantly, which is disadvantageous when considering internal structures and cost. The computational cost is mainly dependent on the size of the mesh, it is shown that performing high-fidelity aerodynamic shape optimization requires on average 2114 [CPU](#) hours. It is advisable to parallelize the framework in order to reduce the computational time significantly.

Wind turbines are performing in a range of wind speeds. Therefore, a multipoint optimization from cut-in to rated wind speed with an equally weighted averaged torque coefficient is performed. The increase in torque for every wind speed for the optimized design is approximately 22%. When considering the Annual Energy Production ([AEP](#)) at the coast of the Netherlands, a 22.2% of increase is obtained. The shape of the optimal design is comparable with the single-point optimization. Small differences between single-point and multipoint optimized airfoil shapes can be found.

Given the above results, it is suggested that high-fidelity aerodynamic shape optimization de-

veloped in this dissertation can be a useful design tool for rotational flow problems, such as wind turbines and helicopters. For future research, this tool can be extended to aerostructural and aeroelasticity optimization, as already done for aircraft wind design [246, 245]. The optimization procedure is mainly made possible by using a large-scale sequential quadratic programming optimizer and tackling total derivatives of hundreds of design variables efficiently using the adjoint method. This numerical optimization certainly offers a new tool to help designers finding the best possible design.

6.2 Contributions

The optimization methodology represents the current state-of-the-art gradient-based high-fidelity aerodynamic shape optimization for rotating flow problems. The main contributions of this work are listed below:

1. An efficient and robust high-fidelity aerodynamic shape optimization methodology is developed for rotating flow problems. The optimization method is a gradient-based technique based on the [RANS](#) equations with a discrete adjoint method.
2. [SUMad](#) is debugged for performing analysis on rotating flow problems. Analysis can also be performed on periodic boundary conditions. Fortran codes are wrapped in Python code for communication purposes in the optimization procedure.
3. Turkel's low speed preconditioner is developed for obtaining a higher rate of convergence at low speed flow conditions for the density-based [CFD](#) solver [SUMad](#).
4. Verification is performed on total derivatives of the adjoint method by using complex step and finite difference method.
5. Convergence analysis of [RANS](#)-based [CFD](#) analysis and optimization method is performed.
6. [RANS](#)-based [CFD](#) solver [SUMad](#) is validated by comparing computational results with [NREL](#) VI sequence S experimental results. Torque, thrust, and pressure distributions are employed for validation. It is shown that [SUMad](#) is capable of accurately representing attached flow conditions.
7. [RANS](#)-based aerodynamic shape optimization of the [NREL](#) VI wind turbine blade is performed. The effects of shape, twist, pitch design variables, and single versus multipoint formulation were quantified and discussed. The contribution of not using a cylindrical connection part of the [NREL](#) VI part is presented.

6.3 Recommendations

This work raised additional research questions that can improve the optimization methodology. This would eventually lead to better designs for wind turbines and helicopters. A list of possible recommendations are presented below:

1. The mesh perturbations are currently incompatible with periodic boundary conditions, since it will perturb periodic faces resulting in nonidentical mirrored volume cells at the faces inducing

significant numerical errors. When resolving this issue, a more refined mesh can be used with approximately the same computational cost of the same optimization for a higher accuracy.

2. Currently, the discrete adjoint method is only able to obtain total derivatives when using the SA turbulence model. However, the automatic difference adjoint is not limited to one turbulence model and thus additional turbulence models can be implemented easily. This would be beneficial to analyze the effect of turbulence models on optimization results, but also the accuracy for designs, that exhibit flow separation, would increase significantly when using better turbulence models, such as two-equation turbulence models.
3. Given the intrinsic unsteadiness of the flow at the cylindrical part of the NREL VI blade, no steady-state adjoint solutions can be obtained. In order to circumvent this problem, the adjoint method can be extended to the time domain. For further information, see following references [280, 281]. This would not only be beneficial for root optimization at wind turbine blades, but also other unsteady aerodynamic shape optimization problems can be executed, such as flapping wings, noise, yaw flow, etc. Ultimately, high-fidelity aeroelasticity optimization would obtain an important role in some of the engineering applications, such as wind turbines and helicopters.
4. Further improvements on the problem statement of the optimization can be made. Instead of only focussing on maximizing torque without aerodynamic constraints, bending moments and thrust constraints can be added for establishing a more realistic optimization design. In some of the optimization results, flow separation at the trailing edge appeared. This is disadvantageous for controlling the wind turbine blade. Flow separation constraints can circumvent this problem by stating that no separation can occur on the optimal design. For further interest, the objective function can be changed to minimizing the bending moments or thrust while maintaining the initial torque value. In order to take discrepancies between numerical representation and reality into account, uncertainty quantification methods can be applied on the optimization method. These discrepancies can include numerical approximations and manufacturing tolerances.
5. When performing multipoint optimization, the pitch angle and angular velocity can be employed as design variables for each wind speed. The pitch angle would mainly resolve the issue of having flow separation, since the blade can always be aligned with the inflow. When the angular velocity of the rotor varies for each wind speed, the torque cannot be used as an objective function. Therefore, it is suggested to consider the power coefficient as objective function. Furthermore, the weight factors of the weighted averaged objective function should be dependent on the distribution frequency of the velocity at a certain location.
6. The NREL VI blade is an outdated wind turbine blade. It is suggested to use a more modern wind turbine, such as the DTU 10-MW reference wind turbine [282], to benchmark optimization results. The NREL VI blade is merely used for its large number of high qualitative experimental results.
7. The aerodynamic shape optimization methodology for rotating flow problems can be extended to aerostructural optimization. The problem statement can be extended to maximizing torque

while keeping the blade mass constant. For financial purposes, the cost of material can be used as an objective function or constraint.

8. Instead of only applying this optimization methodology on wind turbine rotors, it can also be used for other rotating flow problems such as helicopter rotors, propellers, turbines, ventilators, etc. Note that the [CFD](#) tool is a density based solver, which should not cause any difficulties for solving compressible flow problems.

APPENDICES

APPENDIX A

NREL VI wind turbine blade computations with SU2

In this appendix, a brief overview of RANS-based CFD results obtained by SU2 are presented. SU2 is an unstructured, density-based, open-source solver that is capable of solving a range of different flow problems, such as potential flow, electrodynamics, chemically reacting flows, and many others [283]. SU2 has the capability of performing aerodynamic shape optimization and thus the solver is considered to be a possible candidate for performing optimization on wind turbine blades. However, the reason for not choosing SU2 for aerodynamic shape optimization is its high computational cost compared to SUMad.

A.1 Unstructured computational domain

The mesh of the NREL VI blade with blunt trailing edge is developed using the mesh software Pointwise. An unstructured surface mesh is developed for obtaining a volume mesh that is marched out by an anisotropic tetrahedral algorithm called T-rex. The surface mesh is shown in Fig. A.1. The volume mesh is a hybrid mesh that contains approximately 7.8 million volume cells (tetrahedra, prisms, and pyramids cells).

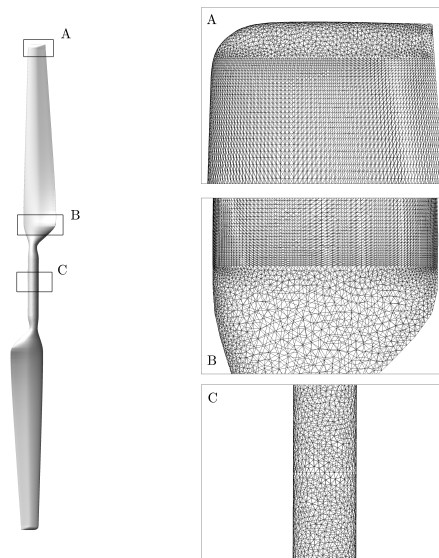


Figure A.1: Unstructured surface mesh of NREL VI wind turbine blade

In Fig. A.2, a section of the hybrid mesh at a radius of 3 m is shown. First, the boundary layer is resolved by marching out the surface mesh with high-aspect ratio tetrahedra that can be processed to a stack of prisms. Once the boundary layer is resolved, other geometrical figures are used for the far field.

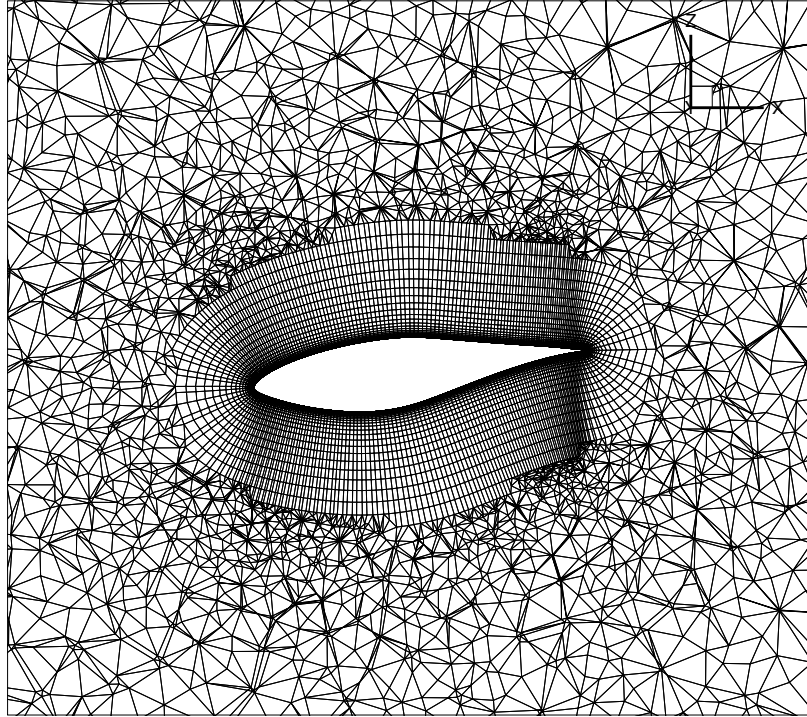


Figure A.2: Unstructured volume mesh of NREL VI wind turbine blade

A.2 Convergence analysis

As in SUMad, the residual of density of SU2 stagnates due to intrinsic flow behavior at the root of the NREL VI rotor. In Fig. A.3, the stagnation of the residual of density is observed, while the torque converges towards one value. This behavior is considered to be similar as SUMad.

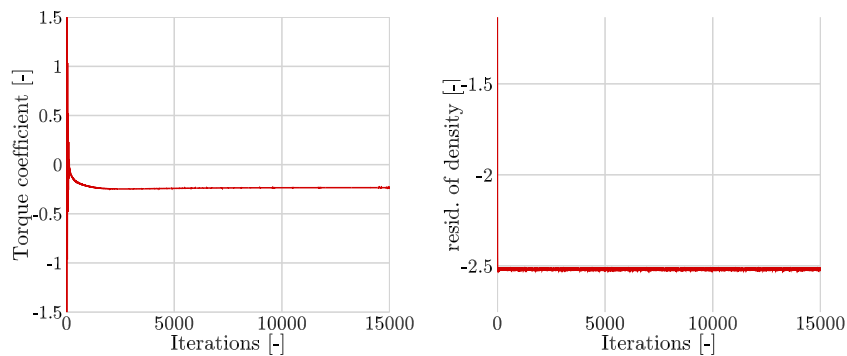


Figure A.3: Convergence analysis of SU2 for NREL VI wind turbine blade

A.3 SU2 analysis results

When setting up the rotating flow problem discussed in Section 3.1 in SU2 using SA turbulence model, various flow problems can be solved according to the free-stream velocity. For brevity, only two flow problems will be shown: attached and unattached flow conditions. In Fig. A.5, the pressure distribution at 7 m/s is shown. As expected, the computational results approximately agree with the attached flow conditions. However, compared to SUMad and experimental results, the pressure distribution along the trailing edge deviates. A considerable negative pressure peak can be observed at the blunt trailing edge of the NREL VI blade. Even though the flow is considered to be incompressible, the density-based solver SU2 has a higher peak than a $C_p = 1$. This phenomenon is also observed for SUMad at $z/R = 30\%$, but does not propagate along the span. At the lower side of the blade along the trailing edge, some pressure coefficient fluctuations are observed. This can be an artifact of the unstructured mesh in which the pressure cannot be smoothly interpolated. In general, SU2 overestimates the pressure coefficient compared to the experimental results. Note that the same spatial discretization and pseudo-time stepping method is used in SUMad.

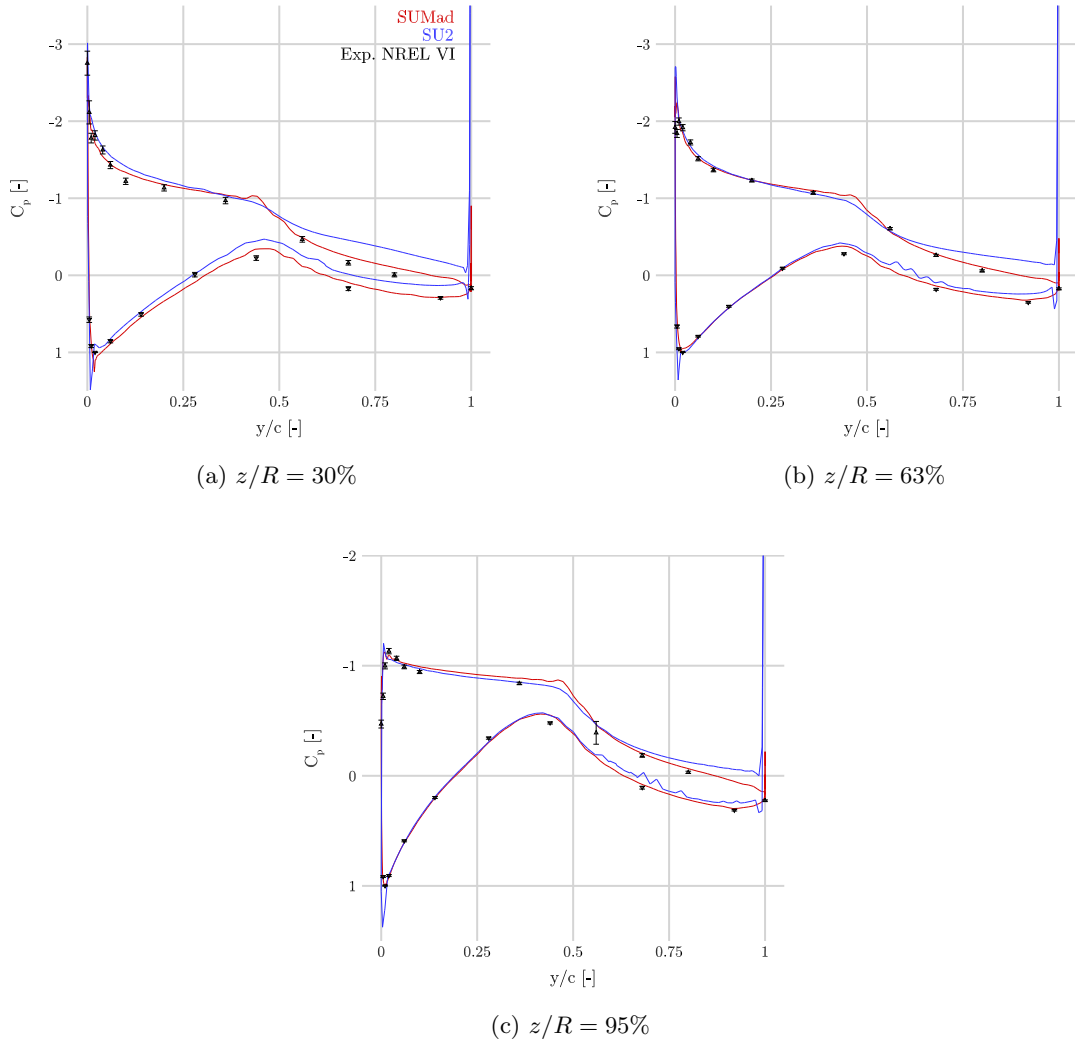


Figure A.4: C_p distributions at $U_\infty = 7$ m/s

For unattached flow conditions, both CFD solvers have problems with accurately representing

flow conditions. At root section of the NREL VI wind turbine blade, **SU2** has a strange bump around $y/c = 0.25$, which definitely will influence the performance of the wind turbine blade. On the other hand, **SU2** seems to predict flow separation accurately at the mid section of the wind turbine blade. At tip region, **SU2** is incorrect with predicting attached flow conditions. Again along the trailing edge at lower part of the blade, there are some pressure fluctuations.

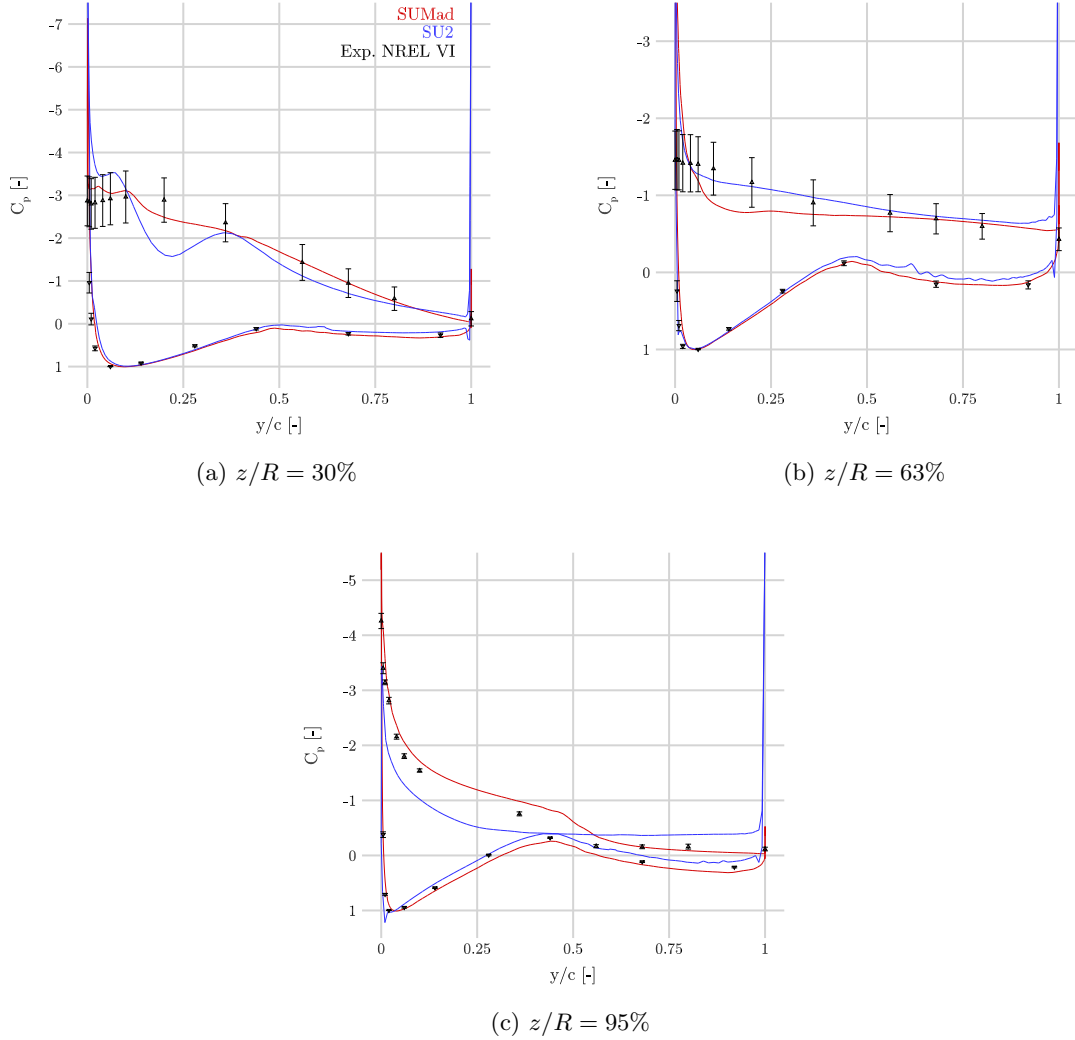


Figure A.5: C_p distributions at $U_\infty = 13$ m/s

Based on the above results, it is concluded that **SUMad** results in more accurate flow solutions than **SU2**. It is shown that **SU2** estimates the pressure coefficient at trailing edge for attached flow conditions too negatively. For separated flow conditions, **SU2** can have correct flow solutions at certain locations, but its inconsistent distinction in attached and separated flow conditions is considered to be disadvantageous when performing optimization.

A.4 Computational cost

In order to perform efficient gradient-based optimization, the computational time of the analysis model should be kept low. Therefore, a comparison between the computational time of **SUMad** and **SU2** is performed. With using approximately the same mesh size and set-up, a fully attached flow

condition of the NREL VI blade (7 m/s) is computed with both solvers. In table A.1, SUMad is approximately ten times faster than SU2. Clearly, it is advisable to use SUMad for aerodynamic shape optimization purposes.

Table A.1: Computational time of SUMad and SU2 at attached flow conditions for NREL VI blade

Solver	CPU hours
SU2	±29
SUMad	±3.2

A.5 Discussion and conclusion

Despite its ease in mesh generation for SU2, the accuracy and computational cost are disadvantageous for performing high-fidelity aerodynamic shape optimization. For fully attached flows, SU2 seems to estimate the pressure coefficient along trailing edge too negatively. This might be due to incorrect meshing, insufficient numbers of volume cells or insufficient turbulence modeling. For separated flow conditions, both SU2 and SUMad are inaccurate in approximating pressure coefficients of blade section. Concerning computational cost, SUMad is approximately ten times faster than SU2. As conclusion, SUMad would be the best choice in performing high-fidelity aerodynamic shape optimization.

APPENDIX B

Additional SUMad results and optimization

In this appendix, additional results are presented for clarification purposes.

B.1 Thrust Comparison between RANS-based CFD solvers

The thrust comparison between CFD solvers is shown in Fig. B.1.

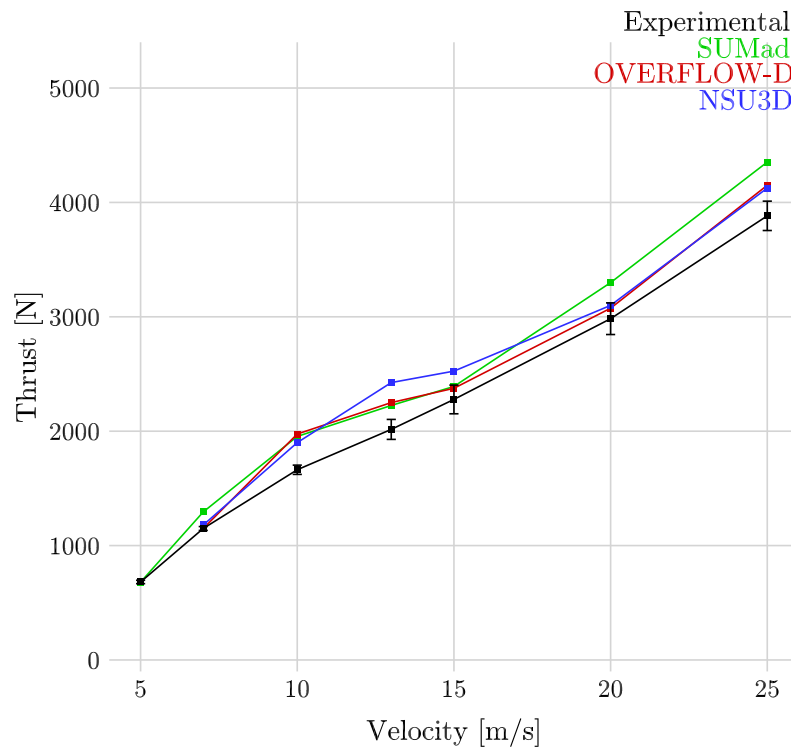


Figure B.1: Thrust comparison of various RANS-based CFD solvers

B.2 Flow separation behavior of the modified NREL VI blade

The flow separation of the modified NREL VI blade is considered to be similar as the original NREL VI blade. This is shown in Fig. B.2.

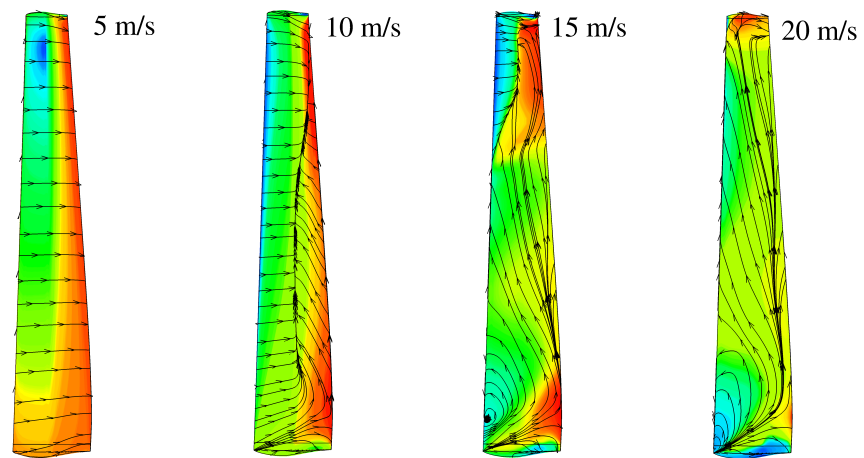


Figure B.2: Flow separation behavior of the modified NREL VI

BIBLIOGRAPHY

BIBLIOGRAPHY

- [1] Wengenmayr, R. and Bührke, T., *Renewable energy: Sustainable energy concepts for the future*, John Wiley & Sons, 2011.
- [2] Ashuri, T., van Bussel, G. J. W., and Mieras, S., “Development and validation of a computational model for design analysis of a novel marine turbine,” *Wind Energy*, Vol. 16, No. 1, 2013, pp. 77–90. doi:10.1002/we.530.
- [3] Kaldellis, J. K. and Zafirakis, D., “The wind energy (r) evolution: A short review of a long history,” *Renewable Energy*, Vol. 36, No. 7, 2011, pp. 1887–1901.
- [4] Ashuri, T. and Zaaijer, M. B., “Review of design concepts, methods and considerations of offshore wind turbines,” *European Offshore Wind conference and exhibition, Berlin, Germany*, European Wind Energy Association, 2007, pp. 1–10.
- [5] Ashuri, T. and Zaaijer, M. B., “The future of offshore wind turbines,” *3rd PhD seminar on wind energy in Europe, Pamplona, Spain*, European Academy of Wind Energy, 2007.
- [6] Ashuri, T. and Zaaijer, M. B., “Size effect on wind turbine blade’s design drivers,” *The proceedings of the European Wind Energy Conference and exhibition, Brussels, Belgium*, European Wind Energy Association, 2008, pp. 1–6.
- [7] Ashuri, T., Michiel B., Z., Joquaim R. R. A., M., and Jie, Z., “Multidisciplinary Design Optimization of Large Wind Turbines – Technical, Economic, and Design Challenges,” *Energy Conversion and Management*, Vol. 123, 2016, pp. 56–70. doi:10.1016/j.enconman.2016.06.004.
- [8] Ashuri, T., *Beyond Classical Upscaling: Integrated Aeroservoelastic Design and Optimization of Large Offshore Wind Turbines*, Ph.D. thesis, Delft University of Technology, the Netherlands, 2012.
- [9] Chehouri, A., Younes, R., Ilinca, A., and Perron, J., “Review of performance optimization techniques applied to wind turbines,” *Applied Energy*, Vol. 142, 2015, pp. 361–388.
- [10] Ning, S. A., Damiani, R., and Moriarty, P. J., “Objectives and constraints for wind turbine optimization,” *Journal of Solar Energy Engineering*, Vol. 136, No. 4, 2014, pp. 1–12.
- [11] Lyu, Z., Xu, Z., and Martins, J. R. R. A., “Benchmarking optimization algorithms for wing aerodynamic design optimization,” *8th International Conference on Computational Fluid Dynamics (ICCFD8)*, 2014, pp. 1–18.
- [12] Ashuri, T., Rotea, M., Xiao, Y., Li, Y., and Ponnurangam, C. V., “Wind Turbine Performance Decline and its Mitigation via Extremum Seeking Controls,” *AIAA Science and Technology Forum and Exposition (SciTech), Wind Energy Symposium, San Diego, California*, American Institute of Aeronautics and Astronautics, 2016, pp. 1–11.
- [13] Sørensen, N. N. and Madsen, H. A., “Modelling of transient wind turbine loads during pitch motion,” *European Wind Energy Conference*, European Wind Energy Association, 2006.

- [14] Van der Meulen, M. B., Ashuri, T., van Bussel, G. J. W., and Molenaar, D. P., “Influence of nonlinear irregular waves on the fatigue loads of an offshore wind turbine,” *The Science of Making Torque from Wind, Oldenburg, Germany*, European Academy of Wind Energy, 2012, pp. 1–10.
- [15] Ashuri, T., Zhang, T., Qian, D., and Rotea, M., “Uncertainty Quantification of the Levelized Cost of Energy for the 20MW Research Wind Turbine Model,” *AIAA Science and Technology Forum and Exposition (SciTech), Wind Energy Symposium, San Diego, California*, American Institute of Aeronautics and Astronautics., 2016, p. 1998.
- [16] Rankine, W. J. M., *On the mechanical principles of the action of propellers*, Transactions of the Institution of Naval Architects, 1865.
- [17] Froude, R. E., “On the part played in propulsion by differences of fluid pressure,” *Transactions of the Institute of Naval Architects*, Vol. 30, 1889, pp. 390–405.
- [18] Betz, A., “Das maximum der theoretisch möglichen ausnützung des windes durch windmotoren,” *Zeitschrift für das gesamte Turbinenwesen*, Vol. 26, No. 307-309, 1920, pp. 8.
- [19] Lanchester, F. W., “A contribution to the theory of propulsion and the screw propeller,” *Journal of the American Society for Naval Engineers*, Vol. 27, No. 2, 1915, pp. 509–510.
- [20] Joukowski, N. E., “Windmill of the NEJ type,” *Transactions of the Central Institute of Aerohydrodynamics of Moscow*, 1920.
- [21] van Kuik, G. A. M., “The Lanchester–Betz–Joukowski limit,” *Wind Energy*, Vol. 10, No. 3, 2007, pp. 289–291.
- [22] Stoddard, F. S., “Momentum theory and flow states for windmills,” *Wind Technology Journal*, Vol. 1, 1978, pp. 3–9.
- [23] Eggleston, D. M. and Stoddard, F., *Wind turbine engineering design*, Van Nostrand Reinhold Co. Inc., New York, NY, 1987.
- [24] Gessow, A., *Flight Investigation of Effects of Rotor-blade Twist on Helicopter Performance in the High-speed and Vertical-autorotative-descent Conditions* gessow1948flight, National Advisory Committee for Aeronautics, 1948.
- [25] Buhl, M. L., *A new empirical relationship between thrust coefficient and induction factor for the turbulent windmill state*, National Renewable Energy Laboratory, 2005.
- [26] Glauert, H., “Airplane propellers,” *Aerodynamic theory*, Springer, 1935, pp. 169–360.
- [27] Sharpe, D. J., “A general momentum theory applied to an energy-extracting actuator disc,” *Wind Energy*, Vol. 7, No. 3, 2004, pp. 177–188.
- [28] Mikkelsen, R., *Actuator disc methods applied to wind turbines*, Ph.D. thesis, Technical University of Denmark, 2003.
- [29] Sørensen, J. N. and Myken, A., “Unsteady actuator disc model for horizontal axis wind turbines,” *Journal of Wind Engineering and Industrial Aerodynamics*, Vol. 39, No. 1, 1992, pp. 139–149.
- [30] Rasmussen, F., Hansen, M. H., Thomsen, K., Larsen, T. J., Bertagnolio, F., Johansen, J., Madsen, H. A., Bak, C., and Hansen, A. M., “Present status of aeroelasticity of wind turbines,” *Wind energy*, Vol. 6, No. 3, 2003, pp. 213–228.
- [31] Drzewiecki, S., *Théorie générale de l’hélice: hélices aériennes et hélices marines*, Gauthier-Villars et cie., 1920.

- [32] Lock, C. N. H., Bateman, H., Townend, H. C. H., Committee, A. R., et al., *Experiments to verify the independence of the elements of an airscrew blade*, HM Stationery Office, 1925.
- [33] Prandtl, L., *Vier abhandlungen zur hydrodynamik und aerodynamik*, Vol. 3, Universitätsverlag Göttingen, 2010.
- [34] Shen, W. Z., Mikkelsen, R., Sørensen, J. N., and Bak, C., “Tip loss corrections for wind turbine computations,” *Wind Energy*, Vol. 8, No. 4, 2005, pp. 457–475.
- [35] Spera, D. A., “Introduction to modern wind turbines,” *Wind turbine technology: fundamental concepts of wind Turbine engineering*. ASME Press, New York, 1994, pp. 47–72.
- [36] Haans, W., Sant, T., van Kuik, G., and van Bussel, G., “Stall in yawed flow conditions: A correlation of blade element momentum predictions with experiments,” *Journal of Solar Energy Engineering*, Vol. 128, No. 4, 2006, pp. 472–480.
- [37] Schepers, J. G., *An engineering model for yawed conditions, developed on the basis of wind tunnel measurements*, Vol. 99, Netherlands Energy Research Foundation ECN, Petten (Netherlands), 1998.
- [38] He, Y. L., Liu, W., Li, Q. M., Liu, J., and Shi, B. N., “Research on the aerodynamic of the wind turbine in the state of steady yaw,” *Journal of Machine Design*, Vol. 4, 2010, pp. 24.
- [39] Madsen, H. A., Sørensen, N. N., and Schreck, S., “Yaw aerodynamics analyzed with three codes in comparison with experiment,” *ASME 2003 Wind Energy Symposium*, American Society of Mechanical Engineers, 2003, pp. 94–103.
- [40] Dai, J. C., Hu, Y. P., Liu, D. S., and Long, X., “Aerodynamic loads calculation and analysis for large scale wind turbine based on combining BEM modified theory with dynamic stall model,” *Renewable Energy*, Vol. 36, No. 3, 2011, pp. 1095–1104.
- [41] Bjorck, A., Thor, S. E., and Brand, A. J., “Dynamic stall and 3D effects,” Tech. rep., ECN-Renewable Energy, Netherlands, 1995.
- [42] Truong, V. K., “A 2-D dynamic stall model based on a hopf bifurcation,” *European rotorcraft forum*, Vol. 19, Associazione Italiana di aeronautica ed astronautica, 1993, pp. 1–14.
- [43] Suzuki, A., *Application of dynamic inflow theory to wind turbine rotors*, Ph.D. thesis, The University of Utah, 2000.
- [44] Viterna, L. A. and Corrigan, R. D., “Fixed pitch rotor performance of large HAWTs,” *NASA Workshop on Large HAWTs. Cleveland, OH*, 1981, pp. 69–85.
- [45] Eggers, A. J. and Digumarthi, R. V., “Approximate scaling of rotational effects of mean aerodynamic moments and power generated by the combined experiment rotor blades operating in deepstalled flow,” Tech. Rep. 12: 33-43, 11th ASME Wind Energy Syrup, ASME Solar Eng. Div., 1992.
- [46] Butterfield, C. P., Scott, G., and Musial, W., “Comparison of wind tunnel airfoil performance data with wind turbine blade data,” *Journal of solar energy engineering*, Vol. 114, No. 2, 1992, pp. 119–124.
- [47] Butterfield, C. P., *Three-dimensional airfoil performance measurements on a rotating wing*, Solar Energy Research Institute, 1989.
- [48] Chaviaropoulos, P. K. and Hansen, M. O. L., “Investigating three-dimensional and rotational effects on wind turbine blades by means of a quasi-3D Navier-Stokes solver,” *Journal of Fluids Engineering*, Vol. 122, No. 2, 2000, pp. 330–336.

- [49] Johansen, J. and Sørensen, N. N., “Aerofoil characteristics from 3D CFD rotor computations,” *Wind Energy*, Vol. 7, No. 4, 2004, pp. 283–294.
- [50] Snel, H., Houwink, R., Bosschers, J., Piers, W. J., van Bussel, G. J. W., and Bruining, A., *Sectional prediction of 3-D effects for stalled flow on rotating blades and comparison with measurements*, Netherlands Energy Research Foundation ECN, 1993.
- [51] Bak, C., Johansen, J., and Andersen, P. B., “Three-dimensional corrections of airfoil characteristics based on pressure distributions,” *Proceedings of the European Wind Energy Conference & Exhibition (EWEC)*, 2006, pp. 1–10.
- [52] Paraschivoiu, I., “Double-multiple streamtube model for studying vertical-axis wind turbines,” *Journal of propulsion and power*, Vol. 4, No. 4, 1988, pp. 370–377.
- [53] Beri, H., Yao, Y., et al., “Double multiple streamtube model and numerical analysis of vertical axis wind turbine,” *Energy and Power Engineering*, Vol. 3, No. 03, 2011, pp. 262.
- [54] Mieras, S., Ashuri, T., Scheijground, P., and van Bussel, G. V., “Structural Design Analysis of a novel Tidal Turbine,” *European Wind Energy Conference and Exhibition, Warsaw, Poland*, The European Wind Energy Association, 2010, pp. 1–6.
- [55] Camporeale, S. M. and Magi, V., “Streamtube model for analysis of vertical axis variable pitch turbine for marine currents energy conversion,” *Energy conversion and management*, Vol. 41, No. 16, 2000, pp. 1811–1827.
- [56] Savenije, L. B., Ashuri, T., van Bussel, G. J. W., and Staerdahl, J. W., “Dynamic modeling of a spar-type floating offshore wind turbine,” *European Wind Energy Conference and Exhibition, Warsaw, Poland*, European Wind Energy Association, 2010, pp. 1–10.
- [57] Prandtl, L., “Tragflügel-Theorie, 1. u. 2,” 1918.
- [58] Prandtl, L., *Applications of modern hydrodynamics to aeronautics*, National Advisory Committee for Aeronautics, 1923.
- [59] Kutta, W. M., “Auftriebskräfte in strömenden Flüssigkeiten,” *Illustrierte Aeronautische Mitteilungen*, Vol. 6, 1902, pp. 133–135.
- [60] Joukowski, N., “Sur les tourbillons adjoints,” 1906.
- [61] Richardson, S. M. and Cornish, A. R. H., “Solution of three-dimensional incompressible flow problems,” *Journal of fluid Mechanics*, Vol. 82, No. 02, 1977, pp. 309–319.
- [62] Van Garrel, A., *Development of a wind turbine aerodynamics simulation module*, Citeseer, 2003.
- [63] Bhagwat, M. J. and Leishman, J. G., “Generalized viscous vortex model for application to free-vortex wake and aeroacoustic calculations,” *Annual forum proceedings American helicopter society*, Vol. 58, AMERICAN HELICOPTER SOCIETY, INC, 2002, pp. 2042–2057.
- [64] Scully, M. and Sullivan, J. P., *Helicopter rotor wake geometry and airloads and development of laser Doppler velocimeter for use in helicopter rotor wakes*, MIT Aerophysics Laboratory, 1972.
- [65] Vatistas, G. H., Kozel, V., and Mih, W. C., “A simpler model for concentrated vortices,” *Experiments in Fluids*, Vol. 11, No. 1, 1991, pp. 73–76.
- [66] Gould, J. and Fiddes, S. P., “Computational methods for the performance prediction of HAWTS,” *Journal of Wind Engineering and Industrial Aerodynamics*, Vol. 39, No. 1, 1992, pp. 61–72.

- [67] Robison, D. J., Coton, F. N., Galbraith, R. A. M. C. D., and Vezza, M., “Application of a prescribed wake aerodynamic prediction scheme to horizontal axis wind turbines in axial flow,” *Wind Engineering*, Vol. 19, No. 1, 1995, pp. 41–51.
- [68] Coton, F. N. and Wang, T., “The prediction of horizontal axis wind turbine performance in yawed flow using an unsteady prescribed wake model,” *Proceedings of the Institution of Mechanical Engineers, Part A: Journal of Power and Energy*, Vol. 213, No. 1, 1999, pp. 33–43.
- [69] Currin, H. D., Coton, F. N., and Wood, B., “Dynamic prescribed vortex wake model for AERODYN/FAST,” *Journal of Solar Energy Engineering*, Vol. 130, No. 031007, 2008, pp. 1–7.
- [70] Afjeh, A. A. and Keith, T. G., “A simplified free wake method for horizontal-axis wind turbine performance prediction,” *Journal of fluids engineering*, Vol. 108, No. 4, 1986, pp. 400–406.
- [71] Simoes, F. J. and Graham, J. M. R., “Application of a free vortex wake model to a horizontal axis wind turbine,” *Journal of Wind Engineering and Industrial Aerodynamics*, Vol. 39, No. 1, 1992, pp. 129–138.
- [72] Afjeh, A. A. and Keith, T. G., “A vortex lifting line method for the analysis of horizontal axis wind turbines,” *Journal of solar energy engineering*, Vol. 108, No. 4, 1986, pp. 303–309.
- [73] Miller, R. H., “The aerodynamics and dynamic analysis of horizontal axis and wind turbines,” *Journal of Wind Engineering and Industrial Aerodynamics*, Vol. 15, No. 1, 1983, pp. 329–340.
- [74] Koh, S. G. and Wood, D. H., “Formulation of a vortex wake model for horizontal-axis wind turbines,” *Wind Engineering*, Vol. 15, No. 4, 1991, pp. 196–210.
- [75] Bertin, J. J. and Smith, M. L., *Aerodynamics for engineers*, Prentice Hall, 1998.
- [76] Mughal, B. and Drela, M., “A calculation method for the three-dimensional boundary-layer equations in integral form,” *AIAA Paper*, Vol. 786, 1993, pp. 1–10.
- [77] Riziotis, V. A. and Voutsinas, S. G., “Dynamic stall on wind turbine rotors: comparative evaluation study of different models,” *EWEC conference, 1997*, pp. 481–484.
- [78] Chaviaropoulos, P. K., Nikolaou, I. G., Aggelis, K. A., Sørensen, N. N., Johansen, J., Hansen, M. O. L., Gaunaa, M., Hambræus, T., von Geyr, H., and Hirsch, C., “Viscous and aeroelastic effects on wind turbine blades. The VISCEL project. Part I: 3D Navier–Stokes rotor simulations,” *Wind Energy*, Vol. 6, No. 4, 2003, pp. 365–385.
- [79] Katz, J. and Plotkin, A., *Low-speed aerodynamics*, Vol. 13, Cambridge University Press, 2001.
- [80] Preuss, R. D., Suci, E. O., and Morino, L., “Unsteady potential aerodynamics of rotors with applications to horizontal-axis windmills,” *AIAA Journal*, Vol. 18, No. 4, 1980, pp. 385–393.
- [81] Datta, A., Nixon, M., and Chopra, I., “Review of rotor loads prediction with the emergence of rotorcraft CFD,” *Journal of the American Helicopter Society*, Vol. 52, No. 4, 2007, pp. 287–317.
- [82] Reynolds, O., “On the dynamical theory of incompressible viscous fluids and the determination of the criterion,” *Philosophical Transactions of the Royal Society of London*, 1895, pp. 123–164.
- [83] Brodeur, R. R. and Van Dam, C. P., “Transition prediction for a two-dimensional reynolds-averaged navier–stokes method applied to wind turbine airfoils,” *Wind Energy*, Vol. 4, No. 2, 2001, pp. 61–75.
- [84] Schmitt, F. G., “About Boussinesq’s turbulent viscosity hypothesis: historical remarks and a direct evaluation of its validity,” *Comptes Rendus Mécanique*, Vol. 335, No. 9, 2007, pp. 617–627.

- [85] Baldwin, B. S. and Lomax, H., *Thin layer approximation and algebraic model for separated turbulent flows*, Vol. 257, American Institute of Aeronautics & Astronautics, 1978.
- [86] Spalart, P. R. and Allmaras, S. R., “A one-equation turbulence model for aerodynamic flows,” *AIAA Journal*, Vol. 92, No. 0439, 1992, pp. 1–22.
- [87] Baldwin, B. S. and Barth, T. J., *A one-equation turbulence transport model for high Reynolds number wall-bounded flows*, National Aeronautics and Space Administration, Ames Research Center, 1990.
- [88] Launder, B. E. and Spalding, D. B., “The numerical computation of turbulent flows,” *Computer methods in applied mechanics and engineering*, Vol. 3, No. 2, 1974, pp. 269–289.
- [89] Wilcox, D. C., “Formulation of the k - ω Turbulence Model Revisited,” *American Institute of Aeronautics & Astronautics*, Vol. 46, No. 11, 2008, pp. 2823–2838.
- [90] Menter, F. R., “Two-equation eddy-viscosity turbulence models for engineering applications,” *American Institute of Aeronautics & Astronautics*, Vol. 32, No. 8, 1994, pp. 1598–1605.
- [91] Baxevanou, C. A., Chaviaropoulos, P. K., Voutsinas, S. G., and Vlachos, N. S., “Evaluation study of a Navier–Stokes CFD aeroelastic model of wind turbine airfoils in classical flutter,” *Journal of wind engineering and industrial aerodynamics*, Vol. 96, No. 8, 2008, pp. 1425–1443.
- [92] Potsdam, M. A. and Pulliam, T. H., “Turbulence modeling treatment for rotorcraft wakes,” *AHS Specialist’s Conference on Aeromechanics*, 2008, pp. 23–25.
- [93] El Kasmi, A. and Masson, C., “An extended k - ϵ model for turbulent flow through horizontal-axis wind turbines,” *Journal of Wind Engineering and Industrial Aerodynamics*, Vol. 96, No. 1, 2008, pp. 103–122.
- [94] Gómez-Elvira, R., Crespo, A., Migoya, E., Manuel, F., and Hernández, J., “Anisotropy of turbulence in wind turbine wakes,” *Journal of Wind Engineering and Industrial Aerodynamics*, Vol. 93, No. 10, 2005, pp. 797–814.
- [95] Le Pape, A. and Lecanu, J., “3D Navier–Stokes computations of a stall-regulated wind turbine,” *Wind Energy*, Vol. 7, No. 4, 2004, pp. 309–324.
- [96] Launder, B. E., Reece, G. J., and Rodi, W., “Progress in the development of a Reynolds-stress turbulence closure,” *Journal of fluid mechanics*, Vol. 68, No. 03, 1975, pp. 537–566.
- [97] Réthoré, P. E., *Wind turbine wake in atmospheric turbulence*, Ph.D. thesis, Aalborg: Department of Civil Engineering, 2009.
- [98] Strelets, M., *Detached eddy simulation of massively separated flows*, American Institute of Aeronautics & Astronautics, 2001.
- [99] Bechmann, A. and Sørensen, N. N., “Hybrid RANS/LES method for wind flow over complex terrain,” *Wind Energy*, Vol. 13, No. 1, 2010, pp. 36–50.
- [100] Lopes, A. S., Palma, J. M. L. M., and Castro, F. A. A., “Simulation of the Askervein flow. Part 2: Large-eddy simulations,” *Boundary-layer meteorology*, Vol. 125, No. 1, 2007, pp. 85–108.
- [101] Piomelli, U., “Wall-layer models for large-eddy simulations,” *Progress in aerospace sciences*, Vol. 44, No. 6, 2008, pp. 437–446.
- [102] Sørensen, N. N., “CFD modelling of laminar-turbulent transition for airfoils and rotors using the γ - Re_θ model,” *Wind Energy*, Vol. 12, No. 8, 2009, pp. 715–733.
- [103] Benjanirat, S., Sankar, L. N., and Xu, G., “Evaluation of turbulence models for the prediction of wind turbine aerodynamics,” *ASME 2003 Wind Energy Symposium*, American Society of Mechanical Engineers, 2003, pp. 73–83.

- [104] Xu, G. and Sankar, L. N., “Effects of transition, turbulence and yaw on the performance of horizontal axis wind turbines,” *AIAA paper*, Vol. 48, No. 16910, 2000, pp. 259–265.
- [105] Germano, M., Piomelli, U., Moin, P., and Cabot, W. H., “A dynamic subgrid-scale eddy viscosity model,” *Physics of Fluids A: Fluid Dynamics (1989-1993)*, Vol. 3, No. 7, 1991, pp. 1760–1765.
- [106] Smagorinsky, J., “General circulation experiments with the primitive equations: I. The basic experiment*,” *Monthly weather review*, Vol. 91, No. 3, 1963, pp. 99–164.
- [107] Geurts, B. J. and Holm, D. D., “Regularization modeling for large-eddy simulation,” *Physics of Fluids (1994-present)*, Vol. 15, No. 1, 2003, pp. L13–L16.
- [108] Hughes, T. J. R., Mazzei, L., and Jansen, K. E., “Large eddy simulation and the variational multiscale method,” *Computing and Visualization in Science*, Vol. 3, No. 1-2, 2000, pp. 47–59.
- [109] Lilly, D. K., “A proposed modification of the Germano subgrid-scale closure method,” *Physics of Fluids A: Fluid Dynamics (1989-1993)*, Vol. 4, No. 3, 1992, pp. 633–635.
- [110] Piomelli, U. and Balaras, E., “Wall-layer models for large-eddy simulations,” *Annual review of fluid mechanics*, Vol. 34, No. 1, 2002, pp. 349–374.
- [111] Monin, A. S. and Obukhov, A. M., “Basic laws of turbulent mixing in the atmosphere near the ground,” *Tr. Akad. Nauk SSSR Geofiz. Inst*, Vol. 24, No. 151, 1954, pp. 163–187.
- [112] Klein, M., Sadiki, A., and Janicka, J., “A digital filter based generation of inflow data for spatially developing direct numerical or large eddy simulations,” *Journal of computational Physics*, Vol. 186, No. 2, 2003, pp. 652–665.
- [113] Lund, T. S., Wu, X., and Squires, K. D., “Generation of turbulent inflow data for spatially-developing boundary layer simulations,” *Journal of computational physics*, Vol. 140, No. 2, 1998, pp. 233–258.
- [114] Mann, J., “Wind field simulation,” *Probabilistic engineering mechanics*, Vol. 13, No. 4, 1998, pp. 269–282.
- [115] Veers, P. S., “Three-dimensional wind simulation,” Tech. rep., Sandia National Labs., Albuquerque, NM (USA), 1988.
- [116] Jarrin, N., Benhamadouche, S., Laurence, D., and Prosser, R., “A synthetic-eddy-method for generating inflow conditions for large-eddy simulations,” *International Journal of Heat and Fluid Flow*, Vol. 27, No. 4, 2006, pp. 585–593.
- [117] Moeng, C. H., “A large-eddy-simulation model for the study of planetary boundary-layer turbulence,” *Journal of the Atmospheric Sciences*, Vol. 41, No. 13, 1984, pp. 2052–2062.
- [118] Stovall, T. D., Pawlas, G., and Moriarty, P. J., “Wind farm wake simulations in OpenFOAM,” *AIAA Paper*, Vol. 825, 2010, pp. 1–13.
- [119] Karman, T., “von: Mechanische Ähnlichkeit und Turbulenz. Nachr. Ges. Wiss. Göttingen,” *Proc. 3. Int. Cong. Appl. Mech*, Vol. 58–76, 1930, pp. 322–346, Math.-Phys. Kl.(1930).
- [120] George, W. K., “Is there a universal log law for turbulent wall-bounded flows?” *Philosophical Transactions of the Royal Society A: Mathematical, Physical and Engineering Sciences*, Vol. 365, No. 1852, 2007, pp. 789–806.
- [121] Spalart, P., “Turbulence. Are we getting smarter,” *Fluid dynamics award lecture, 36th fluid dynamics conference and exhibit, San Francisco, CA*, 2006, pp. 5–8.
- [122] Nikuradse, J., “Strömungsgestze in rauhen Röhren,” *Forschung Arb. VDI Verlag*, Vol. 361, 1933, pp. 1–22.

- [123] Cebeci, T. and Bradshaw, P., *Momentum transfer in boundary layers*, Vol. 1, Hemisphere Publishing Corp., 1977.
- [124] Tabor, G. R. and Baba-Ahmadi, M. H., “Inlet conditions for large eddy simulation: a review,” *Computers & Fluids*, Vol. 39, No. 4, 2010, pp. 553–567.
- [125] Hargreaves, D. M. and Wright, N. G., “On the use of the $k-\varepsilon$ model in commercial CFD software to model the neutral atmospheric boundary layer,” *Journal of Wind Engineering and Industrial Aerodynamics*, Vol. 95, No. 5, 2007, pp. 355–369.
- [126] Thompson, J. F., Warsi, Z. U. A., and Mastin, C. W., *Numerical grid generation: foundations and applications*, Vol. 45, North-holland Amsterdam, 1985.
- [127] Clarke, D. K., Hassan, H. A., and Salas, M. D., “Euler calculations for multielement airfoils using Cartesian grids,” *AIAA Journal*, Vol. 24, No. 3, 1986, pp. 353–358.
- [128] Peraire, J., Vahdati, M., Morgan, K., and Zienkiewicz, O. C., “Adaptive remeshing for compressible flow computations,” *Journal of computational physics*, Vol. 72, No. 2, 1987, pp. 449–466.
- [129] Cieslak, S., Khelil, S. B., Choquet, I., and Merlen, A., “Cut cell strategy for 3-D blast waves numerical simulations,” *Shock Waves*, Vol. 10, No. 6, 2001, pp. 421–429.
- [130] Gao, F., Ingram, D. M., Causon, D. M., and Mingham, C. G., “The development of a Cartesian cut cell method for incompressible viscous flows,” *International journal for numerical methods in fluids*, Vol. 54, No. 9, 2007, pp. 1033–1053.
- [131] Ingram, D. M., Causon, D. M., and Mingham, C. G., “Developments in Cartesian cut cell methods,” *Mathematics and Computers in Simulation*, Vol. 61, No. 3, 2003, pp. 561–572.
- [132] Johnson, M. W., “A novel Cartesian CFD cut cell approach,” *Computers & Fluids*, Vol. 79, 2013, pp. 105–119.
- [133] Shu, C. W., “High-order finite difference and finite volume WENO schemes and discontinuous Galerkin methods for CFD,” *International Journal of Computational Fluid Dynamics*, Vol. 17, No. 2, 2003, pp. 107–118.
- [134] Zahle, F. and Sørensen, N. N., “Overset grid flow simulation on a modern wind turbine,” *AIAA Paper*, Vol. 6727, 2008, pp. 1–17.
- [135] Nemec, M., Aftosmis, M. J., and Wintzer, M., “Adjoint-based adaptive mesh refinement for complex geometries,” *AIAA Paper*, Vol. 725, 2008, pp. 1–23.
- [136] Berger, M. J. and Olinger, J., “Adaptive mesh refinement for hyperbolic partial differential equations,” *Journal of computational Physics*, Vol. 53, No. 3, 1984, pp. 484–512.
- [137] Wintzer, M., Nemec, M., and Aftosmis, M. J., “Adjoint-based adaptive mesh refinement for sonic boom prediction,” *AIAA Paper*, Vol. 6593, 2008, pp. 1–19.
- [138] Kim, H. J. and Nakahashi, K., “Output-based error estimation and adaptive mesh refinement using viscous adjoint method,” *American Institute of Aeronautics and Astronautics, Paper AIAA-2006-1395*, Vol. 1395, 2006, pp. 1–17.
- [139] Oliver, T. A., *A high-order, adaptive, discontinuous Galerkin finite element method for the Reynolds-averaged Navier-Stokes equations*, Ph.D. thesis, Massachusetts Institute of Technology (MIT), 2008.
- [140] Hartmann, R., Held, J., and Leicht, T., “Adjoint-based error estimation and adaptive mesh refinement for the RANS and $k-\omega$ turbulence model equations,” *Journal of Computational Physics*, Vol. 230, No. 11, 2011, pp. 4268–4284.

- [141] Fidkowski, K. J. and Darmofal, D. L., “Review of output-based error estimation and mesh adaptation in computational fluid dynamics,” *AIAA Journal*, Vol. 49, No. 4, 2011, pp. 673–694.
- [142] Müller, J. -D. and Giles, M. B., “Solution adaptive mesh refinement using adjoint error analysis,” *AIAA Paper*, Vol. 2550, 2001, pp. 1–10.
- [143] Sørensen, N. N. and Hansen, M. O. L., “Rotor performance predictions using a Navier-Stokes method,” *American Institute of Aeronautics & Astronautics*, Vol. 98, 1998, pp. 52–59.
- [144] Sørensen, N. N., Michelsen, J. A., and Schreck, S., “Navier–Stokes predictions of the NREL phase VI rotor in the NASA Ames 80 ft× 120 ft wind tunnel,” *Wind Energy*, Vol. 5, No. 2-3, 2002, pp. 151–169.
- [145] Choi, Y. H. and Merkle, C. L., “The application of preconditioning in viscous flows,” *Journal of Computational Physics*, Vol. 105, No. 2, 1993, pp. 207–223.
- [146] Chaviaropoulos, P. K., Sørensen, N. N., Hansen, M. O. L., Nikolaou, I. G., Aggelis, K. A., Johansen, J., Gaunaa, M., Hambaas, T., von Geyr, H. F., and Hirsch, C., “Viscous and aeroelastic effects on wind turbine blades. The VISCEL project. Part II: Aeroelastic stability investigations,” *Wind Energy*, Vol. 6, No. 4, 2003, pp. 387–403.
- [147] Simms, D. A., Schreck, S., Hand, M., and Fingersh, L. J., *NREL unsteady aerodynamics experiment in the NASA-Ames wind tunnel: a comparison of predictions to measurements*, National Renewable Energy Laboratory, 1617 Cole Boulevard Golden, Colorado USA, 2001.
- [148] Duque, E. P. N., Burklund, M. D., and Johnson, W., “Navier-Stokes and comprehensive analysis performance predictions of the NREL phase VI experiment,” *American Institute of Aeronautics & Astronautics*, Vol. 125, No. 4, 2003, pp. 457–467.
- [149] Johansen, J., Sørensen, N. N., Michelsen, J. A., and Schreck, S., “Detached-eddy simulation of flow around the NREL phase-VI blade,” *ASME 2002 Wind Energy Symposium*, American Society of Mechanical Engineers, 2002, pp. 106–114.
- [150] Li, Y., Paik, K. J., Xing, T., and Carrica, P. M., “Dynamic overset CFD simulations of wind turbine aerodynamics,” *Renewable Energy*, Vol. 37, No. 1, 2012, pp. 285–298.
- [151] Stone, C., Lynch, C. E., and Smith, M. J., “Hybrid RANS/LES simulations of a horizontal axis wind turbine,” *48th AIAA Aerospace Sciences Meeting, AIAA-2010-459, Orlando, FL*, Vol. 459, 2010, pp. 1–22.
- [152] Zahle, F., Sørensen, N. N., and Johansen, J., “Wind turbine rotor-tower interaction using an incompressible overset grid method,” *Wind Energy*, Vol. 12, No. 6, 2009, pp. 594–619. doi:10.1002/we.327.
- [153] Potsdam, M. A. and Mavriplis, D. J., “Unstructured mesh CFD aerodynamic analysis of the NREL Phase VI rotor,” *AIAA paper*, Vol. 1221, 2009, pp. 1–18.
- [154] Wissink, A. M., Kamkar, S., Pulliam, T. H., Sitaraman, J., and Sankaran, V., “Cartesian adaptive mesh refinement for rotorcraft wake resolution,” *28th Applied Aerodynamics Conference*, 2010, pp. 1–18.
- [155] Yelmule, M. M., and Anjuri, E. V. S. J., “CFD predictions of NREL phase VI rotor experiments in NASA/AMES wind tunnel,” *International Journal of Renewable Energy Research (IJRER)*, Vol. 3, No. 2, 2013, pp. 261–269.
- [156] Sørensen, N. N., Bechmann, A., and Zahle, F., “3D CFD computations of transitional flows using DES and a correlation based transition model,” *Wind Energy*, Vol. 14, No. 1, 2011, pp. 77–90.

- [157] Hansen, M. O. L. and Johansen, J., “Tip studies using CFD and comparison with tip loss models,” *Wind Energy*, Vol. 7, No. 4, 2004, pp. 343–356.
- [158] Johansen, J. and Sørensen, N. N., “Aerodynamic investigation of winglets on wind turbine blades using CFD,” Tech. rep., Risø National Laboratory, 2006.
- [159] Zahle, F. and Sørensen, N. N., “Characterization of the unsteady flow in the nacelle region of a modern wind turbine,” *Wind Energy*, Vol. 14, No. 2, 2011, pp. 271–283.
- [160] Johansen, J., Madsen, H. A., Sørensen, N. N., and Bak, C., “Numerical Investigation of a Wind Turbine Rotor with an aerodynamically redesigned hub-region,” *2006 European Wind Energy Conference and Exhibition, Athens, Greece*, 2006, pp. 1–9.
- [161] Chao, D. D. and Van Dam, C. P., “Computational aerodynamic analysis of a blunt trailing-edge airfoil modification to the NREL Phase VI rotor,” *Wind Energy*, Vol. 10, No. 6, 2007, pp. 529–550.
- [162] Kim, T., Jeon, M., Lee, S., and Shin, H., “Numerical simulation of flatback airfoil aerodynamic noise,” *Renewable Energy*, Vol. 65, 2014, pp. 192–201.
- [163] Ranft, K., Ameri, A. A., Alexander, J. I. D., and Envia, E., “Acoustic Analysis of the NREL Phase VI Wind Turbine,” *ASME Turbo Expo 2010: Power for Land, Sea, and Air*, American Society of Mechanical Engineers, 2010, pp. 911–922.
- [164] Williams, J. E. F. and Hawkings, D. L., “Sound generation by turbulence and surfaces in arbitrary motion,” *Philosophical Transactions of the Royal Society of London. Series A, Mathematical and Physical Sciences*, Vol. 264, No. 1151, 1969, pp. 321–342.
- [165] Hansen, M. O. L., Sørensen, N. N., and Michelsen, J. A., “Extraction of lift, drag and angle of attack from computed 3-D viscous flow around a rotating blade,” *European Wind Energy Conference*, 1997, pp. 1–9.
- [166] Sezer-Uzol, N., Gupta, A., and Long, L. N., “3-D time-accurate inviscid and viscous CFD simulations of wind turbine rotor flow fields,” *Parallel Computational Fluid Dynamics 2007*, Springer, 2009, pp. 457–464.
- [167] Tongchitpakdee, C., Benjanirat, S., and Sankar, L. N., “Numerical simulation of the aerodynamics of horizontal axis wind turbines under yawed flow conditions,” *Journal of solar energy engineering*, Vol. 127, No. 4, 2005, pp. 464–474.
- [168] Zahle, F. and Sørensen, N. N., “On the influence of far-wake resolution on wind turbine flow simulations,” *Journal of Physics: Conference Series*, Vol. 75, IOP Publishing, 2007, pp. 1–9.
- [169] Schmitz, S. and Chattot, J. J., “A coupled Navier–Stokes/Vortex–Panel solver for the numerical analysis of wind turbines,” *Computers & fluids*, Vol. 35, No. 7, 2006, pp. 742–745.
- [170] Vermeer, L. J., Sørensen, J. N., and Crespo, A., “Wind turbine wake aerodynamics,” *Progress in aerospace sciences*, Vol. 39, No. 6, 2003, pp. 467–510.
- [171] Sanderse, B., van der Pijl, S. P., and Koren, B., “Review of computational fluid dynamics for wind turbine wake aerodynamics,” *Wind Energy*, Vol. 14, No. 7, 2011, pp. 799–819.
- [172] Haghi, R., Ashuri, T., van der Valk, P. L. C., and Molenaar, D. P., “Integrated multidisciplinary constrained optimization of offshore support structures,” *Journal of Physics: Conference Series*, Vol. 555, No. 1, 2014, pp. 012046. doi:10.1088/1742-6596/555/1/012046.
- [173] Zwick, D., Muskulus, M., and Moe, G., “Iterative optimization approach for the design of full-height lattice towers for offshore wind turbines,” *Energy Procedia*, Vol. 24, 2012, pp. 297–304.

- [174] Thiry, A., Rigo, P., Buldgen, L., Raboni, G., and Bair, F., “Optimization of monopile offshore wind structures,” *Marine structures*, 2011.
- [175] Li, J. Y., Li, R., Gao, Y., and Huang, J., “Aerodynamic optimization of wind turbine airfoils using response surface techniques,” *Proceedings of the Institution of Mechanical Engineers, Part A: Journal of Power and Energy*, Vol. 224, No. 6, 2010, pp. 827–838.
- [176] Bizzarrini, N., Grasso, F., and Coiro, D. P., “Genetic algorithms in wind turbine airfoil design,” *EWEA*, Brussels, Belgium, 2011, pp. 1–13.
- [177] Grasso, F., “Usage of numerical optimization in wind turbine airfoil design,” *Journal of Aircraft*, Vol. 48, No. 1, 2011, pp. 248–255.
- [178] Grasso, F., “Hybrid optimization for wind turbine thick airfoils,” *AIAA Proceedings, 9th AIAA Multidisciplinary Design Optimization Specialist Conference*, 2012, pp. 23–26.
- [179] Chen, X. and Agarwal, R., “Optimization of Flatback Airfoils for Wind Turbine Blades Using a Multi-Objective Genetic Algorithm,” *ASME 2012 6th International Conference on Energy Sustainability collocated with the ASME 2012 10th International Conference on Fuel Cell Science, Engineering and Technology*, American Society of Mechanical Engineers, 2012, pp. 1313–1324.
- [180] Ju, Y. P. and Zhang, C. H., “Multi-point robust design optimization of wind turbine airfoil under geometric uncertainty,” *Proceedings of the Institution of Mechanical Engineers, Part A: Journal of Power and Energy*, Vol. 0, 2011, pp. 1–17.
- [181] Maniaci, D. C., “An investigation of WT_perf convergence issues,” *49th AIAA Aerospace Sciences Meeting including the New Horizons Forum and Aerospace Exposition*, Vol. 150, 2011, pp. 1–13.
- [182] Selig, M. S. and Coverstone-Carroll, V. L., “Application of a genetic algorithm to wind turbine design,” *Journal of Energy Resources Technology*, Vol. 118, No. 1, 1996, pp. 22–28.
- [183] Benini, E. and Toffolo, A., “Optimal design of horizontal-axis wind turbines using blade-element theory and evolutionary computation,” *Journal of Solar Energy Engineering*, Vol. 124, No. 4, 2002, pp. 357–363.
- [184] Jureczko, M., Pawlak, M., and Mezyk, A., “Optimisation of wind turbine blades,” *Journal of Materials Processing Technology*, Vol. 167, No. 2, 2005, pp. 463–471.
- [185] Ning, S. A., “A simple solution method for the blade element momentum equations with guaranteed convergence,” *Wind Energy*, Vol. 17, 2013, pp. 19. doi:10.1002/we.1636.
- [186] Méndez, J. and Greiner, D., “Wind blade chord and twist angle optimization using genetic algorithms,” *Proceedings of the Fifth International Conference on Engineering Computational Technology*, B. Topping, G. Montero, and R. Montenegro, eds., Las Palmas de Gran Canaria, Spain, Civil-Comp Press, 2006, pp. 1–19.
- [187] Liu, X., Chen, Y., and Ye, Z., “Optimization model for rotor blades of horizontal axis wind turbines,” *Frontiers of Mechanical Engineering in China*, Vol. 2, No. 4, 2007, pp. 483–488.
- [188] Xuan, H., Weimin, Z., Xiao, L., and Jieping, L., “Aerodynamic and aeroacoustic optimization of wind turbine blade by a genetic algorithm,” *Proceedings of 46th AIAA Aerospace Sciences Meeting and Exhibit*, Vol. 1331, 2008, pp. 1–12.
- [189] Clifton-Smith, M. J., “Wind turbine blade optimisation with tip loss corrections,” *Wind engineering*, Vol. 33, No. 5, 2009, pp. 477–496.

- [190] Lee, K. H., Kim, K. H., Lee, D. H., Lee, K. T., and Park, J. P., “Two-step optimization for wind turbine blade with probability approach,” *Journal of Solar Energy Engineering*, Vol. 132, No. 034503, 2010, pp. 1–5.
- [191] Kenway, G. K. W. and Martins, J. R. R. A., “Aerostructural shape optimization of wind turbine blades considering site-specific winds,” *Proceedings of the 12th AIAA/ISSMO Multidisciplinary Analysis and Optimization Conference*, September 2008.
- [192] Ashuri, T., Zaaier, M. B., Martins, J. R. R. A., van Bussel, G. J. W., and van Kuik, G. A. M., “Multidisciplinary design optimization of offshore wind turbines for minimum levelized cost of energy,” *Renewable Energy*, Vol. 68, 2014, pp. 893–905. doi:10.1016/j.renene.2014.02.045.
- [193] Jeong, J., Park, K., Jun, S., Song, K., and Lee, D. H., “Design optimization of a wind turbine blade to reduce the fluctuating unsteady aerodynamic load in turbulent wind,” *Journal of mechanical science and technology*, Vol. 26, No. 3, 2012, pp. 827–838.
- [194] Fuglsang, P. and Thomsen, K., “Site-specific design optimization of 1.5–2.0 MW wind turbines,” *Journal of solar energy engineering*, Vol. 123, No. 4, 2001, pp. 296–303.
- [195] Xudong, W., Shen, W. Z., Zhu, W. W., Sørensen, J. N., and Jin, C., “Shape optimization of wind turbine blades,” *Wind Energy*, Vol. 12, No. 8, 2009, pp. 781–803.
- [196] Wang, L., Wang, T. G., and Luo, Y., “Improved non-dominated sorting genetic algorithm (NSGA)-II in multi-objective optimization studies of wind turbine blades,” *Applied Mathematics and Mechanics*, Vol. 32, 2011, pp. 739–748.
- [197] Djavareshkian, M. H., Bidarouni, A. L., and Saber, M. R., “New Approach to High-Fidelity Aerodynamic Design Optimization of a Wind Turbine Blade,” *International Journal of Renewable Energy Research (IJRER)*, Vol. 3, No. 3, 2013, pp. 725–734.
- [198] Burger, C. and Hartfield, R., “Wind turbine airfoil performance optimization using the vortex lattice method and a genetic algorithm,” *Proc. of 4th AIAA Energy Conversion Conference, San Diego, CA*, 2006, pp. 1–19.
- [199] Ashuri, T., van Bussel, G. J. W., Zaaier, M. B., and van Kuik, G. A. M., “An analytical model to extract wind turbine blade structural properties for optimization and up-scaling studies,” *The Science of making Torque from Wind, Heraklion, Crete, Greece*, European Academy of Wind Energy, 2010.
- [200] Ashuri, T., van Bussel, G. J. W., Zaaier, M. B., and van Kuik, G. A. M., “Controller design automation for aeroservoelastic design optimization of wind turbines,” *The Science of making Torque from Wind, Heraklion, Crete, Greece*, European Academy of Wind Energy, 2010, pp. 1–7.
- [201] Capponi, P. C., Ashuri, T., van Bussel, G. J. W., and Kallesøe, B., “A non-linear upscaling approach for wind turbine blades based on stresses,” *European Wind Energy Conference and Exhibition, Brussels, Belgium*, European Wind Energy Association, 2011, pp. 1–8.
- [202] Anderson, W. K. and Venkatakrishnan, V., “Aerodynamic design optimization on unstructured grids with a continuous adjoint formulation,” *Computers & Fluids*, Vol. 28, No. 4, 1999, pp. 443–480.
- [203] Beux, F. and Dervieux, A., “Exact-gradient shape optimization of a 2-D Euler flow,” *Finite Elements in Analysis and Design*, Vol. 12, No. 3, 1992, pp. 281–302.
- [204] Hou, G. J. W., Taylor, A. C., and Korivi, V. M., “Discrete shape sensitivity equations for aerodynamic problems,” *International journal for numerical methods in engineering*, Vol. 37, No. 13, 1994, pp. 2251–2266.

- [205] Peter, J. E. V. and Dwight, R. P., “Numerical sensitivity analysis for aerodynamic optimization: A survey of approaches,” *Computers & Fluids*, Vol. 39, No. 3, 2010, pp. 373–391.
- [206] Economou, T. D., Palacios, F., and Alonso, J. J., “A viscous continuous adjoint approach for the design of rotating engineering applications,” *AIAA Paper*, Vol. 2580, 2013, pp. 1–19.
- [207] Ribeiro, A. F. P., Awruch, A. M., and Gomes, H. M., “An airfoil optimization technique for wind turbines,” *Applied Mathematical Modelling*, Vol. 36, No. 10, 2012, pp. 4898–4907.
- [208] Kwon, H. I., You, J. Y., and Kwon, O. J., “Enhancement of wind turbine aerodynamic performance by a numerical optimization technique,” *Journal of mechanical science and technology*, Vol. 26, No. 2, 2012, pp. 455–462.
- [209] Hicks, R. M., Murman, E. M., and Vanderplaats, G. N., “An assessment of airfoil design by numerical optimization,” Tech. Rep. NASA-TM-X-3092, NASA, Moffett Field, CA, 94035, July 1974.
- [210] Hicks, R. M. and Henne, P. A., “Wing design by numerical optimization,” *Journal of Aircraft*, Vol. 15, No. 7, 1978, pp. 407–412.
- [211] Kuruvila, G. and Ta’asan, S., “Pseudo-time method for optimal shape design using the Euler equations,” *Institute for Computer Applications in Science and Engineering*, 1995, pp. 1–21.
- [212] Brown, P. N. and Saad, Y., “Hybrid Krylov methods for nonlinear systems of equations,” *SIAM Journal on Scientific and Statistical Computing*, Vol. 11, No. 3, 1990, pp. 450–481.
- [213] Barth, T. J. and Linton, S. W., “An unstructured mesh newton solver for compressible fluid flow and its parallel implementation,” *AIAA paper*, Vol. 95, No. 0221, 1995, pp. 1–16.
- [214] Arabshahi, A. and Whitfield, D. L., “A multi-block approach to solving the three-dimensional unsteady Euler equations about a wing-pylon-store configuration,” *AIAA Paper*, Vol. 3401, No. 462–474, 1989.
- [215] Walters, R. W., Reu, T., McGrory, W. D., Thomas, J. L., and Richardson, P. F., “A longitudinally-patched grid approach with applications to high speed flows,” *AIAA Paper*, Vol. 88, No. 0715, 1988, pp. 1–13.
- [216] Meakin, R. L., “Moving body overset grid methods for complete aircraft tiltrotor simulations,” *AIAA paper*, Vol. 3350, 1993, pp. 576–588.
- [217] Degand, C. and Farhat, C., “A three-dimensional torsional spring analogy method for unstructured dynamic meshes,” *Computers & structures*, Vol. 80, No. 3, 2002, pp. 305–316.
- [218] Lynch, D. R. and O’Neill, K., “Elastic grid deformation for moving boundary problems in two space dimensions,” *Finite elements in water resources*, Vol. 2, 1980, pp. 111–120.
- [219] Kenway, G. K. W., Kennedy, G. J., and Martins, J. R. R. A., “A CAD-free approach to high-fidelity aerostructural optimization,” *Proceedings of the 13th AIAA/ISSMO Multidisciplinary Analysis Optimization Conference, Fort Worth, TX*, 2010, pp. 1–18.
- [220] Tsai, H. M., Wong, F. A. S., Cai, J., Zhu, Y., and Liu, F., “Unsteady flow calculations with a parallel multiblock moving mesh algorithm,” *AIAA Journal*, Vol. 39, No. 6, 2001, pp. 1021–1029.
- [221] Samareh, J. A., “Survey of shape parameterization techniques for high-fidelity multidisciplinary shape optimization,” *AIAA journal*, Vol. 39, No. 5, 2001, pp. 877–884.
- [222] Pironneau, O., “On optimum profiles in Stokes flow,” *Journal of Fluid Mechanics*, Vol. 59, No. 01, 1973, pp. 117–128.

- [223] Pironneau, O., “On optimum design in fluid mechanics,” *Journal of Fluid Mechanics*, Vol. 64, No. 01, 1974, pp. 97–110.
- [224] Jameson, A., “Aerodynamic design via control theory,” *Journal of scientific computing*, Vol. 3, No. 3, 1988, pp. 233–260.
- [225] Reuther, J. J., Jameson, A., Alonso, J. J., Rimlinger, M. J. J., and Saunders, D., “Constrained multipoint aerodynamic shape optimization using an adjoint formulation and parallel computers, part 1,” *Journal of Aircraft*, Vol. 36, No. 1, 1999, pp. 51–60.
- [226] Reuther, J. J., Jameson, A., Alonso, J. J., Rimlinger, M. J., and Saunders, D., “Constrained multipoint aerodynamic shape optimization using an adjoint formulation and parallel computers, part 2,” *Journal of Aircraft*, Vol. 36, No. 1, 1999, pp. 61–74.
- [227] Martins, J. R. R. A., Alonso, J. J., and Reuther, J. J., “High-fidelity aerostructural design optimization of a supersonic business jet,” *Journal of Aircraft*, Vol. 41, No. 3, 2004, pp. 523–530.
- [228] Anderson, W. K. and Bonhaus, D. L., “Airfoil design on unstructured grids for turbulent flows,” *AIAA journal*, Vol. 37, No. 2, 1999, pp. 185–191.
- [229] Drela, M., “Pros and cons of airfoil optimization,” Chapter in *Frontiers of Computational Fluid Dynamics*, 1998, 1998.
- [230] Nielsen, E. J. and Anderson, W. K., “Aerodynamic design optimization on unstructured meshes using the Navier-Stokes equations,” *AIAA journal*, Vol. 37, No. 11, 1999, pp. 1411–1419.
- [231] Brezillon, J. and Dwight, R. P., “Applications of a discrete viscous adjoint method for aerodynamic shape optimisation of 3D configurations,” *CEAS Aeronautical Journal*, Vol. 3, No. 1, 2012, pp. 25–34.
- [232] Dwight, R. P. and Brezillon, J., “Efficient and robust algorithms for solution of the adjoint compressible Navier–Stokes equations with applications,” *International journal for numerical methods in fluids*, Vol. 60, No. 4, 2009, pp. 365–389.
- [233] Lyu, Z., Kenway, G. K. W., Paige, C., and Martins, J. R. R. A., “Automatic differentiation adjoint of the Reynolds-averaged Navier-Stokes equations with a turbulence model,” *43rd AIAA Fluid Dynamics Conference and Exhibit*, June 2013.
- [234] Chen, S., Lyu, Z., Kenway, G. K. W., and Martins, J. R. R. A., “Aerodynamic shape optimization of the Common Research Model Wing-Body-Tail Configuration,” *Journal of Aircraft*, 2015, pp. 1–29.
- [235] Lyu, Z. and Martins, J. R. R. A., “Aerodynamic design optimization studies of a blended-wing-body aircraft,” *Journal of Aircraft*, 2014, pp. 1–14.
- [236] Lyu, Z., Kenway, G. K. W., and Martins, J. R. R. A., “Aerodynamic shape optimization investigations of the Common Research Model wing benchmark,” *AIAA Journal*, 2014, pp. 1–18.
- [237] Le Pape, A. and Beaumier, P., “Numerical optimization of helicopter rotor aerodynamic performance in hover,” *Aerospace science and technology*, Vol. 9, No. 3, 2005, pp. 191–201.
- [238] Nielsen, E. J., Lee-Rausch, E., and Jones, W. T., “Adjoint-based design of rotors in a noninertial reference frame,” *Journal of Aircraft*, Vol. 47, No. 2, 2010, pp. 638–646.
- [239] Dumont, A., Le Pape, A., Peter, J., and Huberson, S., “Aerodynamic shape optimization of hovering rotors using a discrete adjoint of the Reynolds-Averaged Navier–Stokes Equations,” *Journal of the American Helicopter Society*, Vol. 56, No. 3, 2011, pp. 1–11.

- [240] Choi, S., Lee, K., Potsdam, M. M., and Alonso, J. J., “Helicopter rotor design using a time-spectral and adjoint-based method,” *Journal of Aircraft*, Vol. 51, No. 2, 2014, pp. 412–423.
- [241] Allen, C. B. and Rendall, T. C. S., “CFD-based optimization of hovering rotors using radial basis functions for shape parameterization and mesh deformation,” *Optimization and Engineering*, Vol. 14, No. 1, 2013, pp. 97–118.
- [242] Ganguli, R., “A survey of recent developments in rotorcraft design optimization,” *Journal of Aircraft*, Vol. 41, No. 3, 2004, pp. 493–510.
- [243] Martins, J. R. R. A., Alonso, J. J., and Reuther, J. J., “A coupled-adjoint sensitivity analysis method for high-fidelity aero-structural design,” *Optimization and Engineering*, Vol. 6, No. 1, 2005, pp. 33–62.
- [244] Liem, R. P., Kenway, G. K. W., and Martins, J. R. R. A., “Multimission Aircraft Fuel-Burn Minimization via Multipoint Aerostructural Optimization,” *AIAA Journal*, Vol. 53, No. 1, 2014, pp. 104–122.
- [245] Kenway, G. K. W., Kennedy, G. J., and Martins, J. R. R. A., “Scalable parallel approach for high-fidelity steady-state aeroelastic analysis and adjoint derivative computations,” *AIAA Journal*, Vol. 52, No. 5, 2014, pp. 935–951.
- [246] Kenway, G. K. W. and Martins, J. R. R. A., “Multipoint High-Fidelity Aerostructural Optimization of a Transport Aircraft Configuration,” *Journal of Aircraft*, Vol. 51, No. 1, 2014, pp. 144–160.
- [247] Schaller, R. R., “Moore’s law: past, present and future,” *Spectrum, IEEE*, Vol. 34, No. 6, 1997, pp. 52–59.
- [248] Johnson, F. T., Tinoco, E. N., and Yu, N. J., “Thirty years of development and application of CFD at Boeing Commercial Airplanes, Seattle,” *Computers & Fluids*, Vol. 34, No. 10, 2005, pp. 1115–1151.
- [249] Gallard, F., Meaux, M., Montagnac, M., and Mohammadi, B., “Aerodynamic aircraft design for mission performance by multipoint optimization,” *21st AIAA Computational Fluid Dynamics Conference. American Institute of Aeronautics and Astronautics*, 2013, pp. 1–17.
- [250] Hand, M. M., Simms, D. A., Fingersh, L., Jager, D. W., Cotrell, J. R., Schreck, S., and Larwood, S. M., *Unsteady aerodynamics experiment phase VI: wind tunnel test configurations and available data campaigns*, National Renewable Energy Laboratory, 2001.
- [251] Huyer, S. A., Simms, D., and Robinson, M. C., “Unsteady aerodynamics associated with a horizontal-axis wind turbine,” *AIAA journal*, Vol. 34, No. 7, 1996, pp. 1410–1419.
- [252] Mader, C. A. and Martins, J. R. R. A., “Derivatives for time-spectral computational fluid dynamics using an automatic differentiation adjoint,” *AIAA journal*, Vol. 50, No. 12, 2012, pp. 2809–2819.
- [253] van der Weide, E., Kalitzin, G., Schluter, J., and Alonso, J. J., “Unsteady turbomachinery computations using massively parallel platforms,” *AIAA Paper*, Vol. 421, 2006, pp. 1–16.
- [254] Roe, P. L., “Approximate Riemann solvers, parameter vectors, and difference schemes,” *Journal of computational physics*, Vol. 43, No. 2, 1981, pp. 357–372.
- [255] Van Leer, B., “Towards the ultimate conservative difference scheme. V. A second-order sequel to Godunov’s method,” *Journal of computational physics*, Vol. 32, No. 1, 1979, pp. 101–136.
- [256] Van Albada, G. D., Van Leer, B., and Roberts Jr, W. W., “A comparative study of computational methods in cosmic gas dynamics,” *Astronomy and Astrophysics*, Vol. 108, 1982, pp. 76–84.

- [257] Van Leer, B., “Towards the ultimate conservative difference scheme. II. Monotonicity and conservation combined in a second-order scheme,” *Journal of computational physics*, Vol. 14, No. 4, 1974, pp. 361–370.
- [258] Harten, A. and Osher, S., *Uniformly high-order accurate nonoscillatory schemes*, Springer, 1997.
- [259] Jameson, A., Schmidt, W., and Turkel, E., “Numerical solutions of the Euler equations by finite volume methods using Runge-Kutta time-stepping schemes,” *AIAA Paper*, Vol. 1259, 1981, pp. 1–19.
- [260] Jameson, A., *Transonic flow calculations for aircraft*, Vol. 1127, Springer, 1985.
- [261] Turkel, E., “Preconditioned methods for solving the incompressible and low speed compressible equations,” *Journal of computational physics*, Vol. 72, No. 2, 1987, pp. 277–29.
- [262] Lee, D., *Local preconditioning of the Euler and Navier-Stokes equations*, Ph.D. thesis, University of Michigan, 1996.
- [263] Van Leer, B., Lee, W. T., and Roe, P. L., “Characteristic time-stepping or local preconditioning of the Euler equations,” *10th Computational Fluid Dynamics Conference*, Vol. 1, 1991, pp. 260–282.
- [264] Turkel, E., Radespiel, R., and Kroll, N., “Assessment of preconditioning methods for multidimensional aerodynamics,” *Computers & Fluids*, Vol. 26, No. 6, 1997, pp. 613–634.
- [265] Kalitzin, G., Medic, G., Iaccarino, G., and Durbin, P., “Near-wall behavior of RANS turbulence models and implications for wall functions,” *Journal of Computational Physics*, Vol. 204, No. 1, 2005, pp. 265–291.
- [266] Truong, A. H., Oldfield, C. A., and Zingg, D. W., “Mesh movement for a discrete-adjoint Newton-Krylov algorithm for aerodynamic optimization,” *AIAA journal*, Vol. 46, No. 7, 2008, pp. 1695–1704.
- [267] Reuther, J. J., Jameson, A., Farmer, J., Martinelli, L., and Saunders, D., *Aerodynamic shape optimization of complex aircraft configurations via an adjoint formulation*, Research Institute for Advanced Computer Science, NASA Ames Research Center, 1996.
- [268] Spekrijse, S. P., Prananta, B. B., and Kok, J. C., “A simple, robust and fast algorithm to compute deformations of multi-block structured grids,” Tech. Rep. 105, Nationaal Lucht en Ruimtevaartlaboratorium (NLR), 2002.
- [269] Hascoët, L., “TAPENADE: a tool for Automatic Differentiation of programs,” *Proceedings of 4th European congress on computational methods, ECCOMAS*, 2004, pp. 1–14.
- [270] Mader, C. A., Martins, J. R. R. A., and Alonso, J. J. Van Der Weide, E., “ADjoint: An approach for the rapid development of discrete adjoint solvers,” *AIAA journal*, Vol. 46, No. 4, 2008, pp. 863–873.
- [271] Gill, P. E., Murray, W., and Saunders, M. A., “SNOPT: An SQP algorithm for large-scale constrained optimization,” *SIAM journal on optimization*, Vol. 12, No. 4, 2002, pp. 979–1006.
- [272] Broyden, C. G., “The convergence of single-rank quasi-Newton methods,” *Mathematics of Computation*, Vol. 24, No. 110, 1970, pp. 365–382.
- [273] Martins, J. R. R. A., Sturdza, P., and Alonso, J. J., “The Complex-Step Derivative Approximation,” *ACM Transactions on Mathematical Software*, Vol. 29, No. 3, September 2003, pp. 245–262. doi:10.1145/838250.838251.

- [274] Bertagnolio, F., Sørensen, N. N., Johansen, J., and Fuglsang, P., “Wind turbine airfoil catalogue,” Tech. Rep. Risø- R - 1280(EN), Risø National Laboratory, Roskilde, Denmark, 2001.
- [275] Johansen, J., Sørensen, N. N., and Michelsen, J., “Detached-eddy simulation of flow around the S809 airfoil,” Tech. rep., European Wind Energy Conference and Exhibition (EWEC), 2001.
- [276] Sherry, M., Nemes, A., Jacono, D. L., Blackburn, H. M., and Sheridan, J., “The interaction of helical tip and root vortices in a wind turbine wake,” *Physics of Fluids (1994-present)*, Vol. 25, No. 117102, 2013, pp. 1–16.
- [277] Donkers, J., Brand, A., and Eecen, P., *Offshore wind atlas of the Dutch part of the North Sea*, EWEA, 2011.
- [278] Bak, C., Bitsche, R., Yde, A., Kim, T., Hansen, M. H., Zahle, F., Gaunaa, M., Blasques, J. P. A. A., Døssing, M., Wedel Heinen, J.-J., et al., “Light Rotor: The 10-MW reference wind turbine,” *European Wind Energy Conference & Exhibition*, European Wind Energy Association, 2012.
- [279] Ashuri, T., Martins, J. R. R. A., Zaaijer, M. B., van Bussel, G. J. W., and van Kuik, G. A. M., “Aeroservoelastic design definition of a 20 MW common research wind turbine model,” *Wind Energy*, 2016. doi:10.1002/we.1970.
- [280] Economon, T. D., Palacios, F., and Alonso, J. J., “An Unsteady Continuous Adjoint Approach for Aerodynamic Design on Dynamic Meshes,” *AIAA Paper*, Vol. 2300, 2014, pp. 1–23.
- [281] Mani, K., Lockwood, B. A., and Mavriplis, D. J., “Adjoint-based Unsteady Airfoil Design Optimization with Application to Dynamic Stall,” *AHS Forum*, Vol. 68, 2012, pp. 1–12.
- [282] Zahle, F. and Bak, C. and Guntur, S. and Sørensen, N. N. and Troldborg, N., “Comprehensive aerodynamic analysis of a 10 mw wind turbine rotor using 3D cfd,” *32nd ASME Wind Energy Symposium*, 2014, pp. 1–15.
- [283] Palacios, F., Colonno, M. R., Aranake, A. C., Campos, A., Copeland, S. R., Economon, T. D., Lonkar, A. K., Lukaczyk, T. W., Taylor, T. W. R., and Alonso, J. J., “Stanford University Unstructured (SU2): An open-source integrated computational environment for multi-physics simulation and design,” *AIAA Paper*, Vol. 287, 2013, pp. 1–60.